LAWRENCE
LIVERMORE
NATIONAL
LABORATORY

UCRL-TR-212120

Weighted Essentially Non-Oscillatory Simulations and Modeling of Complex Hydrodynamic Flows. Part 2. Single-Mode Richtmyer-Meshkov Instability with Reshock

M. Latini, O. Schilling

May 10, 2005

This work was performed under the auspices of the U.S. Department of Energy by University of California, Lawrence Livermore National Laboratory under Contract W-7405-Eng-48.

Weighted Essentially Non-Oscillatory Simulations and Modeling of Complex Hydrodynamic Flows. Part 2. Single-Mode Richtmyer-Meshkov Instability with Reshock

Marco Latini* Oleg Schilling†

June 30, 2004

Abstract

The Richtmyer-Meshkov instability is a fundamental fluid instability that occurs when perturbations on an interface separating gases with different properties grow following the passage of a shock. This instability is typically studied in shock tube experiments, and constitutes a fundamental example of a complex hydrodynamic flow. Numerical simulations and models for the instability growth and evolution have also been used to further elucidate the physics of the Richtmyer-Meshkov instability. In the present work, the formally high-order accurate weighted essentially non-oscillatory (WENO) shock-capturing method using a third-order total-variation diminishing (TVD) Runge-Kutta time-evolution scheme (as implemented in the `HOPE` code [68]) is applied to simulate the single-mode Richtmyer-Meshkov instability with reshock in two spatial dimensions. The initial conditions and computational domain for the simulations are modeled after the Collins and Jacobs [29] single-mode, Mach 1.21 air(acetone)/SF_6 shock tube experiment. The following boundary conditions are used: (1) periodic in the spanwise direction corresponding to the cross-section of the test section; (2) outflow at the entrance of the test section in the streamwise direction, and; (3) reflecting at the end wall of the test section in the streamwise direction. The present investigation has three principal motivations: (1) to provide additional validation of the `HOPE` code against available experimental data; (2) to provide numerical simulation data for detailed analysis of mixing induced by the Richtmyer-Meshkov instability with reshock, and; (3) to systematically investigate the dependence of mixing properties on both the order of WENO reconstruction and on the spatial resolution. The present study constitutes the first *comprehensive* application of the high-resolution WENO method to the Richtmyer-Meshkov instability with reshock, as well as analysis of the resulting mixing.

First, analytical, semi-analytical, and phenomenological impulsive, point vortex, perturbation, potential flow, and asymptotic power-law models for the growth of a single- and multi-mode perturbation are reviewed, including models for diffuse and reshocked interfaces. A model for baroclinic circulation deposition is also reviewed. Numerical simulations are performed using the third-, fifth-, and ninth-order WENO method with spatial resolutions corresponding to a uniform grid with 128, 256, and 512 points per initial perturbation wavelength. The density from the fifth- and ninth-order simulation is compared to the corrected experimental PLIF images of Collins and Jacobs at selected times. The amplitude

*Applied and Computational Mathematics, California Institute of Technology, Pasadena, CA 91125. *E-mail:* `mlatini@acm.caltech.edu`

†University of California, Lawrence Livermore National Laboratory, Livermore, CA 94551. *E-mail:* `schilling1@llnl.gov`

obtained from the fifth-order simulation at a resolution of 256 points per initial perturbation wavelength is compared to the experimental data of Collins and Jacobs and to the predictions of linear and nonlinear amplitude growth models before and after reshock. The prediction of the Zhang-Sohn nonlinear amplitude growth model is found to be in best agreement with the amplitude from the simulation prior to reshock. The simulation amplitude data is also in excellent agreement with the experimentally-measured amplitude prior to reshock. The absence of the initial rarefaction wave (resulting from the rupture of the membrane that generates the first shock) in the numerical simulations results in a time lag between the numerical and experimental interface evolution following reshock. The results of this component of the present investigation also serve as an additional validation of the `HOPE` code as applied to a shock-induced hydrodynamic instability.

Second, local and global properties of the mixing during the linear, nonlinear, pre- and post-reshock, and late-time phases are investigated and discussed, including a quantitative investigation of the time-dependence and structure of various related mixing parameters defined in terms of the mole fraction and one-dimensional energy spectra. Spatial averaging of quantities along the spanwise (periodic) flow direction yields streamwise profiles, and is used to define instantaneous Reynolds and Favre averages and fluctuations. The fluctuations are Fourier-transformed along the spanwise direction to define time-dependent energy spectra as a function of the one-dimensional wavenumber. Global statistics are obtained by integrating these spectra over all wavenumbers. Several time-dependent volume-averaged quantities are also considered. The effects of reshock on these quantities are examined and discussed in detail. A comparison of simulations with reflecting and outflow boundary conditions at the end wall of the test section exhibits the effects of additional reflected wave interactions following reshock on the quantities considered. The simulations are carried out to much longer times ($t = 18$ ms) than reported in the experiment ($t = 11$ ms) to study the evolution of profiles, spectra, and statistics in the decay and quasi-decay regimes (corresponding to outflow and reflecting boundary conditions, respectively)—quantities that are not currently experimentally-measurable.

Third, the dependence of the mixing layer width, mixing properties, spectra, and statistics on the grid resolution and on the order of WENO spatial flux reconstruction is comprehensively investigated. Simulations with varying orders of reconstruction and grid resolutions have different intrinsic numerical diffusion arising from the truncation and other numerical errors in the algorithm. Quantities such as mixing fractions and energy spectra are sensitive to the numerical diffusion prior to reshock: it is shown that these sensitivities are significantly amplified following reshock when the energy deposited by the shock on the evolving interface induces the formation of small-scale structures and amplifies the fluctuations of all quantities within the mixing layer. It is shown that simulations on coarse grids and using low orders of WENO reconstruction preserve large-scale structures and symmetry even at late times, while simulations on fine grids and using higher orders of reconstruction exhibit fragmentation of the structures, breaking of symmetry, and increased mixing. The differences between the simulations can be quantified by the time-evolution of the fluctuating kinetic energy and enstrophy, as well as the density and pressure variance. The investigation suggests that similar flow features are qualitatively and quantitatively captured by either increasing the spatial resolution or the order of reconstruction. The computational scaling shows that increasing the order of reconstruction from third to fifth or from fifth to ninth approximately doubles the computational cost. However, for a given order of reconstruction, doubling the spatial resolution from 128 to 256 or from 256 to 512 points per initial perturbation wavelength incurs a five- to eight-fold increase in computational cost.

Based on the results of the present investigation, it is concluded that the WENO method using high-order reconstruction is well-suited for the simulation and analysis of complex hydrodynamic flows induced by shock-interface interactions.

Contents

List of Figures

List of Tables

List of Symbols

$a(t)$	mixing layer amplitude, defined in Eq. (6), page 25
$\hat{a}_0$	dimensionless initial perturbation amplitude, page 38
$a_0^{-(+)}$	pre-shock (post-shock) initial perturbation amplitude, page 27
$a_1^{-(+)}$	pre-reshock (post-reshock) perturbation amplitude, page 76
$a_b(t)$	bubble amplitude, page 25
$\overline{A}$	average of pre-shock and post-shock Atwood numbers A^+ and A^-, page 30
$a_b^{RT(RM)}(t)$	amplitude of a Rayleigh-Taylor (Richtmyer-Meshkov) bubble, page 39
α	angle between the interface and the direction of shock propagation, page 53
$A^{-(+)}$	pre-shock (post-shock) Atwood number, page 27
$a_s(t)$	spike amplitude, page 25
$a_s^{RT(RM)}(t)$	amplitude of a Rayleigh-Taylor (Richtmyer-Meshkov) spike, page 39
β_∞	scaling exponent for the bubble curvature, page 45
$c_r(x, y, t)$	molar concentration of fluid r, defined in Eq. (211), page 64
$c_s(x, y, t)$	speed of sound, page 141
D	mass diffusion coefficient, page 29
$\frac{\mathrm{d}}{\mathrm{d}t}$	convective derivative, page 18
$\overline{\delta}$	average of pre-shock and post-shock characteristic width of the interface δ^+ and δ^-, page 30
$\delta^{-(+)}$	pre-shock (post-shock) characteristic width of the interface, page 30
$\delta(t)$	Dirac delta function, page 26
Δx	grid spacing in the x-direction, page 59
$(\Delta x)_{coarse}$	spacing on the coarse grid, page 126
$(\Delta x)_{fine}$	spacing on the fine grid, page 126
$(\Delta x)_{medium}$	spacing on the medium grid, page 126
Δy	grid spacing in the y-direction, page 59
$\mathbf{e_{exp}}$	vector difference between model predictions when model parameters are obtained from experimental data and simulation mixing layer amplitude, page 75
$\mathbf{e_{sim}}$	vector difference between model predictions when model parameters are obtained from simulation data and simulation mixing layer amplitude, page 75

$E_{\omega''\omega''}(t)$	fluctuating enstrophy per unit volume, defined in Eq. (262), page 110
$E_{\omega''\omega''}(k,t)$	fluctuating enstrophy spectrum, page 101
$E_{\phi\phi}(t)$	statistic, defined in Eq. (258), page 107
$E_{\phi\psi}(k,t)$	energy spectrum corresponding to the correlation of ϕ and ψ, defined in Eq. (249), page 100
$E_{p'p'}(t)$	density variance, defined in Eq. (264), page 110
$E_{p'p'}(k,t)$	pressure variance spectrum, page 104
ϵ_A	small positive distance dependent on the Atwood number, page 32
$\varepsilon(r,\Delta x)$	spatial truncation error of a high-order method with spatial order of accuracy r, defined in Eq. (267), page 179
ϵ_Γ	parameter modifying the initial vortex circulation, page 33
$E_{\rho'\rho'}(t)$	density variance, defined in Eq. (263), page 110
$E_{\rho'\rho'}(k,t)$	density variance spectrum, page 104
$\eta(y,t)$	interfacial perturbation, defined in Eq. (1), page 17
η_{comp}	compression factor, defined in Eq. (223), page 66
$\eta^{(n)}(x,y,t)$	series expansion for the interfacial perturbation $\eta(x,y,t)$, page 34
$E(t)$	total fluctuating kinetic energy per unit volume, defined in Eq. (261), page 107
$E(k,t)$	total fluctuating kinetic energy spectrum, defined in Eq. (253), page 101
$E_{u''u''}(t)$	streamwise fluctuating kinetic energy per unit volume, defined in Eq. (259), page 107
$E_{u''u''}(k,t)$	streamwise fluctuating kinetic energy spectrum, page 101
$E_{v''v''}(t)$	spanwise fluctuating kinetic energy per unit volume, defined in Eq. (260), page 107
$E_{v''v''}(k,t)$	spanwise fluctuating kinetic energy spectrum, page 101
$f_r(x,y,t)$	volume fraction of fluid r, defined in Eq. (194), page 51
g	acceleration, page 26
$\Gamma(t)$	circulation of a vortex sheet, defined in Eq. (46), page 31
$\Gamma^{-(+)}(t)$	negative (positive) circulation, page 77
γ_r	adiabatic exponent of fluid r, page 53
$\gamma(x)$	vortex sheet strength, page 31

$h(t)$	mixing layer width, defined in Eq. (5), page 25
k	wavenumber, page 17
κ	bubble or spike curvature, page 40
$k_{\max}$	Nyquist wavenumber, defined in Eq. (187), page 50
k_n	discrete wavenumber, defined in Eq. (248), page 100
λ	wavelength of perturbation, page 17
$\langle \lambda_i \rangle$	average wavelength of bubbles, page 48
λ_i	bubble diameter, page 47
$\ell_b(t)$	bubble location, page 65
$\ell_{int}(t)$	interface location, page 65
$\ell_s(t)$	spike location, page 65
L_y	spanwise width of the test section, page 59
Ma	shock Mach number, page 17
$\overline{M}(x,y,t)$	mean molecular weight, defined in Eq. (214), page 64
M_r	molecular weight of fluid r, page 64
$m_r(x,y,t)$	mass fraction of fluid r, defined in Eq. (211), page 64
$\mathbf{n}$	normal vector to the interface, page 37
∇^2	Laplacian, page 39
$\omega(x,y,t)$	vorticity field, page 18
$\omega(\lambda_i, \lambda_{i+1})$	bubble merger rate, page 47
$\Omega(t)$	enstrophy, defined in Eq. (255), page 101
$\Omega(x,y,t)$	enstrophy density, defined in Eq. (254), page 101
$\Omega(x,y,t)''$	fluctuating enstrophy density, defined in Eq. (256), page 101
$\Omega(t)''$	fluctuating enstrophy, defined in Eq. (257), page 101
$p(x,y,t)$	pressure field, page 18
$\Phi(x,y,t)$	Schlieren function, defined in Eq. (224), page 69
$\langle \phi \rangle (x,t)$	average of the function $\phi(x,y,t)$ over the periodic (spanwise) direction y, defined in Eq. (234), page 90
$\widetilde{\phi}(x,t)$	Favre average of ϕ, defined in Eq. (236), page 90

$\widehat{\phi}(k,x,t)$	Fourier transform of $\phi(x,y,t)$ in the periodic y-direction, defined in Eq. (246), page 100
$\widehat{\phi}(k_n,x,t)$	discrete Fourier transform of $\phi(x,y,t)$ in the periodic y-direction, defined in Eq. (247), page 100
$\phi(x,y,t)'$	Reynolds fluctuating field, defined in Eq. (235), page 90
$\phi(x,y,t)''$	Favre fluctuating field, defined in Eq. (237), page 90
$\phi_r(x,y,t)$	potential function in fluid r, page 34
$\phi_r^{(n)}(x,y,t)$	terms in series expansion for the potential function $\phi_r(x,y,t)$, page 34
$\langle\phi\rangle_{xy}(t)$	volume average of $\phi(x,y,t)$, defined in Eq. (245), page 98
$P_M^N(z)$	Padé approximant, defined in Eq. (76), page 36
$\psi^{-(+)}$	pre-shock (post-shock) growth reduction factor, page 29
$\psi_1^{-(+)}$	pre-reshock (post-reshock) growth reduction factor, page 76
$\psi(x,y)$	streamfunction, page 32
$P_m(t)$	maximum production fraction, defined in Eq. (242), page 97
$P_t(t)$	production fraction, defined in Eq. (241), page 97
R	radius of curvature, page 44
r	density ratio, page 53
$Re_{\Delta x}$	grid Reynolds number, page 141
$\rho(x,y,t)$	density field, page 18
$\overline{\rho}$	average density, defined in Eq. (29), page 29
$\mathbf{s}$	tangential vector to interface, page 37
σ	initial perturbation growth, defined in Eq. (65), page 34
t	time
t_0	characteristic timescale of the Richtmyer-Meshkov instability, defined in Eq. (151), page 45
τ	rescaled time, defined in Eq. (222), page 65
θ	power-law growth exponent for the mixing layer width, page 49
θ_b	power-law growth exponent for the bubble amplitude, page 48
θ_s	power-law growth exponent for the spike amplitude, page 48
$\Theta(t)$	molecular mixing fraction, defined in Eq. (244), page 98

$\theta(x,t)$	molecular mixing profile, defined in Eq. (240), page 94
$t^{-(+)}$	time before (after) reshock, page 117
$[u]$	jump in u velocity due to the passage of the shock, defined in Eq. (9), page 26
$[u]_1$	jump in u velocity following reshock, page 76
$\overline{\mathbf{u}}(x,y,t)$	density-weighted average velocity, defined in Eq. (88), page 37
$u(x,y,t)$	streamwise velocity, page 18
$\mathbf{u}(x,y,t)$	velocity field, page 18
$v_b(\lambda_i)$	velocity of bubble with diameter λ_i, defined in Eq. (170), page 47
$U^{-(+)}$	first (second) half period, page 77
u_{shock}	shock velocity, page 28
$v(x,y,t)$	spanwise velocity, page 18
v_0	Richtmyer velocity, defined in Eq. (12), page 27
ϖ	eigenvalue in the Duff-Harlow-Hirt analysis for diffuse interfaces, defined in Eq. (31), page 29
$\varpi_0(x/y)$	dimensionless bubble merger rate, page 48
$\langle v_b(\lambda_i)\rangle$	mean velocity for bubbles, page 48
$v_b^{RT(RM)}$	velocity of a Rayleigh-Taylor (Richtmyer-Meshkov) bubble, page 41
$v_s^{RT(RM)}$	velocity of a Rayleigh-Taylor (Richtmyer-Meshkov) spike, page 41
$W(t)$	integral lengthscale, defined in Eq. (198), page 51
$w(z)$	complex potential, defined in Eq. (179), page 49
x	streamwise coordinate in the direction of shock propagation
$X(x,y,t)$	mole fraction, defined in Eq. (216), page 64
$\Xi(t)$	mixing fraction, defined in Eq. (243), page 98
$\xi_b^{RT(RM)}$	parabolic bubble tip approximation for the Rayleigh-Taylor (Richtmyer-Meshkov) instability, defined in Eq. (115), page 41
$\xi(Ma)$	normalized pressure jump, defined in Eq. (208), page 54
$\xi_s^{RT(RM)}$	parabolic spike tip approximation for the Rayleigh-Taylor (Richtmyer-Meshkov) instability, defined in Eq. (115), page 41
$\xi(x,t)$	mixing profile, defined in Eq. (239), page 92
$X_p(x,y,t)$	product mole fraction, defined in Eq. (238), page 92

X_s	parameter for determining $X_p(x, y, t)$, page 92
y	spanwise coordinate in the periodic direction
$Y(t)$	regularized Heaviside function
z	complex variable $z = x + i\,y$, page 49
z_0	separation between vortices, page 49

1 Introduction

The Richtmyer-Meshkov instability occurs when perturbations on the interface separating two different fluids grow following the passage of a shock and eventually develop complex structure. The instability derives its name from the linear instability analysis and numerical work of Richtmyer [106], who considered the instability generated by a shock impulsively accelerating a sinusoidally-perturbed interface. The predictions of Richtmyer were subsequently confirmed in shock tube experiments by Meshkov [82]. This instability is of great fundamental interest in fluid dynamics [127, 18], as well as of interest to inertial confinement fusion [75, 96, 76, 13], and to supernovae dynamics [40, 11, 12, 57, 10]. One of the challenges in understanding the Richtmyer-Meshkov instability is modeling the growth of the mixing layer in the nonlinear phase and following reshock, as well as predicting the statistical properties and dynamics of turbulent mixing induced by this instability.

The classical Richtmyer-Meshkov instability is typically investigated experimentally in shock tubes. Consider a two-dimensional flow, where x is the streamwise direction (the direction of shock propagation) and y is the spanwise direction. Two gases with different densities are initially at rest and separated by a perturbed interface $\eta(y, t = 0)$. A multi-mode initial perturbation can be represented as a superposition of sinusoidal modes

$$\eta(y,0) = \sum_{n=1}^{N} a_n \sin\left(k_n y\right), \tag{1}$$

where $\{a_n\}$ are the initial amplitudes, and

$$\begin{aligned} k_n &= \frac{2\pi}{\lambda_n} \\ &= \frac{2\pi n}{\lambda} \end{aligned} \tag{2}$$

are the wavenumbers with wavelengths $\{\lambda_n\}$. Only a single sinusoidal mode

$$\eta(y,0) = a_0 \sin\left(k\, y\right) \tag{3}$$

is considered in the present investigation (with corresponding wavenumber $k = 2\pi/\lambda$ and $a_1 \rightarrow a_0$), and the gases are taken to be a mixture of air and acetone [denoted air(acetone) in the sequel] and sulfur hexafluoride (SF_6). A planar shock with Mach number Ma is generated in the air(acetone) gas by the rupture of a diaphragm, propagates down the shock tube, enters the test section, and interacts with the perturbed interface.

In the present work, the evolution of the Richtmyer-Meshkov instability is considered in two spatial dimensions using the `HOPE` code (see Part 1 of this report [68] for the governing equations and a detailed description of the code and numerical method). A particular validation of the `HOPE` code using shock refraction theory was also presented in Part 1 [68] of this report. Two-dimensional simulations, analysis and modeling of the Richtmyer-Meshkov instability resulting from the interaction of a planar shock with a perturbed inclined interface, including a study of the effects of shock-interface angle, Mach number, perturbation amplitude, perturbation wavelength, and gas composition are presented in Part 3 of this report [69]. Two- and three-dimensional simulations, analysis, and modeling of the Richtmyer-Meshkov instability with reshock are presented in Part 4 of this report [70]. Molecular dissipation and diffusion effects are

neglected in the present simulations. Hence, these simulations can be regarded as monotone-integrated (or implicit) large-eddy simulations [17, 37, 38].

As the shock passes through the interface, the misalignment of the pressure and density gradients causes a deposition of vorticity through the baroclinic production mechanism illustrated in Fig. 1. Defining the vorticity $\omega = \nabla \times \mathbf{u}$, where $\mathbf{u}$ is the velocity, the vorticity evolution equation (shown here for three dimensions and in the absence of dissipation terms)

$$\frac{\mathrm{d}\omega}{\mathrm{d}t} = (\omega \cdot \nabla)\,\mathbf{u} - \omega\,\nabla \cdot \mathbf{u} + \frac{\nabla\rho \times \nabla p}{\rho^2} \tag{4}$$

describes the dynamics of vorticity generation, where $\mathrm{d}/\mathrm{d}t = \partial/\partial t + \mathbf{u} \cdot \nabla$ is the convective derivative, ρ is the density, and p is the pressure. The first term on the right side is the vortex-stretching term, which is zero in the present two-dimensional investigation, as the vorticity and velocity field are orthogonal. Vortex stretching is a fundamental mechanism in the dynamics of turbulence and distinguishes 'two-dimensional turbulence' [64] from actual three-dimensional turbulence. In particular, vortex stretching is associated with the cascade of energy from large scales to smaller scales through an inertial subrange at sufficiently large Reynolds numbers. In two-dimensional turbulent flows, the energy transfer is predominantly from small scales to larger scales, resulting in the generation of larger and more coherent structures than observed in three-dimensional flows [28]. Vortex stretching enhances dissipation, resulting in more diffuse and smaller scale structures in three dimensions. Thus, the properties of turbulent mixing are expected to be significantly different in two and three dimensions. These differences will be examined in detail in Part 4 [70] of this report. The second term on the right side is the compression term, and does not contribute significantly to the vorticity evolution. The third term on the right side is the baroclinic production term, and constitutes the principal mechanism of vorticity generation by the Richtmyer-Meshkov instability. This term is large when the shock passes through the interface and when waves interact with the interface. Following the passage of the shock, the perturbed interface is set in motion along the direction of shock propagation, a reflected shock returns back into the air(acetone) gas, and a transmitted shock enters the SF_6 gas.

The vorticity baroclinically deposited on the interface by the shock drives the evolution of the instability, with spikes of the heavier fluid (SF_6) penetrating the lighter fluid [air(acetone)] and bubbles of the lighter fluid "rising" in the heavier fluid. When the fluids are miscible, molecular mixing occurs between these interpenetrating fluids, generating a mixing layer and a topologically-complex flow. In the present investigation, explicit molecular mixing is not modeled; instead, numerical diffusion across the interface models the 'molecular mixing' process. At late times, the vorticity coalesces into strong cores causing the characteristic mushroom roll-ups to form, as illustrated in Fig. 1. Additional deposition of vorticity and enhanced mixing occurs when the interface interacts with another shock wave, as in the configuration considered here. The transmitted shock from the initial shock-interface interaction reflects from the end wall of the shock tube test section and interacts with the evolving layer, as illustrated in Fig. 2. This second interaction (referred to as *reshock* in the sequel) deposits vorticity of opposite sign so that bubbles transform into spikes and vice versa in a process called *inversion*. The inversion process induces the formation of additional complex structures, with additional disorganized small-scale flow features observed at late times, as shown in Fig. 3. Following reshock, the interface changes its direction of motion and now moves away from the end wall of the test section: a transmitted shock enters the air(acetone) and a reflected rarefaction returns into the SF_6. Unlike in the case of the first shock-interface interaction, the reflected

wave is now a rarefaction wave, as the shock refracts from the heavier SF_6 gas into the lighter air(acetone) gas. The rarefaction wave is reflected from the end wall of the test section and interacts with the evolving interface, resulting in the formation of additional complex, small-scale structures. Throughout the evolution of the instability, both prior to and following reshock, shear due to the secondary Kelvin-Helmholtz instability [35, 36, 80] develops at the interface. This secondary instability further enhances the development of a complex interface topology with increasing length in two dimensions and surface area in three dimensions, eventually resulting in a mixing layer that becomes turbulent at sufficiently large Reynolds numbers. The single-mode Richtmyer-Meshkov instability with reshock is considered in the present work, as it offers the possibility to observe two phases of the instability development and their coupling: the nonlinear phase prior to reshock, and the post-reshock phase. As summarized below in § 1.1 and 1.2, this flow configuration has not been extensively studied either experimentally or numerically.

1.1 Previous single-mode Richtmyer-Meshkov instability experiments with reshock

Many experiments have been performed to investigate different aspects of the Richtmyer-Meshkov instability (see Brouillette [18] for a recent review). However, most of the experiments conducted to date only consider the evolution of the instability in the linear and nonlinear regimes. Relatively few experiments have been performed to study the dynamics of the flow following reshock. Briefly summarized below are *single-mode, compressible experiments with reshock in a planar geometry*, which are relevant to the present investigation (multi-mode experiments are summarized in Part 4 [70] of this report). The present discussion is limited to classical fluid (shock tube) experiments and does not consider high-energy density (laser-driven) experiments.

Houas and Chemouni [50] performed shock tube experiments using CO_2/He, CO_2/Ar, and CO_2/Kr over a range of shock Mach numbers Ma = 2–4.7 to determine the power-law governing the width of the mixing layer before and after reshock. The measurements were compared against the linear [87] and $t^{2/3}$ [15] growth power-laws, and it was concluded that the data was in good agreement with the $t^{2/3}$ law both before and after reshock. Sadot et al. [110] performed a shock tube experiment using air/SF_6 with $\lambda = 2.6$ cm, $a_0 = 0.2$ cm, and $Ma = 1.3$. Collins and Jacobs [29] performed shock tube experiments using air(acetone)/SF_6 with $\lambda = 5.93$ cm, $a_0 = 0.229$ cm and 0.183 cm for $Ma = 1.11$ and 1.21, respectively. The experimental amplitude growth prior to reshock was compared to the predictions of models. The Collins-Jacobs experiments are described in more detail in § 3.1. The quantitative data obtained from these experiments was mainly limited to perturbation amplitude growth: no detailed data concerning the mixing properties within the layer were available.

1.2 Previous numerical simulations of single-mode Richtmyer-Meshkov instability with reshock

The vast majority of numerical simulations of single- and multi-mode Richtmyer-Meshkov instabilities to date have considered the flow evolution initiated by only a single shock-interface interaction. As in the case of experiments, very few simulations have considered the effects of reshock on an evolving interface. Briefly summarized below are *single-mode, compressible simulations with reshock in a planar geometry*, which are relevant to the present investigation

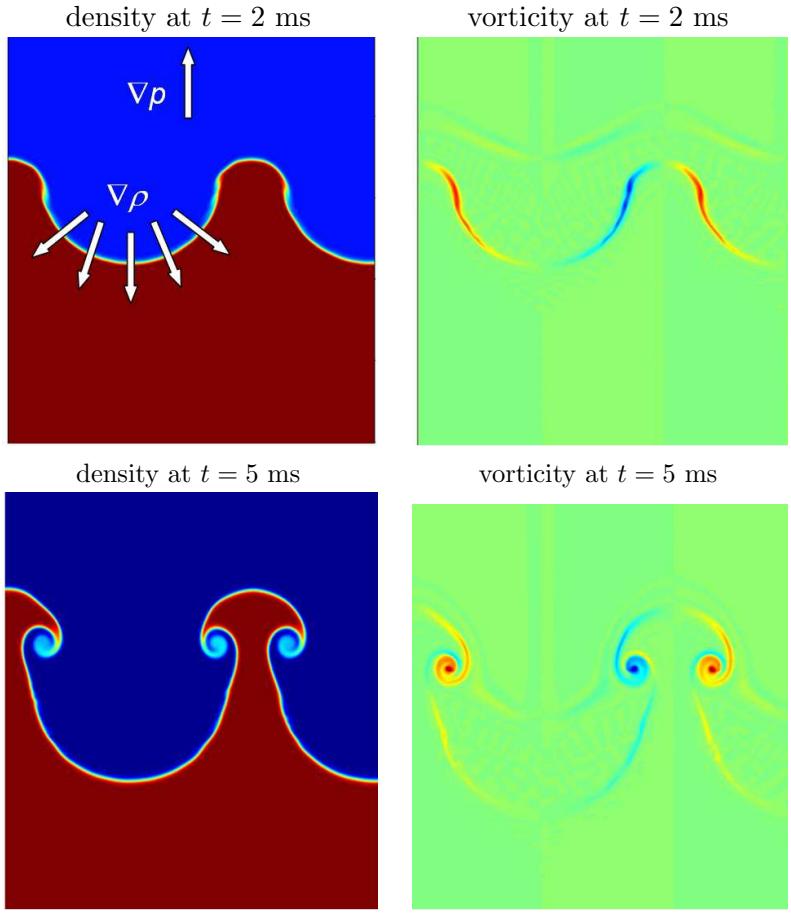

Figure 1: The Richtmyer-Meshkov instability occurs when perturbations on an interface separating two fluids with different properties grow following the passage of a shock. The vorticity deposited baroclinically through the misalignment of the density and pressure gradients drives the evolution of the instability. As the instability develops, spikes of heavier fluid penetrate into the lighter fluid and bubbles of the lighter fluid penetrate into the heavier fluid. The vorticity coalesces into vortices with strong cores forming the characteristic "mushrooms" at late times. The images are taken from the simulation described in § 3.

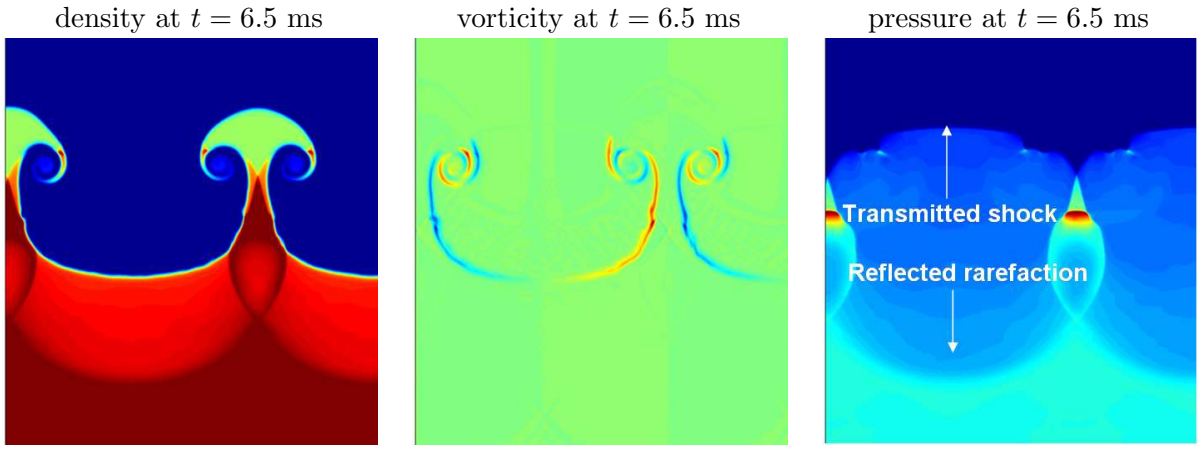

Figure 2: The single-mode Richtmyer-Meshkov instability during reshock. The reflected shock compresses the interface and deposits vorticity of opposite sign on the interface. Note the reflected rarefaction wave and the transmitted shock wave in the pressure. The images are taken from the simulation described in § 3.

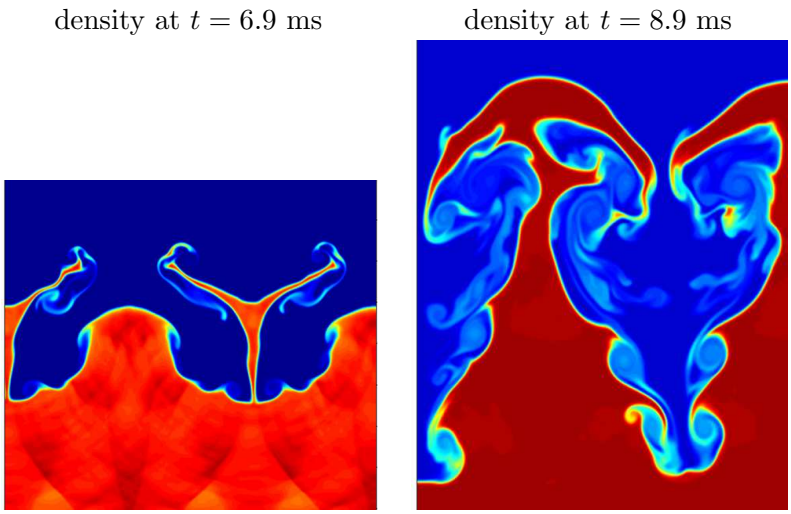

Figure 3: Following reshock of the evolving interface, bubbles transform into spikes and vice versa during the inversion process, causing additional structures to form. At late times, the roll-ups develop more disorganized, small-scale structures. The images are taken from the simulation described in § 3.

(multi-mode simulations are summarized in Part 4 [70] of this report). The present discussion is limited to classical fluid (shock tube) simulations and does not consider simulations in converging geometry.

Mikaelian [91] performed two-dimensional arbitrary Lagrangian-Eulerian (ALE) simulations of gas configurations consisting of three layers, 1/2/1, with fluid 1 representing semi-infinite layers of air and fluid 2 representing a finite-thickness layer of freon, SF_6, or helium, having perturbations either on the upstream or downstream side. These perturbations were in phase (sinuous) or out of phase (varicose). The shock Mach number was 1.5. The primary purpose of the simulations was to investigate freeze-out, interface coupling, and feedthrough. Sadot et al. [110] compared the amplitude growth from their single-mode reshock experiment to numerical simulation data and found very good agreement prior to the arrival of the rarefaction wave from the end wall. As in the case of experiments, the quantitative data obtained from these simulations was mainly limited to the consideration of perturbation amplitude growth.

1.3 Objectives of the current investigation

A central objective of the present work is to establish a systematic methodology for investigating the dynamics of the mixing process induced by the Richtmyer-Meshkov instability, and more generally by complex hydrodynamic flows. The methods used are adapted from classical investigations of turbulence and turbulent mixing, and synthesize high-resolution numerical simulation data, theoretical models for instability growth, and available experimental data. This procedure results in:

1. the application of a modern, high-resolution, flexible, robust numerical method that has been validated against available experimental data;

2. a numerical database that provides quantities that can be compared to model predictions and to experimental measurements, as well as quantities that have not been modeled (or are difficult to model) or are not available experimentally;

3. numerical data for configurations extended to times beyond what is possible to achieve experimentally, or for configurations that are difficult to achieve experimentally;

4. a systematic understanding of the important effects of spatial resolution and formal order of the method on quantities of interest to modeling the instability evolution and mixing.

The present set of simulations can be regarded as numerical experiments with initial and boundary conditions, and flow geometry, selected to closely approximate the Collins-Jacobs Mach 1.21 shock tube experiment. This study is part of a larger, longer-term program directed at:

1. developing improved theoretical models for instability growth in the nonlinear regime, as well as for the more disordered and possibly turbulent evolution following reshock;

2. investigating turbulence closure models for ensemble-averaged descriptions of turbulent transport and mixing, as well as for the development and assessment of subgrid-scale models for large-eddy simulations;

3. improving the numerical methods used to simulate complex hydrodynamic flows induced by shocks;

4. aiding the design of novel experimental configurations and new experimental diagnostics.

This report is organized according to three principal components. First, a comprehensive review of the principal linear and nonlinear models for single- and multi-mode perturbation amplitude growth is presented in § 2, including impulsive, vortex, perturbation, potential flow, and asymptotic power-law growth models. Models for diffuse and reshocked interfaces are also reviewed. Two-dimensional numerical simulations of the single-mode Richtmyer-Meshkov instability with reshock using the fifth-order WENO method (using the `HOPE` code) and a uniform grid resolution based on 256 points per initial perturbation wavelength are performed. The initial conditions and computational domain for the simulations are adapted from the Mach 1.21 air(acetone)/SF_6- shock tube experiment of Collins and Jacobs [29]. The interface (density) evolution is compared to the experimental PLIF images of Collins and Jacobs before and after reshock in § 3. In addition, the mixing layer amplitude from the simulation before and after reshock is compared to the experimental data and to the predictions of the analytical, semi-analytical, and phenomenological models summarized in § 2.

Second, a comprehensive quantitative analysis of the local and global properties of mixing is presented in § 4. The analysis characterizes the mixing process along the direction of shock propagation using mole fractions and a fast kinetic reaction model. The modal distribution of energy in the mixing layer is quantified using a Fourier (spectral) analysis of the fluctuating kinetic energy (and its streamwise and spanwise components) and enstrophy, as well as the pressure variance and the density variance. The evolution of mixing is characterized using mixing fractions before and after reshock up to time $t = 18$ ms. Finally, statistics (wavenumber-integrated energy spectra) are considered to understand the time-evolution of energy present in the fluctuations. Furthermore, to investigate the decay of fluctuations in the mixing layer in the absence of additional waves interacting with the evolving interface following reshock, the boundary condition at the end of the computational domain (corresponding to the end wall of the test section) is changed from reflecting to outflow to allow the reflected rarefaction wave to exit the domain. At late time, this case is referred to as the *decay regime*, as distinguished from the *quasi-decay regime* occurring when reflected waves interact with the evolving interface following reshock. Comparisons of mole fractions, spatially-integrated mixing profiles and fractions, and statistics between the reflecting and outflow boundary condition cases are presented and discussed.

Third, a comprehensive investigation of the dependence of the mixing layer amplitude and of mixing quantities on the order of reconstruction and on the grid resolution is presented in § 5. The results from two-dimensional numerical simulations using third-, fifth-, and ninth-order WENO reconstruction and three different uniform grid resolutions corresponding to 512, 256, and 128 points per initial perturbation wavelength are compared. Simulations with different grid resolutions and orders of reconstruction have different numerical diffusion properties introduced by the algorithm. In particular, high-order, high-resolution simulations have lower numerical diffusion than low-order, low-resolution simulations. The differences in the time-evolution and structure of the mole fractions, spectra, mixing fractions, and statistics are investigated before and after reshock. A temporal progression of the density and vorticity fields is presented at intervals of 1 ms for the three orders of reconstruction and three grid resolutions in § 5.8.

2 Models for perturbation amplitude and mixing layer growth, and for baroclinic circulation deposition

The prediction and modeling of the mixing layer growth in the nonlinear and turbulent regimes resulting from the Richtmyer-Meshkov instability is of great interest. An overview of the principal models categorized according to the underlying physical assumptions on the flow is presented in this section. Note that it is implicitly assumed in all of these models that molecular dissipation and diffusion effects, as well as surface tension and other effects, are negligible (extensions of some of the models to include such effects have been developed, but are not discussed here). While each of these models has important limitations and a limited domain of applicability, they represent an effort to better understand the fundamental aspects of Richtmyer-Meshkov instability growth into the nonlinear regime and following reshock.

Figure 4 shows an illustration of the bubble and spike amplitudes a_b and a_s, respectively, and the mixing layer width h. The blue contour shows a typical early-time evolution of the interface induced by the Richtmyer-Meshkov instability. The spikes penetrate into the lighter fluid and roll up, while bubbles "rise" into the heavier fluid. The solid red line shows the location of the shocked, unperturbed interface used as a reference for the measurements of the bubble and spike amplitudes. The distance from the unperturbed interface to the tip of the bubble represents the bubble amplitude a_b, while the distance from the unperturbed interface to the tip of the spike represents the spike amplitude a_s. The *mixing layer width* is defined as the sum of the bubble and spike amplitudes

$$h(t) = a_b(t) + a_s(t)\,. \tag{5}$$

The *mixing layer amplitude* predicted by the models presented in this section is the average of the bubble and spike amplitude

$$\begin{aligned} a(t) &= \frac{a_b(t) + a_s(t)}{2} \\ &= \frac{h(t)}{2}\,, \end{aligned} \tag{6}$$

i.e., one-half the mixing layer width.

Impulsive models based on representing the shock as a δ-function acceleration are reviewed in § 2.1. Models based on representing the vorticity deposited by the shock as point vortices are reviewed in § 2.2. Models based on asymptotic expansions of the perturbed compressible fluid dynamics equations are reviewed in § 2.3. Models based on potential theory are reviewed in § 2.4. Scaling laws for multi-mode initial conditions are reviewed in § 2.5. Finally, models for the deposition of circulation by a shock are reviewed in § 2.6.

2.1 Impulsive models

Impulsive models based on representing the shock as an instantaneous δ-function acceleration are briefly reviewed and summarized here. Impulsive models for the Richtmyer-Meshkov instability were developed by adapting existing models for the Rayleigh-Taylor instability to the case of an impulsive acceleration. These models predict a linear growth in time for the mixing layer that captures the early stages of the instability evolution before nonlinear effects become dominant.

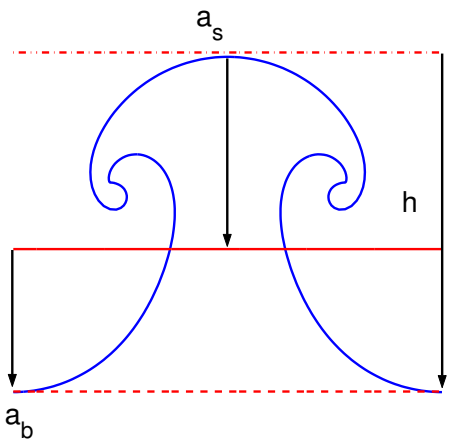

Figure 4: Schematic of the bubble and spike amplitudes a_b and a_s and the mixing layer width h. The solid blue line represents a typical interface evolving according to the single-mode Richtmyer-Meshkov instability with spikes penetrating the lighter fluid and rolling up, and bubbles rising in the lighter fluid. The solid red line is the location of the shocked unperturbed interface and is used as the reference to measure the bubble and spike amplitudes a_b and a_s. The mixing layer width is $h = a_b + a_s$ and the amplitude of the perturbation is $a = (a_b + a_s)/2$. The image is from a simulation of the Richtmyer-Meshkov instability using a point vortex method [67].

2.1.1 The Richtmyer model

The first impulsive model proposed to predict the growth of a single-mode perturbation is due to Richtmyer [106]. Richtmyer modified earlier work by Taylor [119] for the growth of a small perturbation with amplitude $a(t)$ and wavenumber k when a dense fluid is accelerated continuously into a lighter fluid, and the fluids are initially separated by a single-mode interfacial perturbation (the Rayleigh-Taylor instability). Taylor showed that the initial growth of the amplitude of a perturbation under gravitational acceleration g is given by

$$\frac{\mathrm{d}^2 a}{\mathrm{d}t^2} = g\, A\, k\, a\,, \tag{7}$$

where

$$A = \frac{\rho_2 - \rho_1}{\rho_2 + \rho_1} \tag{8}$$

is the Atwood number and ρ_1 and ρ_2 are the densities of the lighter and heavier fluid, respectively. Richtmyer argued that, in the presence of a shock, the acceleration g is very large during a very short time interval. Let

$$[u] = \int g\, \mathrm{d}t \tag{9}$$

represent the change in velocity imparted to the interface by the shock, so that integrating Eq. (7) once gives

$$\frac{\mathrm{d}a}{\mathrm{d}t} = k\,[u]\,A^-\,a_0^-\,, \tag{10}$$

where $a_0^- \equiv a(0)$ is the initial (pre-shock) perturbation amplitude and A^- is the pre-shock Atwood number. Richtmyer argued that the use of a_0^- is almost certainly incorrect, as the initial amplitude is compressed by the shock, and therefore, a smaller value should be used.

To further understand the development of the instability, Richtmyer derived and solved the perturbation equations in the case when the shock propagates from a lighter fluid into a heavier fluid ($A^- > 0$) using a finite-difference scheme. Richtmyer showed that agreement between the numerical solution and the prediction of Eq. (10) is obtained when the post-shock Atwood number A^+ and post-shock amplitude a_0^+ are used:

$$\frac{\mathrm{d}a}{\mathrm{d}t} = v_0 \,, \tag{11}$$

where the Richtmyer velocity is

$$v_0 \equiv k\,[u]\,A^+\,a_0^+ \,, \tag{12}$$

so that

$$\begin{aligned} a(t) &= a_0^+ + v_0\,t \\ &= \left(1 + k\,[u]\,A^+\,t\right) a_0^+ \,. \end{aligned} \tag{13}$$

2.1.2 The Meyer-Blewett model

Meyer and Blewett [83] performed numerical simulations of the Richtmyer-Meshkov instability and computed growth rates corresponding to a shock propagating from a light to a heavy gas and from a heavy to a light gas. They found good agreement with Richtmyer's formula, Eq. (11), for the light to heavy case, but in the heavy to light case they found better agreement by averaging the pre- and post-shock amplitudes

$$\frac{\mathrm{d}a}{\mathrm{d}t} = k\,[u]\,A^+\,\frac{a_0^+ + a_0^-}{2} \,, \tag{14}$$

so that

$$a(t) = a_0^+ + k\,[u]\,A^+\,\frac{a_0^+ + a_0^-}{2}\,t \,. \tag{15}$$

2.1.3 The Fraley model

Fraley [41] presented an analytic solution to the linearized perturbation equations in the case of a reflected shock wave. The complete set of linearized, compressible perturbation equations was first considered by Richtmyer [106], who solved them numerically. Fraley reconsidered the perturbation equations for a single-mode initial perturbation and solved the equations using Laplace transform techniques in time. For weak shocks the solution is given by (see [18])

$$\frac{\mathrm{d}a}{\mathrm{d}t} = k\,[u]\,a_0^- \left[A^- + \epsilon\,\frac{F(c, A^-)}{\gamma_1}\right] , \tag{16}$$

where

$$F(c, A) = \left\{ \frac{(c-1)^2}{2} - \frac{1+A}{1-A} - c + \frac{1}{c}\left[\frac{(1+A)^2}{1-A} + (1-A)\,c^2\right]\right\} \frac{1-A}{c+1} \,, \tag{17}$$

$$c = \sqrt{\frac{(1+A^-)\,\gamma_2}{(1-A^-)\,\gamma_1}} \,, \tag{18}$$

with the Richtmyer model of Eq. (10) recovered in the limit $\epsilon \to 0$. Thus,

$$a(t) = a_0^+ + k\,[u]\left[A^- + \epsilon\,\frac{F(c, A^-)}{\gamma_1}\right] a_0^-\, t. \tag{19}$$

This solution was first recognized by Mikaelian [90] as the most accurate solution for the initial growth of the perturbation. In particular, Mikaelian showed that when A^+ is chosen to be zero, the Richtmyer formula (11) predicts a zero growth rate—the so-called "freeze-out". However, numerical simulations do not show a freeze-out for $A^+ = 0$. Instead, freeze-out is observed when the values of the parameters in Eq. (16) are chosen so that $\mathrm{d}a/\mathrm{d}t = 0$.

2.1.4 The Vandenboomgaerde et al. model

Vandenboomgaerde, Mügler and Gauthier [122] developed an amplitude growth model based on modifying the impulsive acceleration assumption of Richtmyer [106]. Returning to the Rayleigh-Taylor instability result for incompressible flows, Eq. (7), the constant values of the acceleration g, Atwood number A, and amplitude a were replaced by linearly time-varying values from the pre- to post-shock quantities. The linear variation occurs as the shock crosses the interface between times $t_0^- = -a_0^-/(2u_{shock})$ and $t_0^+ = a_0^-/(2u_{shock})$. Therefore,

$$g(t) = \frac{u_{shock}\,[u]}{a_0^-}\, Y_-\,(1 - Y_+)\,, \tag{20}$$

$$A(t) = (1 - Y_-)\,A^- + Y_-\,(1 - Y_+)\left[\frac{u_{shock}\,(A^+ - A^-)\,t}{a_0^-} + \frac{A^+ + A^-}{2}\right] + Y_+\,A^+\,, \tag{21}$$

$$a(t) = (1 - Y_-)\,a_0^- + Y_-\,(1 - Y_+)\left[\frac{u_{shock}\left(a_0^+ - a_0^-\right)t}{a_0^-} + \frac{a_0^+ + a_0^-}{2}\right] + Y_+\,a_0^+\,, \tag{22}$$

where $Y_\pm = Y(t - t_0^\pm)$ and $Y(t)$ is the regularized Heaviside function

$$Y(t) \equiv \begin{cases} 0 & t < -\delta \\ \frac{t+\delta}{2\,\delta} + \sin\left(\frac{\pi t}{\delta}\right) & -\delta \le t \le \delta \\ 1 & t > \delta \end{cases}\,. \tag{23}$$

Substituting Eqs. (20)–(22) into Eq. (7) and integrating gives

$$\frac{\mathrm{d}a}{\mathrm{d}t} = \frac{1}{2}\,k\,[u]\left(A^+\,a_0^+ + A^-\,a_0^-\right) - \frac{1}{6}\,k\,[u]\left(A^+ - A^-\right)\left(a_0^+ - a_0^-\right), \tag{24}$$

so that

$$a(t) = a_0^- + k\,[u]\left\{\frac{A^+\,a_0^+ + A^-\,a_0^-}{2} - \frac{(A^+ - A^-)\left(a_0^+ - a_0^-\right)}{6}\right\} t\,. \tag{25}$$

Note that the last term on the right side, in which the difference in Atwood numbers across the shock is multiplied by the difference in initial perturbation amplitudes, is usually very small compared to the second term on the right side, and is therefore neglected. The Meyer-Blewett formula (14) takes into account the variation in amplitude for a shocked interface, whereas the above formulation also considers the change in Atwood number.

To determine the range of validity of Eq. (24), the predicted amplitude is compared to the exact solution of the linearized perturbation equations provided by Fraley [41] using a

normalized growth rate analysis. In this analysis [90], the normalized growth rates obtained via Eq. (16) and Eq. (24) are plotted as a function of the shock strength. The region over which the two formulae agree constitutes the region of validity for the Vandenboomgaerde model. Such an analysis can also be applied to other amplitude growth models.

2.1.5 The Duff-Harlow-Hirt model for a diffuse interface in the Rayleigh-Taylor instability

Duff, Harlow, and Hirt [39] performed Rayleigh-Taylor instability experiments in which a mixture of argon-bromine falls under the influence of gravity into air or helium. To model the growth rate observed in the experiments, a new model based on consideration of a diffuse interface was developed. The analysis begins with the linear eigenvalue equation for the perturbation velocity u corresponding to a sinusoidally-perturbed, arbitrary density profile subject to a gravitational acceleration (see [26])

$$\frac{\mathrm{d}}{\mathrm{d}x}\left(\rho\,\frac{\mathrm{d}u}{\mathrm{d}x}\right) = \left(\rho - \frac{g}{\varpi^2}\,\frac{\mathrm{d}\rho}{\mathrm{d}x}\right) u\,k^2 \tag{26}$$

$$\frac{\mathrm{d}^2 a}{\mathrm{d}t^2} = \varpi^2\,a, \tag{27}$$

where the eigenvalue $\varpi^2 = gAk$ is appropriate for a discontinuous interface. For a diffuse interface, Duff, Harlow, and Hirt proposed the profile

$$\rho(x) = \overline{\rho}\left[1 + A\,\mathrm{erf}\left(\frac{x}{\delta}\right)\right], \tag{28}$$

where

$$\overline{\rho} = \frac{\rho_1 + \rho_2}{2} \tag{29}$$

and δ is a diffusion lengthscale related to the mass diffusion coefficient D by

$$\delta = 2\sqrt{D\,t}\,. \tag{30}$$

Duff, Harlow, and Hirt proposed a reduction of the growth rate that accounts for a diffuse interface

$$\varpi^2 = \frac{g\,A\,k}{\psi}\,, \tag{31}$$

where ψ is the *growth reduction factor* and is, in general, a function of the interface width and the Atwood number. Substituting this expression into Eq. (27), ψ becomes the new eigenvalue to be determined by the solution of

$$\delta\,\frac{\mathrm{d}}{\mathrm{d}x}\left\{\left[1 + A\,\mathrm{erf}\left(\frac{x}{\delta}\right)\right]\frac{\mathrm{d}u}{\mathrm{d}x}\right\} = u\left\{1 + A\,\mathrm{erf}\left(\frac{x}{\delta}\right) - \frac{\psi}{k}\,\frac{\mathrm{d}}{\mathrm{d}x}\left[\mathrm{erf}\left(\frac{x}{\delta}\right)\right]\right\}. \tag{32}$$

For the case $A = 0$, Eq. (32) has solution given by the integral equation

$$u(x) = \int_x^\infty (\xi - x)\,u(\xi)\left[1 - \frac{2\,\psi}{k\sqrt{\pi}}\,\exp\left(\frac{\xi^2}{k^2\,\delta^2}\right)\right]\mathrm{d}\xi\,. \tag{33}$$

Expanding the velocity and the eigenvalue in a perturbation series for $k\delta \ll 1$

$$u(x) = e^{-kx} + k\,\delta\,u_1\left(\frac{x}{\delta}\right) + (k\,\delta)^2\,u_2\left(\frac{x}{\delta}\right), \tag{34}$$

$$\psi = 1 + \gamma_1\,k\,\delta + \gamma_2\,(k\,\delta)^2\,, \tag{35}$$

and substituting in Eq. (33) gives

$$\psi = 1 + \sqrt{\frac{2}{\pi}}\, k\, \delta \tag{36}$$

to lowest order. For the case of $A \neq 0$ the governing equations must be solved numerically.

2.1.6 The Mikaelian model for a diffuse interface in the Richtmyer-Meshkov instability

Mikaelian [88] extended the work of Duff, Harlow, and Hirt [39] to the Richtmyer-Meshkov instability. In addition to a diffuse interface given by Eq. (28), Mikaelian also considered the density profile

$$\rho(x) = \overline{\rho}\,[1 + A \tanh(\beta\, x)]\ , \tag{37}$$

used by Saffman and Meiron [111], where the transition from ρ_1 to ρ_2 occurs over a distance $1/\beta$.

The equation for the amplitude evolution from the linear instability analysis is Eq. (27) with ϖ given by Eq. (31). For the Rayleigh-Taylor instability, the solution is

$$\begin{aligned} a^{RT}(t) &= a_0\, e^{\varpi t} \\ &= a_0\, \exp\left(\frac{g\, A\, k}{\psi}\, t\right). \end{aligned} \tag{38}$$

For the Richtmyer-Meshkov instability, $g = [u]\delta(t)$ is substituted into Eq. (31) to give

$$a^{RM}(t) = a_0^- + a_0^+\, \frac{k\,[u]\, A^+}{\psi}\, t\,. \tag{39}$$

Mikaelian then solved Eq. (27) for the two density profiles using an N-layer matrix method [84, 85]. The solution converges rapidly, so that $N = 202$ corresponds closely with the solution of the equations. In addition, predictions for the growth rate from a moment method [86], which gives analytic (but approximate) expressions for the growth rate, were also compared with the numerical predictions of the matrix method applied to the hyperbolic tangent initial density profile of Eq. (37). The agreement was limited, as the moment method does not include finite Atwood number effects.

2.1.7 The Brouillette-Sturtevant model for a diffuse interface

Brouillette and Sturtevant [21] followed the same procedure described by Mikaelian [88] with a slightly different initial density profile

$$\rho(x) = \overline{\rho}\left[1 + \overline{A}\ \mathrm{erf}\left(\frac{x}{\overline{\delta}}\right)\right], \tag{40}$$

where $\overline{A} = (A^- + A^+)/2$, and $\overline{\delta} = (\delta^- + \delta^+)/2$. Note that δ is the characteristic width of the interface, taken to be the maximum slope of the density profile at a time τ after molecular diffusion ensues. The growth reduction factor is larger for smaller Atwood number, and $\psi = 1 + \pi\overline{\delta}/\lambda$ in the limit $\overline{A} \to 0$. In the limit of a thin interface with $\overline{\delta}/\lambda = 0$, it follows that $\psi = 1$. Also, $\psi = 1$ in the limit $\overline{A} \to 1$.

When the width of the interface is larger than the wavelength of the perturbation, $\overline{\delta}/\lambda > 1$,

$$\psi = 1 + C\,\frac{\overline{\delta}}{\lambda}\,, \tag{41}$$

where C is a constant. This yields

$$\frac{\mathrm{d}a}{\mathrm{d}t} = \frac{2\pi}{\overline{\delta}}\,\frac{A^+\,[u]\,a_0^+}{C}\,, \tag{42}$$

so that

$$a(t) = \left(1 + \frac{2\pi}{\overline{\delta}}\,\frac{A^+\,[u]\,a_0^+}{C}\,t\right) a_0^+\,. \tag{43}$$

2.2 Point vortex models

Presented in this section are point vortex models for the two-dimensional Richtmyer-Meshkov instability. These models represent the shocked interface by a finite set of point vortices with positive and negative initial circulations Γ. In these models, the velocity field is represented in terms of a streamfunction.

2.2.1 The Jacobs-Sheeley model

Jacobs and Sheeley [55] developed a point vortex model for the amplitude growth measured in their incompressible (or impulsive) Richtmyer-Meshkov instability experiments. This model was presented together with other models to reconcile their experimental results with the model predictions available at the time. Jacobs and Sheeley considered the 'impulsive Richtmyer-Meshkov instability' observed when a tank containing two liquids is impulsively accelerated by rapidly decelerating it after a short drop. The use of liquids allows sharper initial interfaces without the presence of a membrane, as liquids do not diffuse very rapidly. Furthermore, the experimental configuration with the free-fall component removes any effect from gravity.

Jacobs and Sheeley argued that the appearance of mushrooms in the Richtmyer-Meshkov instability is a manifestation of the coalescence of the initial sheet of vorticity into vortices with well-defined cores located at the midpoints along the interface. The strength of the initial vortex sheet γ can be computed using linear analysis as

$$\gamma(x) = -2\,v_0 \sin\left(kx\right), \tag{44}$$

where v_0 is the initial growth rate of the interface and k is the perturbation wavenumber. As the vortex sheet coalesces into single point vortices, it is possible to determine the circulation

$$\Gamma = \int_0^{\pi/k} \gamma(x)\,\mathrm{d}x \tag{45}$$

$$= -\frac{4}{k}\,v_0\,. \tag{46}$$

Additional mechanisms for the production of vorticity can be neglected, as they are typically much smaller compared to the baroclinic production mechanism arising from the passage of the shock.

Assume that a periodic array of point vortices with alternating signs is initially located along the interface at points midway between the peaks and troughs of the initial perturbation. The velocity field generated by this set of vortices is determined by the streamfunction

$$\psi(x,y) = \frac{\Gamma}{4\pi} \ln \left[\frac{\cosh(ky) + \sin(kx)}{\cosh(ky) - \sin(kx)} \right]. \tag{47}$$

As the instability evolves in time, the flow will distort the interface and wrap it around the vortex cores. The growth of the mixing layer is determined by the velocity of the point located between two successive vortices. The component of the velocity normal to the array of vortices is

$$\begin{aligned} v(x,y) &= -\frac{\partial \psi}{\partial x} \\ &= -\frac{k\,\Gamma}{2\pi} \frac{\cosh(ky)\cos(kx)}{\cosh^2(ky) - \sin^2(kx)}. \end{aligned} \tag{48}$$

At the midpoints $x = \pm n\pi/k$, the normal velocity is given by

$$v(y) = \pm \frac{1}{2\pi} \frac{k\,\Gamma}{\cosh(ky)}, \tag{49}$$

and the vertical position $y(t)$ is equivalent to the amplitude of the mixing layer $a(t)$. Therefore, the initial value problem for the amplitude

$$\frac{\mathrm{d}a}{\mathrm{d}t} = v(t) \quad , \quad a(0) = a_0^+ \tag{50}$$

is solved via a substitution from Eq. (45) with the result

$$a(t) = \frac{1}{k} \sinh^{-1} \left[\frac{2}{\pi}\, k\, v_0^+\, t + \sinh\left(k a_0^+\right) \right]. \tag{51}$$

It was found that this model underestimates the observed data, but yields a late-time logarithmic scaling of the amplitude, corresponding to a $1/t$ scaling of the velocity. To address the discrepancy between the model prediction and the data, it was suggested that this model becomes valid when the initial sheet of vorticity has had sufficient time to coalesce into a single vortex. At this point, the interface has already developed for some time and, therefore, a larger value for ka_0^+ must be used. With this correction, the model overestimates the data, but somewhat better agreement is obtained at late times.

2.2.2 The Likhachev-Jacobs model

Likhachev and Jacobs [74] modified the Jacobs-Sheeley [55] vortex model to allow for finite Atwood numbers. In the Jacobs-Sheeley model, it is assumed that the vortices are *evenly spaced*, which is valid only in the limit of very small Atwood numbers as the baroclinic production mechanism rapidly breaks the symmetric spacing. Perturb the position of the positive circulation vortices by a small positive distance ϵ_A (dependent on the Atwood number) and the negative circulation vortices by a negative distance $-\epsilon_A$, so that the streamfunction generalizing Eq. (47) is

$$\psi(x,y) = \frac{\Gamma}{4\pi} \ln \left\{ \frac{\cosh(ky) + \sin\left[k\left(x + \epsilon_A\right)\right]}{\cosh(ky) - \sin\left[k\left(x - \epsilon_A\right)\right]} \right\}. \tag{52}$$

The vertical velocity component generalizing Eq. (48) is

$$v(x,y) = \frac{k\,\Gamma\cos(k\epsilon_A)}{2\pi}\,\frac{\cosh(ky)\sin(kx) - \sin(k\epsilon_A)}{[\cosh(ky) - \cos(kx - k\epsilon_A)]\,[\cosh(ky) + \cos(kx + k\epsilon_A)]}\,. \tag{53}$$

Note that the row of perturbed vortices moves upward in the direction of the light fluid with a constant velocity

$$v_0 = \frac{k\,\Gamma}{4\pi}\,\tan(k\epsilon_A)\,. \tag{54}$$

In a coordinate system moving with constant velocity v_0, evaluating the vertical velocity at the midpoints [so that $y = a_b$ or $y = a_s$ when $x = \pm\pi/(2k)$] gives the velocity of the bubbles and spikes in the reference frame moving with speed v_0

$$\frac{\mathrm{d}a_{vb}}{\mathrm{d}t} = -\frac{k^2\,\Gamma}{2\pi}\left[\frac{\cos(k\epsilon_A)}{\cosh(a_{vb}) + \sin(k\epsilon_A)} - \frac{\tan(k\epsilon_A)}{2}\right], \tag{55}$$

$$\frac{\mathrm{d}a_{vs}}{\mathrm{d}t} = \frac{k^2\,\Gamma}{2\pi}\left[\frac{\cos(k\epsilon_A)}{\cosh(a_{vs}) - \sin(k\epsilon_A)} - \frac{\tan(k\epsilon_A)}{2}\right], \tag{56}$$

respectively. The bubble and spike amplitudes are then translated into the laboratory frame by

$$a_b(t) = |a_{vb}| - v_0\,t\,, \tag{57}$$

$$a_s(t) = |a_{vs}| + v_0\,t\,. \tag{58}$$

The initial circulation of Eq. (45) is now given by

$$\Gamma = -\epsilon_\Gamma\,\frac{4\,v_0}{k}\,, \tag{59}$$

where $\epsilon_\Gamma = 1.55$ is a parameter that accounts for the uncertainty in the estimate of the circulation in this new model. The predictions of this model were shown to be in good agreement with the experimental results of Niederhaus and Jacobs [98] when $k\epsilon_A = 0.085$ is chosen.

2.3 Perturbation models

Models based on the asymptotic expansion of the perturbation equations are reviewed here. These models generate asymptotic series with limited radii of convergence: the convergence can be improved using Padé approximants.

2.3.1 The Zhang-Sohn model

Zhang and Sohn [130] developed a model to investigate the growth rate of a two-dimensional Richtmyer-Meshkov unstable interface, valid for compressible fluids from early to late times in the case of a reflected shock (light-to-heavy transition). The dynamics of the initially-perturbed interface are modeled using the linear, compressible flow equations for early times and using the nonlinear, incompressible flow equations for later times.

Let $y = \eta(x,t)$ denote the initial perturbation, and let $\phi_1(x,y,t)$ and $\phi_2(x,y,t)$ denote the velocity potentials for the inviscid, irrotational fluids 1 and 2. Then, the differential equations

$$\nabla^2\phi_i = 0 \quad \text{in fluid } i \tag{60}$$

govern the potential flow: the boundary conditions at the interface are given by

$$\left.\frac{\partial \eta}{\partial t}\right|_{y=\eta} - \left.\frac{\partial \phi_1}{\partial x}\,\frac{\partial \eta}{\partial x}\right|_{y=\eta} + \left.\frac{\partial \phi_1}{\partial y}\right|_{y=\eta} = 0 \tag{61}$$

$$\left.\frac{\partial \eta}{\partial t}\right|_{y=\eta} - \left.\frac{\partial \phi_2}{\partial x}\,\frac{\partial \eta}{\partial x}\right|_{y=\eta} + \left.\frac{\partial \phi_2}{\partial y}\right|_{y=\eta} = 0 \tag{62}$$

$$\begin{aligned}\rho_1 \left.\frac{\partial \phi_1}{\partial t}\right|_{y=\eta} - \rho_2 \left.\frac{\partial \phi_2}{\partial t}\right|_{y=\eta} + \frac{\rho_2}{2}\left.\left[\left(\frac{\partial \phi_2}{\partial x}\right)^2 + \left(\frac{\partial \phi_2}{\partial y}\right)^2\right]\right|_{y=\eta} \\ - \frac{\rho_1}{2}\left.\left[\left(\frac{\partial \phi_1}{\partial x}\right)^2 + \left(\frac{\partial \phi_1}{\partial y}\right)^2\right]\right|_{y=\eta} = 0\,.\end{aligned} \tag{63}$$

The initial conditions are

$$\eta(x,0) = a_0^+ \cos(kx) \quad , \quad \left.\frac{d\eta}{dt}\right|_{t=0} = a_0^+\,\sigma \cos(kx)\,, \tag{64}$$

where

$$\sigma = k\,A^+\,[u] \tag{65}$$

is a constant given by the linear initial growth predicted by the Richtmyer model [see Eq. (11)].

A perturbation solution is assumed, and each term is further expanded in a series as

$$\eta(x,t) = \sum_{n=1}^{\infty} \eta^{(n)}(x,t) \tag{66}$$

$$\phi_i(x,y,t) = \sum_{n=0}^{\infty} \phi_i^{(n)}(x,y,t) \tag{67}$$

$$\eta^{(n)}(x,t) = \sum_{j=1}^{n} a_j^{(n)}(t)\cos(jkx) \tag{68}$$

$$\phi_1^{(n)}(x,y,t) = \sum_{j=0}^{n} b_{1j}^{(n)}(t)\cos(jkx)\,\mathrm{e}^{-jky} \tag{69}$$

$$\phi_2^{(n)}(x,y,t) = \sum_{j=0}^{n} b_{2j}^{(n)}(t)\cos(jkx)\,\mathrm{e}^{jky}\,. \tag{70}$$

Collecting terms of the same order leads to a system of ordinary differential equations in time that can be easily integrated. The first three terms of the solution are given by

$$\begin{aligned}\eta^{(1)}(x,t) &= \left(a_0^+ + a_0^+\,\sigma\,t\right)\cos(kx) \\ \eta^{(2)}(x,t) &= \tfrac{1}{2}\,k\left(a_0^+\right)^2\ \sigma^2\,A^+\,t^2\cos(2kx) \\ \eta^{(3)}(x,t) &= -\tfrac{1}{24}\,k^2\left(a_0^+\right)^3\,\sigma\left\{\left[4\left(A^+\right)^2+1\right]\sigma^2\,t^3 + 3\,\sigma\,t^2 + 6\,t\right\}\cos(kx) \\ &\quad + \tfrac{1}{8}\,k^2\left(a_0^+\right)^3\,\sigma\left\{\left[4\left(A^+\right)^2-1\right]\sigma^2\,t^3 - 3\,\sigma\,t^2\right\}\cos(3kx)\end{aligned} \quad . \tag{71}$$

As evident from the expression for $\eta^{(3)}$, additional higher-order terms in the perturbation series become quite complicated.

The series approximation can be evaluated at the locations of the spike and bubble to yield the mixing layer amplitude. The bubble and spike are located at $x = 0$ and $x = \pi/k$, respectively; thus, the amplitude defined as half the distance between the spike and bubble is

$$a(t) = \frac{1}{2}\left[\eta(0,t) - \eta\left(\frac{\pi}{k}, t\right)\right]. \tag{72}$$

The above formulation yields an independent series for the spike and the bubble. These two separate series can be used to evaluate models for the amplitude of the bubble or spike. The growth of the mixing layer is given by

$$\frac{\mathrm{d}a}{\mathrm{d}t} = v_0\left\{1 - k^2\, v_0\, t\, a_0^+ + \left[\left(A^+\right)^2 - \frac{1}{2}\right] k^2\, v_0^2\, t^2\right\}, \tag{73}$$

where k is the wavenumber of the initial perturbation, and v_0 is the Richtmyer velocity (12). Unfortunately, the range of validity of this finite Taylor series approximation is limited. For this reason, Padé approximations (see below) are used to extend the approximation into the nonlinear regime:

$$\frac{\mathrm{d}a}{\mathrm{d}t} = \frac{v_0}{1 + k^2\, v_0\, a_0^+\, t + \max\left[0, \left(k\, a_0^+\right)^2 - \left(A^+\right)^2 + \frac{1}{2}\right] k^2\, v_0^2\, t^2}. \tag{74}$$

Thus, the amplitude is given by

$$a(t) = \frac{2}{k\sqrt{4\,\max\left[0, \left(k\, a_0^+\right)^2 - \left(A^+\right)^2 + \frac{1}{2}\right] - \left(k\, a_0^+\right)^2}} \times \tan^{-1}\left\{\frac{k\, a_0^+ + 2\max\left[0, \left(k\, a_0^+\right)^2 - \left(A^+\right)^2 + \frac{1}{2}\right] k\, v_0\, t}{\sqrt{4\,\max\left[0, \left(k\, a_0^+\right)^2 - \left(A^+\right)^2 + \frac{1}{2}\right] - \left(k\, a_0^+\right)^2}}\right\}. \tag{75}$$

The choice of the Padé approximant P_2^0 for $\left(ka_0^+\right)^2 \geq \left(A^+\right)^2 - 1/2$ and P_1^0 for $\left(ka_0^+\right)^2 \leq \left(A^+\right)^2 - 1/2$ matches the asymptotic growth observed experimentally for large t. The amplitude growth predicted by the model was in excellent agreement with numerical simulation results and with experimental data obtained using air/SF_6.

To clarify the role of Padé approximations, a brief review following Bender and Orszag [16] is presented. Padé approximations arise in the context of summation of perturbation series. It is often the case that only a few terms are available when a perturbation series is formed for a small parameter ϵ. These terms often converge very slowly to the desired solution, or they may diverge due to the existence of a singularity. Padé approximations offer the possibility of improving the behavior of diverging perturbation series based on the knowledge of only a few terms. Padé approximations are also used to improve the convergence properties of diverging power series. In many instances, the regular power series may diverge as it reaches the boundaries of the region of convergence: Padé approximants can further extend the range of validity.

In a Padé approximation, the power series $\sum_n a_n z^n$ is replaced by a sequence of rational functions P_M^N called the *Padé approximants*. The indices M and N denote the order of the polynomial in the denominator and in the numerator, respectively. Thus, the Padé approximant

can be expressed as

$$P_M^N(z) = \frac{\sum_{n=0}^{N} A_n\, z^n}{\sum_{n=0}^{M} B_n\, z^n} \tag{76}$$

with coefficients $\{A_n\}_{n=0}^{N}$ and $\{B_n\}_{n=0}^{M}$. Note that, without loss of generality, $B_0 = 1$. The other $M+N+1$ terms are chosen so that the first $M+N+1$ terms in the Taylor series for P_M^N match the $M+N+1$ terms in the series $\sum_n a_n z^n$. As M and N increase, $P_M^N(z)$ converges even if the series $\sum_n a_n z^n$ diverges or even in regions where the series summation is no longer convergent.

It is straightforward to determine the values of the coefficients of a Padé series given the series $\sum_n a_n z^n$. The coefficients B_i satisfy the matrix equation

$$\mathbf{C} \begin{bmatrix} B_1 \\ B_2 \\ \vdots \\ B_M \end{bmatrix} = - \begin{bmatrix} a_{N+1} \\ a_{N+2} \\ \vdots \\ a_{N+M} \end{bmatrix}, \tag{77}$$

$$\mathbf{C}_{ij} = a_{N+i-j}\,. \tag{78}$$

The elements of the matrix $\mathbf{C}$ are constant along diagonals. Also note that if the index $N+i-j<0$, then its value can be taken to be zero. Once the B_i are determined, the A_i are computed as

$$A_i = \sum_{j=0}^{i} a_{i-j}\, B_j\,, \tag{79}$$

and $B_j = 0$ for $j > M$.

2.3.2 The Vandenboomgaerde et al. model

Vandenboomgaerde, Gauthier, and Mügler [121] proposed a simplified version of the perturbation expansion of Zhang and Sohn [130]. First, choose

$$\sigma = \frac{k\,[u]}{2}\left(A^+ + \frac{A^-}{1-\frac{[u]}{u_{shock}}}\right) \tag{80}$$

so that $a_0\sigma$ gives the right side of Eq. (24). Noting that an accurate perturbation series can be obtained by retaining only the secular terms (*i.e.*, the terms with the largest unbounded part), only the largest power from each term of the Zhang and Sohn solution Eq. (71) must be retained. This yields

$$\begin{aligned}
\eta^{(1)}(x,t) &= \left(a_0^+ + a_0^+\,\sigma\,t\right)\cos\left(kx\right) \\
\eta^{(2)}(x,t) &= \tfrac{1}{2}\left(a_0^+\right)^2\, k\,\sigma^2\,A^+\,t^2\cos\left(2kx\right) \\
\eta^{(3)}(x,t) &= -\tfrac{1}{8}\,k^2\left(a_0^+\right)^2\,\sigma^3\,t^3\left\{\tfrac{1}{3}\left[4\left(A^+\right)^2+1\right]\cos\left(kx\right) - \left[4\left(A^+\right)^2-1\right]\cos\left(3kx\right)\right\}
\end{aligned} \tag{81}$$

Such an approximation is usually valid for large times, but in this case the first two terms of the series are identical to the series of Zhang and Sohn, so that good agreement is expected between the predictions of this model and the Zhang-Sohn model, even at small times. Another advantage of this method is that high-order terms can be easily computed. As only the

high-order terms in the series are retained, the determination of the coefficients shifts from integrating in time to solving an algebraic system. Using this method gives the series solution up to eleventh-order for the growth of the mixing layer:

$$a(t) = a_0^+ + \frac{1}{k}\sum_{n=0}^{5} P_{2n+1}\left(ka_0^+\sigma t\right)^{2n+1}, \tag{82}$$

where

$$\begin{aligned}
&P_1(x) = 1\\
&P_3(x) = -\tfrac{1}{6}\left(1-2\,x^2\right)\\
&P_5(x) = \tfrac{1}{240}\left(19-125\,x^2+92\,x^4\right)\\
&P_7(x) = -\tfrac{1}{5040}\left(264-3686\,x^2+6997\,x^5-3234\,x^6\right)\\
&P_9(x) = \tfrac{1}{2903040}\left(117663-2855274\,x^2+10086083\,x^4-11093856\,x^6+3805728\,x^8\right)\\
&P_{11}(x) = -\tfrac{1}{159667200}(5507319-206796915\,x^2+1168865775\,x^4-2250383605\,x^6\\
&\qquad +1755444326\,x^8-483163144\,x^{10})
\end{aligned} \tag{83}$$

This series solution diverges at $t \approx (ka_0^+\sigma)^{-1}$; therefore, Padé approximants are used to extend the validity of the solution. Note that the Padé approximation is constructed for the amplitude growth rate $\mathrm{d}a/\mathrm{d}t$ and not for the amplitude itself $a(t)$, which yields better results and is also in the spirit of the work of Zhang and Sohn [130]. The growth rate is given by the tenth-degree polynomial

$$\frac{\mathrm{d}a}{\mathrm{d}t} = a_0^+\sigma\sum_{n=0}^{5}(2n+1)\,P_{2n+1}\left(ka_0^+\sigma t\right)^{2n}. \tag{84}$$

A P_6^4 Padé approximant is constructed as

$$P_6^4(t) = \frac{\sum_{n=0}^{4} A_n\left(ka_0^+\sigma t\right)^n}{\sum_{n=0}^{6} B_n^n\left(ka_0^+\sigma t\right)} \tag{85}$$

with the Padé coefficients $\{A_n\}$ and $\{B_n\}$ computed as described above (the values are not presented here as the analytical expressions are complicated and can be easily computed).

2.3.3 The Matsuoka-Nishihara-Fukuda model

Matsuoka, Nishihara, and Fukuda [79] proposed a new formulation of the kinematic boundary conditions in the perturbation expansion of the Zhang-Sohn potential flow to account for stretching at the interface. They replaced Eqs. (61) and (62) with

$$\overline{\mathbf{u}}\cdot\mathbf{n} = \left.\frac{\rho_1\nabla\phi_1\cdot\mathbf{n}+\rho_2\nabla\phi_2\cdot\mathbf{n}}{\rho_1+\rho_2}\right|_{y=\eta} \tag{86}$$

$$\overline{\mathbf{u}}\cdot\mathbf{s} = \left.\frac{\rho_1\nabla\phi_1\cdot\mathbf{s}+\rho_2\nabla\phi_2\cdot\mathbf{s}}{\rho_1+\rho_2}\right|_{y=\eta}, \tag{87}$$

where

$$\overline{\mathbf{u}} \equiv \frac{\rho_1\,\mathbf{u_1}+\rho_2\,\mathbf{u_2}}{\rho_1+\rho_2} \tag{88}$$

is the average, density-weighted velocity, $\mathbf{s}$ is the tangential vector to the interface, and $\mathbf{n}$ is the normal vector to the interface. The perturbation expansion is performed and yields different

expansions for the bubble and spike. When the first three terms are considered, the bubble and spike velocities are

$$\frac{\mathrm{d}a_b}{\mathrm{d}\tau} = \left(-A^2+\frac{1}{2}\right)\tau^2 + \left(-2A^2\,\hat{a}_0 + A + \hat{a}_0\right)\tau + \left(-2A^2+\frac{3}{2}\right)\hat{a}_0^2 + \frac{A\,\hat{a}_0}{2} - 1\,, \quad (89)$$

$$\frac{\mathrm{d}a_s}{\mathrm{d}\tau} = \left(A^2-\frac{1}{2}\right)\tau^2 + \left(2A\,\hat{a}_0 + A - \hat{a}_0\right)\tau + \left(2A^2-\frac{3}{2}\right)\hat{a}_0^2 + \frac{A\,\hat{a}_0}{2} + 1\,, \quad (90)$$

where $\hat{a}_0 = 2\pi a_0^+/\lambda$ is a dimensionless initial perturbation amplitude, and $\tau = kv_0t$ is a rescaled time. Note that this model includes a dependence on the initial perturbation amplitude. The radius of convergence of the perturbation series can be extended using a P_2^0 Padé approximant to give

$$\frac{\mathrm{d}a_b}{\mathrm{d}\tau} = \frac{\alpha_b^3}{\left[\alpha_b\left(A^2-\frac{1}{2}\right) + \left(-2A^2\,\hat{a}_0 + A + \hat{a}_0\right)^2\right]\tau^2 - \alpha_b\left(-2A^2\,\hat{a}_0 + A + \hat{a}_0\right)\tau + \alpha_b^2} \quad (91)$$

$$\frac{\mathrm{d}a_s}{\mathrm{d}\tau} = \frac{\alpha_s^3}{\left[\alpha_s\left(A^2-\frac{1}{2}\right) + \left(2A^2\,\hat{a}_0 + A - \hat{a}_0\right)^2\right]\tau^2 - \alpha_s\left(2A^2\,\hat{a}_0 + A - \hat{a}_0\right)\tau + \alpha_s^2}\,, \quad (92)$$

where

$$\alpha_b = \left(-2A^2+\frac{3}{2}\right)\hat{a}_0^2 + \frac{A\,\hat{a}_0}{2} - 1 \quad (93)$$

$$\alpha_s = \left(2A^2-\frac{3}{2}\right)\hat{a}_0^2 + \frac{A\,\hat{a}_0}{2} + 1\,. \quad (94)$$

2.4 Potential flow models

Potential flow models can describe the amplitude evolution of both the Rayleigh-Taylor and Richtmyer-Meshkov instabilities through the late-time, nonlinear regime by the evolution of the bubble and spike velocity. Layzer [71] developed the first potential flow model to describe the Rayleigh-Taylor instability, which was subsequently extended to the Richtmyer-Meshkov instability by others. These models predict that the bubble velocity in a Richtmyer-Meshkov instability approaches zero at asymptotic times.

2.4.1 The Layzer model for the Rayleigh-Taylor instability

Layzer [71] derived analytic solutions for the flow observed when an ideal, incompressible fluid contained in the upper half of a vertical tube falls under the action of gravity. In the experiments, the lower half of the tube was empty and the surface was initially flat. Disturbances were applied so that a single "vacuum" bubble rose at the center of the tube. Layzer obtained solutions for the velocity of the bubble tip in the case of a two-dimensional channel and a three-dimensional circular tube. Note that the density ratio of the two fluids in the system above is effectively infinite, corresponding to an Atwood number $A = 1$.

For inviscid fluids initially at rest, the velocity field can be described by a scalar potential $\phi(x, y, t)$ and $\phi(x, y, z, t)$ in two and three dimensions, respectively, satisfying the Laplace and Bernoulli equations. The Laplace equation is

$$\nabla^2\phi = 0\,, \quad (95)$$

where $\nabla^2 = \partial^2/\partial x^2 + \partial^2/\partial y^2$ in two dimensions and $\nabla^2 = \partial^2/\partial x^2 + \partial^2/\partial y^2 + \partial^2/\partial z^2$ in three dimensions. The Bernoulli equations are

$$\left.\frac{\partial\phi}{\partial t}\right|_{y=\eta} - \frac{1}{2}\left[\left(\frac{\partial\phi}{\partial x}\right)^2 + \left(\frac{\partial\phi}{\partial y}\right)^2\right]\Bigg|_{y=\eta} - g\,\eta\Big|_{y=\eta} = constant\,, \tag{96}$$

$$\left.\frac{\partial\phi}{\partial t}\right|_{z=\eta} - \frac{1}{2}\left[\left(\frac{\partial\phi}{\partial r}\right)^2 + \left(\frac{\partial\phi}{\partial z}\right)^2\right]\Bigg|_{z=\eta} - g\,\eta\Big|_{z=\eta} = constant \tag{97}$$

in two and three dimensions, respectively, where the three-dimensional equation is written in polar coordinates. The interface further satisfies the kinematic condition

$$\left.\frac{\partial\phi}{\partial z}\right|_{y=\eta} = \left.\frac{\partial\eta}{\partial t}\right|_{y=\eta} + \left.\frac{\partial\phi}{\partial x}\,\frac{\partial\eta}{\partial x}\right|_{y=\eta}, \tag{98}$$

$$\left.\frac{\partial\phi}{\partial z}\right|_{z=\eta} = \left.\frac{\partial\eta}{\partial t}\right|_{z=\eta} + \left.\frac{\partial\phi}{\partial r}\,\frac{\partial\eta}{\partial r}\right|_{z=\eta}, \tag{99}$$

in two and three dimensions, respectively. The ansatz for the perturbation is

$$\phi(x,y,t) = F(t)\,\mathrm{e}^{-y}\cos x\,, \tag{100}$$

$$\phi(r,z,t) = F(t)\,\mathrm{e}^{-z}\,J_0(r) \tag{101}$$

in two and three dimensions, respectively, where $J_0(r)$ is the Bessel function of order zero and is used to simulate a perturbation with cylindrical symmetry.

Let $g = 1$ and define

$$T(t) = 1 + \int_{t_0}^{t} F(t)\,\mathrm{d}t, \tag{102}$$

so that $F(t) \equiv \mathrm{d}T(t)/\mathrm{d}t$ and η satisfy

$$\mathrm{e}^{\eta} = T\left[1 - \frac{r^2}{8}\left(1 - \frac{1}{T^2}\right)\right]. \tag{103}$$

Substituting these expressions into the Bernoulli equation gives a nonlinear ordinary differential equation

$$T\left(T^2+1\right)\frac{\mathrm{d}^2T}{\mathrm{d}t^2} - \left(\frac{\mathrm{d}T}{\mathrm{d}t}\right)^2 - T^2\left(T^2-1\right) = 0\,, \tag{104}$$

$$T\left(2\,T^3+1\right)\frac{\mathrm{d}^2T}{\mathrm{d}t^2} - \left(T^3-1\right)\left(\frac{\mathrm{d}T}{\mathrm{d}t}\right)^2 - T^2\left(T^3-1\right) = 0 \tag{105}$$

in two and three dimensions, respectively.

Let $a_b^{RT}(t)$ denote the amplitude of the Rayleigh-Taylor bubble, related to $T(t)$ by

$$a_b^{RT}(t) = \log T(t)\,, \tag{106}$$

and let v_b^{RT} denote the velocity of the bubble. Then, for $a_b^{RT}(0) = 0$, it follows that Eqs. (104) and (105) can be integrated to give

$$v_b^{RT}(t) = \frac{\mathrm{d}a_b^{RT}}{\mathrm{d}t} = \sqrt{\frac{\exp\left(3\,a_b^{RT}\right) - 3\,\eta - 1}{3\left[\exp\left(3\,a_b^{RT}\right) + \frac{1}{2}\right]}}\,, \tag{107}$$

$$v_b^{RT}(t) = \frac{\mathrm{d}a_b^{RT}}{\mathrm{d}t} = \sqrt{\frac{\exp\left(2\,a_b^{RT}\right) - 2\,\eta - 1}{\exp\left(2\,a_b^{RT}\right) + 1}} \tag{108}$$

in two and three dimensions, respectively. These equations can then be integrated to obtain the position of the bubble tip. For late times, the asymptotic velocities are

$$v_b^{RT} = \sqrt{\frac{g}{3\,k}}\,, \tag{109}$$

$$v_b^{RT} = \sqrt{\frac{g\,R}{\beta_1}} \tag{110}$$

in two and three dimensions, respectively, where $\beta_1 \approx 3.832$ is the first zero of the Bessel function of order one, and R represents the radius of the tube.

2.4.2 The Hecht-Alon-Shvarts model for the Richtmyer-Meshkov instability

Hecht, Alon, and Shvarts [45] extended the Layzer model to the Richtmyer-Meshkov instability. The two-dimensional equations for the potential ϕ are modified so that $g = 0$, and an initial velocity perturbation $v_b^{RM}(0)$ equal to the change in velocity after the shock is introduced. The late-time velocity is

$$v_b^{RM}(t) = \frac{2}{3\,k\,t}\,, \tag{111}$$

and is independent of the initial velocity perturbation. The asymptotic bubble curvature is

$$\kappa = \frac{3\,\lambda}{2\pi}\,, \tag{112}$$

which is also the same as for Rayleigh-Taylor bubbles. The predictions of this model were in good agreement with numerical simulations for $A = 1$.

2.4.3 The Mikaelian model for arbitrary initial perturbations

Mikaelian [92] extended the Layzer model to the case when $a_b(0) \neq 0$ for both the Rayleigh-Taylor and the Richtmyer-Meshkov instability. Equations for the bubble velocity in the Rayleigh-Taylor and Richtmyer-Meshkov instabilities were derived in two- and three-dimensional geometries. The late-time limit of v_b^{RT} in two and three dimensions was shown to be consistent with the values determined by Layzer in Eqs. (109) and (110), respectively. For the Richtmyer-Meshkov instability, the late-time two- and three-dimensional bubble velocities are

$$v_b^{RM}(t) = \frac{2}{3\,k\,t}\,, \tag{113}$$

$$v_b^{RM}(t) = \frac{R}{\beta_1\,t}\,, \tag{114}$$

respectively, in agreement with the earlier result of Hecht, Alon and Shvarts [45] in Eq. (111).

2.4.4 The Zhang model for the velocity of spikes

Zhang [129] extended the Layzer model to determine the velocity of spikes for both the Richtmyer-Meshkov and the Rayleigh-Taylor instabilities in two and three dimensions. Expressions for the spike and bubble velocity were determined by assuming that the interface is locally parabolic,

$$\eta(y,t) = a(t) + \xi(t)\, k\, y^2 \,. \tag{115}$$

Substitution into the governing equations gives a system of ordinary differential equations for $a(t)$ and $\xi(t)$ in terms of $F(t)$ from Eq. (100):

$$\frac{\mathrm{d}a}{\mathrm{d}t} = F\, k\, \mathrm{e}^{-ka} \,, \tag{116}$$

$$\frac{\mathrm{d}\xi}{\mathrm{d}t} = -F\, k^2 \left(3\,\xi + \frac{1}{2}\right) \mathrm{e}^{-ka} \,, \tag{117}$$

$$k\, \mathrm{e}^{-ka} \left(\xi + \frac{1}{2}\right) \frac{\mathrm{d}F}{\mathrm{d}t} = -F^2\, k^3\, \xi\, \mathrm{e}^{-2ka} - g\, \xi \,. \tag{118}$$

Eliminating $F(t)$ from the first two equations yields

$$\xi(a(t)) = \left\{ \left[\xi(0) + \frac{1}{6}\right] \mathrm{e}^{-3k[a-a(0)]} - \frac{1}{6} \right\} \tag{119}$$

and a nonlinear ordinary differential equation for $v(t) = \mathrm{d}a(t)/\mathrm{d}t = v(\xi(t))$:

$$-\frac{k^2}{4}\,(6\,\xi + 1)\,\frac{\mathrm{d}v^2}{\mathrm{d}\xi} + \frac{k^2}{2\,\xi + 1}\, v^2 + \frac{2\,\xi}{2\,\xi + 1}\, g = 0 \,. \tag{120}$$

Given a solution of Eq. (120), an expression $v = v(a(t))$ can be obtained via the substitution $\xi = \xi(a(t))$ in Eq. (119) to give the velocity of the bubble and spike,

$$v = \sqrt{\frac{9\,[2\,\xi(0) + 1]\, k\, v(0)^2 - 6\,[6\,\xi(0) + 1][a - a(0)]\, k\, g + 2\left(\mathrm{e}^{3k[z-z(0)]} - 1\right) g}{3\, k\left[6\,\xi(0) + 1 + 2\,\mathrm{e}^{3k[a-a(0)]}\right]}} \,. \tag{121}$$

In the case of a sinusoidal initial perturbation, $\xi(0) = -a(0)k/2$ for the bubble and $\xi(0) = a(0)k/2$ for the spike. The late-time asymptotic solutions are

$$v_b^{RT}(t \to \infty) = \sqrt{\frac{g}{3\,k}} \qquad \xi_b^{RT} \;\longrightarrow\; -\frac{1}{6} \tag{122}$$

$$v_s^{RT}(t \to \infty) = -g\, t \qquad \xi_s^{RT} \;\longrightarrow\; \infty \tag{123}$$

$$v_b^{RM}(t \to \infty) = \frac{2}{3\, k\, t} \qquad \xi_b^{RM} \;\longrightarrow\; -\frac{1}{6} \tag{124}$$

$$v_s^{RM}(t \to \infty) = v_0 \sqrt{\frac{6\,\xi_0 + 3}{6\,\xi_0 + 1}} \qquad \xi_s^{RM} \;\longrightarrow\; \infty \,, \tag{125}$$

where b and s denote the bubble and spike, respectively. The novel components of this model are the spike equations (123) and (125). The equations for the bubble in two dimensions, (122) and (124), were previously derived by Layzer [71] in Eq. (109) and by Hecht, Alon and Shvarts [45] in Eq. (113). The model predicts constant linear acceleration for a spike in the Rayleigh-Taylor instability and constant velocity in the Richtmyer-Meshkov instability (depending on the initial conditions v_0 and ξ_0). The solutions are consistent with the results of numerical computations based on conformal mapping [81] and on finite-differencing [7].

2.4.5 The Goncharov model for arbitrary Atwood numbers

Goncharov [42] extended the two-dimensional Layzer model to the case of $A \neq 1$ for both the Rayleigh-Taylor and the Richtmyer-Meshkov instability. The Bernoulli equation is modified to include the density, and is given at $y = \eta$ by

$$\left\{ \rho_1 \frac{\partial \phi_1}{\partial t} + \frac{\rho_1}{2} \left[\left(\frac{\partial \phi_1}{\partial x} \right)^2 + \left(\frac{\partial \phi_1}{\partial y} \right)^2 \right] + \rho_1 \, g \, y \right\} - \left\{ \rho_2 \frac{\partial \phi_2}{\partial t} + \frac{\rho_2}{2} \left[\left(\frac{\partial \phi_2}{\partial x} \right)^2 + \left(\frac{\partial \phi_2}{\partial y} \right)^2 \right] + \rho_2 \, g \, y \right\} = f(t) \,, \quad (126)$$

where $f(t)$ is an arbitrary function, and $\eta(t)$ is given by Eq. (115). The velocity potentials for the two fluids ϕ_1 and ϕ_2 assume the form

$$\phi_1(x, y, t) = a_1(t) \cos(kx) \, \mathrm{e}^{-k(y - \eta_0)} \,, \quad (127)$$

$$\phi_2(x, y, t) = b_1(t) \cos(kx) \, \mathrm{e}^{k(y - \eta_0)} + b_2(t) \, y \,, \quad (128)$$

where a_1, b_1 and b_2 are unknown functions. The form of the potential is dictated by the boundary conditions. The equations are again expanded around (115) and solved. Note that ξ is related to the curvature by $\kappa = -1/(2\xi)$. The final results for the bubble velocities are

$$v_b^{RT}(t \to \infty) = \sqrt{\frac{2 \, A \, g}{3 \, (1 + A) \, k}} \;, \;\; \xi_b^{RT} \longrightarrow -\frac{k}{6} \,, \quad (129)$$

$$v_b^{RM}(t \to \infty) = \frac{3 + A}{3 \, (1 + A) \, k \, t} \;, \;\; \xi_b^{RM} \longrightarrow -\frac{k}{6} \,. \quad (130)$$

The spike velocity for the Rayleigh-Taylor instability in two dimensions is given by

$$v_s^{RT}(t \to \infty) = \sqrt{\frac{2 \, A \, g}{3 \, (1 - A) \, k}} \,. \quad (131)$$

Comparison of the model predictions with numerical simulations shows that the spike velocity does not saturate for $A > 0.1$, indicating that additional mechanisms not captured by the model are important.

The analysis is extended to three dimensions and the velocities of the bubble are given by

$$v_b^{RT}(t \to \infty) = \sqrt{\frac{2 \, A \, g}{(1 + A) \, k}} \;, \;\; \xi_b^{RT} \longrightarrow -\frac{k}{8} \,, \quad (132)$$

$$v_b^{RM}(t \to \infty) = \frac{2}{(1 + A) \, k \, t} \;, \quad (133)$$

for the Rayleigh-Taylor and Richtmyer-Meshkov instability, respectively.

2.4.6 The Mikaelian model for the evolution of the single-mode Rayleigh-Taylor and Richtmyer-Meshkov instability

Mikaelian [93] presented a simple analytic expression for the evolution of a single-mode Rayleigh-Taylor and Richtmyer-Meshkov instability by using a technique attributed by Layzer [71] to

Fermi. In this technique, the perturbation amplitude grows in the linear regime until the asymptotic velocity is attained. After this time, the amplitude is given by solving the ordinary differential equation for the asymptotic velocity. When applied to the Rayleigh-Taylor and Richtmyer-Meshkov instabilities, this technique is modified so that the transition from the linear to asymptotic velocities is determined by the amplitude of the perturbation rather than by the velocity. The asymptotic velocities used for the Rayleigh-Taylor and Richtmyer-Meshkov instabilities are the asymptotic bubble velocities of the Goncharov model.

The amplitudes given by the linear theory for the Rayleigh-Taylor and Richtmyer-Meshkov instabilities in the case of a single-mode initial perturbation are

$$a^{RT}(t) = a_0 \cosh\left(\sqrt{g\,k\,A}\,t\right), \tag{134}$$

$$a^{RM}(t) = a_0^+ \left(1 + [u]\,k\,A^+\,t\right), \tag{135}$$

and for a three-dimensional initial perturbation with cylindrical symmetry of radius R

$$a^{RT}(t) = a_0 \cosh\left(\sqrt{\frac{g\,\beta_1\,A}{R}}\,t\right), \tag{136}$$

$$a^{RM}(t) = a_0^+ \left(1 + \frac{[u]\,\beta_1\,A^+}{R}\,t\right), \tag{137}$$

where $\beta_1 \approx 3.832$ is the first zero of the Bessel function of order one.

For the Rayleigh-Taylor instability, the transition between the linear and asymptotic model is taken at $a = 1/(3k)$ in two dimensions, giving the amplitude

$$\begin{aligned} a^{RT}(t) = a_0 + \frac{3+A}{3\,(1+A)\,k}\,\ln\Bigg\{&\cosh\left[\frac{\sqrt{6\,g\,k\,A\,(1+A)}}{3+A}\,t\right] \\ &+ \frac{v^{RT}(0)}{v_b^{RT}(t\to\infty)}\,\sinh\left[\frac{\sqrt{6\,g\,k\,A\,(1+A)}}{3+A}\,t\right]\Bigg\}, \end{aligned} \tag{138}$$

where $v_b^{RT}(t \to \infty)$ is given by Eq. (129). For three dimensions, the transition occurs at $a = R/(2\beta_1)$, yielding

$$\begin{aligned} a^{RT}(t) = a_0 + \frac{2\,R}{\beta_1\,(1+A)}\,\ln\Bigg\{&\cosh\left[\sqrt{\frac{g\,\beta_1\,A\,(1+A)}{2\,R}}\,t\right] \\ &+ \frac{v^{RT}(0)}{v_b^{RT}(t\to\infty)}\,\sinh\left[\sqrt{\frac{g\,\beta_1\,A\,(1+A)}{2\,R}}\,t\right]\Bigg\}, \end{aligned} \tag{139}$$

where $v_b^{RT}(t \to \infty)$ is given by Eq. (132).

For the Richtmyer-Meshkov instability in two dimensions, the transition is taken at $a = 1/(3k)$, giving the amplitude

$$a^{RM}(t) = a_0^+ + \frac{3+A^+}{3\,(1+A^+)\,k}\,\ln\left[1 + \frac{3\,v^{RM}(0)\,k\,(1+A^+)}{3+A^+}\,t\right]. \tag{140}$$

The asymptotic velocity derived from this expression is in agreement with Eq. (130). In three dimensions, the transition occurs at $a = R/(2\,\beta_1)$, giving

$$a^{RM}(t) = a_0^+ + \frac{2\,R}{(1+A^+)\,\beta_1}\,\ln\left[1 + \frac{v^{RM}(0)\,\beta_1\,(1+A^+)}{2\,R}\,t\right]. \tag{141}$$

The asymptotic velocity derived from this expression is in agreement with Eq. (133).

2.4.7 The Sohn model

Sohn [115] also extended the Layzer model to fluids with arbitrary density ratio. The approach differs from the Goncharov model in the use of a simpler form for the potential functions from Layzer [71] in Eq. (100). The shape of the interface near a bubble tip is assumed to be parabolic [see Eq. (115)]. Substituting this form and expanding yields the system of equations of Zhang, Eqs. (116)–(118), with Eq. (118) now modified to include an arbitrary Atwood number:

$$k\,\mathrm{e}^{-ka}\left(\xi+\frac{1}{2}\right)\frac{\mathrm{d}F}{\mathrm{d}t} = -AF^2\,k^3\,\xi\,\mathrm{e}^{-2ka} - A\,g\,\xi\,. \tag{142}$$

The asymptotic bubble velocities are determined by solving the evolution equations to obtain

$$v_b^{RT} \;\longrightarrow\; \sqrt{\frac{A\,g}{(2+A)\,k}}\;,\quad \xi_b^{RT}\longrightarrow -\frac{k}{6}\,, \tag{143}$$

$$v_b^{RM}(t) \;\longrightarrow\; \frac{2}{(2+A)\,k\,t}\;,\quad \xi_b^{RM}\longrightarrow -\frac{k}{6}\,. \tag{144}$$

The predictions of this model were validated against numerical simulations in two dimensions.

2.4.8 The Abarzhi models

Abarzhi [1] also considered a potential flow model with a single-mode approximation. Near highly symmetric points such as at the tip of the bubble or at the tip of the spike, the potential function ϕ and the free surface η can be expanded in a Fourier series. The Fourier series is then truncated and the equations are expanded around the periodic directions $x=0$ and $y=0$ and at the interface $z=\eta$. If $\kappa(t)$ represents the curvature at the symmetric point, then the expansion is valid if

$$\left(\frac{v_0}{c_s}\right)^2 \ll 1\;,\quad |\kappa(0)|\,\lambda \ll 1\,. \tag{145}$$

The first condition requires that the flow must be incompressible, and the second condition requires the surface to be nearly flat initially. In addition to the two-dimensional sinusoidal initial perturbation, various symmetric flow configurations are considered in three dimensions, including a tubular, a hexagonal, and a square configuration. The late-time velocities for bubbles and spikes in each configuration are given by

$$\text{2D}\qquad \frac{2\,v_b^{RM}\,t}{\lambda} = 0.212\;,\quad \frac{v_s^{RM}}{v_0} = \sqrt{3} \tag{146}$$

$$\text{3D tubular}\qquad \frac{2\,v_b^{RM}\,t}{\lambda} = 0.261\;,\quad \frac{v_s^{RM}}{v_0} = \sqrt{2} \tag{147}$$

$$\text{3D hexagonal}\qquad \frac{2\,v_b^{RM}\,t}{\lambda} = 0.275\;,\quad \frac{v_s^{RM}}{v_0} = \sqrt{2} \tag{148}$$

$$\text{3D square}\qquad \frac{2\,v_b^{RM}\,t}{\lambda} = 0.319\;,\quad \frac{v_s^{RM}}{v_0} = \sqrt{2}\,. \tag{149}$$

The values for the radius of curvature R were also determined. For spikes, the radius of curvature scales as

$$R \sim -\frac{\lambda}{2}\,\mathrm{e}^{-t/t_0}\,, \tag{150}$$

where

$$t_0 \sim \frac{1}{k\,|v_0|} \tag{151}$$

is a characteristic timescale of the system. The late time radii of curvature are given by

$$\text{2D} \qquad \frac{2\,R_b^{RM}}{\lambda} = 0.955 \;\;,\;\; \frac{\lambda}{2\,|v_0|\,t_0} = 16.32 \tag{152}$$

$$\text{3D tubular} \qquad \frac{2\,R_b^{RM}}{\lambda} = 1.044 \;\;,\;\; \frac{\lambda}{2\,|v_0|\,t_0} = 10.84 \tag{153}$$

$$\text{3D hexagonal} \qquad \frac{2\,R_b^{RM}}{\lambda} = 1.103 \;\;,\;\; \frac{\lambda}{2\,|v_0|\,t_0} = 10.26 \tag{154}$$

$$\text{3D square} \qquad \frac{2\,R_b^{RM}}{\lambda} = 1.274 \;\;,\;\; \frac{\lambda}{2\,|v_0|\,t_0} = 8.89\,. \tag{155}$$

The results indicate that the dynamics of the spike are governed by the initial conditions. By contrast, the bubble velocity decreases asymptotically and the curvature approaches a finite value independent of the initial conditions.

In later work [2, 3], the Layzer-type approach was generalized to include additional modes. This generalization allows the modeling of the interaction of harmonics in the nonlinear regime and also recovers the flat bubble top observed in experiments and in numerical simulations. In addition, it is observed that at late times a single-mode solution violates the condition of continuity of the normal component of the velocity at the interface, and is therefore unphysical. In the new approach, the potential function is represented as

$$\phi(x,y,z) = \sum_{m=0}^{\infty}\sum_{n=0}^{\infty} \phi_{mn}(t)\left[\cos(mkx)\cos(nky)\,\frac{\mathrm{e}^{-kz\sqrt{m^2+n^2}}}{k\sqrt{m^2+n^2}} + z\right]. \tag{156}$$

Retaining only one harmonic yields the Layzer-type solution. When additional harmonics are included, a new solution for the bubble velocity can be obtained by asymptotic expansions. It is found that the radius of curvature satisfies the asymptotic relation

$$R_b^{RM} \sim \frac{1}{k}\left(\frac{t}{t_0}\right)^{\beta_\infty}\;, \tag{157}$$

where the exponent β_∞ is expected to be negative, recovering the flattening of the bubble top. The new velocities are given by

$$\text{2D} \qquad \frac{2\,v_b^{RM}\,t}{\lambda} = 0.66 \;\;,\;\; \beta_\infty = -2.27 \tag{158}$$

$$\text{3D hexagonal} \qquad \frac{2\,v_b^{RM}\,t}{\lambda} = 1.12 \;\;,\;\; \beta_\infty = -2.24 \tag{159}$$

$$\text{3D square} \qquad \frac{2\,v_b^{RM}\,t}{\lambda} = 1.28 \;\;,\;\; \beta_\infty = -2.42\,. \tag{160}$$

The results indicate that the flat bubbles rise much faster than the bubbles with finite curvature.

Finally, the results were extended to fluids with a finite density ratio [4, 5] using the same multiple harmonic expansion technique. It was found that in the linear regime, $t < \lambda/v_0$, where

v_0 is the initial Richtmyer velocity of Eq. (11), the velocities and curvatures of the bubbles scale as

$$\text{2D} \qquad v_b^{RM} - v_0 \sim \frac{v_0^2\, t}{\lambda} \;\;,\;\; \kappa_b^{RM} \sim -\frac{k\, t\, v_0}{\lambda} \tag{161}$$

$$\text{3D hexagonal} \qquad v_b^{RM} - v_0 \sim \frac{v_0^2\, t}{\lambda} \;\;,\;\; \kappa_b^{RM} \sim \frac{4\pi t\, v_0}{\lambda^2\sqrt{3}} \tag{162}$$

$$\text{3D square} \qquad v_b^{RM} - v_0 \sim \frac{v_0^2\, t}{\lambda} \;\;,\;\; \kappa_b^{RM} \sim \frac{2\pi t\, v_0}{\lambda^2}. \tag{163}$$

For times well into the nonlinear regime, $t \gg \lambda/v_0$, all of the velocities and curvatures scale as

$$v_b^{RM} = \frac{3}{A\, k\, t} \;\;,\;\; \kappa_b^{RM} = 0\,. \tag{164}$$

2.4.9 The Sadot et al. empirical model for the Richtmyer-Meshkov instability

The Sadot et al. [99] empirical model for the Richtmyer-Meshkov instability is based on fits to experimental data and on asymptotic growth laws. The model was presented in the context of providing a single formula that could capture the initial linear growth, as well as the later nonlinear growth for both the bubbles and the spikes. Let $a_b(t)$ and $a_s(t)$ denote the amplitudes of the bubbles and spikes, and let $v_0 = kA^+[u]a_0$ be the Richtmyer velocity, but using the post-shock Atwood number. The Sadot model for the velocities of the bubble, spike, and mixing layer is

$$\frac{\mathrm{d}a_b}{\mathrm{d}t} = \frac{v_0\,(1 + k\, v_0\, t)}{1 + (1 + A^+)\, k\, v_0\, t + \frac{1}{2\pi C}\, k^2\, v_0^2\, t^2}\,, \tag{165}$$

$$\frac{\mathrm{d}a_s}{\mathrm{d}t} = \frac{v_0\,(1 + k\, v_0\, t)}{1 + (1 - A^+)\, k\, v_0\, t + \frac{1-A^+}{1+A^+}\, \frac{1}{2\pi C}\, k^2\, v_0^2\, t^2}\,, \tag{166}$$

$$\frac{\mathrm{d}a}{\mathrm{d}t} = \frac{1}{2}\left(\frac{\mathrm{d}a_b}{\mathrm{d}t} + \frac{\mathrm{d}a_s}{\mathrm{d}t}\right). \tag{167}$$

The value of C is determined using experimental data, and it is found that for $A^+ \geq 0.5$, $C = 1/(3\pi)$. In the limit $A^+ \to 0$, $C = 1/(2\pi)$. For intermediate values of the Atwood number, the value of C is poorly-determined. The bubble and spike amplitudes corresponding to these growth rates are

$$a_b(t) = a_b(0) + \frac{2 - 2\pi C\,(1 + A^+)}{k\sqrt{\frac{2}{\pi C} - (1 + A^+)^2}}\, \tan^{-1}\left[\frac{1 + A^+ + \frac{k\, v_0\, t}{\pi C}}{\sqrt{\frac{2}{\pi C} - (1 + A^+)^2}}\right] + \frac{\pi\, C}{k}\, \ln\left[1 + \left(1 + A^+\right) k\, v_0\, t + \frac{(k\, v_0\, t)^2}{2\pi C}\right], \tag{168}$$

$$a_s(t) = a_s(0) + \frac{2 - 2\pi C\,(1 + A^+)}{k\sqrt{\frac{2}{\pi C}\,\frac{1-A^+}{1+A^+} - (1 - A^+)^2}}\, \tan^{-1}\left[\frac{1 - A^+ + \frac{1-A^+}{1+A^+}\,\frac{k\, v_0\, t}{\pi C}}{\sqrt{\frac{2}{\pi C}\,\frac{1-A^+}{1+A^+} - (1 - A^+)^2}}\right] + \frac{\pi\, C}{k}\, \frac{1 + A^+}{1 - A^+}\, \ln\left[1 + \left(1 - A^+\right) k\, v_0\, t + \frac{1 - A^+}{1 + A^+}\, \frac{(k\, v_0\, t)^2}{2\pi C}\right]. \tag{169}$$

This model was extensively tested against experimental data, and excellent agreement was found for both the spike and bubble growth. Furthermore, the model appears to be valid over the range $Ma = 1.3$–3.5. As the model is mainly based on incompressible flow considerations, the authors conclude that compressibility effects are not significant in modeling the growth of the mixing layer.

2.5 Power-law models for multi-mode initial perturbations and following reshock

Scaling laws for the mixing layer amplitude or width arising from a multi-mode initial interfacial perturbation and following reshock of an evolving interface are presented here. In both cases, the shock-interface interaction generates a complex and possibly turbulent mixing layer at late times. The determination of the late-time or asymptotic scaling laws for the growth of the mixing layer in the Richtmyer-Meshkov instability remains an open question, and is not considered in the present work.

Multi-mode initial perturbations are particularly relevant, as such perturbations are typically found in nature, e.g., at the interfaces separating gas layers in supernovae and at the material interfaces in inertial confinement fusion (ICF) capsules. Understanding the effects of reshock, occurring as the interface undergoes multiple impulsive accelerations by waves, is also of great interest. Reshock occurs in a shock tube experiment when the transmitted shock following the initial interaction with the interface reflects from the end wall of the test section and interacts with the evolving interface. Following reshock, a transmitted shock continues in the first fluid and a reflected rarefaction wave returns into the second fluid. The reflected rarefaction wave reflects from the end wall and interacts again with the evolving interface, generating a reflected compression wave. The reflected compression wave reflects from the end wall and again interacts with the evolving interface. Eventually, the interface comes to rest following a sufficient number of such interactions. Each interaction with a reflected wave deposits additional baroclinic vorticity on the complex evolving interface, and imparts additional energy into the mixing layer. The amount of energy deposited depends on the characteristic of the small scales: for this reason, different growth characteristics are expected in the reshocked, single-mode Richtmyer-Meshkov instability than in the multi-mode Richtmyer-Meshkov instability without reshock.

2.5.1 The Alon et al. bubble merger model for $A = 1$

Alon et al. [6] developed a statistical bubble merger model for the late-time evolution of a two-dimensional Richtmyer-Meshkov bubble front in the limit $A = 1$ corresponding to fluids with very large density ratios; the choice of the Atwood number allows the use of potential theory to model the flow. The use of bubbles is justified by the observation that the late-time evolution of a Richtmyer-Meshkov unstable interface can be modeled by the rise and merger of large bubbles.

The bubbles are characterized by their diameter or wavelength λ_i and are initially arranged along a line with some distribution for λ given by $g(\lambda)$. The bubbles begin rising at velocities

$$v_b(\lambda_i) = \frac{\lambda_i}{3\pi t} \tag{170}$$

and two adjacent bubbles merge at the rate $\omega(\lambda_i, \lambda_{i+1})$, giving rise to a new bubble of diameter $\lambda_i + \lambda_{i+1}$ with velocity $v_b(\lambda_i + \lambda_{i+1})$. The amplitude of the interface $a_b(t)$ is obtained using

the average of the bubble velocities,

$$\frac{\mathrm{d}a_b}{\mathrm{d}t} = \langle v_b \rangle \,. \tag{171}$$

As observed earlier [8], the dynamics eventually reach a scale-invariant regime in which the distribution of the bubble sizes scales with the average bubble size. In this regime, the mean bubble velocity $\langle v_b \rangle$, the average wavelength $\langle \lambda \rangle$, and the scaling exponent θ_b satisfy the relations

$$\langle v_b \rangle = \frac{\langle \lambda \rangle}{3\pi t} \,, \tag{172}$$

$$\frac{\mathrm{d}\langle \lambda \rangle}{\mathrm{d}t} = \frac{\theta_b \, \langle \lambda \rangle}{t} \,, \tag{173}$$

$$\theta_b = \int_0^\infty \int_0^\infty \varpi_0\!\left(\frac{x}{y}\right) f(x)\, f(y)\, \mathrm{d}x\, \mathrm{d}y \,, \tag{174}$$

where $\varpi_0(x/y)$ is the dimensionless merger rate and $f(x)$ is the scaled distribution function that is independent of the initial distribution of bubbles. These equations yield the power-law scaling

$$a_b(t) \sim a(\lambda_0, \theta_b)\left(\frac{t}{t_0}\right)^{\theta_b} \quad , \quad a(\lambda_0, \theta_b) = \frac{\lambda_0}{3\pi\, \theta_b} \tag{175}$$

for the width of the bubble front in Richtmyer-Meshkov unstable flows, where t_0 is an arbitrary time in the scale-invariant regime, λ_0 is the average wavelength at that time, and $\theta_b = 0.4$. This scaling can also be related to the initial conditions (see [7]) by

$$a_b(t) = \frac{c_B\, \overline{\lambda}_0}{\theta_b} \left[\frac{\overline{v}_b(0)\, t}{\overline{\lambda}_0\, \eta}\right]^{\theta_b} , \tag{176}$$

where $\overline{\lambda}_0$ and $\overline{v}_b(0)$ are the average initial wavelength and bubble velocity, $\eta = O(1)$ is a parameter depending on the initial spectrum, and c_B is the scaling constant in the scale-invariant regime with $\langle v_b \rangle = c_B \langle \lambda \rangle / t$. Comparison with numerical simulations showed good agreement with the model prediction.

The model was later extended to arbitrary density ratios [7] by assuming that the merger rate ϖ of Eq. (174) is insensitive to Atwood number variations. Therefore, the scaling law with $\theta_b = 0.4$ does not change for smaller Atwood numbers. A scaling law was also derived for the amplitude of the spikes

$$a_s(t) \sim \overline{\lambda}_0 \left(\frac{\overline{u}_0\, t}{\overline{\lambda}_0}\right)^{\theta_s(A)} , \tag{177}$$

where

$$\theta_s(A) = 1 - \beta(A)\,(1 - \theta_b) \tag{178}$$

depends on the Atwood number. The sum $h = a_b + a_s$ gives the total mixing layer width corresponding to a multi-mode Richtmyer-Meshkov instability at all Atwood numbers.

2.5.2 The Rikanati et al. vortex model for bubble merger when $A \to 0$

Rikanati, Alon and Shvarts [108] reconsidered the modeling of the bubble merger process in the limit of $A \to 0$. Noting that the potential flow model (which is the basis of the Alon et al. [6] model) is no longer appropriate at small Atwood numbers, an alternative model based

on the Jacobs and Sheeley [55] vortex model was proposed, as vortices form shortly after the passage of the shock.

Consider an initial array of identical vortices forming a vortex line, for which the complex-valued potential is

$$\begin{aligned} w(z) &= \frac{i\Gamma}{2\pi} \sum_{n=-\infty}^{\infty} \ln\left(z - n\, z_0\right) \\ &= \frac{i\Gamma}{2\pi} \ln\left[\sin\left(\frac{\pi z}{z_0}\right)\right], \end{aligned} \tag{179}$$

where z_0 is the constant separation between the vortices and Γ is the vortex circulation. The single-mode Richtmyer-Meshkov instability can be modeled by two periodic arrays with vortices of opposite strength adjacent to one other. When the initial perturbation is sinusoidal, it is possible to obtain an expression for $\Gamma = a_0/k$, which yields

$$h(t) = \frac{1}{k} \sinh^{-1}\left(\frac{\Gamma\, k^2}{2\pi t}\right) \tag{180}$$

for the mixing layer width. Thus, the asymptotic velocity scales as

$$v_b(t) = \frac{\lambda}{2\pi t}\,, \tag{181}$$

compared to the asymptotic velocity in the case $A = 1$ [45] based on the potential model,

$$v_b(t) = \frac{\lambda}{3\pi t}\,. \tag{182}$$

The difference between the two values is due to the added mass in the case $A = 0$.

Now consider the case of a periodic array of bubbles with two different strengths. The bubble merger rate was then approximated as

$$\omega\left(\frac{\lambda_1}{\lambda_2}\right) = \frac{1}{\Delta t_m}\,, \tag{183}$$

where t_m is the merger time—the time required for the tip of a small bubble to go from positive to negative. This result for ω and the resulting asymptotic velocity for the single bubble in Eq. (181) are used in the bubble merger model, which yields the scaling law for the bubble amplitude in Eq. (176) with $\theta_b = 0.4$. Note that the value of θ_b is the same for $A = 0$ and $A = 1$, further confirming the observation of [7].

2.5.3 The Prasad et al. late-time model

Prasad et al. [103] performed experiments to study the late-time evolution of the single-mode Richtmyer-Meshkov instability and developed an empirical power-law model based on their data. At late times, the mixing layer width was assumed to scale according a power-law

$$h(t) = c\, t^{\theta} \tag{184}$$

where c is a constant having appropriate units.

Experiments were performed for a $Ma = 1.55$ shock refracting at a perturbed air/SF_6 interface with different initial amplitudes and wavelengths. The width of the interface was measured up to 32 initial perturbation wavelengths from the initial location to determine the power-law that best fits the data. The scatter from different measurements with different initial amplitudes and wavenumbers is reduced if the data is normalized by the wavenumber k. A composite least-squares fit to the data yielded

$$\begin{aligned} k\,h(t) &= 0.96\,(k\,x)^{0.33} \\ &= 0.96\,(k\,[u]\,t)^{0.33} \end{aligned} \tag{185}$$

with $x = [u]\,t$. In a separate study, the empirical scaling

$$\begin{aligned} h(t) &= 2.43\,(\lambda\,x)^{0.26} \\ &= 2.43\,(\lambda\,[u]\,t)^{0.26} \end{aligned} \tag{186}$$

was shown to minimize the scatter of the data and to give the best fit.

2.5.4 The Youngs model for multi-mode initial conditions

Youngs [126] proposed a model for the late-time scaling of the mixing layer width emerging from the multi-mode Richtmyer-Meshkov instability. Youngs considered random initial amplitudes a_0 chosen from a Gaussian distribution. The standard deviation in the region $k < k_{\max}$ is flat, where

$$k_{\max} = \frac{\pi}{\Delta y} \tag{187}$$

is the Nyquist wavenumber. Therefore, the relation

$$\sigma^2 = C \int_0^{k_{\max}} \mathrm{d}k \tag{188}$$

between the standard deviation σ and the integral of the wavenumbers was obtained in two dimensions. For a single-mode Richtmyer-Meshkov instability, $\sigma^2 = a_0^2/2$. The random initial kinetic energy is

$$K_0 = \frac{1}{3}\,(\rho_1 + \rho_2)\,k_{\max}\,(\sigma\,A\,[u])^2\ . \tag{189}$$

Most of the initial kinetic energy arises from modes with wavenumbers near $k_{\max}$ corresponding to an initial wavelength $\lambda_{\min}$. A turbulent layer is assumed to develop when the mixing layer width becomes of order $\lambda_{\min}$. This layer was shown to have width evolving as t^θ with $\theta < 1$. The following model was developed to explain this.

Assuming that the velocity field is characterized by a lengthscale L and magnitude V, the kinetic energy dissipation rate scales as $\epsilon \sim V^3/L$. The model equations are

$$\frac{\mathrm{d}}{\mathrm{d}t}\big(L\,V^2\big) = -a\,V^3\,, \tag{190}$$

$$\frac{\mathrm{d}W}{\mathrm{d}t} = V\,, \tag{191}$$

$$L = b\,W + c\,\lambda_{\min}\,, \tag{192}$$

where a, b, and c are model parameters, and W is an integral lengthscale [9]. This lengthscale is defined in terms of the averaged volume fractions $\langle f_1 \rangle$ and $\langle f_2 \rangle$ according to

$$W(t) = \int_{a_s(t)}^{a_b(t)} \langle f_1 \rangle \langle f_2 \rangle \, \mathrm{d}x \,, \tag{193}$$

where the angle brackets denote a spatial average over the periodic direction(s) (see § 4.1). This lengthscale provides a measure of the diffusive width of the mixing layer, and is less sensitive to statistical fluctuations than h. The volume fractions of the two fluids f_r are defined in terms of their mass fractions $m_r(x, y, t)$ by [126]

$$f_r(x, y, t) = \frac{\frac{m_r(x,y,t)}{\rho_r}}{\frac{m_1(x,y,t)}{\rho_1} + \frac{m_2(x,y,t)}{\rho_2}} \,, \tag{194}$$

such that $f_1 + f_2 = 1$. Note that W provides an alternative measure of the mixing layer width. The initial value of V is given by

$$V_0 = \left(\frac{\mathrm{d}W}{\mathrm{d}t} \right)_{t=0} = c \sqrt{\langle u_0^2 \rangle} \,, \tag{195}$$

$$c = \frac{1}{\sqrt{2}} \int_0^\infty [1 - \mathrm{erf}(s)] \, \mathrm{d}s = 0.564 \,, \tag{196}$$

$$\sqrt{\langle u_0^2 \rangle} = \frac{k_{\max} \, \sigma \, U}{\sqrt{2}} \, |A| \,. \tag{197}$$

Therefore, for the initial conditions $W(0) = 0$ and $V(0) = V_0$, the power-law solution

$$W(t) = \frac{c}{b} \, \lambda_{\min} \left[\left(1 + \frac{V_0 \, t \, b}{\theta \, a \, \lambda_{\min}} \right)^\theta - 1 \right] \tag{198}$$

is obtained, where

$$\theta = \frac{2}{3 + a \, b} \,. \tag{199}$$

For the case when no kinetic energy dissipation occurs (corresponding to $a = 0$), the classical $\theta = 2/3$ result of Barenblatt [15] is recovered. When kinetic energy dissipation occurs, the equations predict $\theta < 2/3$.

Youngs compared the predictions of the model (198) with the growth rates obtained from multi-mode, monotone-integrated large-eddy simulations in two and three dimensions. Initially, the growth rate of $W/\lambda_{\min}$ was the same in two and three dimensions. At intermediate times, $W/\lambda_{\min}$ was larger for the three-dimensional simulations, indicating that mixing is more rapid in three dimensions. At later times, the larger dissipation of kinetic energy in three dimensions causes the value of $W/\lambda_{\min}$ to become smaller than that observed in two-dimensional simulations. For late times, the three-dimensional data was fitted to the model equation with $\theta = 0.30$.

2.5.5 The Mikaelian model for a reshocked interface

A linear power-law model for the mixing layer width following reshock was developed by Mikaelian [87] based on the experimental results of Read [105] and Youngs [124] for the width of a Rayleigh-Taylor mixing layer

$$h(t) = 0.14\, A\, g\, t^2\,, \tag{200}$$

where A is the Atwood number and g is the acceleration. Differentiating this expression twice, taking $g = [u]_1 \delta(t)$ (where $[u]_1$ is the change in velocity resulting from the reshock), and integrating twice gives (assuming no dependence on initial conditions and neglecting molecular dissipation effects) the linear-in-time expression

$$h(t) = 0.28\, [u]_1\, A_1^+\, t \tag{201}$$

where A_1^+ is the post-reshock Atwood number [87].

2.5.6 The Brouillette-Sturtevant model for a reshocked interface

Brouillette and Sturtevant [19] performed shock tube experiments to measure the effect of a thick, diffuse interface on the growth of the Richtmyer-Meshkov instability. In these experiments, a thin metal plate initially separated air and SF_6 or air and Freon-22 gas. Prior to launching the shock wave in air, the plate was slowly withdrawn to generate a quasi-sinusoidal perturbation, leaving a thick, diffuse interface separating the two gases. The shock launched in air at Mach numbers 1.12–1.66 refracted at the interface and was transmitted into the second gas. The transmitted shock reflected from the end wall of the shock tube test section and reshocked the interface.

The growth of the width of a single-mode interface following $N+1$ impulsive accelerations was empirically modeled by generalizing the Richtmyer model:

$$\left(\frac{\mathrm{d}h}{\mathrm{d}t}\right)_N = 2\,k \sum_{i=0}^{N} \frac{[u]_i\, A_i^+\, a_i^+}{\psi_i^+}\,, \tag{202}$$

where k is the initial perturbation wavenumber, $[u]_i$ is the change in the velocity of the interface corresponding to the ith wave, A_i^+ and a_i^+ are the post-shock Atwood number and interface width, ψ_i^+ is the post-shock growth reduction factor of Duff et al. [39] (see § 2.1.7), and the factor of 2 accounts for the mixing layer width (which is twice the mixing layer amplitude a). As the growth is based on the Richtmyer model for each impulsive acceleration, the Brouillette-Sturtevant model predicts piecewise-linear-in-time amplitude growth phases. This model for shocks can also be used for reflected rarefaction waves and, thus, constitutes a model for the description of the reshock phase, as it accounts for the multiple waves that successively interact with the interface. The reflected shock refracts at the evolving interface during reshock to produce an expansion wave. This expansion wave reflects from the end wall of the shock tube and interacts with the interface, producing a reflected compression wave. The compression wave reflects from the end wall and interacts again with the interface, and this process continues. Brouillette and Sturtevant reported good agreement between their experimental data and the prediction of Eq. (202).

2.6 The Samtaney-Zabusky-Ray model for baroclinic circulation deposition

Samtaney and Zabusky [113] and Samtaney, Ray and Zabusky [112, 104] derived analytical scaling laws for the circulation Γ per unit unshocked length deposited on a planar interface by a shock. The interaction can be classified as fast/slow or slow/fast based on the relative speed of the incident and transmitted shocks. Fast/slow interactions occur when the refraction is from a lighter fluid into a heavier fluid, and is associated with a reflected shock wave. Slow/fast interactions occur when the refraction is from a heavier fluid to a lighter fluid, and is usually associated with a reflected rarefaction wave. In the present investigation, a slow/fast interaction is observed for the initial shock refraction from air(acetone) into SF_6, and a fast/slow interaction is observed at reshock.

The circulation deposition model is derived from shock polar analysis (see [68]). In shock refraction, five regions can be identified when the flow is considered in a frame moving with the triple-point, as shown in Fig. 5. The parameters of the model are the density ratio $r \equiv \rho_1/\rho_2$, the angle between the interface and the shock α, the shock Mach number Ma, and the adiabatic exponents of the two gases γ_r. Note that in Part 1 of the present report [68], β was the angle between the interface and the direction of shock propagation. As a result $\beta + \alpha = \pi/2$. For scaling purposes, the adiabatic exponents are taken to be equal.

In the case of a fast/slow interaction in the limit of a strong shock $Ma \to \infty$, the circulation deposition Γ is given by

$$\frac{\Gamma}{Ma} \longrightarrow \frac{\sqrt{\gamma}}{\sin\alpha}\left(\sqrt{1-\frac{2\,p_\infty \sin^2\alpha}{(\gamma+1)\,r}}-\sqrt{1-\frac{2\,(1+\mu^2\,p_\infty)\sin^2\alpha}{(\gamma+1)\left(\frac{1}{\mu^2}+\frac{1+\mu^2}{p_\infty}\right)}}\right)\frac{\cos\alpha}{\cos\left(\alpha-\delta_{b\infty}\right)}\,, \tag{203}$$

where $\mu \equiv (\gamma-1)/(\gamma+1)$, $p_\infty \equiv p_5/Ma^2$, and $\delta_{b\infty}$ represents the asymptotic flow turning angle in region 2 as $Ma \to \infty$.

For weak shocks with $Ma \to 1$,

$$\Gamma = \frac{2\sqrt{\gamma}}{\gamma+1}\,\frac{\sqrt{r}-1}{\sqrt{r}}\,\sin\alpha\left(1+\frac{1}{Ma}+\frac{2}{Ma^2}\right)(Ma-1)\,. \tag{204}$$

For small density discontinuities across the interface, the circulation is expressed as a series in $r' = 1 - 1/\sqrt{r}$.

The proposed circulation scaling law is

$$\Gamma = \frac{2\sqrt{\gamma}}{\gamma+1}\left(1-\frac{1}{\sqrt{\gamma}}\right)\sin\alpha\left(1+\frac{1}{Ma}+\frac{2}{Ma^2}\right)(Ma-1)\,. \tag{205}$$

In the case of a slow/fast interaction and for strong shocks ($Ma \to \infty$),

$$\Gamma \longrightarrow \frac{K(r,\alpha,\gamma)}{\sqrt{1-\xi(Ma)}}\,, \tag{206}$$

where

$$K(r,\alpha,\gamma) = \frac{\sqrt{\gamma+1}\cot\alpha}{\sqrt{2}\cos\left(\alpha-\delta_b\right)} \tag{207}$$

$$\times\left(\sqrt{1-\frac{1}{r}\,\frac{4\,\gamma\,p^{(\gamma-1)/\gamma}\sin^2\alpha}{(1+\mu^2)^{(\gamma-1)/\gamma}\,(\gamma+1)^2}}-\sqrt{1-\frac{4\,\gamma\,p^{(\gamma-1)/\gamma}\sin^2\alpha}{(1+\mu^2)^{(\gamma-1)/\gamma}\left[(\gamma+1)^2-4\,\gamma\sin^2\alpha\right]}}\right),$$

and

$$\xi(Ma) = \frac{\frac{2\gamma}{\gamma+1}\left(Ma^2-1\right)}{1+\frac{2\gamma}{\gamma+1}\left(Ma^2-1\right)} \tag{208}$$

is the normalized pressure jump.

In the limit of weak shocks with $Ma \to 1$,

$$\Gamma = \frac{2}{\sqrt{\gamma}}\left(1-\frac{1}{\sqrt{r}}\right)\xi(Ma)\sin\alpha\,. \tag{209}$$

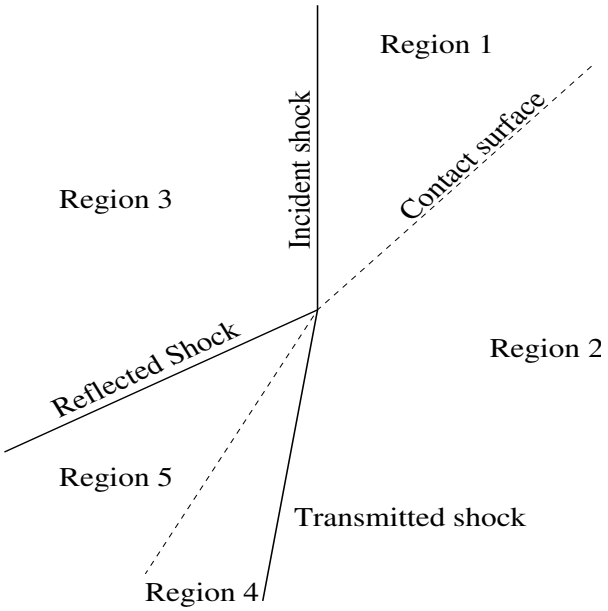

Figure 5: The wave structure of a shock interacting with a contact surface in a reference frame moving with the point of contact. Note the reflected and the transmitted shocks.

3 Numerical simulations of two-dimensional, single-mode Richtmyer-Meshkov instability with reshock

In this section the `HOPE` code, based on the formally high-order accurate weighted essentially non-oscillatory (WENO) shock-capturing method with a third-order TVD Runge-Kutta time-evolution scheme, is used to simulate the two-dimensional, single-mode Richtmyer-Meshkov instability with reshock (see Part 1 of this report [68] for a detailed discussion of the WENO method and a description of the `HOPE` code). The WENO method is a modern, high-resolution reconstruction-evolution method for shock-capturing [66, 73]. As such, the numerical algorithm based on the discretization of the equations contains implicit truncation errors that can be regarded as a nonlinear numerical dissipation. Hence, the present simulations can be interpreted as a class of *monotone integrated large-eddy simulations* (MILES) [17, 37, 38], in which the discrete equations are implicitly filtered and the implicit numerical dissipation is a surrogate for a dissipation provided by an explicit subgrid-scale model. As the non-dissipative compressible fluid dynamics equations are formally ill-posed [27], this numerical dissipation regularizes the method and renders it numerically stable for increasingly fine grids. Formally higher-order reconstructions are less dissipative than lower-order reconstructions. MILES methods typically dissipate velocity and scalar fluctuations approximately in the same manner numerically. Thus, the numerical Schmidt number is of $O(1)$, which may provide a reasonable approximate model for the mixing of gases. However, this approximation is clearly not valid for the case for fluids with large (molecular) Schmidt numbers. It should be noted that the present work should not be regarded as an endorsement of the WENO method or of MILES in general; rather, this work should be regarded as a preliminary investigation of the properties of this method as applied to the Richtmyer-Meshkov instability with reshock. Ultimately, the WENO method should be further modified to reduce the numerical dissipation and improve its resolving power: the hybridization of the WENO method with a central difference scheme, based on multi-resolution analysis, represents one such approach (see [68]). In addition, molecular dissipation terms and an explicit subgrid-scale model should be added.

It should be noted that the WENO method was previously applied to the Richtmyer-Meshkov instability. Kremeyer et al. [65] used a fifth-order WENO method with a third-order TVD Runge-Kutta time-evolution scheme to perform two-dimensional simulations of the Richtmyer-Meshkov instability evolution in a shock tube containing gases with different initial transverse density profiles to investigate shock splitting and, in particular, the role of shock bowing and vorticity dynamics. Top-hat shaped perturbations, including those shaped as a notch, were considered instead of a single-mode sinusoidal perturbation considered in classical investigations of this instability. Zhang et al. [131] used the fifth- and seventh-order WENO method to simulate the interactions between planar Mach 1.095 and 1.2 shocks with an SF_6 gas cylinder in two dimensions in order to qualitatively and quantitatively study the dynamical mechanisms of baroclinic vorticity and circulation generation. The results from the WENO simulations were also compared to the results obtained using the `FLASH` code. The interface between the vertical cylinder and surrounding air was modeled by a transition layer of finite thickness. In addition to flow visualizations at different evolution times, cylinder lengths, integrated positive and negative vorticity components, normalized circulation, the distributions of the velocity and density gradient, and cylinder aspect ratio were extracted from the numerical simulation data as a function of time.

The initial conditions for the present simulations are described in § 3.1. The density fields obtained from the simulations are compared to experimental PLIF images in § 3.2. The

mixing layer amplitude is compared to experimental data and to the predictions of models before and after reshock in § 3.3 and § 3.4, respectively. The time-evolution of the circulation is considered in § 3.5. Local and global analysis of the mixing properties are considered in § 4. Comparisons of quantities obtained from simulations using different orders of reconstruction and grid resolutions are presented later in § 5.

3.1 Numerical simulation parameters

The initial conditions for the present numerical simulations were taken from the experimental shock tube configuration of Collins and Jacobs [29]. The Mach 1.21 experiment was selected for additional validation of the `HOPE` code by comparing the numerical results to the high-resolution density PLIF images showing the evolution of the instability and to the measured mixing layer amplitude prior to reshock. The experiments were conducted in a shock tube using a novel technique to generate a membrane-less perturbed interface. The entire shock tube had a length of 4.3 m with a square test section having cross-section 8.9 cm × 8.9 cm and length 75 cm. The shock was generated through the rupture of a membrane and was launched into a mixture of 75% air and 25% acetone by volume [referred to as air(acetone)] at standard room temperature and pressure. The shock then refracted at a perturbed interface separating the air(acetone) mixture and the denser sulfur hexafluoride (SF_6) gas, giving rise to the Richtmyer-Meshkov instability.

The membrane-less interface was generated through a technique described by Jones and Jacobs [56]. The shock tube contained horizontal slots on two opposite walls. The gases entered the shock tube from opposite ends, flowed toward each other, and exited through the two slots, resulting in a fine, diffuse interface. A perturbation was then generated by gently oscillating the vertical shock tube at a prescribed frequency to establish a standing wave. The diffuse interface was estimated to be 0.5 cm wide, and the oscillations produced a sinusoidal perturbation. Planar laser-induced fluorescence (PLIF) was used to visualize the instability evolution using a mixture of fluorescent acetone with air. The PLIF images were corrected for the non-uniform laser illumination and Beer's law attenuation.

A set of experiments was conducted for shocks with $Ma = 1.11 \pm 0.01$ and $Ma = 1.21 \pm 0.02$, and images were captured up to 11 ms following the initial shock-interface interaction. The evolution of the instability with spikes of heavier fluid penetrating the lighter fluid and bubbles of lighter fluid "rising" in the heavier fluid was investigated. The reshock phase observed when the transmitted shock reflects from the end wall of the test section and interacts with the evolving interface was also described. Concurrent with the arrival of the reflected shock, a reflected rarefaction wave also interacted with the interface, as seen in Fig. 4 of [29]. This initial rarefaction wave was created by the rupture of the membrane used to generate the initial shock, was subsequently reflected from the end (top) wall of the shock tube, and then interacted with the evolving interface. This interaction with the reflected rarefaction wave induced the formation of additional complex structure on the evolving interface.

3.1.1 Initial gas composition

The experiment was performed using a mixture of air and acetone initially separated from sulfur hexafluoride (SF_6) by a diffuse interface. See Table 1 in Part 1 of this report [68] for a summary of the thermodynamic properties of the air(acetone) and SF_6 gases. In order to specify a single value of the adiabatic exponent to be used in the simulations, a mixture of 50% air(acetone) and 50% SF_6 by volume was assumed, yielding $\gamma = 1.24815$. The pre-shock

Atwood number was $A^- = 0.604$. Only the Mach 1.21 experiment is considered in the present report. The conditions in region 1 ahead of the shock are $p_1 = 0.925551$ bar, $T_1 = 296$ K, and $u_1 = 0$ cm/s. Cook, Cabot and Greenough [30] also considered this experiment prior to reshock, and modified their simulation parameters to account for non-ideal effects in the shock tube, such as an effectively smaller Mach number due to the outflow of gas through the slots. In the present investigation, no such modifications are used.

3.1.2 Computational domain and interfacial perturbation

To match the shock tube test section dimensions [29], the computational domain has spanwise dimension $L_y = 8.9$ cm, with the perturbed initial interface located 3 cm from the edge of the shock tube. To obtain a test section length of 75 cm, the total length of the computational domain along the streamwise direction is $L_x = 78$ cm, as illustrated in the top of Fig. 6. The adaptive domain capability in the `HOPE` code [68] allows the initial domain in x to be much smaller than L_x. In the present simulation, the initial value of L_x is chosen to be approximately 9.3 cm (see Table 3 in § 5 for the values used in the simulations). The computational domain in the x direction is elongated in increments of 3 cm until a total length of 78 cm is attained. *All of the numerical results presented in this section were obtained using the fifth- and ninth-order WENO method with a grid resolution $\Delta x = \Delta y$ corresponding to* 256 *points per initial perturbation wavelength. A CFL number of 0.75 was used.*

As in the experiment, the sinusoidal interfacial perturbation of Eq. (3) had amplitude $a_0 = 0.2$ cm and wavelength $\lambda = 5.93333$ cm, and the diffuse interface had width $\delta = 0.5$ cm in the numerical simulation. Thus, $ka_0 = 0.21 \ll 1$, so that the initial growth is in the linear regime. The initial conditions are illustrated on the bottom of Fig. 6, where the density Schlieren is plotted. The Schlieren is defined in Eq. (224) in § 3.3.3 and shows the width of the diffuse interface, and that the shock is captured with two grid points in the direction of shock propagation.

3.2 Qualitative comparison of instability evolution to experimental PLIF images

In Fig. 7, corrected PLIF density images from the Collins and Jacobs Mach 1.21 shock tube experiment are compared to the density fields from the numerical simulations at selected times before reshock: the experimental images are presented in the middle row, the fields from the ninth-order WENO simulation are presented in the top row, and the fields from the fifth-order WENO simulation are presented in the bottom row. The grid resolution of both simulations was 256 points per initial perturbation wavelength, and both simulations were identical in every other respect. Very good agreement is observed between the numerical and experimental images. The density obtained from the ninth-order simulation shows sharper roll-ups than that from the fifth-order simulation.

Figure 8 continues this comparison of the experimental images to the simulation densities for selected times following reshock. The ninth-order simulation captures the secondary instability within the roll-ups at $t = 6$ ms. The agreement continues to be very good, although an increasing time discrepancy between the numerical and experimental results develops, with the simulation images lagging in time behind the PLIF images. This time delay can be explained by the arrival of the initial rarefaction wave in the experiment, which decelerates the evolving interface, causing a progressively larger delay in the time of reshock. The rarefaction wave also causes the formation of small-scale structures on the interface that are amplified during

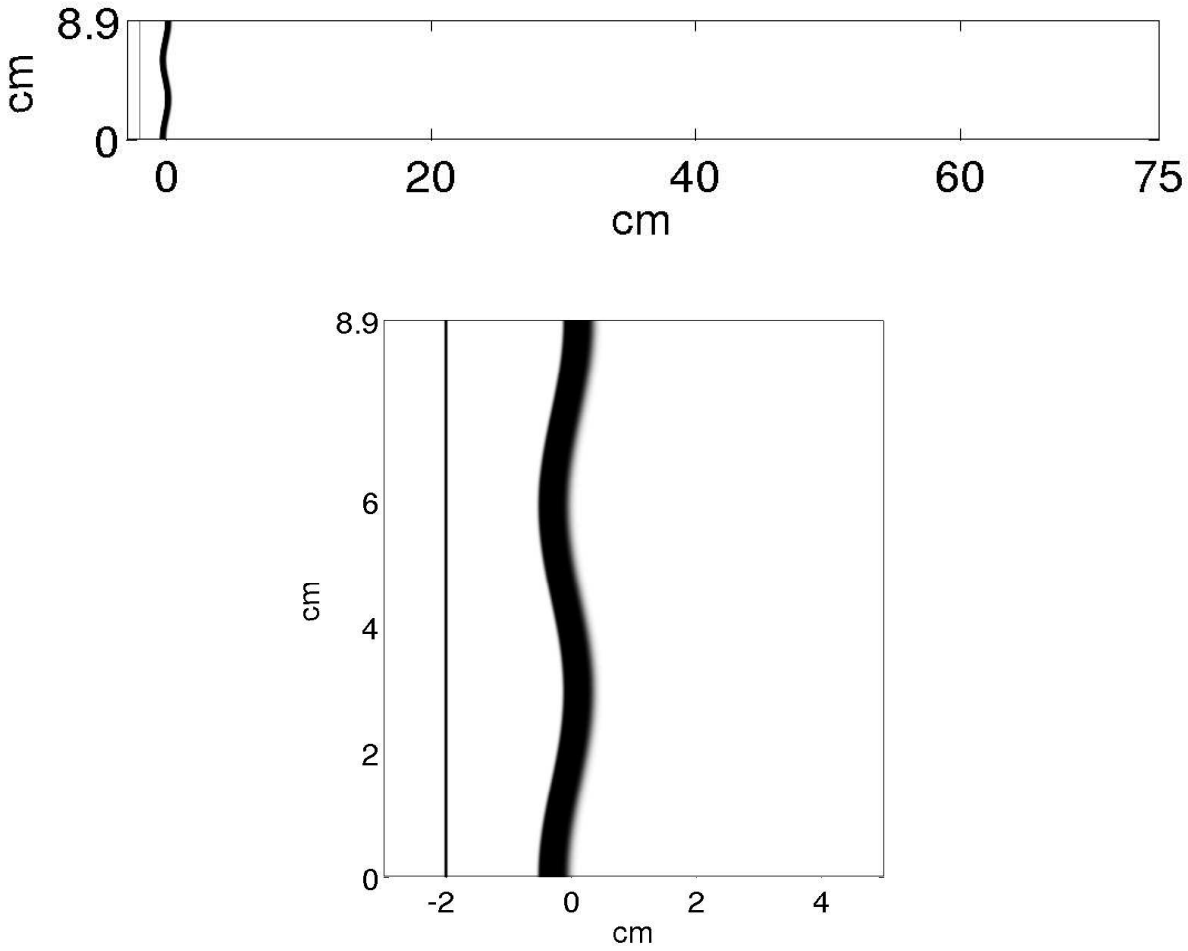

Figure 6: Illustration of the shock tube test section (top) and density Schlieren of the initial condition (bottom) with the shock on the left at $x = -2$ cm and the diffuse interface on the right.

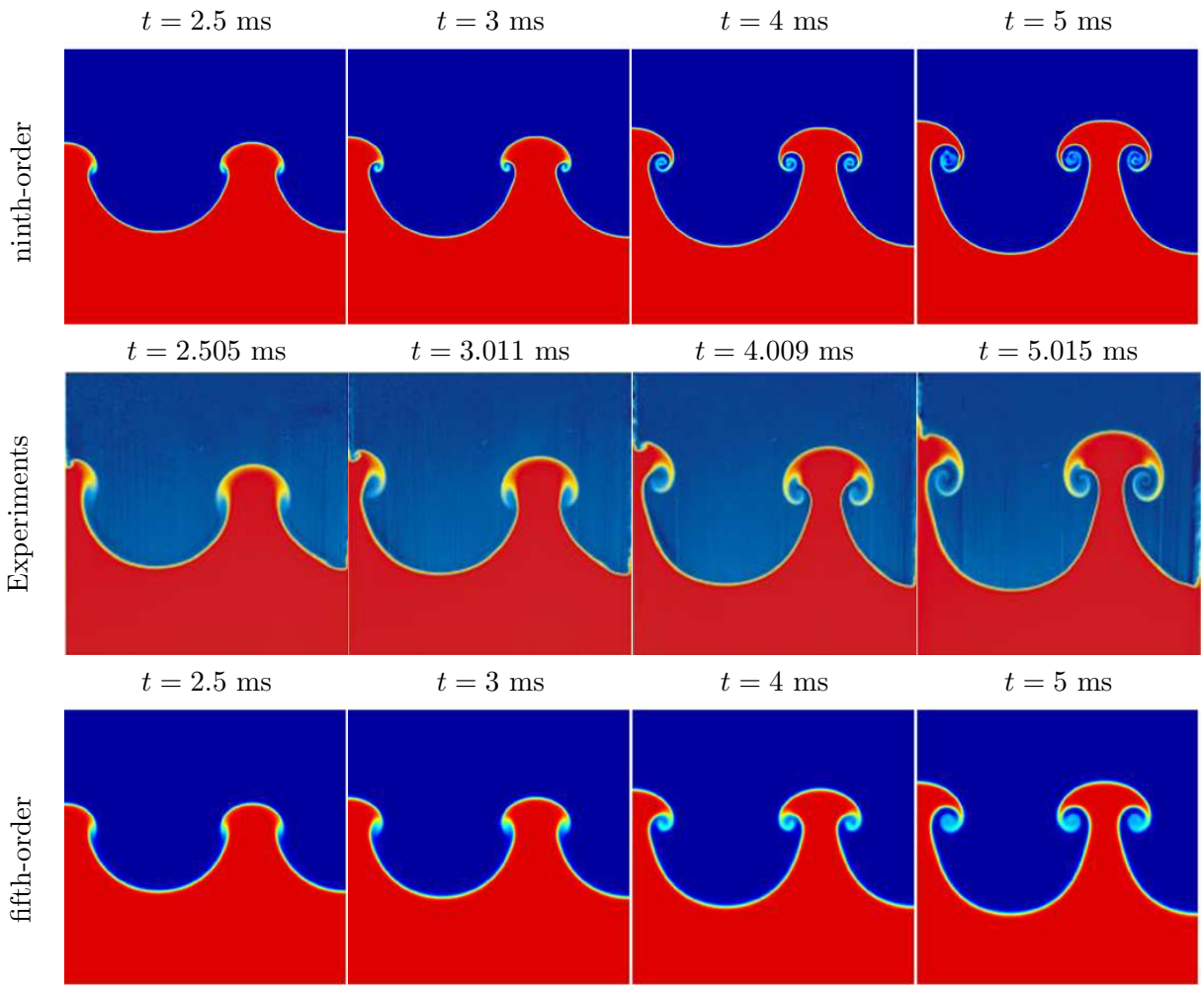

Figure 7: Comparison of corrected PLIF images from the experiment of Collins and Jacobs (middle row) and the density from the ninth-order WENO simulation (top row) and from the fifth-order WENO simulation (bottom row), both on the medium resolution grid. The gases are air(acetone) (blue) and SF_6 (red). Note the very good agreement between the experiment and simulation. The ninth-order simulation captures more of the structure of the roll-up observed in the experiment at late times than does the fifth-order simulation. The experimental images are taken from Fig. 6 of Collins and Jacobs [29] (reprinted with the permission of Cambridge University Press).

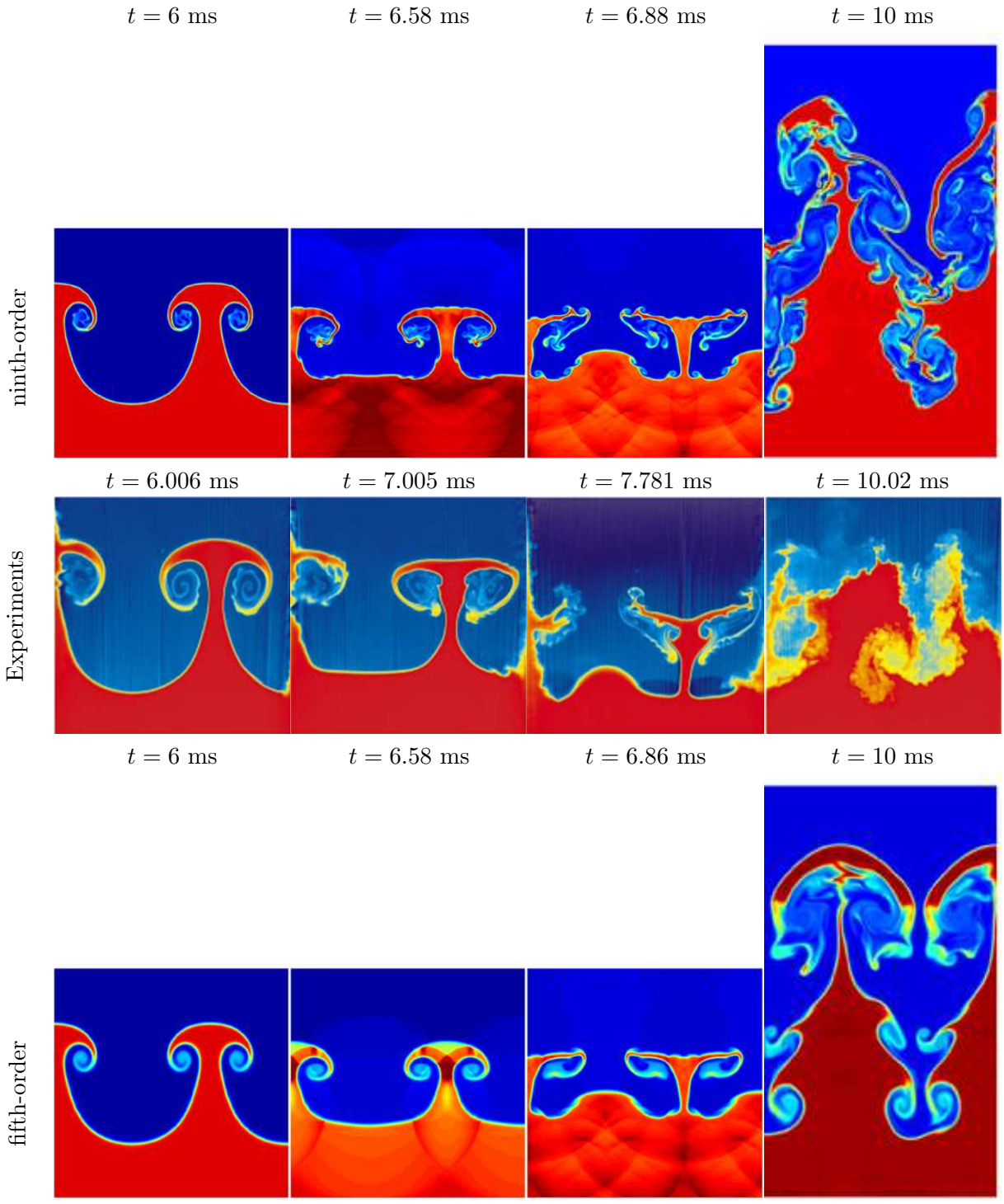

Figure 8: Further comparison of the corrected PLIF images from the experiment of Collins and Jacobs and the density from the numerical simulations (see Fig. 7). A progressively larger time delay develops between the experimental and simulation images due to the rarefaction wave in the experiment, which is not captured in the simulations. The rarefaction wave decelerates the interface, causing reshock to occur later in time in the experiment compared to the simulation. The experimental images are taken from Fig. 6 of Collins and Jacobs [29] (reprinted with the permission of Cambridge University Press).

reshock. Note that at late time ($t = 10$ ms), the experimental data shows increased mixing and fragmentation of large structures. By contrast, the numerical simulations show that large structures persist. This is due to the excitation of fluctuations in the third spatial dimension caused by the initial rarefaction wave present in the experiment and subsequently amplified by reshock, which is not modeled in the numerical simulation. However, the numerical simulations show that more complex, finer and disordered structures form following reshock. In addition, the fluid interface observed from the ninth-order simulation shows the appearance of small-scale roll-ups that are not present in the experimental and fifth-order images. This is due to molecular dissipation effects present experimentally, and to the relatively large numerical dissipation of the fifth-order simulation that is significantly reduced in the ninth-order simulation.

The qualitative comparison above shows that it is possible to achieve very good agreement between a two-dimensional, high-resolution shock-capturing simulation with high-order reconstruction of the fluxes and experimental density PLIF images *before reshock when three-dimensional effects are not very significant*. The comparison of densities from the fifth- and ninth-order simulations demonstrates that higher-order reconstruction better captures secondary instabilities, the roll-ups appear tighter and sharper, and more fine-scale structures are present. The fields from the numerical simulations also supplement the experimental images by displaying the shock focusing observed during reshock. Following reshock, the experiment and simulations exhibit distinctively different flow structures. This is due to the absence of the reflected rarefaction wave and the increased importance of three-dimensional effects including vortex stretching and associated mechanisms that are not accounted for in the two-dimensional simulations. This results in the formation and persistence of large-scale structures in the simulations, consistent with the inverse cascade of kinetic energy from small scales to larger scales observed in two-dimensional experiments and simulations [64, 58] and explains the much larger amplitude observed in the numerical simulations following reshock compared to the experimental data. The experiments further show the effects of molecular diffusion and dissipation mechanisms which are not explicitly modeled by the equations solved numerically. The numerical simulations contain implicit numerical diffusion and dissipation that may not be comparable to the molecular values in the physical experiment. The comparison of the fifth- and ninth-order simulations shows that as the order is increased, finer and more complex asymmetric structures appear, consistent with a reduced numerical dissipation. These aspects of the model are further investigated in § 5 where a detailed comparison of quantities computed using different orders of reconstruction and grid resolutions, corresponding to different levels of numerical dissipation and diffusion, is performed.

3.3 Evolution of the amplitude prior to reshock

In this section, the perturbation amplitude growth obtained from the fifth-order, medium resolution numerical simulation is compared to the experimentally-measured amplitude from Collins and Jacobs [29] and to the predictions of the models presented in § 2. First, the methods used to determine the mixing layer amplitude, and the bubble and spike amplitudes from the numerical simulation is presented. Next, the amplitude from the numerical simulation is compared to the experimental data points. Reshock is further investigated using simulated density Schlieren images, which provide detailed wave structures and resolution of fine scales. Next a comparison of the mixing layer amplitude to the predictions of impulsive models, point vortex models, potential flow models, and nonlinear perturbation series models is presented,

with the model parameters computed self-consistently from the numerical simulations. Finally, the predictions of the models with parameters obtained from the experiments are also shown for comparison.

3.3.1 Numerical determination of the mixing layer width

The mixing layer width is obtained from the mole fraction as follows. In incompressible or variable-density flows, the mole fraction is typically defined as [31]

$$X(x,y,t) = \frac{\rho(x,y,t) - \rho_2}{\rho_2 - \rho_1}\,. \tag{210}$$

However, this definition is not desirable for compressible flows, as it is unclear how ρ_1 and ρ_2 should be defined. An alternative definition of the mole fraction based on the molecular weights and on the mass fraction is therefore needed. In the present numerical simulations, the mass fraction

$$m_2 = \frac{c_2\,M_2}{c_1\,M_1 + c_2\,M_2} \tag{211}$$

of fluid 2 (SF_6) is evolved, where M_r and c_r are the molecular weight and molar concentration of fluid i, respectively. By definition, the mass fraction of fluid 1 is

$$\begin{aligned} m_1 &= 1 - m_2 \\ &= \frac{c_1\,M_1}{c_1\,M_1 + c_2\,M_2}\,. \end{aligned} \tag{212}$$

Then, the mole fraction of fluid 2 can be defined in terms of the molar concentrations by

$$X = \frac{c_2}{c_1 + c_2}\,. \tag{213}$$

Using the above definitions, define a mean molecular weight

$$\overline{M} = \frac{c_1\,M_1 + c_2\,M_2}{c_1 + c_2}\,, \tag{214}$$

which can also be obtained from the mass fractions m_r by solving Eqs. (211) and (212) for c_1 and c_2 and substituting into Eq. (214) to obtain

$$\overline{M} = \frac{M_1\,M_2}{M_1\,m_2 + M_2\,m_1}\,. \tag{215}$$

Finally, the mole fraction is obtained from the mass fraction m_2 and $\overline{M}$ as

$$X = \frac{\overline{M}\,m_2}{M_2}\,. \tag{216}$$

Equations (215) and (216) yield the desired relation $X = X(M_1, M_2, m_2)$ independent of the densities, and therefore suitable for compressible flows.

The mixing layer width is obtained by spatially-averaging the mole fraction in the periodic y-direction

$$\langle X\rangle = \frac{1}{L_y}\int_0^{L_y} X(x,y,t)\,\mathrm{d}y\,, \tag{217}$$

where L_y is the width of the shock tube in the spanwise direction. The spike and bubble locations, $\ell_s(t)$ and $\ell_b(t)$, are defined as the x position where $\langle X \rangle \geq \epsilon$ and $\langle X \rangle \leq 1 - \epsilon$, respectively, with $\epsilon = 0.01$ in the present investigation (corresponding to a 1–99% criterion in the mole fraction). Therefore, the total mixing layer width is numerically determined by

$$h(t) = \ell_b(t) - \ell_s(t)\,. \tag{218}$$

Note that this definition of the mixing layer width is quite sensitive to the choice of ϵ. This sensitivity will be discussed elsewhere [70].

To obtain the bubble and spike amplitudes separately, a numerical simulation without an initial perturbation, but otherwise identical to the Richtmyer-Meshkov simulation, was performed to obtain the position the position of the interface ℓ_{int}. The bubble and spike amplitudes were then obtained using $\ell_{int}(t)$ as

$$a_b(t) = \ell_b(t) - \ell_{int}(t)\,, \tag{219}$$

$$a_s(t) = \ell_{int}(t) - \ell_s(t)\,, \tag{220}$$

as shown in Fig. (10). As the Atwood number in the present simulation is fairly large, it is expected that the bubble and spike amplitudes grow asymmetrically. In particular, the spikes of SF_6 penetrate deeper into the air(acetone) gas than the bubbles of air(acetone) "rise" into SF_6. The various kinks observed in the amplitudes indicate the arrival of the reflected shock, the reflected rarefaction wave, and the reflected compression wave.

For completeness, Fig. 11 exhibits the locations of the interface and shock in the x-t diagram from the simulation. The locations of the spike $\ell_s(t)$ and of the bubble $\ell_b(t)$ are indicated by the dashed and solid blue lines, respectively. The interface location $\ell_{int}(t)$ is also shown in green. The horizontal distance between the spike and bubble represents the amplitude $a(t)$ (see Fig. 4 for a schematic of the total amplitude and the bubble and spike amplitudes). Reshock occurs at $t \approx 6.5$ ms when the shock wave refracts at the evolving interface, generating a transmitted shock in the air(acetone) and a reflected rarefaction wave in the SF_6. The reflected rarefaction wave is not plotted in the x-t diagram. Note that the transmitted shock moves faster, as indicated by the change in slope, corresponding to a slow-fast refraction [46]. Following reshock, the interface is compressed (as seen from the kink in the bubble and spike locations) and moves back into the shock tube away from the end wall of the test section. Additionally, the amplitude grows more rapidly than prior to reshock. The increased growth is due to the additional vorticity deposited during reshock on the evolving interface. The reshock (inversion) process occurs over ≈ 0.2–0.3 ms.

When comparing the numerical simulation data to the predictions of the models presented in § 2, the following conventions are used. The amplitude growth rate is adjusted to account for the diffuse interface by including the growth reduction factor ψ (see § 2.1.7) by

$$\frac{\mathrm{d}a}{\mathrm{d}t} \longrightarrow \frac{1}{\psi}\,\frac{\mathrm{d}a}{\mathrm{d}t}\,. \tag{221}$$

Furthermore, the time and initial velocity are rescaled according to

$$\tau = k\,v_0\,t \quad , \quad v_0 = k\,A^+\,[u]\,a_0^+\,, \tag{222}$$

where a_0^+ is the post-shock amplitude and A^+ is the post-shock Atwood number. Note that the post-shock amplitude a_0^+ is determined by multiplying the pre-shock amplitude a_0^- by the compression factor

	Experimental data		Simulation data	
$[u]$ (cm/s)	6060		6630	
v_0 (cm/s)	628		711	
η_{comp}			0.8071	
	Pre-shock	Post-shock	Pre-shock	Post-shock
a_0 (cm)	0.183	0.157	0.2	0.1614
A	0.604	0.627	0.6053	0.6274
u_{shock} (cm/s)			35775	18085
ψ	1.17	1.08	1.17	1.08

Table 1: Pre- and post-shock values obtained from the fifth-order simulation on the medium resolution grid with a comparison to the experimental data.

$$\eta_{comp} = 1 - \frac{[u]}{u_{shock}}\,, \tag{223}$$

where u_{shock} is the velocity of the shock. The values of the pre-shock and post-shock quantities from the experiment and from the simulation are summarized in Table 1. Note that, when the model predicts the *growth rate* of the mixing layer $\mathrm{d}a/\mathrm{d}t$, the mixing layer amplitude a is numerically computed by solving an initial value problem using a fourth-order Runge-Kutta scheme [22].

Table 1 shows the values of the parameters used in the amplitude growth model predictions. These parameters are also compared to the values reported in the experiments of Collins and Jacobs (Table 1 in [29]). It is interesting to note that a 10% discrepancy exists between the interface velocity after the passage of the incident shock $[u]$ reported here and the experimental values. The value of the interface velocity $[u]$ is not reported in the experiments and can be inferred from Eq. (11), which Collins and Jacobs use to estimate the initial interface velocity. The experimental value of the interface velocity was also confirmed by Jacobs [52]. The discrepancy in the interface velocity is due to the different values of the adiabatic exponent γ. Physically, the adiabatic exponents for the air(acetone) mixture and for the SF_6 gas are different. However, as discussed above, the present numerical simulations have a single adiabatic exponent for a mixture of 50% air(acetone) and 50% SF_6 by volume. This difference in the adiabatic exponent is reflected in a different shock speed, resulting in different values of $[u]$. This is an intrinsic limitation of the present numerical simulation. An alternative is to slightly decrease the shock Mach number to match the interface velocity observed in the experiment [30]. However, in this case the transmitted shock would differ from the experimental value. As a result, decreasing the shock Mach number may correctly capture the initial shock speed and interface velocity, but does not capture the velocity of the transmitted shock. By contrast, the approach used here matches the experimental amplitude growth results very well, suggesting that the mixing properties inferred from the simulation are nonetheless in very good agreement with those in the experiment.

3.3.2 Quantitative comparison to experimental mixing layer amplitude data

In Fig. 9, the mixing layer amplitude from the simulation (blue) is compared to the experimental amplitude from Collins and Jacobs [29] (red). The mixing layer begins growing immediately

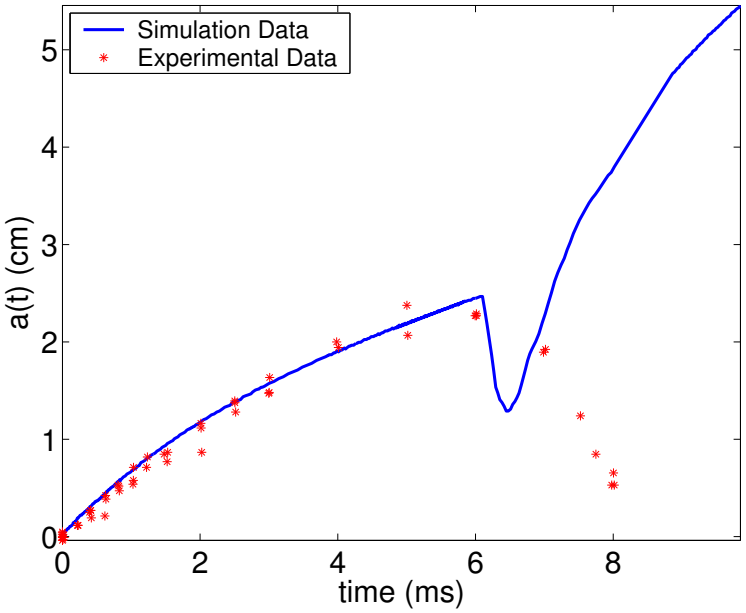

Figure 9: Comparison of the mixing layer amplitude obtained from the numerical simulation to the experimental data from Collins and Jacobs in the case of a Mach 1.21 incident shock. Note the excellent agreement up to reshock. The subsequent large discrepancy is due to the arrival of the initial rarefaction wave not modeled in the simulation.

following the passage of the initial shock. The initial rapid growth saturates at approximately 4 ms, and then reshock occurs approximately 2.5 ms later. During reshock, the interface is compressed by approximately 1 cm and then grows rapidly. Comparison of the numerical data with the experimental data points shows excellent agreement up to reshock. The difference observed after reshock is due to the arrival of the initial rarefaction wave that is not modeled in the present simulations, as discussed in § 3.1. The initial rarefaction wave decelerates the interface and, thus, prolongs the reshock phase to after 8 ms in the experiment. The large difference observed after reshock emphasizes the importance of the reflected rarefaction wave on the evolution of the instability. The instability evolution in this experiment is essentially two-dimensional prior to reshock (by virtue of the manner in which the initial perturbation was produced), and becomes three-dimensional following reshock, as the shock-interface interaction excites fluctuations in all spatial directions. Thus, it may be expected that a two-dimensional numerical simulation can reproduce the experimentally-measured amplitude growth prior to reshock. However, three-dimensional effects presumably become important following reshock, and three-dimensional numerical simulations are necessary to correctly capture the mixing layer width evolution and other quantities. According to Collins and Jacobs [29], the best fit to their amplitude growth data is given by the Sadot et al. [99] model.

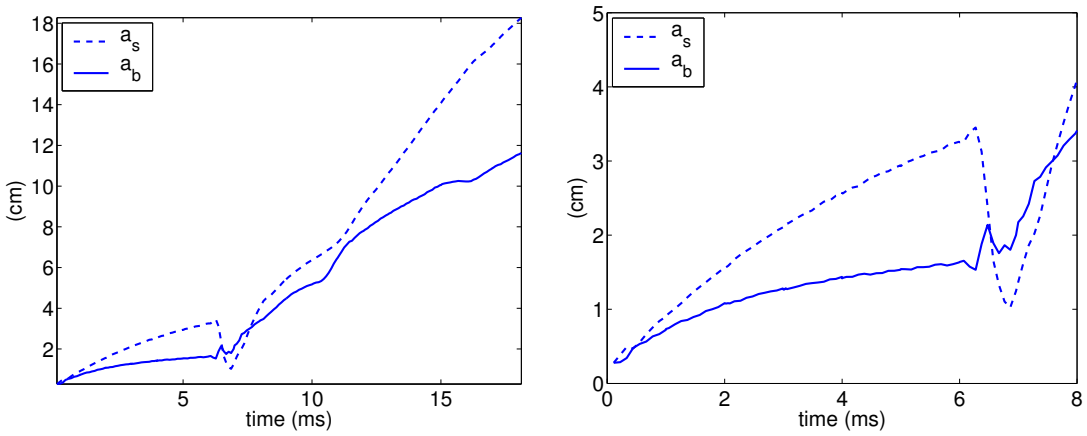

Figure 10: Bubble and spike amplitudes (left) and close-up before reshock (right).

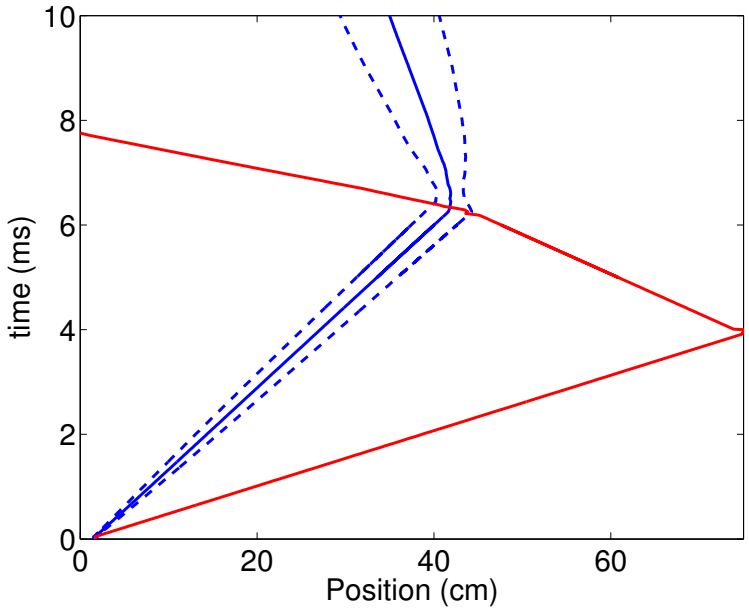

Figure 11: The x-t diagram showing the position of the interface $\ell_{int}(t)$ (green line), shock (red line), and bubble and spike locations $\ell_b(t)$ and $\ell_s(t)$ (solid and dashed blue lines) from the simulation. The horizontal distance between the spike and bubble represents the total amplitude $a(t)$.

3.3.3 Simulated Schlieren images

The detailed wave structure observed in the numerical simulation can be investigated using simulated density Schlieren images. The definition of the Schlieren function Φ used here is [78]

$$\Phi = \exp\left[-\alpha(m_2)\,\frac{|\nabla\rho|}{\max|\rho|}\right], \tag{224}$$

where m_2 denotes the mass fraction of SF_6, and

$$\alpha(m_2) = \begin{cases} 20 & \text{if } m_2 > \overline{\rho} \\ 100 & \text{if } m_2 < \overline{\rho} \end{cases} \tag{225}$$

with $\overline{\rho} = (\rho_1 + \rho_2)/2$. The Schlieren clearly exhibits the density gradients associated with waves and fine-scale mixing structures.

Figure 12 shows a temporal sequence of simulated density Schlieren images from the fifth-order numerical simulation during reshock and at late times. The images sharply capture the diffuse interface, the complex wave structure during reshock, and the small-scale structures at late times. Note the focusing effect of the waves and the inversion of the bubble transforming into the spike and vice versa. The images indicate that reshock occurs over a timescale of approximately 0.2–0.3 ms. The image corresponding to $t = 11$ ms also shows the arrival of the reflected rarefaction produced by the reshock after it has reflected from the end wall of the test section. The rich wave structure displayed by the Schlieren images shows weak, curved waves that interact and cause focusing. As these waves are expected to be weak due to the small shock Mach number, it is unclear what role they play in the flow dynamics. However, it is expected that a uniform, fine grid, high-resolution method is needed to capture these waves, as more dissipative schemes may dissipate the waves. It would be of interest to compare similar structures obtained with other numerical methods: although the large-scale flow dynamics are expected to be similar, these weak, wave structures may be different. Further note that at late times, the wave structures in the unmixed fluids are no longer present. Similar complex wave structures following a shock/interface interaction were also observed in the experimental Schlieren images of Brouillette and Sturtevant [20]. As in the experimental images, the complex structures in the simulations are the result of the 'shock scattering' at the interface. Note that the additional complex structures present in the experimental images are due to the shock/boundary layer interaction that are not captured in the current simulations.

3.3.4 Comparison to the predictions of impulsive models

In this section, numerical and experimental data are compared to the predictions of the linear instability models described in § 2.1. In Fig. 13, the mixing layer amplitude from the simulation is compared to the prediction of the Richtmyer [106] model [see Eq. (11)], the Meyer and Blewett [83] model [see Eq. (14)], the Fraley [41] model [see Eq. (16)] and the Vandenboomgaerde et. al. [122] model [see Eq. (24)]. These models capture the initial linear growth rate of the mixing layer for normalized times $\tau \leq 1$. For times $\tau > 1$, nonlinear effects become significant and the models significantly overestimate the mixing layer amplitude.

For the initial conditions considered here, the Richtmyer model gives the smallest slope as it uses the post-shock Atwood number and amplitudes. The Meyer-Blewett model uses the post-shock Atwood number, but averages the pre- and post-shock amplitudes, resulting in the largest slope. The Vandenboomgaerde model averages the pre- and post-shock amplitudes

Figure 12: Simulated density Schlieren images of the two-dimensional, single-mode Richtmyer-Meshkov instability from the fifth-order simulation on the medium grid showing the diffuse interface, complex wave structure during reshock, and the small-scale structures at late times.

by the pre- and post-shock Atwood numbers, respectively, and thus, has a slightly smaller slope than that predicted by the Meyer-Blewett model, but larger than the slope predicted by the Richtmyer model. The Fraley model, corresponding to the exact initial slope, has a slope intermediate between those predicted by the Meyer-Blewett and the Vandenboomgaerde models. This indicates that the impulsive models can successfully capture the linear growth of the mixing layer, and it is difficult to determine which model agrees best with the data. However, this is not the case for all initial conditions, as a normalized growth rate analysis [90] would show. In this analysis, the normalized growth rate is plotted as a function of the shock strength. The Fraley solution is taken to be the exact solution and the impulsive models are compared to this solution. For large shock strengths, the impulsive models exhibit large deviations from the Fraley solution, indicating that they are no longer valid.

Overall, all of the impulsive models correctly capture the initial growth of the mixing layer for $\tau < 1$. After the initial linear phase, the models do not accurately capture the late-time evolution of the interface, as nonlinear effects become significant and the amplitude growth saturates. Consequently, the late-time evolution ($\tau > 1$) is often referred to as the *nonlinear growth phase*.

3.3.5 Comparison to the predictions of point vortex models

In Fig. 14 the numerical amplitude data and the experimental data are compared to the predictions of the vortex model proposed by Jacobs and Sheeley [55] [see Eq. (51)] in the case $ka_0^+ = 0$ and $ka_0^+ = 2$, and to the model of Likhachev and Jacobs [74] [see Eqs. (57) and (58)] for $\epsilon_\Gamma = 1.55$ and $k\epsilon_A = 0.085$. The first value $ka_0^+ = 0$ corresponds to modeling the deposition of vorticity on the interface by two large point vortices located at the midpoints of the sinusoidal perturbation. The second value $ka_0^+ = 2$ accounts for the delay between the deposition of vorticity and its roll-up into two large vortices of opposite sign. While the model captures an asymptotic $1/t$ amplitude growth, both the numerical and experimental data are in poor agreement with the predictions of the model. The model underestimates the amplitude for $ka_0^+ = 0$, and overestimates the amplitude for $ka_0^+ = 2$. This is expected, as the model is based on the assumption that the initial vorticity deposited by the shock *immediately* coalesces into cores and does not account for the finite-time formation of these cores. Moreover, this model is strictly valid only for very small Atwood numbers. Better agreement is observed with the Likhachev-Jacobs model as expected, as the model is more appropriate for finite Atwood numbers. However, at intermediate and late times the model underestimates the amplitude as expected, as a vortex model provides a simplified model for the vorticity dynamics in the Richtmyer-Meshkov instability evolution.

3.3.6 Comparison to the predictions of potential flow models

In this section the bubble and spike velocities from the numerical simulations are compared to the predictions for the two-dimensional late-time bubble velocity from the Goncharov and Sohn potential flow models for variable-density flows.

The bubble and spike velocity are obtained from the bubble and spike amplitudes of Eqs. (219) and (220) by direct differentiation. Differentiating numerical data introduces mild oscillations and irregularities, as shown in Fig. 15. Figure 15 also shows the asymptotic velocities from the model of Goncharov in Eq. (130), and the model of Sohn in Eq. (144). First note that both models give nearly identical predictions for the case considered here and are virtually

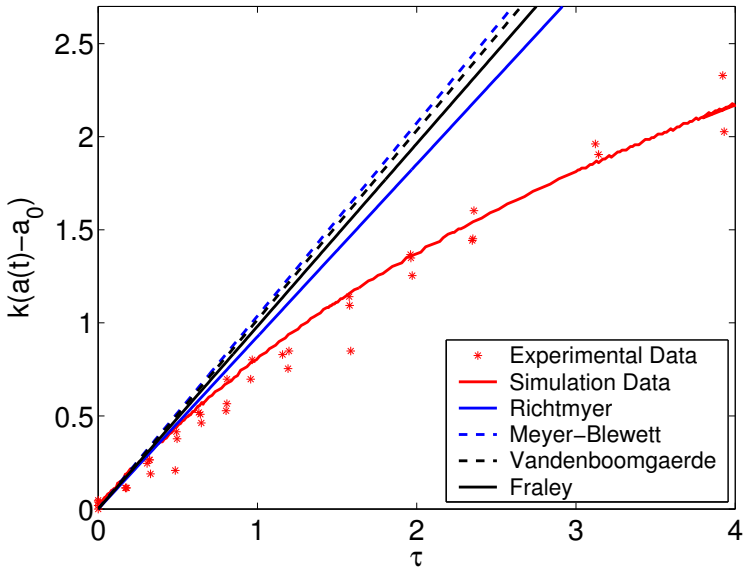

Figure 13: The normalized mixing layer amplitude $k\,[a(t) - a_0]$ from the numerical simulation and the experimental data, together with the predictions of linear models. Time is rescaled such that $\tau = kv_0t$, where $v_0 = kA^+[u]a_0^+$. All linear instability models give good predictions for the initial amplitude growth. For $\tau > 1$, nonlinear effects become relevant and the linear models overestimate the amplitude.

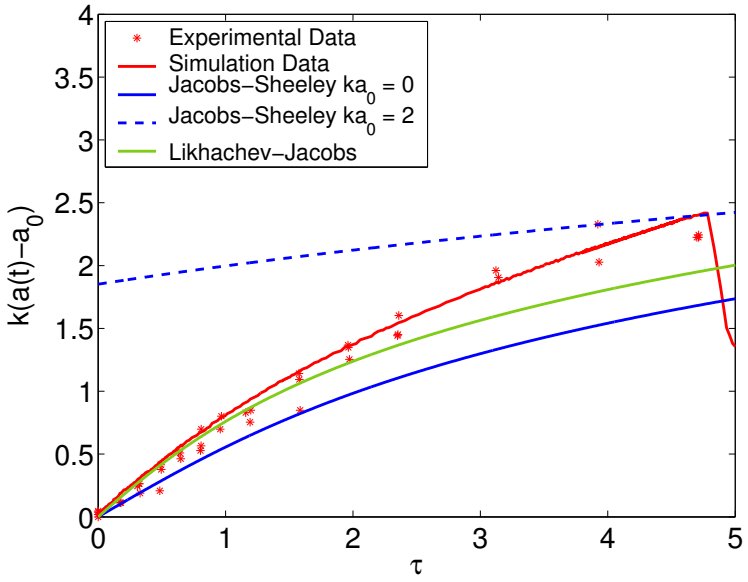

Figure 14: The normalized mixing layer amplitude $k\,[a(t) - a_0]$ from the numerical simulation and the experimental data, together with the predictions of the Jacobs-Sheeley and the Likhachev-Jacobs point vortex models. When $ka_0 = 0$ the Jacobs-Sheeley model underestimates the mixing layer amplitude, and when $ka_0 = 2$ the model overestimates the mixing layer amplitude. Better agreement is observed at early times with the Likhachev-Jacobs model.

indistinguishable. Despite the mild oscillations, excellent agreement is observed between the numerical velocities and the predictions from the models.

Abarzhi also presented a model for the late-time amplitude of a bubble in two-dimensional Richtmyer-Meshkov flow [see Eq. (164)]. The model was found to apply to times much later than the times considered in the present investigation.

3.3.7 Comparison to the predictions of perturbation models

The numerical amplitude data and the experimental data are compared to the predictions of the nonlinear models summarized in § 2.3. In Fig. 16, experimental and numerical data are compared to the perturbation series solutions of Zhang and Sohn [130] [see Eq. (73)], the perturbation series solution of Vandenboomgaerde et al. [121] [see Eq. (82)] of degree 9 and 11, and the perturbation series solution of Matsuoka-Nishihara-Fukuda model [79] [see Eqs. (89) and (90)]. The comparison shows that perturbation series successfully capture the initial growth, but quickly diverge. In particular, note that the result for the eleventh-order Vandenboomgaerde perturbation series has a smaller radius of convergence than the ninth-order series. To expand the radius of convergence, the series are extended via Padé approximants.

In Fig. 17, the experimental and numerical data are compared to the predictions of the nonlinear models extended via Padé approximants. Shown are the P_2^0 Padé approximant of Zhang and Sohn [see Eq. (74)], the P_6^4 Padé approximant of Vandenboomgaerde [see Eq. (85)], and the P_2^0 Padé approximant of Matsuoka et al. [see Eqs. (91) and (92)]. In addition, the prediction of the empirical model of Sadot et al. [99] [see Eq. (167)] is also shown. Note the excellent agreement between the Zhang-Sohn and Vandenboomgaerde Padé models and the experimental data in both the linear and nonlinear regime. The models show slight variations in their respective predictions. In particular, the Padé approximant of Vandenboomgaerde appears to capture the correct behavior at early times for $\tau < 1$, but overestimates the amplitude for later times. The Padé approximant of Zhang and Sohn underestimates the amplitude for $\tau < 1$, but gives the correct behavior for later times. The Padé approximant of Matsuoka et al. correctly predicts the mixing layer amplitude at early times but underestimates the mixing layer amplitude at late times.

To determine which of the models gives the amplitude growth in best agreement with the simulation data, the ratio between the Zhang-Sohn (Padé), Vandenboomgaerde (Padé), Matsuoka et al. (Padé), and Sadot models, and the simulation data, $[a_{model}(t) - a_0]/[a_{sim}(t) - a_0]$, are presented in Fig. 18. The figure indicates that the Zhang-Sohn Padé model is in best agreement with the numerical simulation data. Collins and Jacobs [29] report that their data is in best agreement with the Sadot model.

Finally, Fig. 19 shows the comparison of the bubble and spike amplitudes with the predictions of the Matsuoka et al. model for the bubble and spike amplitudes of Eqs. (91) and (92), respectively, and the Sadot model for the bubble and spike amplitudes of Eqs. (165) and (166), respectively. The Matsuoka et al. model overestimates the mixing layer amplitude for the bubble and spike. The Sadot model shows excellent agreement for the bubble amplitude from the linear, through the nonlinear regime. By contrast, the Sadot model overestimates the spike amplitude obtained from the present simulation.

3.3.8 Comparison of amplitude model predictions using experimentally and numerically determined model parameters

Presented here is a comparison of the predictions of the linear, vortex, and nonlinear models, when the model parameters are computed using the experimental data by Collins and Jacobs (see Table 1 and Table 1 in [29]). A comparison is also presented between the predictions of the nonlinear models when the model parameters are computed using the experimental and the simulation data. Finally, the ratios of the predictions from the models to the simulation results are presented.

The top row of Fig. 20 shows a comparison of the predictions from the linear and vortex models with the model parameters computed using simulation and experimental data. The linear models computed with the parameters from the experimental data capture the early growth of the mixing layer. The agreement is comparable to that observed when the models were computed with the parameters from the simulation data, indicating that the linear models are not affected by small changes in the model parameters. The plots are not very different from the predictions of the linear models with the model parameters computed using the simulation data. The predictions of the vortex models also do not capture the mixing layer growth, but may capture the late-time growth.

The bottom row of Fig. 20 shows a comparison of the predictions from the nonlinear perturbation series models and these models extended via Padé approximants and the simulation and experimental data. The plots of the nonlinear perturbation series models show that they capture the early growth very well but have limited range of convergence, as was observed when the model parameters were computed using the simulation data. The plot of the nonlinear perturbation series extended via Padé approximants and the Sadot model, show increased regions of agreement. In particular, the Sadot model is now in best agreement with the simulation and experimental data. This is consistent with the conclusion reported by Collins and Jacobs.

Therefore, when the amplitude model parameters are computed using the experimental data, the Sadot model gives the best agreement with the experimental and simulation data; by contrast when the model parameters are computed using simulation data, the Zhang-Sohn Padé model gives the best agreement. To further understand this difference, a comparison of the predictions from the Zhang-Sohn Padé, Vandenboomgaerde Padé, and Sadot models computed using experimental and simulation data, is presented in Fig. 21. It is apparent the Zhang-Sohn and the Sadot models are the most sensitive to changes in the model parameters. It is observed that the predictions with model parameters using the simulation data are in general larger than the predictions with the model parameters using the experimental data. This is due to the difference in the initial acceleration of the interface v_0; more specifically, v_0 obtained from the simulation is larger than the corresponding experimental value. By contrast, the Vandenboomgaerde model does not show significant sensitivity to the variation of the model parameters. The predictions obtained with the model parameters using experimental and simulation data are very similar.

The predictions from the nonlinear models and the ratios to the simulation data are presented in Fig. 22. When the model parameters are computed using the experimental data, the Sadot model is in best agreement with the data; when the model parameters are computed using the simulation data, the Zhang-Sohn model is in best agreement with the data. The figure shows that when the model parameters are computed using the simulation data, the Sadot model gives $\approx 10\%$ error and the Zhang-Sohn model gives $\approx 1\%$ error. By contrast,

when the model parameters are computed using the experimental data, the Sadot model gives $\approx 5\%$ error, and the Zhang-Sohn model also gives $\approx 5\%$ error but underpredicts the mixing layer amplitude.

A further quantification of the differences observed between the predictions of the models when the parameters are computed using the experimental and simulation data is obtained using the root-mean-square of the difference between the model predictions and the simulation data

$$||\mathbf{x}||_{rms} = \sqrt{\frac{1}{N}\sum_{i=1}^{N}|x_i|^2}\,. \tag{226}$$

Let $\mathbf{e_{exp}}$ denote the difference between the mixing layer amplitude predicted when the model parameters are computed using experimental data and the mixing layer amplitude obtained from the simulation. Similarly, let $\mathbf{e_{sim}}$ denote the difference between the mixing layer amplitude predicted when the model parameters are computed using simulation data and the mixing layer amplitude obtained from the simulation. Thus, $\mathbf{e_{exp}}$ and $\mathbf{e_{sim}}$ are vectors representing the error between the simulations and the model predictions. Taking the root-mean-square of these vectors for different model predictions provides a quantitative measure of the error and determines which model is in best overall agreement with the data. The results are presented in Table 2: the prediction of the Sadot model with the model parameters obtained using experimental data is in best agreement with the simulation result, and the prediction of the Zhang-Sohn Padé model with the model parameters obtained using the simulation data is in best agreement with the simulation result.

The results in this section show the dependence of amplitude growth models on small changes in the parameters. The experimental parameters from the Collins and Jacobs experiments and the parameters from the present simulation were compared. It was shown that small variations have a dramatic effect on the nonlinear amplitude growth models. In particular, it was shown that when experimental data is used, then the prediction of the Sadot model is in best agreement with the experimental and simulation mixing layer amplitude; by contrast when the simulation data is used, the prediction of the Zhang-Sohn model is in best agreement. The root-mean-square of the difference between the simulation results and the model predictions indicate that: (1) when the model parameters are obtained using experimental data, the root-mean-square is minimized with the Sadot model, and; (2) when the model parameters are obtained using the simulation data, the Zhang-Sohn model minimizes the root-mean-square error.

	Experimental data	Simulation data
	$\|\|\mathbf{e_{exp}}\|\|_{rms}$	$\|\|\mathbf{e_{sim}}\|\|_{rms}$
Zhang-Sohn Padé	0.00173	0.00055
Vandenboomgaerde Padé	0.00091	0.00130
Matsuoka et al. Padé	0.00293	0.00226
Sadot	0.00038	0.002

Table 2: The root-mean-square of the difference between the simulation data and the Zhang-Sohn Padé, Vandenboomgaerde Padé, Matsuoka et al. Padé, and Sadot nonlinear models, when the model parameters are computed using experimental and simulation data.

3.4 Evolution of the mixing layer amplitude following reshock and comparison to the predictions of reshock models

The mixing layer amplitude following reshock is investigated here. The reshock in the simulation occurs at nearly the same time as in the experiment, as confirmed by both the x-t diagram and the mixing layer amplitude. The mixing layer amplitude is compared to the prediction of the Mikaelian [87] reshock model and to that of the Brouillette-Sturtevant [19] reshock model in Fig. 23. Note that the post-reshock flow is essentially incompressible (see § 4.3).

In order to fit the models, the numerical data was shifted in time and the amplitude at reshock was subtracted out so that the new origin coincides with the conditions following reshock. For the Mikaelian model of Eq. (201), the quantities $[u]_1 = 8000$ cm/s and $A_1^+ = 0.6448$ obtained from the simulation are used. For the Brouillette-Sturtevant model of Eq. (202), the expression

$$\left(\frac{\mathrm{d}h}{\mathrm{d}t}\right)_1 = 2\,k\left(\frac{[u]\,A^+\,a_0^+}{\psi^+} + \frac{[u]_1\,A_1^+\,a_1^+}{\psi_1^+}\right) \tag{227}$$

was used, where $a_1^+ = 1.5$ cm, $[u]_1 = 8000$ cm/s, and the value of ψ_1^+ is extrapolated as follows. First recall that ψ is a linear function in $\overline{\delta}/\lambda$ [see Eq. (41)], where $\overline{\delta}$ is the diffuse mixing layer width linear in the post-shock perturbation amplitude a_0^+. As $a_1^+ \approx 10a_0^+$ and the value of ψ^+ is known, the constant C in Eq. (41) can be determined as a function of $\overline{\delta}/\lambda$. Then, substituting the new value for a_1^+ gives the new value of ψ_1^+.

Note that the simulation data agrees very well with the prediction of the Mikaelian model at early times ($t > 2$ ms) following reshock. Vetter and Sturtevant [123] also concluded that their experimental results were in excellent agreement with the prediction of the Mikaelian model. For later times, the Mikaelian model overestimates the growth of the mixing layer, while the Brouillette-Sturtevant model underestimates the growth at all times following reshock. Using the values above yields $(\mathrm{d}h/\mathrm{d}t)_1 = 1444.35$ cm/s and $(\mathrm{d}h/\mathrm{d}t)_1 = 1029.05$ cm/s for the Mikaelian and Brouillette-Sturtevant models, respectively.

The comparison of the mixing layer width from the numerical simulation with the predictions of the phenomenological Mikaelian and Brouillette-Sturtevant models indicates that the growth of the mixing layer is apparently well approximated by a linear-in-time model for very short times (< 2 ms) following reshock. The variations in the growth rate observed in the simulation are due to further wave interactions with the evolving interface, which are not accounted for in the application of these models.

3.5 Baroclinic circulation deposition on the interface

The circulation deposited on the interface by the shock quantifies the driving mechanism for the evolution of the Richtmyer-Meshkov instability. Scaling laws for circulation deposition are of importance to vortex methods and to the analytical models developed by Samtaney, Ray, and Zabusky [113, 112, 104], as reviewed in § 2.6. Presented in this section is an investigation of the circulation deposition computed using the fifth-order, medium resolution numerical simulation.

First, consider the integral of the vorticity in the streamwise x-direction

$$\omega(y,t) \equiv \int \omega(x,y,t)\,\mathrm{d}x \tag{228}$$

shown in Fig. 24, which indicates that the deposition of circulation on the interface has a sinusoidal distribution, as predicted by the Samtaney-Zabusky model [113].

The total circulation on the interface is given by the integral of $\omega(y)$ over the transverse periodic direction y,

$$\Gamma(t) = \int \omega(y,t)\,\mathrm{d}y\,. \tag{229}$$

The circulation $\Gamma(t)$ can also be computed using the contour integral

$$\Gamma(t) = \oint_C \mathbf{u}\cdot\mathrm{d}\mathbf{r}\,, \tag{230}$$

where C is the oriented closed contour, and $\mathrm{d}\mathbf{r}$ is the unit tangent to C.

For two-dimensional simulations, the vorticity field and the outward oriented area element are parallel. Therefore, the circulation can be computed on a uniform rectangular grid with spacings Δx and Δy as [113]

$$\Gamma(t) = \sum_{i,j} \omega(x_i, y_j, t)\,\Delta x\,\Delta y\,, \tag{231}$$

where the double summation is over all of the grid points in the computational domain.

The total circulation $\Gamma(t)$ computed over a period is shown in Fig. 25. The circulation is very close to zero up to $t = 11$ ms, consistent with the sinusoidal deposition shown in Fig. 24 and the preservation of symmetry as the instability develops. The large, positive values for $t > 11$ ms are due to the asymmetry of the complex topological structures observed at late times following reshock. In the region where $\Gamma = 0$ define the positive and negative circulations computed as the vorticity summed over the two halves of the period $U^+ = \{\lambda/2 < y(j) < \lambda\}$ and $U^- = \{y(j) < \lambda\}$:

$$\Gamma^+(t) = \sum_i \sum_{j\in U^+} \omega(x_i, y_j, t)\,\Delta x\,\Delta y\,, \tag{232}$$

$$\Gamma^-(t) = \sum_i \sum_{j\in U^-} \omega(x_i, y_j, t)\,\Delta x\,\Delta y\,. \tag{233}$$

The positive and negative circulations are shown in Fig. 25. Note that reshock deposits vorticity of opposite sign on the interface as the refraction is from a heavier gas into a lighter gas. Consequently, the positive circulation changes sign and becomes negative after reshock and the negative circulation becomes positive. The large values for the negative and positive circulation following reshock are due to the complex structure of the interface, resulting in a larger amount of vorticity deposited by the shock.

Now consider the circulation prior to reshock shown in Fig. 26. First note that the positive and the negative circulation are plotted together. The two curves overlap prior to reshock, indicating the symmetry as the instability evolves. Note that the circulation increases slightly following reshock. This result is consistent with the recent findings of Peng, Zabusky and Zhang [101] showing the amplification of the circulation due to the secondary baroclinic vorticity deposition. The secondary baroclinic circulation can also be used to explain the more pronounced increase in the circulation following reshock, but prior to the arrival of the reflected rarefaction wave. Following the arrival of the reflected rarefaction wave, the negative and positive circulations show an increasing discrepancy due to symmetry breaking. Vortical structures become disordered and may cross from the positive region U^+ into the negative region U^-, inducing the development of asymmetry.

The results above indicate that the deposition of circulation on the interface can be characterized as follows. Immediately following the first interaction with the shock, the circulation has a sinusoidal distribution on the interface, so that integrating over an entire period yields zero total circulation. The positive and negative components of the circulation show an increase following the shock interaction, consistent with secondary baroclinic vorticity deposition. This secondary instability is responsible for the complex structures observed in the roll-ups of the Richtmyer-Meshkov instability and for additional vorticity deposition on the interface. Reshock causes the deposition of additional vorticity of opposite sign, which is further amplified by the secondary baroclinic vorticity deposition. Complex structures form following the interaction with the reflected rarefaction wave and symmetry breaks, resulting in large discrepancies between the positive and negative vorticity: this yields a non-zero total circulation.

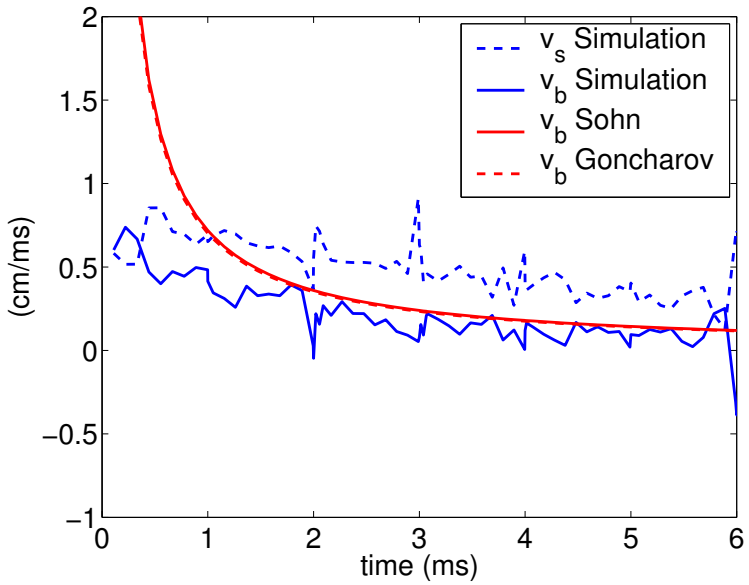

Figure 15: Bubble and spike velocities from the simulation compared to the asymptotic bubble velocity predicted by the Goncharov and Sohn models.

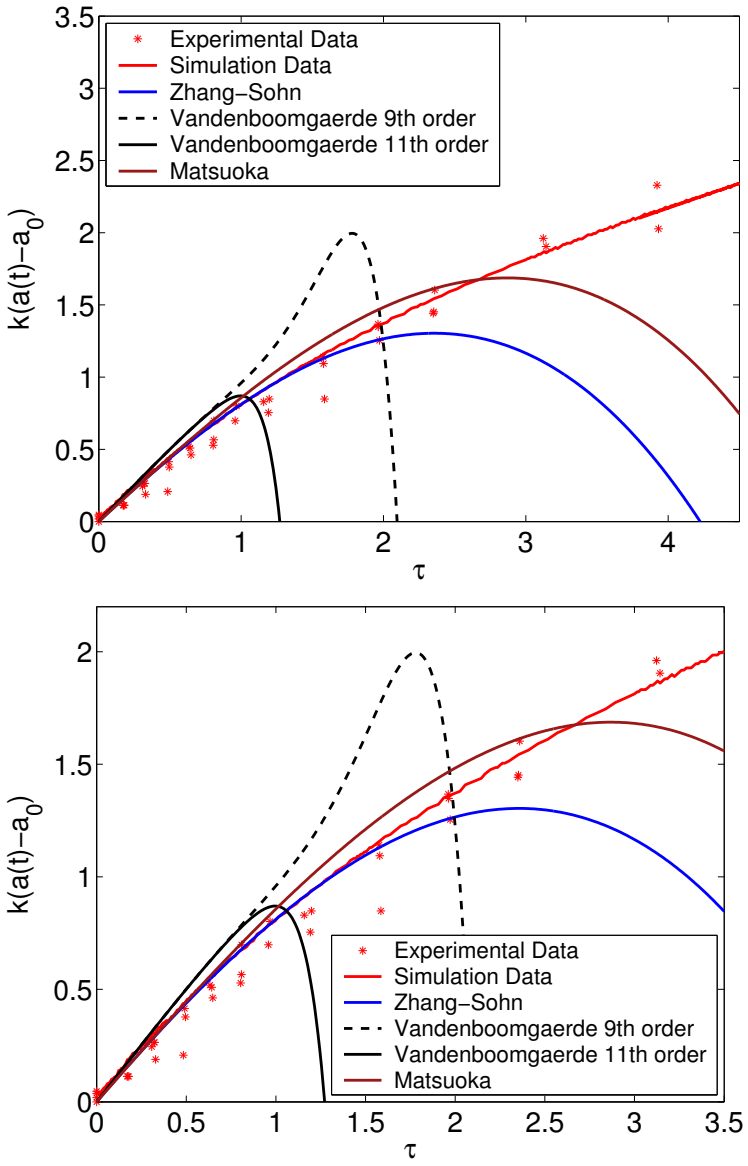

Figure 16: The normalized mixing layer amplitude $k\,[a(t) - a_0]$ from the numerical simulation and the experimental data, together with the predictions of the Padé models of Zhang and Sohn, Vandenboomgaerde, and Matsuoka et al. The series captures the initial growth of the mixing layer into the nonlinear regime, but diverges rapidly. The Vandenboomgaerde eleventh-order series diverges sooner than the ninth-order series.

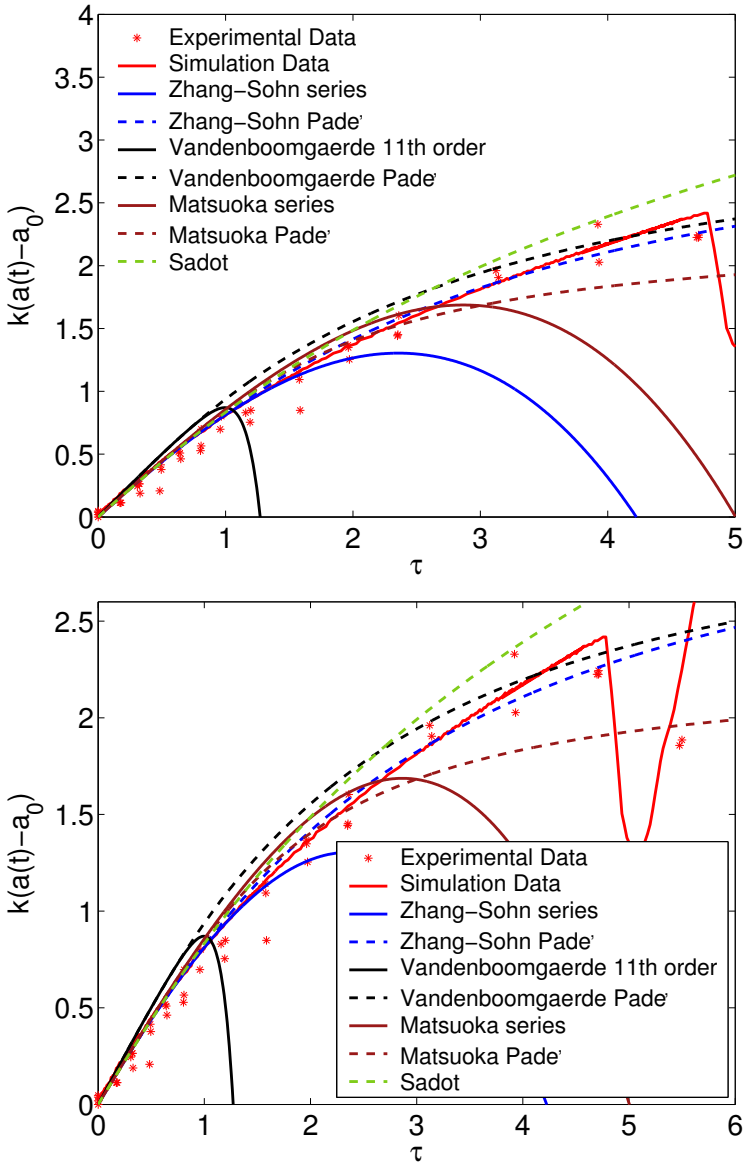

Figure 17: The normalized mixing layer amplitude $k\,[a(t) - a_0]$ from the numerical simulation and the experimental data, together with the predictions of the perturbation series models of Zhang and Sohn, Vandenboomgaerde, and Matsuoka et al. extended via Padé approximants. The prediction of the empirical model of Sadot is also shown. Note the excellent agreement between the models and the experimental amplitude.

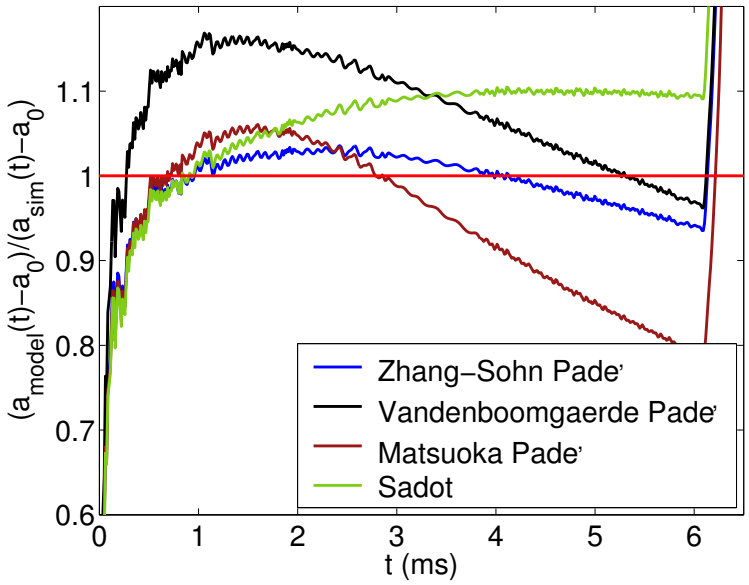

Figure 18: The predictions of the Zhang-Sohn (Padé), Vandenboomgaerde (Padé), Matsuoka et al. (Padé), and Sadot models for the amplitude with the initial perturbation amplitude subtracted out divided by the corresponding numerical simulation data. Well into the nonlinear regime, and just before reshock, the prediction of the Zhang-Sohn model is in best agreement with the simulation data.

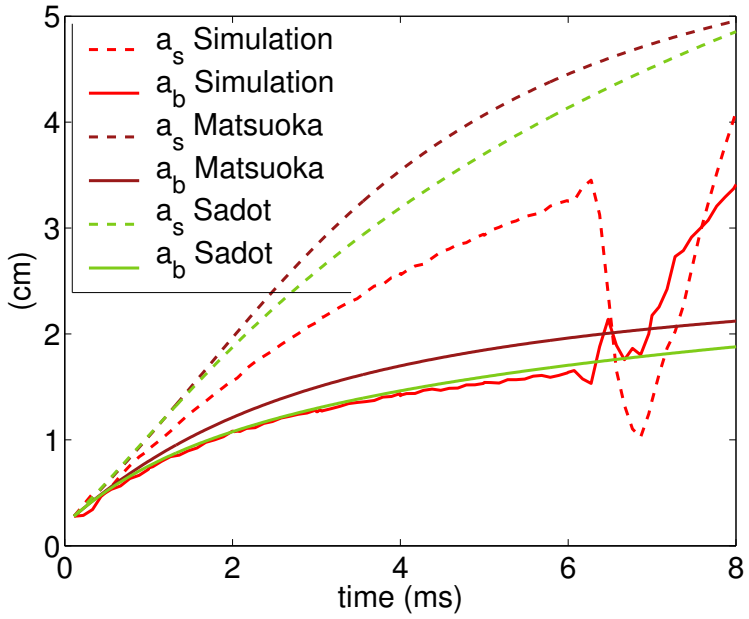

Figure 19: Comparison of bubble and spike amplitudes with the predictions of the Matsuoka et al. (Padé) and Sadot models.

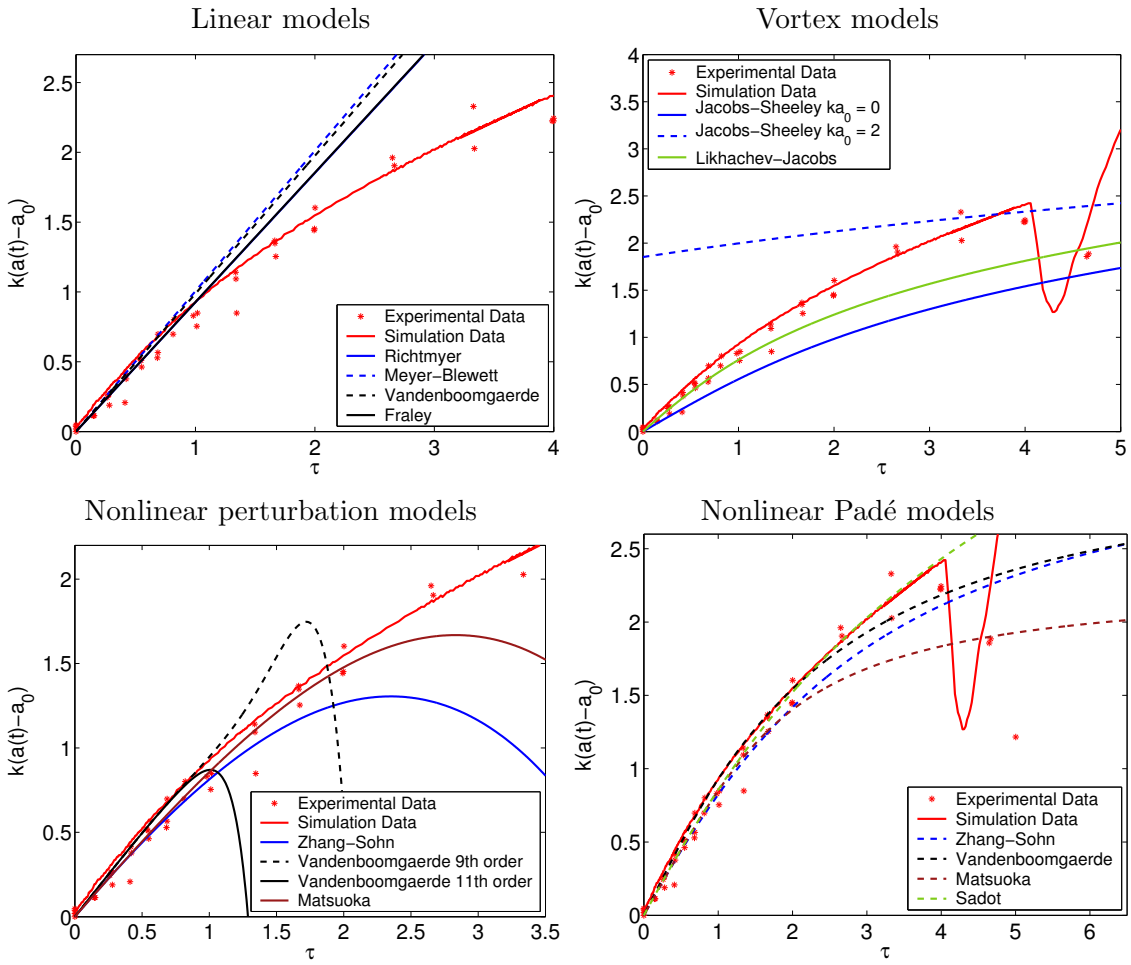

Figure 20: The normalized mixing layer amplitude $k\,[a(t) - a_0]$ from the numerical simulation and the experimental data, together with the predictions of linear, vortex, and nonlinear perturbation and Padé models, when the model parameters are computed using the experimental data. Time is rescaled such that $\tau = kv_0t$, where $v_0 = kA^+[u]a_0^+$.

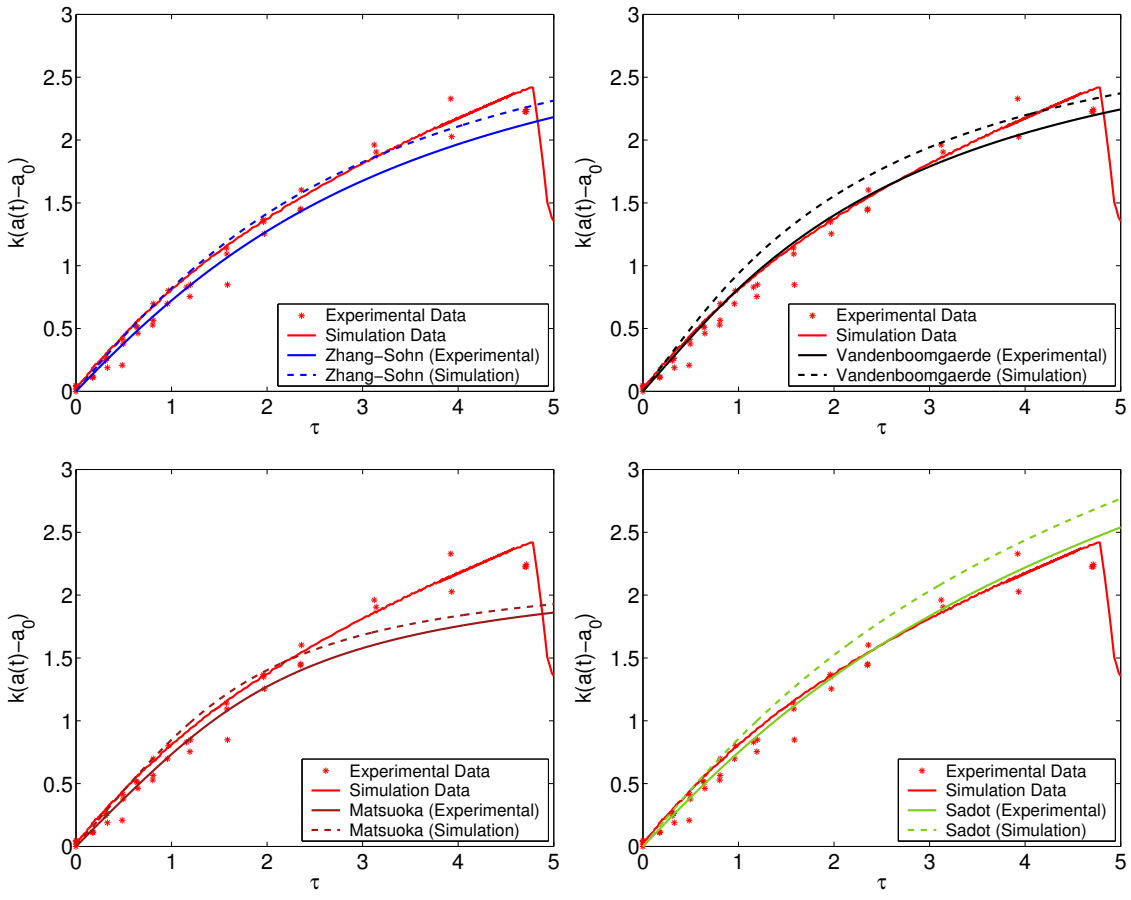

Figure 21: Comparison of the predictions of the nonlinear Zhang-Sohn Padé, Vandenboomgaerde Padé, Matsuoka et al. Padé, and Sadot models with model parameters computed using the experimental and simulation data as presented in Table 1

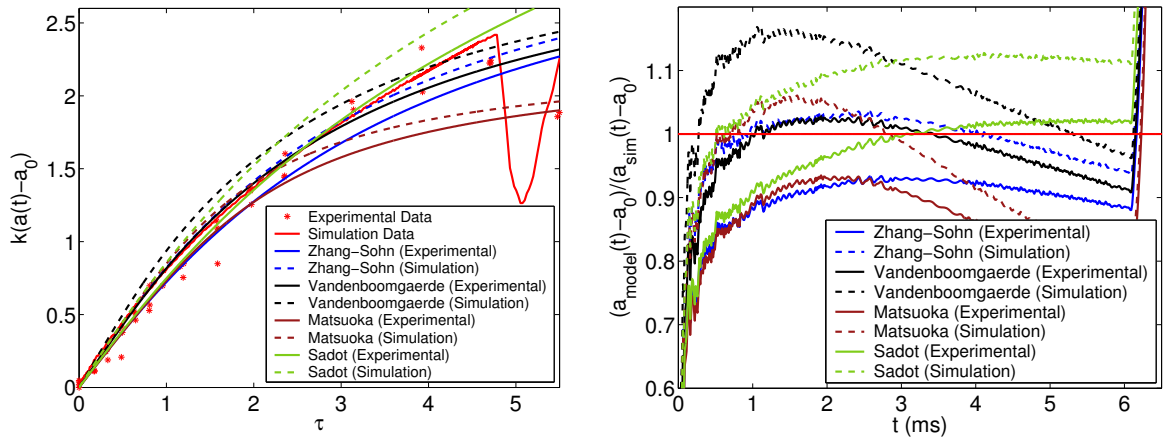

Figure 22: Comparison of the predictions of nonlinear models with model parameters computed using the experimental and simulation data as presented in Table 1. The ratio of the model predictions to the simulation data shows that the Sadot model agrees best with the simulation and experimental data when experimental parameters are used; by contrast, when simulation parameters are used, the Zhang-Sohn model is in best agreement with the simulation and experimental data.

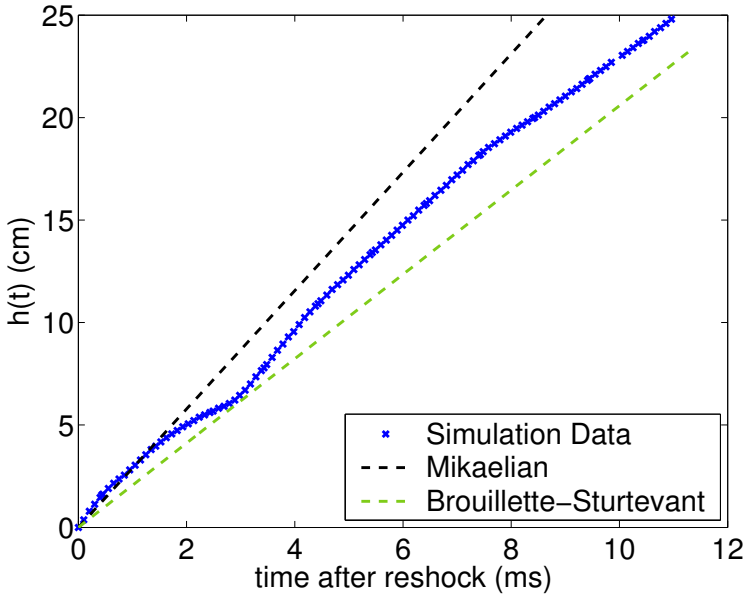

Figure 23: The mixing layer width $h(t)$ of a reshocked interface and the predictions of the Mikaelian and Brouillette-Sturtevant models. The simulation data was shifted in time and the amplitude at reshock was subtracted out so that the new origin coincides with the conditions at reshock.

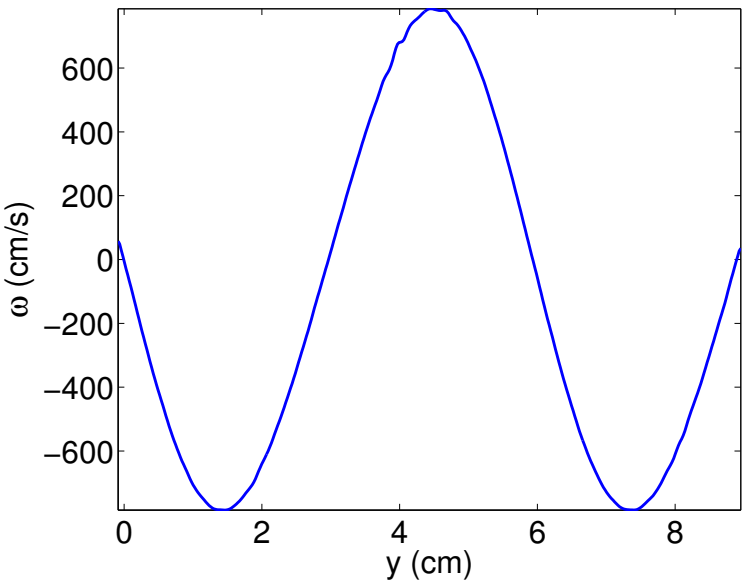

Figure 24: The initial deposition of circulation on the interface.

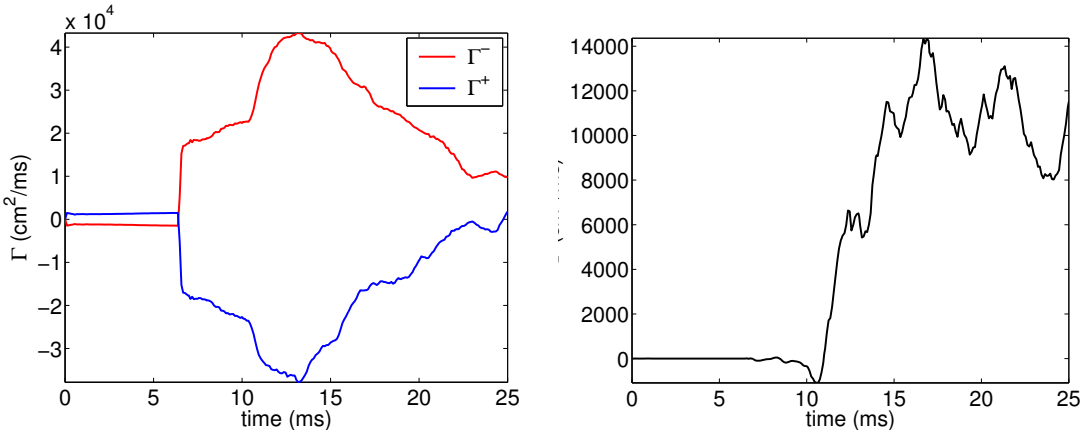

Figure 25: The time-evolution of the positive and negative components of the circulation (left) and the total circulation deposited on the interface (right).

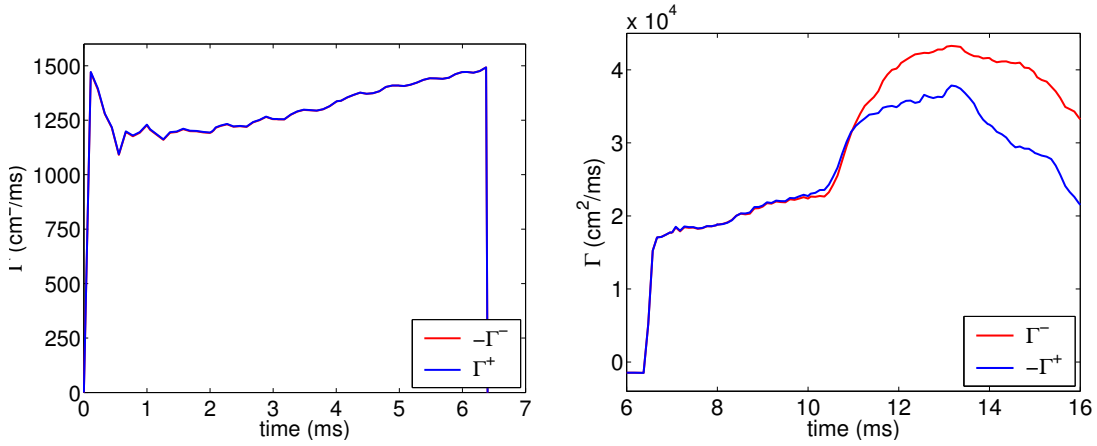

Figure 26: The time-evolution of the positive and negative components of the circulation before reshock (left) and after reshock (right).

4 Local and global analysis of mixing in two-dimensional, single-mode Richtmyer-Meshkov instability with reshock

Presented in this section is a comprehensive investigation of mixing induced by the two-dimensional Richtmyer-Meshkov instability with reshock. The analysis of mixing considers both local and global quantities. *Local analysis* refers to an investigation of a quantity at a given time: two types of quantities are considered—mixing profiles and spectra. Mixing profiles are quantities averaged across the statistically-homogeneous (periodic) y-direction (so that they are only a function of the streamwise coordinate x and time) characterizing the extent and efficiency of mixing. Spectra of quantities within the mixing layer are obtained as a function of the one-dimensional wavenumber k by Fourier-transforming along the periodic (spanwise) direction. *Global analysis* refers to an investigation of a wavenumber-integrated spectrum (a statistic) or a volume-integrated quantity (a mixing fraction or primitive field) as a function of time. Very little previous investigation of these quantities has been performed in Richtmyer-Meshkov instability-induced mixing [126, 94]. However, Youngs [125, 126], Cook and Dimotakis [31], Ristorcelli and Clark [109], and Dimonte et al. [32] have numerically investigated the evolution of mixing fractions and energy spectra for Rayleigh-Taylor instability-induced mixing. The quantities considered in the present analysis can be easily generalized to the case of three-dimensional flows, and will be considered in Part 4 of this report [70].

The analysis described above is applied to the simulation of the Richtmyer-Meshkov instability initialized using the Mach 1.21 Collins and Jacobs shock tube experiment, and using fifth-order WENO reconstruction with a grid resolution of 256 points per initial perturbation wavelength, as discussed in § 3. To investigate the late-time decay of the mixing following reshock, the boundary condition at the end of the simulated test section is modified to outflow so that reflected waves following reshock exit the computational domain and no longer interact with the evolving mixing layer (corresponding to the *decay regime*, as distinct from the *quasi-decay regime*, in which reflected waves are permitted to interact with the mixing layer). Particular emphasis is given to comparing mixing and spectral quantities before and after reshock. The objective of this comprehensive investigation is to quantitatively characterize the mixing induced by the single-mode Richtmyer-Meshkov instability before and after reshock in two dimensions, and to appreciate the manifestations of the reflected waves in the evolution of the reshocked interface.

Note that in the present investigation, the initial condition is deterministic. Furthermore, only one realization of the flow is simulated. Thus, the profiles, spectra, and statistics computed in subsequent sections exhibit variations that would otherwise be reduced if an ensemble average of realizations with a stochastic initial condition was used.

4.1 Time-evolution of mole, volume, and mixing fraction profiles

Several averages must be introduced to define spanwise-averaged quantities across the mixing layer (streamwise profiles), as well as fluctuations required to define energy spectra. Let angle brackets denote an instantaneous average of a function $\phi(x, y, t)$ over the periodic (spanwise) direction y with length L_y:

$$\langle\phi\rangle(x,t) = \frac{1}{L_y}\int_0^{L_y} \phi(x,y,t)\,\mathrm{d}y\,, \tag{234}$$

which can be interpreted as an instantaneous Reynolds average in the present investigation (see [126] for the three-dimensional analog of this average). The Reynolds fluctuating field is

$$\phi(x,y,t)' = \phi(x,y,t) - \langle\phi\rangle(x,t)\,. \tag{235}$$

The instantaneous Favre average of ϕ is

$$\widetilde{\phi}(x,t) = \frac{\langle\rho\,\phi\rangle}{\langle\rho\rangle}\,, \tag{236}$$

which is used for the statistical analysis of variable-density and compressible flows. The Favre fluctuating field is

$$\phi(x,y,t)'' = \phi(x,y,t) - \widetilde{\phi}(x,t)\,. \tag{237}$$

Thus, in the present analysis of two-dimensional data, the Reynolds- and Favre-averaged fields are functions only of the streamwise coordinate x and time, while the fluctuating fields are functions of both the streamwise and spanwise coordinates and time.

Note that throughout this section the profiles of quantities across the mixing layer are presented with the streamwise coordinate rescaled by the mixing layer width $h(t)$ and recentered by the position of the midpoint between the bubble and spike front locations x_{mid}, i.e., $(x - x_{mid})/h(t)$. This rescaling adjusts the profiles so that the rescaled edges of the mixing layer are identical at different times, and results in a loss of information regarding the width of the layer, but facilitates the investigation of the mechanisms of the mixing process and the distribution of mixed mass within the layer.

4.1.1 Evolution of the mole fraction profile $\langle X\rangle$

Quantities previously introduced in the context of the analysis of Rayleigh-Taylor mixing by Youngs [126] and Cook and Dimotakis [31] are considered and adapted to the Richtmyer-Meshkov instability here. First consider the mole fraction $X(x,y,t)$ averaged over the spanwise direction y, $\langle X\rangle(x,t)$. Consider two fluids with constant densities ρ_1 and $\rho_2 > \rho_1$. The mole fraction X defined in Eq. (216) varies from $X = 0$ in the first fluid to $X = 1$ in the second fluid, so that the mole fraction profile $\langle X\rangle(x,t)$ gives the relative distribution of mass of the two fluids within the mixing layer. If the two fluids are uniformly-distributed over the entire volume under consideration, as expected in complete homogeneous mixing, then $\langle X\rangle = 0.5$.

To facilitate the comparison of the mole fraction profile at different times, the streamwise coordinate is recentered by the location of the midpoint between the bubble and spike position. The left column of Fig. 27 shows the recentered mole fraction profile at time intervals of 1 ms from $t = 0$ to $t = 17$ ms. The mole fraction profile increases from $\langle X\rangle = 0$ in the air(acetone) mixture to $\langle X\rangle = 1$ in SF_6. The increasing width of the profile shows the spatial spreading of the mixing layer in time. The profiles further display the varying distribution of mass inside the mixing layer prior to reshock. Initially, at $t = 0$ ms the profile is monotonically-increasing as the initial interface is slightly diffused. After the initial passage of the shock, the profile increases in width and becomes non-monotonic with a peak developing within the air(acetone) gas mixture, and moving to the left and increasing in magnitude with time. This is due to spikes of SF_6 penetrating into the air(acetone), forming the characteristic roll-ups. These roll-ups are a consequence of the entrainment of additional SF_6 within the air(acetone) mixture. The bubbles of air(acetone) "rise" in the SF_6, causing an overall decrease in $\langle X\rangle$ in the SF_6. Reshock compresses the averaged mole fraction, as shown between $t = 6$ and $t = 7$ ms. The width of the

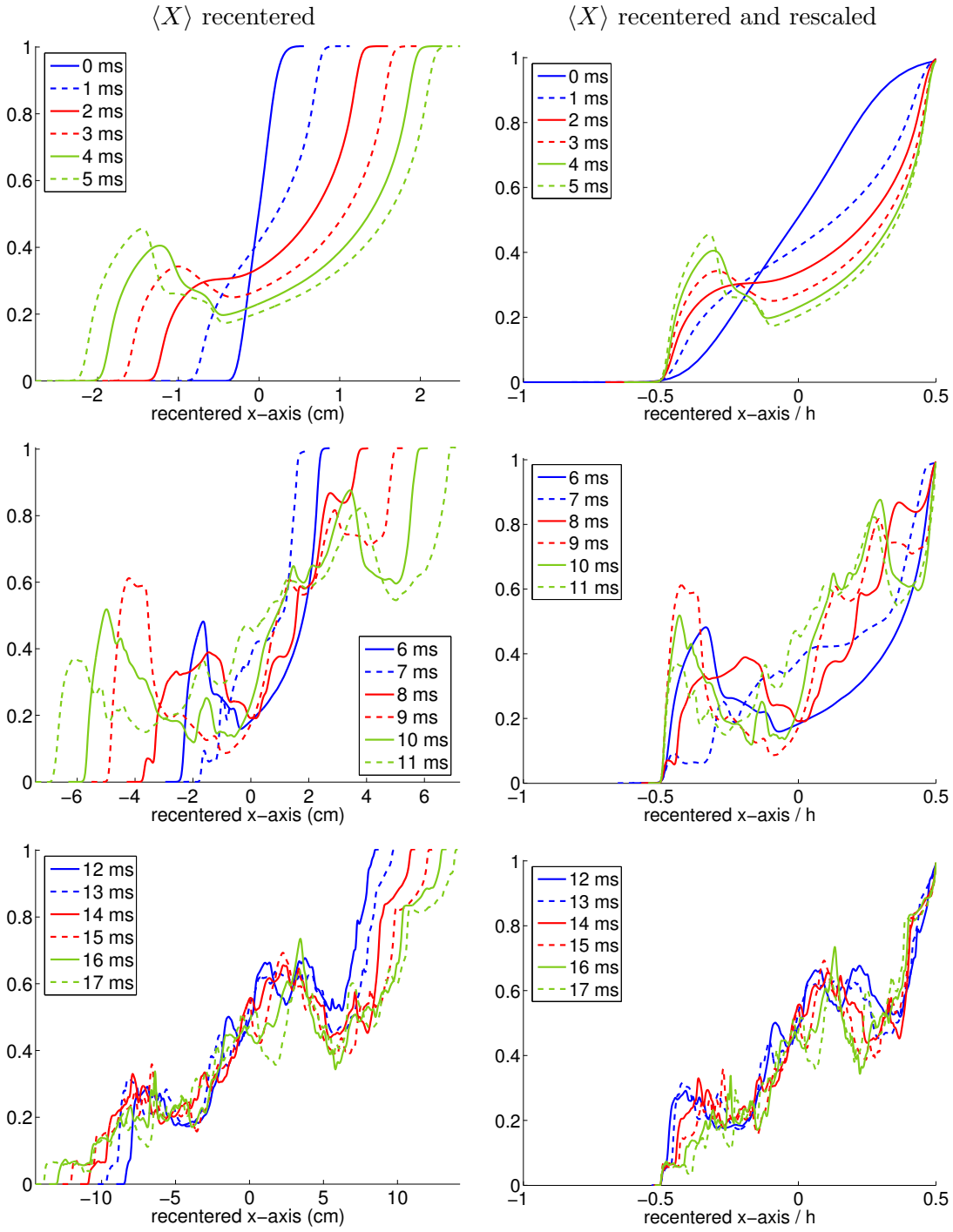

Figure 27: Time-evolution of the mole fraction profile $\langle X \rangle$ with the x-axis recentered (left column), and with the x-axis recentered and rescaled by the total mixing layer width h (right column).

mixed layer increases rapidly following reshock. Reshock also generates additional structure, which is reflected in the distribution of $\langle X \rangle$ (now displaying several localized peaks). For later times, the growth of the mixing layer slows and the localized peaks decrease in magnitude, and $\langle X \rangle$ begins to approach 0.5, indicating a well-mixed distribution of mass within the layer.

The right column of Fig. 27 shows the mole fraction profile $\langle X \rangle$ with the recentered streamwise coordinate rescaled by the mixing layer width h. The figures at early times indicate the transfer of mass between the bubbles and spikes, causing the non-monotonic profiles noted above. Prior to reshock, the profile evolves smoothly in space and time. Reshock causes a fundamental change in the distribution of mass with additional structures forming, as reflected in the more complex structure of the profile than at earlier times. For late times, the profiles begin to collapse and exhibit increased oscillations resulting from the break-up of structures.

The results from this investigation indicate that the mole fraction profile $\langle X \rangle$ is appropriate to measure the evolving redistribution of mass within the mixing layer caused by the creation of bubble- and spike-like structures. In particular, prior to reshock the main mechanisms affecting the mole fraction are the creation of a single, dominant bubble and spike; following reshock, the main mechanism is the excitation of many smaller bubbles and spikes contributing to the highly irregular, topologically-complex structure observed. These additional bubbles and spikes are responsible for elongating the mixing layer, resulting in a distribution of mass that is nearly uniformly increasing across the layer from the air(acetone) to the SF_6 side.

4.1.2 Evolution of the profiles of the averaged chemical product from a fast kinetic reaction $\langle X_p \rangle$, $X_p(\langle X \rangle)$ and of the mixing fraction ξ

A quantitative measure of mixing can be defined as follows. Suppose that the two fluids undergo a fast kinetic reaction, so that the amount of product produced (see Koochesfahani and Dimotakis [61] and Cook and Dimotakis [31]) is

$$X_p(x,y,t) = \begin{cases} \frac{X}{X_s} & \text{for } X \le X_s \\ \frac{1-X}{1-X_s} & \text{for } X > X_s \end{cases}, \tag{238}$$

where X_s is a parameter chosen to be $X_s = 1/2$ here (indicating that the product is composed of one mole of each reactant), and is limited by the amount of reactant (either the heavy or the light fluid). The profile of the averaged product mole fraction $\langle X_p \rangle(x,t) \in [0,1]$ provides information on how well mixed the two reactants are. The maximum amount of reactant mole is $X_p(\langle X \rangle) \ge \langle X_p \rangle$ if the two reactants were homogeneously mixed in the spanwise direction. The ratio

$$\xi(x,t) = \frac{\langle X_p \rangle}{X_p(\langle X \rangle)}, \tag{239}$$

which is between zero and unity, also locally characterizes how well mixed the two fluids are. If the fluids were completely and homogeneously mixed, $\langle X_p \rangle = X_p(\langle X \rangle)$, so that $\xi(x,t) = 1$.

The left column of Fig. 28 shows the time-evolution of the averaged product mole profile $\langle X_p \rangle$. The initial diffusion layer is well-mixed, with a rapid decrease in $\langle X_p \rangle$ between $t = 0$ and 1 ms, as expected; $\langle X_p \rangle$ broadens and rapidly develops sharp cusps at the edges of the mixing layer $x/h(t) \approx \pm 0.5$ as the spikes of heavy fluid penetrate into the lighter fluid and bubbles of the light fluid "rise" in the lighter fluid (and the two fluids become less mixed). At these very early times in the instability evolution, $\langle X_p \rangle$ is nearly-symmetric, with values ranging from $\approx$ 0.05–0.06 over most of the layer. A pronounced asymmetry develops for $t > 2$ ms: as the

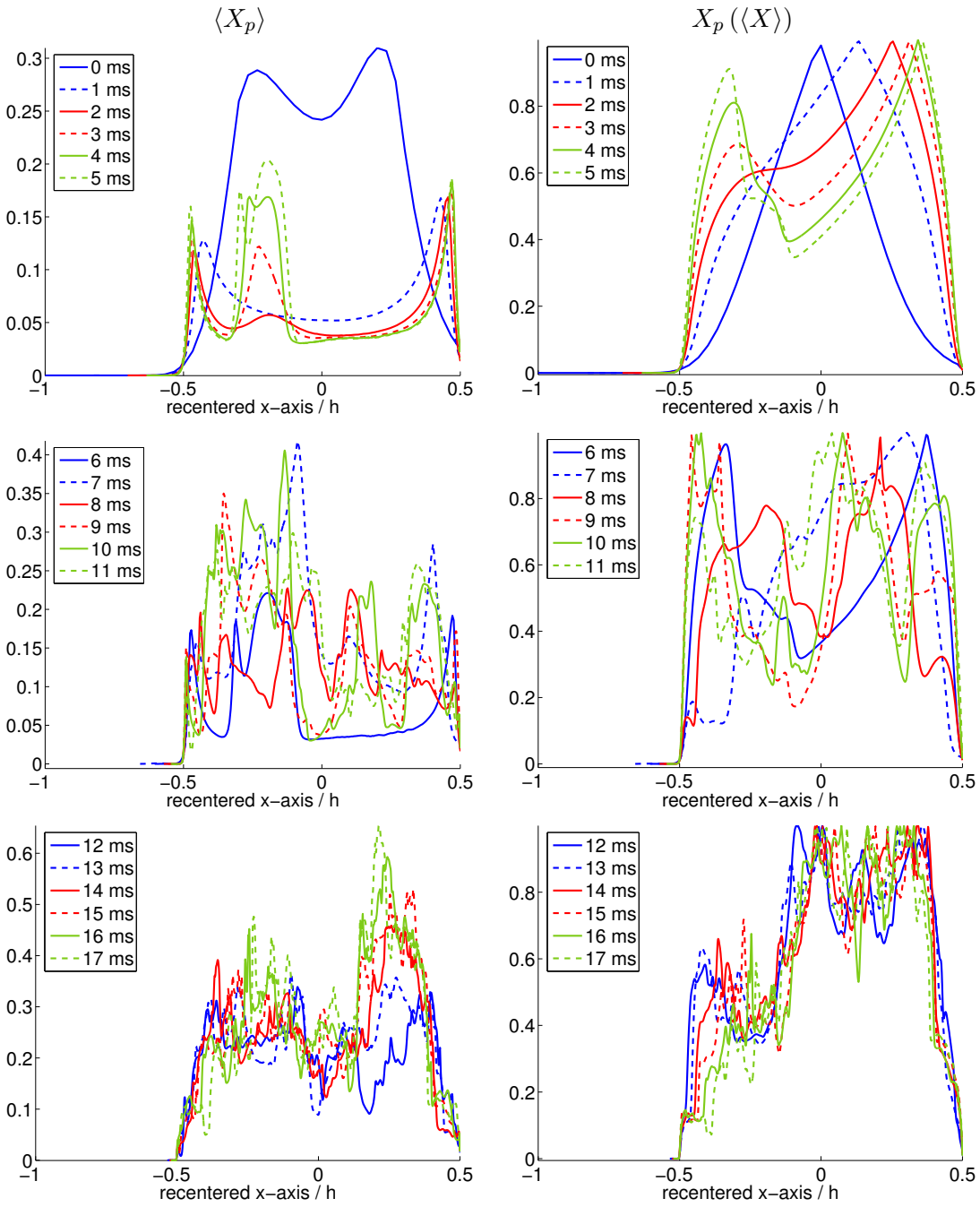

Figure 28: Time-evolution of the product mole fraction profile $\langle X_p \rangle$ (left column) and the product mole fraction if the fluids were homogeneously mixed $X_p\,(\langle X \rangle)$ with the x-axis recentered and rescaled by the total mixing layer width h (right column).

roll-ups form, a further peak within the air(acetone) mixture develops, corresponding to well-mixed fluid in the cores. Reshock significantly increases the product mole $\langle X_p \rangle$, as additional fine-scale structures form; $\langle X_p \rangle$ exhibits significant oscillations following reshock, which persist to late times. At late times the fluids tend to be more mixed and larger peaks develop in the SF_6, corresponding to the arrival of multiple reflected waves that produce increased mixing at one end of the mixing layer. The gases tend to be less mixed in the region closer to the air(acetone) than in the region closer to the SF_6.

The right column of Fig. 28 shows the mole fraction of the chemical product if the two fluids were completely mixed, $X_p(\langle X \rangle)$. This quantity measures the fraction of the maximum amount of product X_p observed if the two reactants were completely mixed $\langle X \rangle$, and indicates the maximum possible value of $\langle X_p \rangle$. At early times, $X_p(\langle X \rangle)$ is peaked at $x/h = 0$. Like $\langle X_p \rangle$, $X_p(\langle X \rangle)$ exhibits a complex spatial structure, with large oscillations following reshock.

The left column of Fig. 30 shows the ratio ξ defined in Eq. (239). This quantity constitutes a local mixing fraction characterizing how well the two fluids are mixed in the layer. For $t > 0$, ξ decreases rapidly, attaining its largest values near the edges of the mixing layer. At early times $t < 2$ ms, $\xi \approx 0.1$ across most of the layer. For $t > 2$ ms, ξ develops peaks on the air(acetone) side. Reshock amplifies ξ and induces strong oscillations across the mixing layer. At times $t > 12$ ms, ξ is strongly peaked on the air(acetone) side.

The results from this investigation suggest that $\langle X_p \rangle$ and $X_p(\langle X \rangle)$ are useful for understanding how well the mass is mixed across the layer. Large peaks are observed at early times due to the diffusive initial conditions; as the spike and bubble evolve through the linear phase, the two peaks separate and as the roll-ups form, additional peaks are observed corresponding to well-mixed fluid within the roll-ups; following reshock, several smaller roll-ups form, contributing to a larger number of peaks indicating large regions with localized well-mixed air and SF_6; at late times the formation of large-scale structures contribute to the appearance of large, wide peaks with smaller peaks of well-mixed fluid. This late-time behavior is consistent with the inverse cascade of small-scale velocity fluctuations to larger scales observed in two-dimensional turbulent flows.

4.1.3 Evolution of the profiles of the volume fractions $\langle f_1 \rangle$, $\langle f_2 \rangle$ and of the mixing fractions ξ and θ

The volume fractions (194) can be averaged over the spanwise direction to give the volume fraction profiles $\langle f_r \rangle(x,t)$. Figure 29 shows the volume fraction profiles $\langle f_1 \rangle$ and $\langle f_2 \rangle$, where the subscripts 1 and 2 correspond to the air(acetone) and SF_6, respectively. Note that the spatio-temporal evolution of $\langle f_2 \rangle$ is very similar to that of $\langle X \rangle$.

The volume fractions provide information on the mixing layer dynamics similar to that obtained from the mass fraction $\langle X \rangle$ for the current flow configuration. In configurations involving gases with much larger Atwood numbers than considered here, the volume and mass fractions provide somewhat different information. These quantities can be compared to experimental data or numerical simulation data depending on which data is more directly available.

The local molecular mixing fraction $\theta(x,t)$ is obtained from the averaged volume fractions and the average of their product [125, 126]

$$\theta(x,t) = \frac{\langle f_1 f_2 \rangle}{\langle f_1 \rangle \langle f_2 \rangle} \,. \tag{240}$$

The mixing fractions ξ and θ are shown in the left and right columns of Fig. 30, respectively. Note the similarity between θ and ξ due to the fact that both quantities are a measure

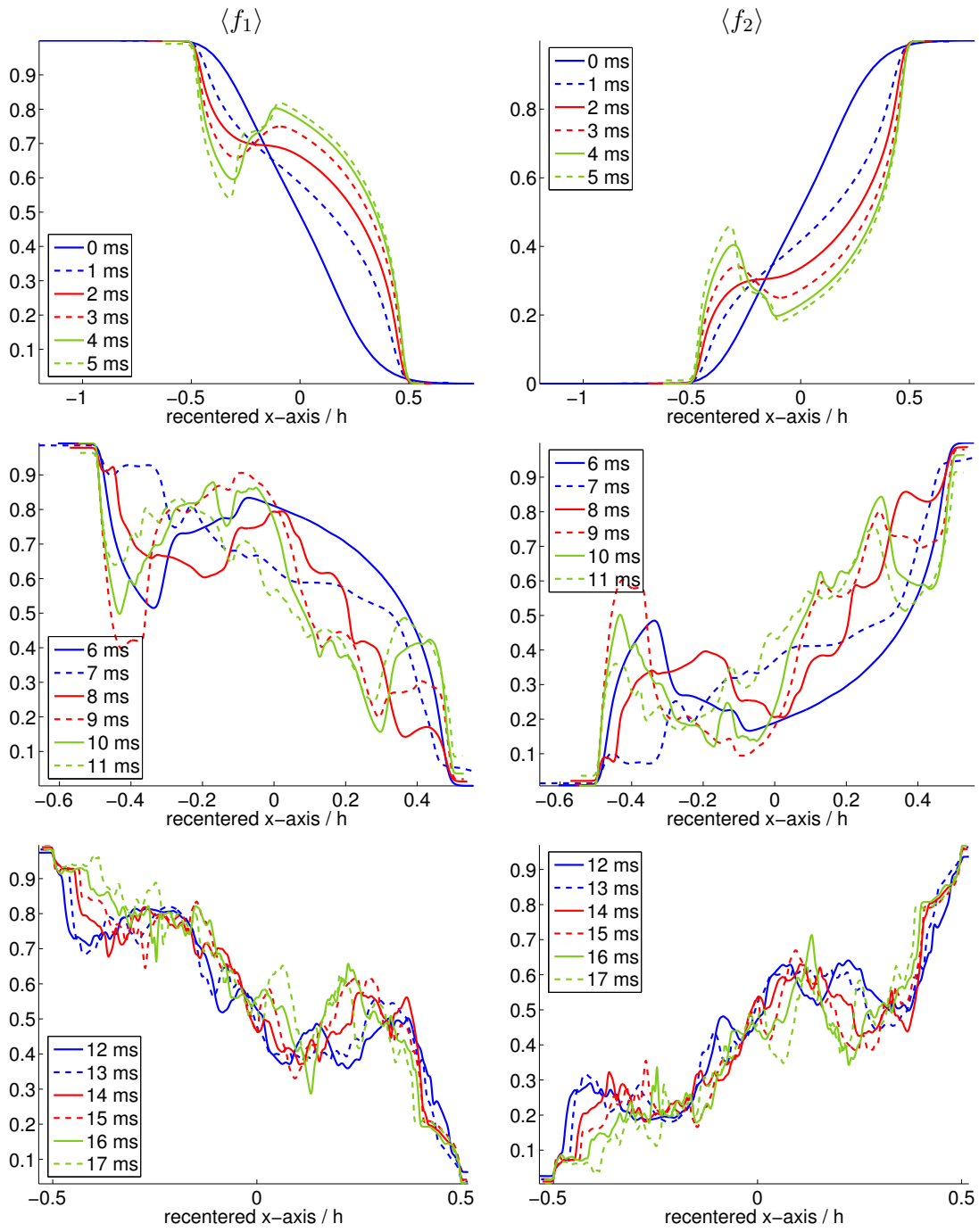

Figure 29: Time-evolution of the volume fractions $\langle f_1 \rangle$ (left column) and $\langle f_2 \rangle$ (right column) with the x-axis recentered and rescaled by the total mixing layer width h.

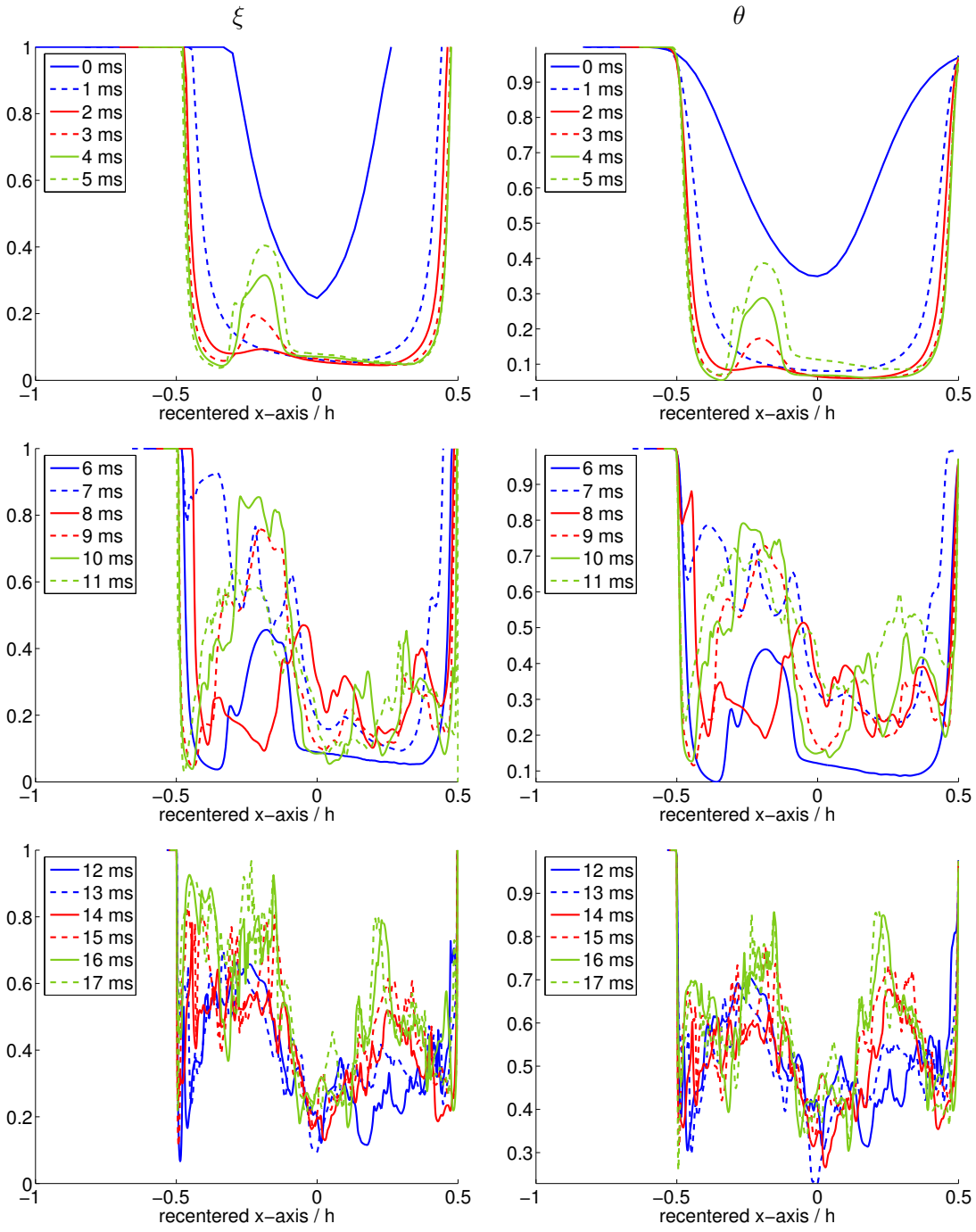

Figure 30: Time-evolution of the molecular mixing fractions ξ (left column) and θ (right column) with the x-axis recentered and rescaled by the total mixing layer width h.

of mixing, indicating that both mechanisms—the fast kinetic reaction and the diffusion process characterized by θ—provide a very similar qualitative description of mixing. *Note that this 'molecular mixing' is induced by stirring and by the numerical diffusion present in the algorithm, rather than by molecular processes.*

4.2 Time-evolution of mixing fractions and of volume-averaged quantities

The time-evolution of global quantities such as the production quantities P_t and P_m, and the mixing fractions Ξ and Θ are presented here. The volume-averaged streamwise and spanwise velocity components, and pressure are also investigated.

4.2.1 Evolution of the lengthscale W

The lengthscale W is shown in the top right of Fig. 31, and qualitatively resembles the evolution of the mixing layer width h shown in the top left of Fig. 31. Note that these lengthscales do not appear to exhibit a simple power-law growth at late times. The value of W is obtained by integrating the volume fractions, and is therefore less sensitive to the cutoff values used to obtain h. In fact, when small features form near the edges of the mixing layer following reshock, the overall mass fraction $\langle X \rangle$ may be just above or below the cutoff used to define h. As a result, h may oscillate whereas W remains smooth. The information provided by W is qualitatively similar to that provided by h, and is not considered further in the present investigation.

4.2.2 Evolution of the mixing fractions P_t, P_m, Θ, and Ξ

From the product mole fraction X_p, the total chemical product P_t is obtained by integrating $\langle X_p \rangle$ over the mixing layer width,

$$P_t(t) = \int_{a_s(t)}^{a_b(t)} \langle X_p \rangle \, \mathrm{d}x \,. \tag{241}$$

The total chemical product P_t can be compared to the maximum amount of chemical product,

$$\begin{aligned} P_m(t) &= \int_{a_s(t)}^{a_b(t)} X_p(\langle X \rangle) \, \mathrm{d}x \\ &\geq P_t(t) \,, \end{aligned} \tag{242}$$

measuring the product obtained if both reactants were homogeneously mixed.

The time-evolution of P_t and P_m is shown in the middle row of Fig. 31. Before reshock, P_t increases, indicating an increase in mixing, while P_m decreases. The decrease in P_m indicates that the maximum molar product decreases due to the presence of the bubble which creates large, unmixed structures within the mixing layer. During reshock, the mixing layer is compressed, inducing additional mixing as measured by P_t. Following reshock, P_t increases rapidly, indicating significantly increased mixing. As the mixing progresses, large unmixed structures form, causing the decrease in P_m.

The ratio of the total and maximum chemical product gives the mixing fraction [31]

$$\Xi(t) = \frac{P_t(t)}{P_m(t)} \,, \tag{243}$$

with increasing values of Ξ signifying more complete mixing. From the local molecular mixing fraction θ, another global molecular mixing fraction can be defined as [125]

$$\Theta(t) = \frac{\int_{a_s(t)}^{a_b(t)} \langle f_1 \, f_2 \rangle \, \mathrm{d}x}{\int_{a_s(t)}^{a_b(t)} \langle f_1 \rangle \langle f_2 \rangle \, \mathrm{d}x} \,, \tag{244}$$

with increasing values of Θ also corresponding to more complete mixing.

The time-evolution of the mixing fractions Θ and Ξ is also shown in the middle row of Fig. 31. As was observed for ξ and θ in Fig. 30, the mixing fractions Ξ and Θ give qualitatively similar information. As the fluids mix following the initial shock passage, the mixing fractions increase. A spike is observed during reshock as the mixing layer is compressed and the overall mixing is increased. Following reshock, the mixing fractions increase at a faster rate than before reshock, indicating that reshock increases mixing.

The results above suggest that integrated mixing fractions Θ and Ξ provide a physical interpretation of the mixing, produced in this case by the numerical algorithm, rather than by the molecular effects present in the physical experiment. The results indicate that mixing is affected in the following way by reshock. Immediately after reshock, the layer is compressed causing a well-mixed region to form, as shown by the formation of a sharply-peaked value in the mixing fractions. This well-mixed region is characterized by the rapid production of small-scale features by the reshock process, as shown earlier. Subsequently, the mixing layer undergoes a rapid growth as the inversion occurs, causing the overall mixing to decrease rapidly over a time interval of approximately two milliseconds. Following this decay, the formation of complex flow features with roll-ups causes the mixing to again increase. As shown here, the combined use of all of the mixing profiles and mixing fractions is needed to obtain a quantitative understanding of the mixing processes caused by reshock.

4.2.3 Evolution of the volume-averaged velocity components and pressure

The time-evolution of the volume-averaged streamwise and spanwise velocities, and pressure are presented here. In two dimensions, define the volume average of $\phi(x, y, t)$ by

$$\langle \phi \rangle_{xy}(t) = \frac{1}{h(t)\, L_y} \int_{a_s(t)}^{a_b(t)} \int_0^{L_y} \phi(x, y, t) \, \mathrm{d}y \, \mathrm{d}x \,. \tag{245}$$

The volume-averaged streamwise and spanwise velocity components $\langle u \rangle_{xy}$ and $\langle v \rangle_{xy}$, respectively, are shown in the bottom row of Fig. 31 as a function of time. As expected, $\langle v \rangle_{xy} = 0$ for all time. Note that $\langle u \rangle_{xy}$ is the velocity of the interface, which rapidly decreases at reshock; $\langle u \rangle_{xy}$ changes sign at reshock and remains nearly constant over $t \approx 6.5$–10.5 ms, indicating an inversion of the direction of the mean motion of the mixing layer, as well as the effect of the reflected rarefaction wave. Note that $\langle u \rangle_{xy} \to 0$ at late times, as the reflected waves following reshock decelerate the interface and eventually bring it to rest.

The volume-averaged pressure $\langle p \rangle_{xy}$ is also shown in the bottom row of Fig. 31 as a function of time. The average pressure reflects the effect of the reshock (which significantly increases the pressure during compression) and of the rarefaction wave (which decreases the pressure). A nearly constant value of $\langle p \rangle_{xy}$ is maintained over $t \approx 6.5$–10.5 ms. The temporal evolution of both $\langle u \rangle_{xy}$ and $\langle p \rangle_{xy}$ clearly show the interaction of the reflected waves with the mixing layer. As expected, the volume-averaged spanwise velocity $\langle v \rangle_{xy}$ is zero with some very small fluctuations at the time of reshock.

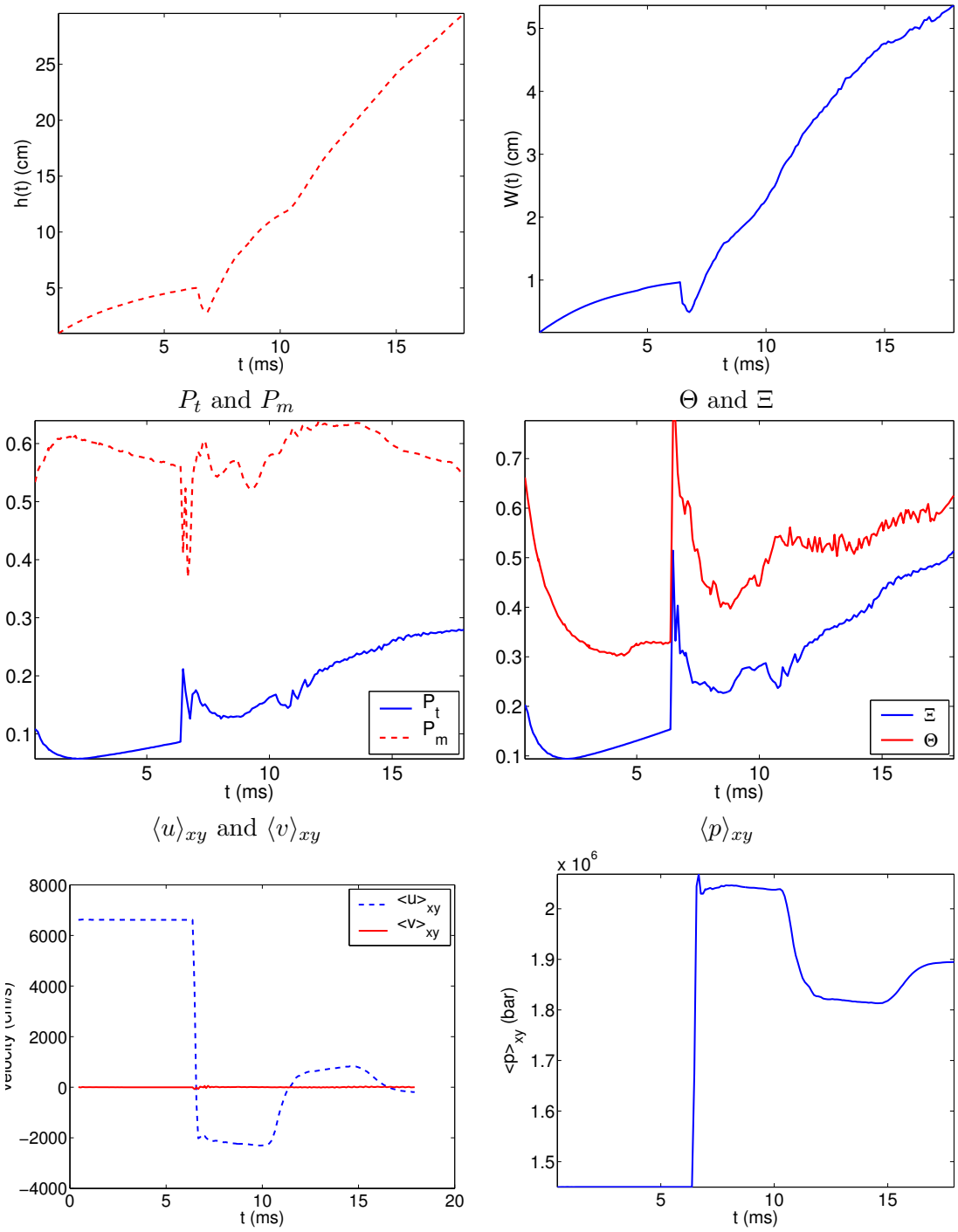

Figure 31: Time-evolution of the mixing layer width as measured by $h(t)$ and $W(t)$ in the top row. The time-evolution of the mixing fractions P_t, P_m, Θ, and Ξ are shown in the middle row. The time-evolution of the volume-averaged streamwise and spanwise velocities $\langle u \rangle_{xy}$ and $\langle v \rangle_{xy}$, and the volume-averaged pressure $\langle p \rangle_{xy}$ are shown in the bottom row.

The results above provide a description of the mean flow and confirm the expected behavior from the wave structure observed here. In particular, the mean pressure and mean streamwise velocity quantify the effects of reflected waves on the averaged dynamics of the mixing layer.

4.3 Time-evolution of the fluctuating kinetic energy, fluctuating enstrophy, density variance, and pressure variance spectra

The time-evolution of the spectra corresponding to the fluctuating kinetic energy, fluctuating enstrophy, density variance, and pressure variance are investigated here. An examination of these spectra provides information on the growth of different scales of the flow, as well as on the energy transfer process among scales. Summarized here is the general procedure used in the present investigation to determine the spectrum of a quantity $\phi(x, y, t)$ defined in the mixing layer $x \in [a_s, a_b]$. Typically, ϕ is a field with Reynolds fluctuation ϕ' defined in Eq. (235) or Favre fluctuation ϕ'' defined in Eq. (237). The spectral analysis used here adapts the formulations of Lesieur et al. [72] and Mügler and Gauthier [94, 95] applied to inhomogeneous flows with a direction of statistical-homogeneity (periodicity). The fundamental procedures of Fourier analysis are reviewed elsewhere [43, 23, 102].

First, the Fourier transform of $\phi(x, y, t)$ is taken in the periodic spanwise direction to obtain

$$\widehat{\phi}(k, x, t) = \frac{1}{2\pi} \int_{-\infty}^{\infty} \phi(x, y, t) \exp(-ik\, y)\, \mathrm{d}y\,. \tag{246}$$

Numerically, the discrete Fourier transform of $\phi(x, y, t)$ is taken in the periodic y-direction to obtain the one-dimensional spectrum,

$$\widehat{\phi}(k_n, x, t) = \frac{1}{N_y} \sum_{n=0}^{N_y-1} \phi_n(x, t) \exp(-ik_n\, \Delta y)\,, \tag{247}$$

where $n = 0, 1, ..., N_y$, and N_y is the number of grid points in the y-direction with uniform grid spacing Δy, and

$$k_n = \frac{2\pi n}{N_y\, \Delta y} \tag{248}$$

is the discrete wavenumber (*n.b.*, in the subsequent analysis, the units of k are cm^{-1}). Such a spectrum is appropriate for a two-dimensional flow having one direction of statistical-homogeneity, in which periodic boundary conditions are assumed.

The energy associated with each Fourier mode k is obtained by averaging over the extent of the mixing layer to obtain the one-dimensional energy spectrum of the quantities ϕ and ψ,

$$E_{\phi\psi}(k, t) = \frac{1}{2\, h(t)} \int_{a_s(t)}^{a_b(t)} \left[\widehat{\phi}(k, x, t)\, \widehat{\psi}(k, x, t)^* + \widehat{\phi}(k, x, t)^*\, \widehat{\psi}(k, x, t)\right] \mathrm{d}x\,, \tag{249}$$

where h is given by Eq. (218) and $*$ indicates complex conjugation. Numerically, this integration over the mixing layer width is performed using the trapezoidal rule. In the results presented below, all modes above the Nyquist wavenumber (187) are neglected [102]. The spectrum $E_{\phi\psi}(k, t)$ provides information on the energy content of all of the scales present in the statistical correlation between ϕ and ψ as a function of time. This constitutes a local analysis, as modal information is obtained within the mixing layer as a function of scale. The characteristic scale of a structure with wavenumber k is $\ell \sim 1/k$.

The spatial profiles of the one-dimensional spectral density

$$E_{\phi\psi}(k_n, x, t) = \frac{\widehat{\phi}(k_n, x, t)\,\widehat{\psi}(k_n, x, t)^* + \widehat{\phi}(k_n, x, t)^*\,\widehat{\psi}(k_n, x, t)}{2} \tag{250}$$

can also be considered, in addition to the spatially-integrated spectra (249). The usual energy spectrum corresponds to $\psi = \phi$:

$$E_{\phi\phi}(k_n, x, t) = \left|\widehat{\phi}(k_n, x, t)\right|^2 \tag{251}$$

with

$$E_{\phi\phi}(k_n, t) = \frac{1}{h(t)} \int_{a_s(t)}^{a_b(t)} \left|\widehat{\phi}(k_n, x, t)\right|^2 \,\mathrm{d}x\,. \tag{252}$$

Figures 32 and 33 show the time-evolution of the streamwise and spanwise fluctuating kinetic energy spectra per unit volume $E_{u''u''}(k,t)$ and $E_{v''v''}(k,t)$, respectively, and the total fluctuating kinetic energy spectrum per unit volume

$$E(k,t) = E_{u''u''}(k,t) + E_{v''v''}(k,t)\,. \tag{253}$$

Oscillations are present in the spectra for small and intermediate wavenumbers k at early times, and following reshock. These oscillations are damped out at late times, as indicated by the smoothly decaying spectra at large t. Reshock induces a jump in the energy spectra between $t = 6$ ms and $t = 7$ ms at all scales of the flow by exciting a wide spatial range of fluctuations, thereby imparting additional energy into the mixing layer. For times $t > 8$ ms, the energy spectra appear to decay very slowly. Note that $E_{u''u''}(k,t)$ is peaked at $k \approx 1.5$, while the peak of $E_{v''v''}(k,t)$ corresponds to the largest scale of the flow. As expected, there is more energy content in the streamwise velocity fluctuations than in the spanwise velocity fluctuations. For the same reason, the evolution of $E(k,t)$ is dominated by that of $E_{u''u''}(k,t)$. There is no apparent power-law scaling of the spectra over the limited range of scales supported by the modest grid resolution. The spectra turn up slightly at large wavenumbers due to aliasing errors.

The enstrophy density is

$$\Omega(x, y, t) = \frac{|\omega(x, y, t)|^2}{2}\,, \tag{254}$$

and the volume integral of the enstrophy density yields

$$\Omega(t) = \iint \Omega(x, y, t)\,\mathrm{d}x\,\mathrm{d}y\,. \tag{255}$$

The fluctuating enstrophy density is

$$\Omega(x, y, t)'' = \frac{|\omega''(x, y, t)|^2}{2}\,, \tag{256}$$

and the volume integral of the fluctuating enstrophy density yields the fluctuating enstrophy

$$\Omega(t)'' = \iint \Omega(x, y, t)''\,\mathrm{d}x\,\mathrm{d}y\,. \tag{257}$$

The time-evolution of the fluctuating enstrophy spectrum per unit volume $E_{\omega''\omega''}(k,t)$ is shown in Fig. 33. In a homogeneous flow, the enstrophy is related to the fluctuating kinetic energy

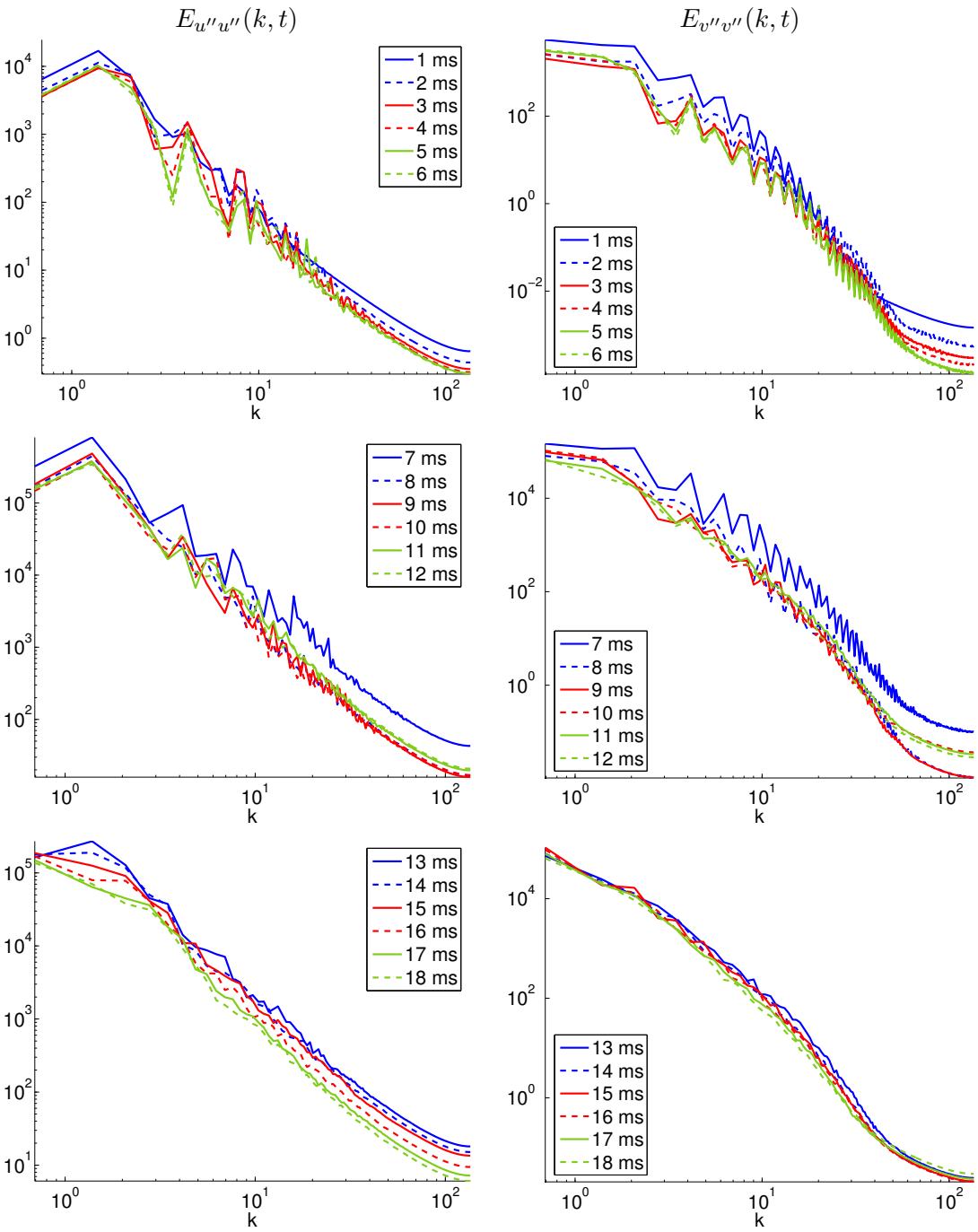

Figure 32: Time-evolution of the streamwise and spanwise fluctuating kinetic energy spectra $E_{u''u''}(k,t)$ (left column) and $E_{v''v''}(k,t)$ (right column), respectively. The units of the fluctuating kinetic energy spectra are $\mathrm{cm}^3/\mathrm{s}^2$.

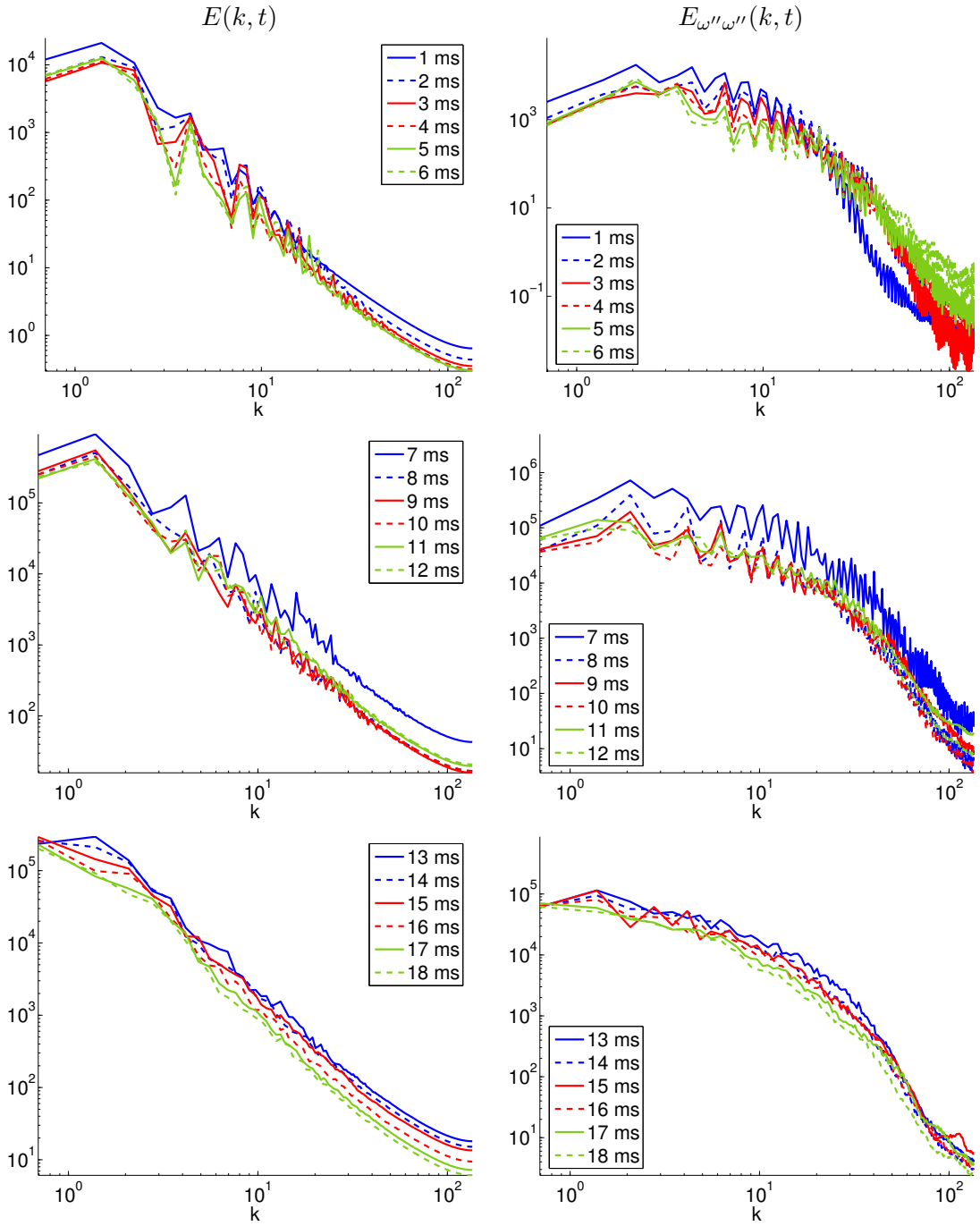

Figure 33: Time-evolution of the (total) fluctuating kinetic energy spectrum $E(k,t) = E_{u''u''}(k,t) + E_{v''v''}(k,t)$ (left column) and fluctuating enstrophy spectrum $E_{\omega''\omega''}(k,t)$ (right column). The units of the fluctuating kinetic energy spectrum are $\mathrm{cm}^3/\mathrm{s}^2$, and the units of the fluctuating enstrophy spectrum are cm/s^2.

spectrum by $E_{\omega''\omega''}(k,t) = k^2 E(k,t)$, so that the peak of the fluctuating enstrophy spectrum is weighted toward smaller scales than that of the kinetic energy spectrum. The enstrophy spectrum is less steep than the fluctuating kinetic energy spectrum. As in the case of $E(k,t)$, reshock primarily amplifies the enstrophy spectrum but does not change its shape. A slow decay of the enstrophy spectrum is also observed for late times. Before and immediately after reshock, the fluctuating enstrophy spectrum is more oscillatory than the fluctuating kinetic energy spectrum, particularly at large wavenumbers.

Spectral anisotropy of the velocity components can be investigated by considering the time-evolution of the ratio of the streamwise and spanwise fluctuating kinetic energy spectra $E_{u''u''}(k,t)/E_{v''v''}(k,t)$, as shown in Fig. 34. Spectral isotropy is achieved if all scales contain the same amount of energy, *i.e.*, if the ratio approaches unity. As seen in the figure, significant spectral anisotropy exists in the intermediate and small scales, with the ratios attaining a nearly constant value at large wavenumbers. It is interesting to note that a sharp increase in the ratio of the streamwise and spanwise fluctuating kinetic energy is observed *following* reshock and the interaction with the reflected rarefaction wave. This is expected as the arrival of the waves excites velocity fluctuations in all directions, thereby reducing the ratio. However, as the instability further evolves following the interaction with the waves, the fluctuations in the streamwise kinetic energy dominate, and this ratio sharply increases. The ratio again decreases at late times, as dissipative mechanisms damp the larger streamwise fluctuations.

Figure 35 shows the time-evolution of the density variance spectrum per unit volume $E_{\rho'\rho'}(k,t)$ and the pressure variance spectrum per unit volume $E_{p'p'}(k,t)$. The density variance spectrum shows very little variation with time, indicating that density fluctuations are not as strongly affected by reshock as other quantities. Moreover, the magnitude of the density variance spectrum is very small for all times, indicating that the density variance is very small and that the flow is nearly-incompressible. Additional numerical evidence exists to support this conclusion in Richtmyer-Meshkov unstable flows [47]. The issue of near-incompressibility after reshock will be revisited in Part 4 of this report [70]. The evolution of the spectrum also shows the interaction of reflected waves with the mixing layer, which have a profound effect on the pressure variance spectrum. The pressure variance spectrum exhibits a jump as a result of reshock at $t = 7$ ms, and also exhibits a jump at $t = 11$ ms when the reflected rarefaction wave interacts with the mixing layer. At late times, both the pressure and density variance spectra exhibit a slow decay in time. There is no apparent power-law scaling of these spectra.

The investigation of the spectral evolution above both prior to and following reshock provides a spectral quantification of the complex features observed in the density and Schlieren images. In particular, the spectral investigation shows that a fairly broad range of scales already exists prior to reshock, despite the fact that the roll-up from a single-mode initial perturbation is considered. This indicates that the Richtmyer-Meshkov instability develops non-trivial spectral content from its inception. At reshock, the fluctuations in all fields (except the density) are amplified nearly uniformly across all scales. From the results obtained here, reshock does not appear to broaden the range of scales, but primarily imparts energy into structures of all sizes. At late times, dissipation mechanisms smooth the spectra. When the shock is far away and the reflected waves become weaker, a very slow decay is observed in the spectra. The density spectrum reveals that the density fluctuations remain small and are not affected strongly by reshock. As a result, measurements of spectral quantities using a density weighting [59, 60] are not expected to provide different conclusions: this was confirmed by comparing both density- and non-density-weighted spectra and is not shown here. Compared

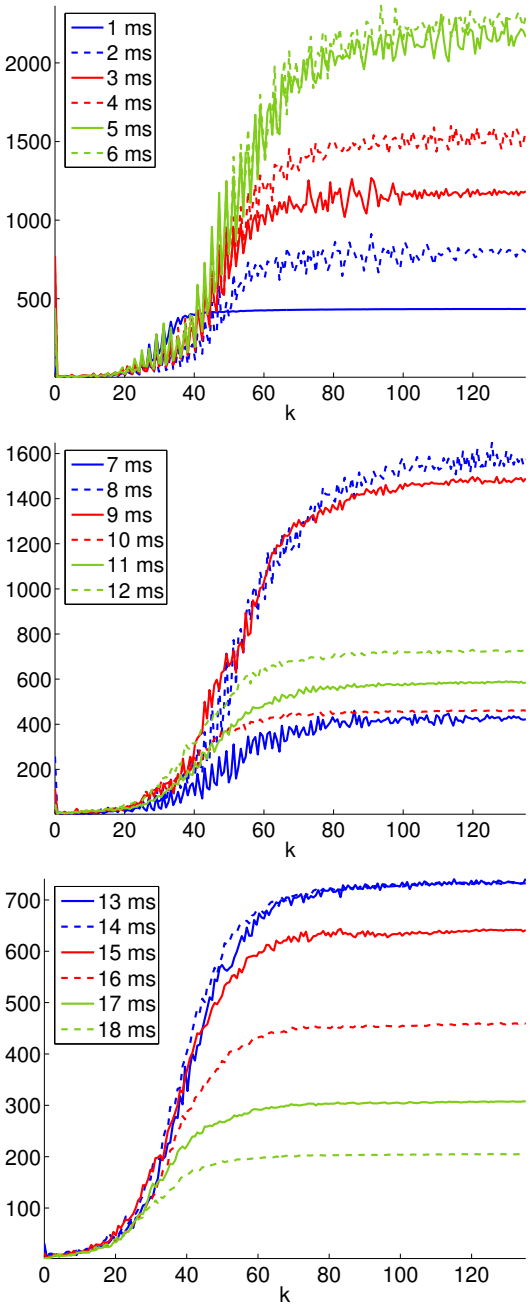

Figure 34: Time-evolution of the ratio of the streamwise and spanwise fluctuating kinetic energy spectra $E_{u''u''}(k,t)/E_{v''v''}(k,t)$.

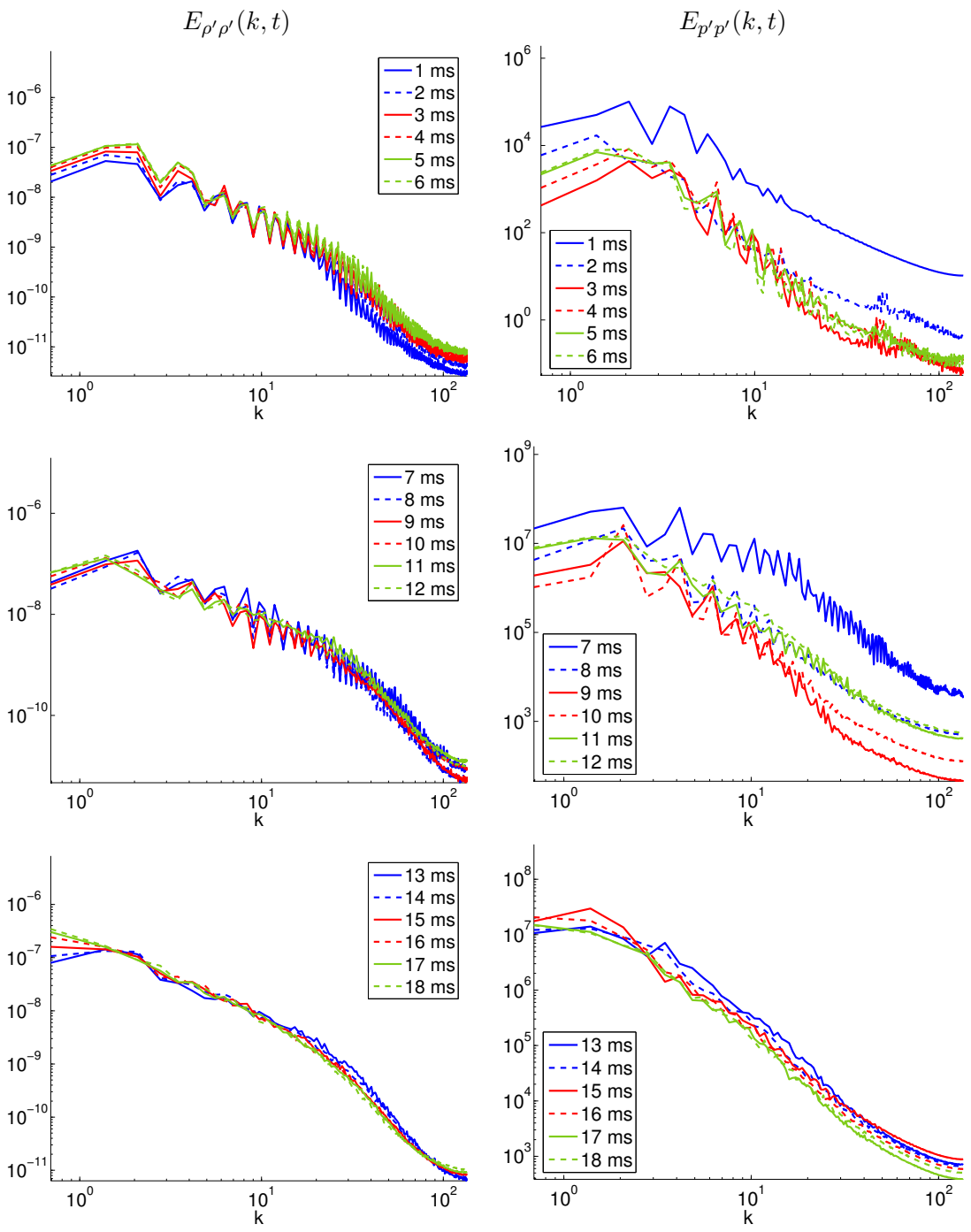

Figure 35: Time-evolution of the density variance spectrum $E_{\rho'\rho'}(k,t)$ (left column) and the pressure variance spectrum $E_{p'p'}(k,t)$ (right column). The units of the density variance spectrum are $\mathrm{g}^2/\mathrm{cm}^5$ and the units of the pressure variance spectrum are $\mathrm{bar}^2\mathrm{cm}$.

to the fluctuating kinetic energy spectrum, the fluctuating enstrophy spectrum shows a more pronounced cascade toward smaller scales, as expected by two-dimensional turbulence phenomenology [116, 58, 117]. Compared to the other spectra, the pressure variance spectrum shows the effects of reflected waves with increased values observed following reshock at $t = 7$ ms and during the arrival of the reflected rarefaction wave at $t = 11$ ms. The decomposition of the fluctuating kinetic energy spectrum into the streamwise and spanwise components indicates that the streamwise component is dominant and that significant statistical anisotropy exists even at late times.

4.4 Time-evolution of statistics

Statistics within the mixing layer were obtained by integrating the energy spectrum per unit volume over all modes,

$$\begin{aligned} E_{\phi\phi}(t) &= \frac{\overline{\phi^2}}{2} \\ &= \int_0^\infty E_{\phi\phi}(k,t)\,\mathrm{d}k\,. \end{aligned} \tag{258}$$

Numerically, this integral is a sum over all wavenumbers up to the Nyquist wavenumber (187) $k_{\max}$. As a numerical verification, statistics were computed by summing the energy spectra over all wavenumbers, $\sum_{n=1}^{N_y} E_{\phi\phi}(k_n,t)$, and directly by a volume integration, $\sum_{i\in S}\sum_{j=1}^{N_y}\phi(x_i,y_j,t)^2/2$ where $S = \{i \;:\; x_i \in [a_s(t), a_b(t)]\}$, to ensure that these results agree.

Figure 36 shows the time-evolution of the streamwise and spanwise fluctuating kinetic energy per unit volume

$$\begin{aligned} E_{u''u''}(t) &= \frac{\overline{u''^2}}{2} \\ &= \int_0^\infty E_{u''u''}(k,t)\,\mathrm{d}k\,, \end{aligned} \tag{259}$$

$$\begin{aligned} E_{v''v''}(t) &= \frac{\overline{v''^2}}{2} \\ &= \int_0^\infty E_{v''v''}(k,t)\,\mathrm{d}k\,, \end{aligned} \tag{260}$$

and the total fluctuating kinetic energy per unit volume

$$E(t) = E_{u''u''}(t) + E_{v''v''}(t)\,, \tag{261}$$

illustrating the relative magnitude of the two components. Initially, $E_{v''v''}(t)$ is much smaller than $E_{u''u''}(t)$ due to the fact that the initial shock primarily excites modes in the streamwise direction (as shown in Fig. 32). The kinetic energy decreases following the initial shock, while reshock deposits additional vorticity and amplifies the kinetic energy. The reshock and the subsequent reflected waves also excite spanwise velocity fluctuations. The contributions from the spanwise and streamwise fluctuations are very similar at late times, indicating an approach of the flow to *statistical* (but not spectral) isotropy. The ratio of the spanwise and streamwise kinetic energy is shown in Fig. 37. The ratio approaches unity at late time, indicating an approach to isotropy.

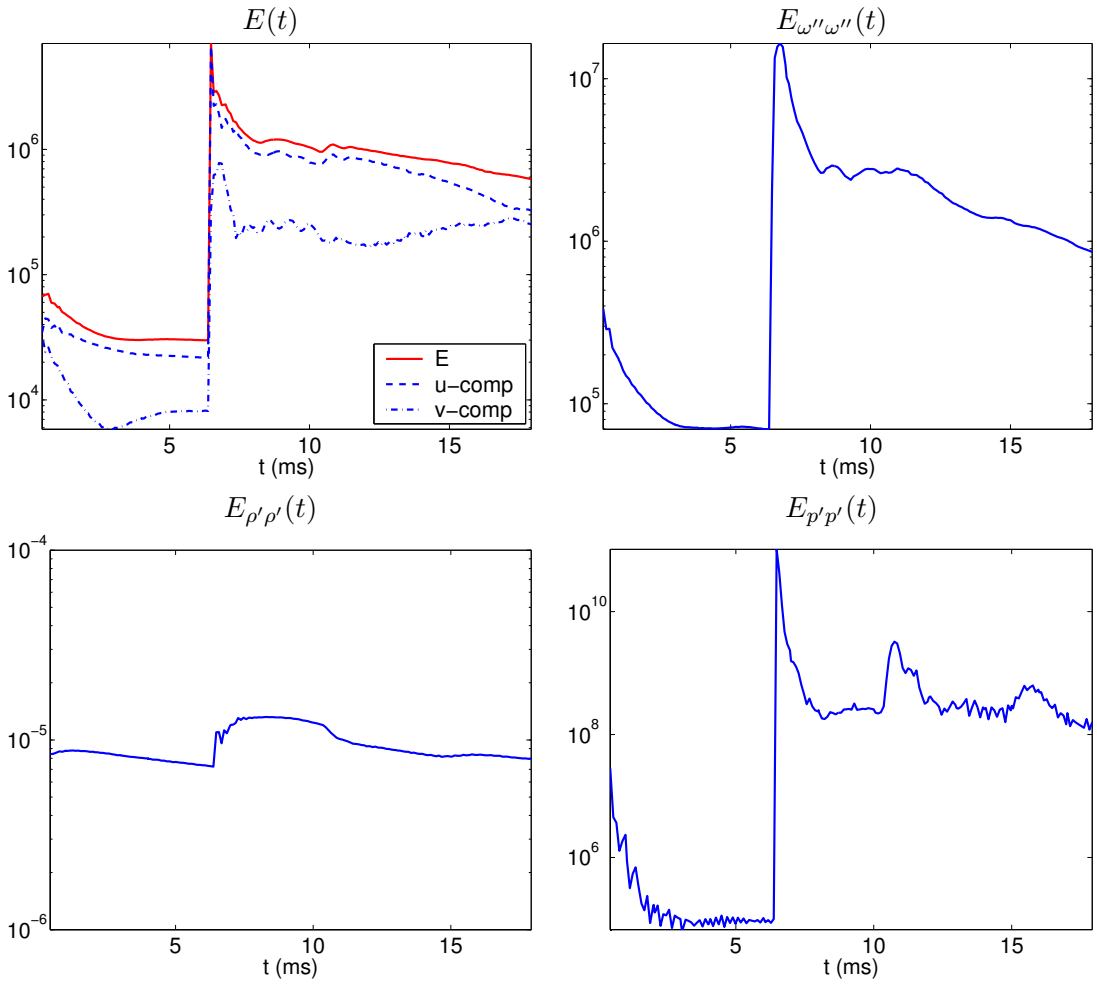

Figure 36: Time-evolution of the fluctuating kinetic energy $E(t)$ and its components, the enstrophy $E_{\omega''\omega''}(t)$, density variance $E_{\rho'\rho'}(t)$, and pressure variance $E_{p'p'}(t)$.

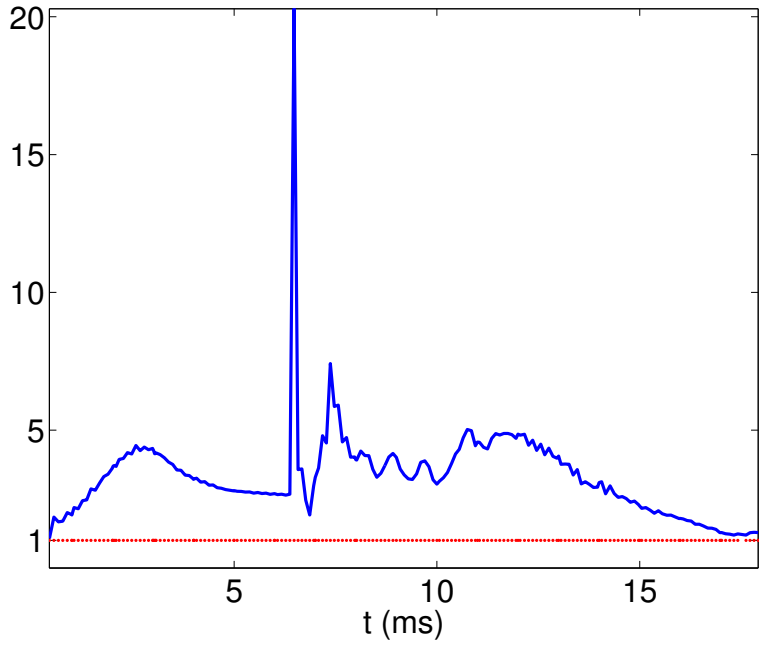

Figure 37: Time-evolution of the ratio of the streamwise and spanwise fluctuating kinetic energy $E_{u''u''}(t)/E_{v''v''}(t)$. The ratio approaches unity at very late time, indicating an approach to statistical isotropy. Note, however, that the kinetic energy spectra are still spectrally-anisotropic at late times.

The time-evolution of the fluctuating enstrophy per unit volume

$$\begin{aligned} E_{\omega''\omega''}(t) &= \frac{\overline{\omega''^2}}{2} \\ &= \int_0^\infty E_{\omega''\omega''}(k,t)\,\mathrm{d}k \end{aligned} \tag{262}$$

is also shown in Fig. 36. Note the large increase in the fluctuating enstrophy during reshock. Following reshock, the enstrophy decays, but the arrival of the reflected waves compensates for the decrease and a nearly constant value is observed for $t \approx 7$–11 ms. Finally, after the interaction of the reflected rarefaction with the mixing layer at $t = 11$ ms, the enstrophy begins to decay again.

Finally, consider the time-evolution of the density variance

$$\begin{aligned} E_{\rho'\rho'}(t) &= \frac{\overline{\rho'^2}}{2} \\ &= \int_0^\infty E_{\rho'\rho'}(k,t)\,\mathrm{d}k \end{aligned} \tag{263}$$

and the pressure variance

$$\begin{aligned} E_{p'p'}(t) &= \frac{\overline{p'^2}}{2} \\ &= \int_0^\infty E_{p'p'}(k,t)\,\mathrm{d}k\,. \end{aligned} \tag{264}$$

The density variance is not as significantly affected by reshock and by other reflected waves as the other quantities, and remains nearly constant in time. By contrast, the pressure variance is much more sensitive, exhibiting peaks as waves interact with the mixing layer. The first peak at $t = 7$ ms corresponds to the arrival of the reflected shock; the second peak at $t = 11$ ms corresponds to the arrival of the reflected rarefaction wave, and; the third peak at $t = 15$ ms corresponds to the arrival of the reflected compression wave generated by the refraction of the rarefaction wave at $t = 11$ ms. The pressure variance is the only quantity considered that captures the effect of this third interaction. With the exception of $E_{\rho'\rho'}(t)$, all of the remaining statistics decrease from their initial values until reshock. Also, with the exception of $E_{\rho'\rho'}(t)$, all of the remaining statistics decrease sharply following reshock. With the present reflecting boundary condition, the simulation does not achieve a purely-decaying state at late times. Later in § 4.6, the reflecting boundary condition is changed to outflow in order to remove the effects of reflected waves following reshock.

The time-evolution of volume-integrated (wavenumber-integrated) variances (statistics) was investigated above. The fluctuating kinetic energy exhibits a sharp peak corresponding to reshock, with a rapid increase followed by a rapid decrease, followed then by a decay. The decay becomes more established following the interaction with the reflected rarefaction wave at $t = 11$ ms. Comparison of the streamwise and spanwise components indicates that statistical isotropy is achieved at late times. In fact, the total energy content of the spanwise component increases following the interaction with the reflected waves, and the large values of the streamwise component decrease due to dissipation. The enstrophy also exhibits a sharp peak corresponding to reshock and then a rapid decay following the interaction with the reflected rarefaction wave. The density variance is very small in magnitude and remains nearly constant,

although signatures of the reflected shock and of the reflected rarefaction are apparent. The pressure variance shows narrow, sharp peaks corresponding to the reshock and to the arrival of the reflected rarefaction wave, and further shows the arrival of the reflected compression wave at late times. In all three cases, the waves excite fluctuations that are apparent in the increased values of the statistics. The fluctuations are damped and the statistics decrease in magnitude as time evolves.

4.5 Comparison of mixing quantities at selected times

In the previous sections, a temporal progression of each quantity was presented at time intervals of 1 ms. Here, comparisons of quantities at selected times are presented together to further elucidate the structure of the mixing as characterized by each quantity. The times are selected to reflect key aspects of the flow evolution:

1. at $t = 6$ ms *after the initial interaction with the shock but before reshock*;
2. at $t = 7$ ms *immediately after reshock*;
3. at $t = 12$ ms for *large times after reshock*, and;
4. at $t = 18$ ms for *late times*.

Also presented is a comparison of quantities immediately before and after reshock to quantitatively investigate the effect of reshock on the mixing process. These quantities include molar profiles, volume fraction profiles, mixing fractions, and fluctuating energy spectra. Note that in the figures, quantities are shown on an x-axis recentered according to the location of the centerline of the mixing layer.

4.5.1 Comparison of mixing quantities at early and late times

Figure 38 shows the mixing profiles and spectra at $t = 6$ ms in the left column and at $t = 7$ ms in the right column. Consider first the mole fraction profile at $t = 6$ ms just before reshock. The mole fraction profile $\langle X \rangle$ shows the distribution of mass, indicating the presence of the well-developed roll-up corresponding to the peak. To its right, the decrease in $\langle X \rangle$ corresponds to the bubble of the lighter air(acetone) rising into the heavier SF_6. The plot of $\langle X_p \rangle$ shows localized peaks, corresponding to the center of the roll-ups where mixing is most intense. The value of $\langle X_p \rangle$ decreases at the boundaries of the roll-up region. The profile of $X\left(\langle X_p \rangle\right)$ shows a first peak corresponding to the entire roll-up region and a second peak corresponding to the tip of the bubble. Finally, the mixing fraction ξ shows a central peak indicating that mixing is most intense at the center of the roll-ups. Additional peaks are observed at the tip of the spike and at the tip of the bubble, resulting from the rapid decrease of $X\left(\langle X_p \rangle\right)$ in those regions. The volume fraction profiles $\langle f_1 \rangle$ and $\langle f_2 \rangle$ show the relative volumetric distribution of the two fluids across the mixing layer. The molecular mixing fraction θ shows that the two fluids are mixed the most in the roll-up region. Finally, the fluctuating kinetic energy spectrum per unit volume $E(k,t)$ shows that most of the energy is contributed by the streamwise velocity component.

Consider the mole fraction profile at $t = 7$ ms shortly after reshock. The mass is more evenly distributed, as measured by the monotonic profile of $\langle X \rangle$. Note that the peak previously observed at $t = 6$ ms has disappeared as a result of the mass redistribution. Mixing is most

intense closer to the pure air(acetone), as measured by $\langle X_p \rangle$ and ξ. The decrease in $X_p(\langle X \rangle)$ close to the air(acetone) mixture indicates the presence of large, low-density regions. The volume fraction profile $\langle f_1 \rangle$ shows qualitatively similar behavior.

Figure 39 shows the mixing profiles and spectra at $t = 12$ ms in the left column and at $t = 18$ ms in the right column. Consider the mole fraction profile $\langle X \rangle$ at $t = 12$ ms, which shows a steadily increasing distribution of mass across the layer. This mass is well-mixed in the layer, as indicated by $\langle X_p \rangle$. However, large structures are present near the center of the layer, as indicated by the large values of $X_p(\langle X \rangle)$. The plot of ξ indicates a well-mixed region closer to the air(acetone). However, large, low-density regions are present as $X_p(\langle X \rangle)$ is very small, due to the very small amount of SF_6, as indicated by $\langle X \rangle$. Instead, a region with more mixing is observed closer to the center of the mixing layer. The quantities at $t = 18$ ms show increased homogeneous mixing as indicated by a: (1) monotonic distribution of mass captured by $\langle X \rangle$, and the volume fraction profiles $\langle f_1 \rangle$ and $\langle f_2 \rangle$; (2) distribution of $\langle X_p \rangle$ that does not exhibit large peaks, and; (3) value of $X_p(\langle X \rangle)$ exhibiting a nearly constant mean value. Further note that the fluctuating kinetic energy spectrum exhibits little change from $t = 12$ ms to $t = 18$ ms. The streamwise component continues to dominate the spanwise component by approximately an order of magnitude in the large and intermediate scales, and by approximately three orders of magnitude in the smallest scales.

The results presented here indicate that a quantitative characterization of the mixing process can be obtained by analyzing the profiles of different mixing quantities. In particular, the profiles of the mole and volume fractions $\langle X \rangle$, $\langle f_1 \rangle$, and $\langle f_2 \rangle$ indicate the relative distribution of mass in the layer; the reaction profile $\langle X_p \rangle$ shows how well the mass is mixed; the reaction profile $X_p(\langle X \rangle)$ indicates the presence of large, unmixed regions, and; the mixing fraction θ quantifies the relative mixing of regions in the layer. Thus, this analysis provides a quantitative basis for the qualitative description of the density evolution. The analysis of these plots at selected times during the mixing process shows that reshock compresses the layer and, as the inversion occurs, a well-mixed region develops close to the SF_6. At late times following reshock, mixing is characterized by the formation of large structures within a nearly uniform and well-mixed distribution of mass. The formation of large structures captured by increased values of $X_p(\langle X \rangle)$ is consistent with what is observed in the density plots and is consistent with two-dimensional turbulence phenomenology and the inverse cascade from small scales to larger scales.

4.5.2 Comparison of mixing quantities immediately before and after reshock

Comparisons of quantities at $t = t^- = 6.38$ ms immediately prior to reshock and at $t = t^+ = 6.68$ immediately following reshock are presented here. The mole fraction profiles are shown in Fig. 40. The x-axis was recentered and rescaled to provide an immediate comparison of the quantities. The following convention is adopted: quantities before and after reshock are shown in blue and red, respectively. The mole fraction profile $\langle X \rangle$ exhibits a complex structure resulting from the compression during reshock. The production quantity $\langle X_p \rangle$ increases during reshock, resulting in greater overall mixing. The largest peak in $\langle X_p \rangle$ located near the pure SF_6 is a consequence of the inversion, which flattens the tip of the bubble and also creates small-scale structures. The volume fractions, as well as the mixing fractions θ and ξ, are shown in Fig. 41. The volume fraction profiles $\langle f_1 \rangle$ and $\langle f_2 \rangle$ show a sharp change close to the pure SF_6 region resulting from the flattening of the bubble front. Note the strongly increased mixing, as measured by the mixing fractions θ and ξ following reshock.

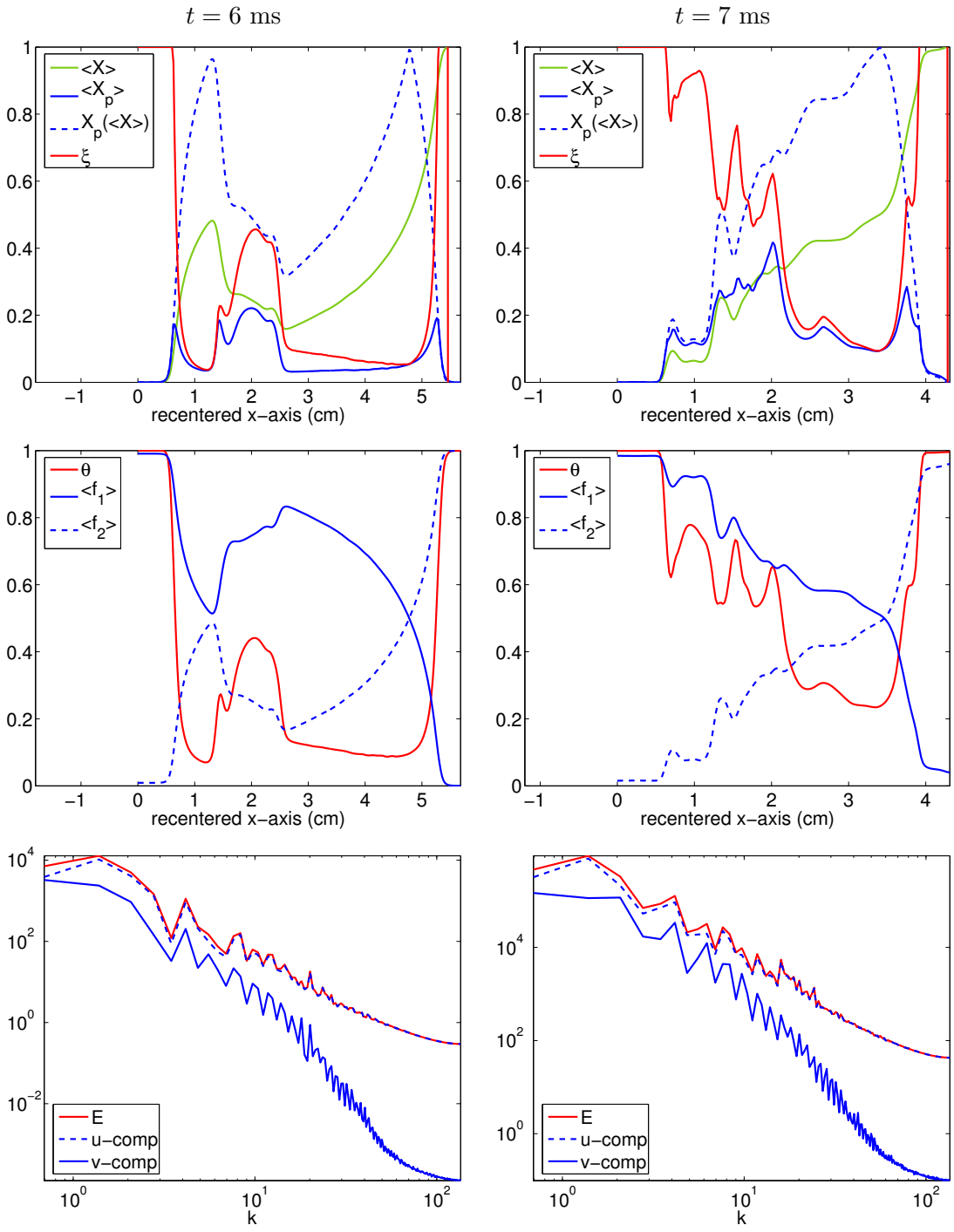

Figure 38: Profiles of $\langle X \rangle$, $\langle X_p \rangle$, $X_p(\langle X \rangle)$, ξ, $\langle f_1 \rangle$, $\langle f_2 \rangle$, θ, and the fluctuating kinetic energy spectrum $E(k,t)$ and its components at $t = 6$ ms (left column) and at $t = 7$ ms (right column).

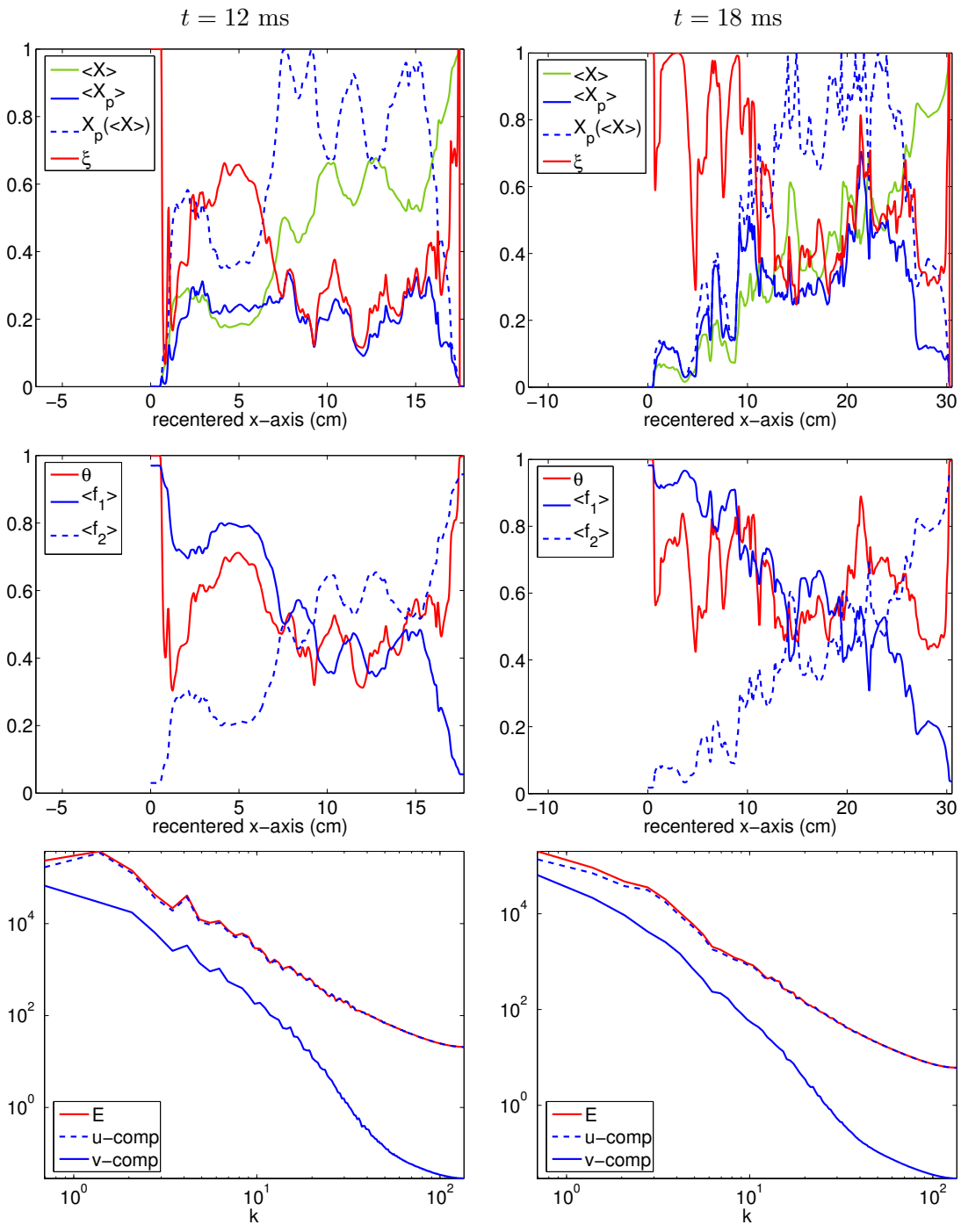

Figure 39: Profiles of $\langle X \rangle$, $\langle X_p \rangle$, $X_p(\langle X \rangle)$, ξ, $\langle f_1 \rangle$, $\langle f_2 \rangle$, θ, and the fluctuating kinetic energy spectrum $E(k,t)$ and its components at $t = 12$ ms (left column) and at $t = 18$ ms (right column).

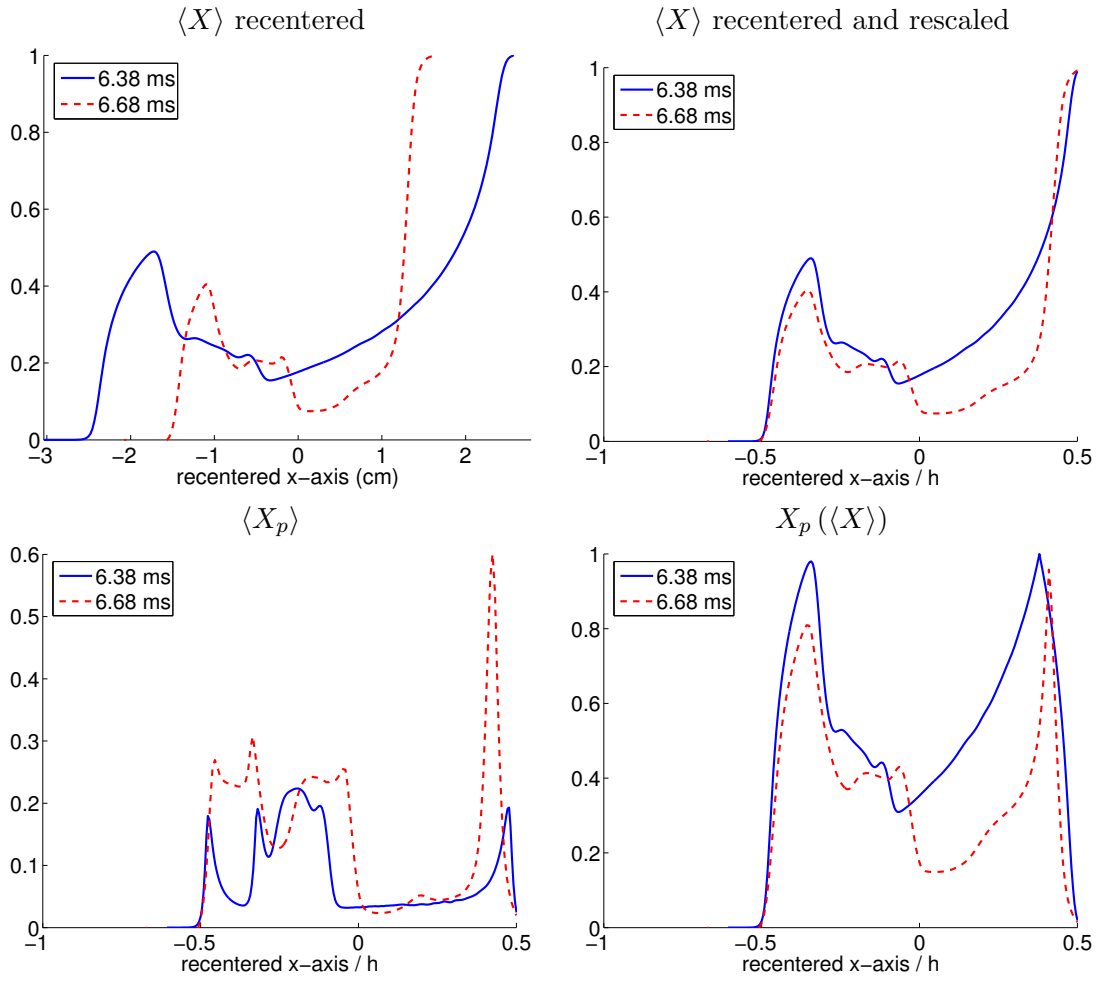

Figure 40: Comparison of $\langle X \rangle$, $\langle X_p \rangle$, and $X_p(\langle X \rangle)$ at $t^- = 6.38$ ms and at $t^+ = 6.68$ ms.

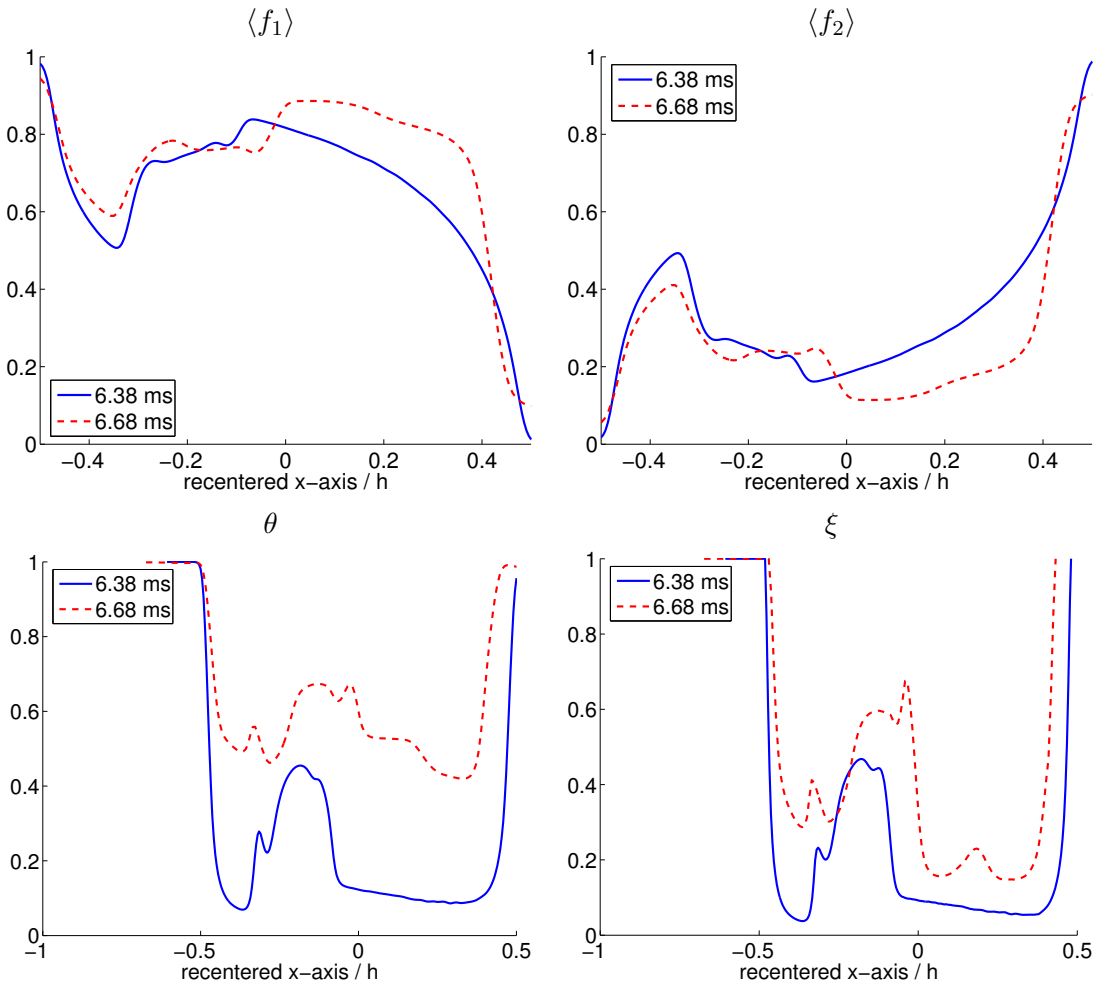

Figure 41: Comparison of $\langle f_1 \rangle$, $\langle f_2 \rangle$, θ, and ξ at $t^- = 6.38$ ms and at $t^+ = 6.68$ ms

The fluctuating kinetic energy spectrum shown in Fig. 42 sharply increases following reshock. The fluctuating enstrophy, and pressure variance spectra also show sharp increases following reshock. By contrast, the density variance spectrum increases only slightly following reshock.

Finally, Fig. 43 shows the ratio of spectral quantities after and before reshock to quantify the amplification in energy as a function of wavenumber k. The fluctuating kinetic energy spectrum $E(k,t)$ is amplified uniformly by a factor of ≈ 200 for large wavenumbers. The largest amplification occurs at the largest scales. For the remaining spectra, the largest amplification occurs in the intermediate scales. The fluctuating enstrophy spectrum $E_{\omega''\omega''}(k,t)$ is amplified differently in different wavenumber regions. The amplification is large for small wavenumbers, reaching a peak of ≈ 1300 near $k = 30$. The amplification reduces for large wavenumbers and oscillates about a value of ≈ 100. The density variance spectrum $E_{\rho'\rho'}(k,t)$ does not undergo significant amplification compared to the other spectra, and shows an average amplification of ≈ 2.5. By contrast, the pressure variance spectrum undergoes the most amplification, showing a peak of $\approx 6 \times 10^6$ for $k \approx 20$–25 before relaxing to $\approx 10^6$ at large wavenumbers.

The results presented here characterize the effects of reshock on the mixing layer, and quantify the energy deposition into the layer due to baroclinic production mechanisms. Reshock compresses the layer and shifts mass from the SF_6 side toward the air(acetone) side, consistent with the direction of reshock from the heavier SF_6 into the lighter air(acetone). Reshock further modifies the structures of mixing, generating a well-mixed region close to the SF_6 and peaks closer to the air(acetone). Reshock generates a very well-mixed, compressed region, as measured by the mixing fractions θ and ξ. The energy deposition by reshock can be quantified by the amplification of the energy spectra. The analysis shows that reshock amplifies (almost uniformly) the kinetic energy spectra by a factor of approximately 200 with slightly larger values for the lower modes. The enstrophy spectrum instead shows a larger amplification in the lower modes and decreasing amplification for higher modes, consistent with the formation of large-scale, vortical structures observed at late times following reshock. The pressure variance is amplified the most by reshock and uniformly across all scales. By contrast, the density variance is slightly amplified by reshock, indicating that it does not have a significant role in the dynamics of the mixing layer following reshock for the flow configuration considered here. This analysis shows that the pressure, kinetic energy, and enstrophy spectra are useful for the characterization of the modal distribution of energy within the mixing layer following reshock.

4.6 The effects of reflected waves: comparison of quantities computed from simulations using outflow and reflecting boundary conditions

Following reshock, the mixing layer undergoes further interactions with reflected waves from the end wall of the shock tube test section. The most significant reflected wave is the rarefaction wave formed during reshock. This wave interacts with the mixing layer at $t \approx 10$ ms. The interaction with the rarefaction wave causes the formation of a compression wave, which interacts with the mixing layer at $t \approx 15$ ms, as seen in $\langle v \rangle_{xy}$ and $\langle p \rangle_{xy}$ in Fig. 31.

In this section, the boundary condition at the right end of the computational domain (corresponding to the end wall of the test section) is varied from reflecting to outflow immediately following reshock. This change allows the reflected rarefaction wave created during reshock to exit the computational domain, so that no further interactions of waves with the mixing layer occur. The purpose of this study is to investigate the properties of mixing in the decay regime, as distinguished from those in the quasi-decay regime occurring when reflected waves inter-

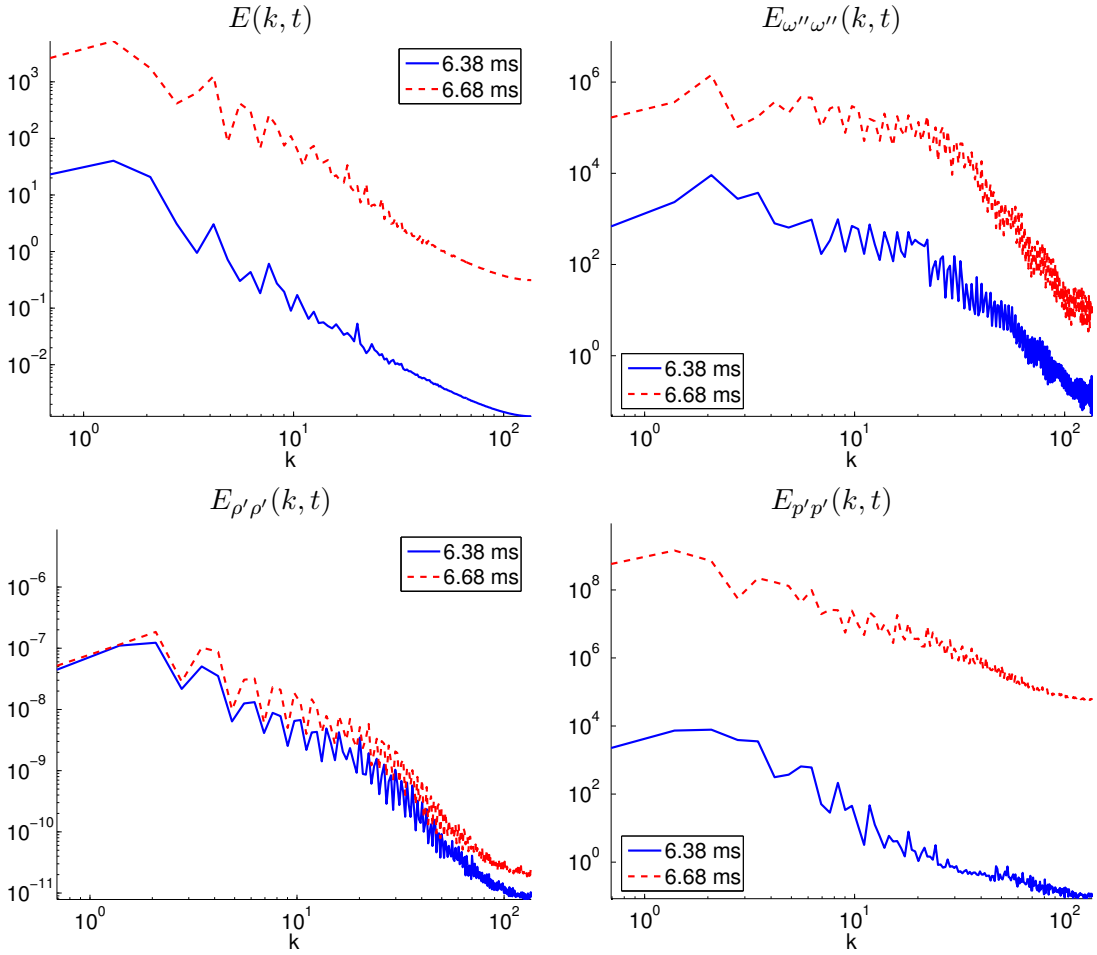

Figure 42: Comparison of the fluctuating kinetic energy spectrum $E(k,t)$, fluctuating enstrophy spectrum $E_{\omega''\omega''}(k,t)$, density variance spectrum $E_{\rho'\rho'}(k,t)$, and pressure variance spectrum $E_{p'p'}(k,t)$ at $t^- = 6.38$ ms and at $t^+ = 6.68$ ms.

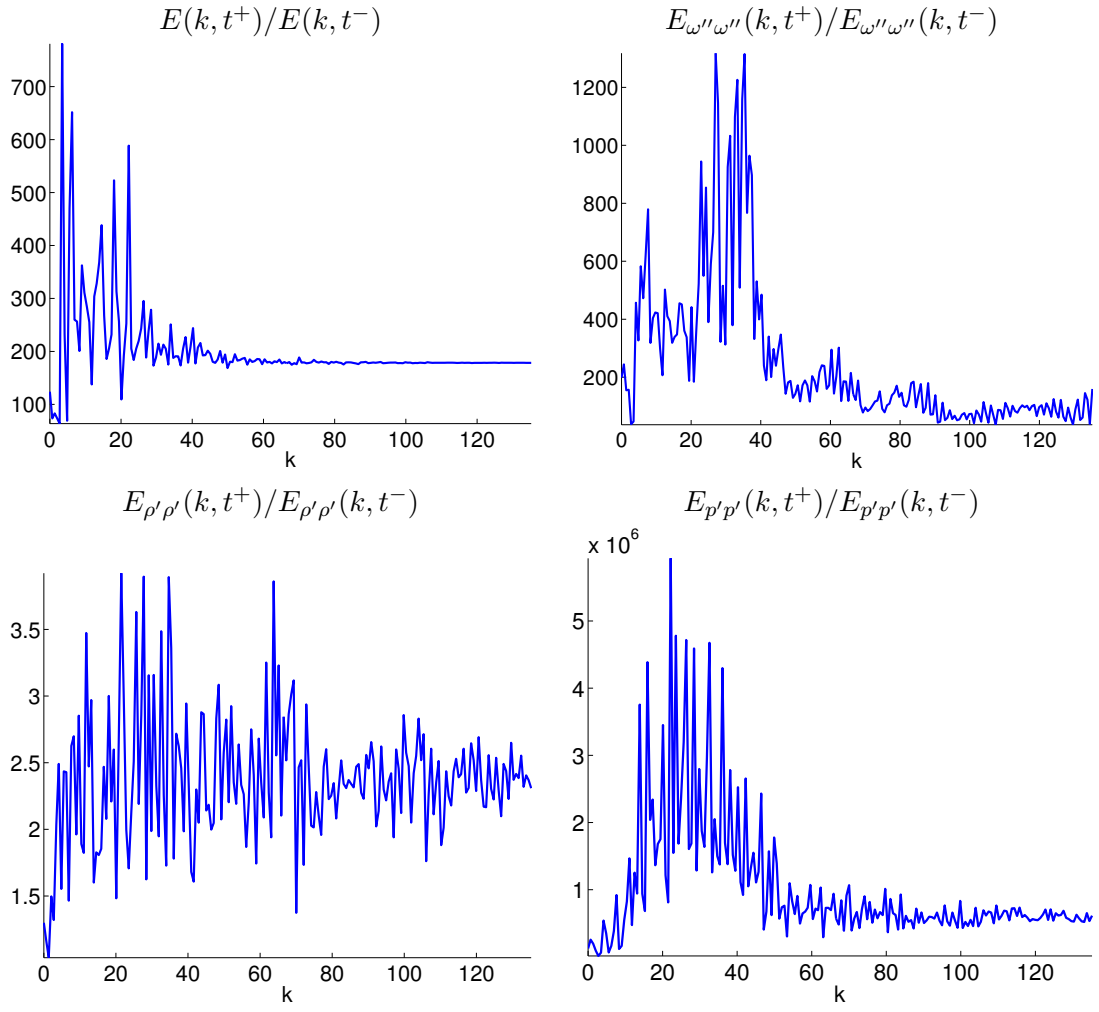

Figure 43: The ratio of fluctuating spectra $E(k,t)$, $E_{\omega''\omega''}(k,t)$, $E_{\rho'\rho'}(k,t)$, and $E_{p'p'}(k,t)$ before reshock at $t^- = 6.38$ ms and after reshock at $t^+ = 6.68$ ms.

act with the evolving interface following reshock. The following convention is adopted in this section. Results obtained when the reflected rarefaction wave exits the computational domain and does not interact with the mixing layer (corresponding to *outflow boundary conditions*) are shown in red, and results obtained when the reflected waves interact with the mixing layer (corresponding to *reflecting boundary conditions*) are shown in blue. The results overlap from the time of reshock $t = 6$ ms until $t \approx 10$ ms when the reflected rarefaction wave interacts with the mixing layer. In general, note that quantities computed with the outflow boundary condition are smoother compared to those computed with the reflecting boundary condition, due to the absence of wave interactions. Another objective of the present investigation is to understand the effects of a reflected rarefaction wave on the evolution of a mixing layer in the same spirit that the study of reshock investigates the effects of a shock wave on an evolving mixing layer.

4.6.1 The effects on the mixing layer width, mixing fractions, and profiles

The top row of Fig. 44 shows the time-evolution of the mixing layer width $h(t)$ and the lengthscale $W(t)$. The reflected rarefaction amplifies the growth rate of the mixing layer. Also shown in the plot of $h(t)$ are the predictions of the Mikaelian and the Brouillette-Sturtevant models for the reshocked interface growth. These quantities were previously shown in Fig. 23 for the case of reflecting boundary conditions. After $t = 11$ ms, the width corresponding to the outflow boundary condition has a considerably smaller growth rate than that corresponding to the reflecting boundary condition, showing that the reflected rarefaction wave amplifies the growth of the mixing layer. The growth of $W(t)$ qualitatively resembles that of $h(t)$.

The production and mixing fractions P_t, P_m, Ξ, and Θ are shown in the middle row of Fig. 44. Consider the time-evolution of P_t and P_m. The simulation with the outflow boundary condition yields a slightly larger value of P_t than with the reflecting boundary condition. The rarefaction wave increases the mixing layer width and therefore, the overall production fraction decreases when averaged over a larger mixing layer. Similarly, P_m corresponding to the outflow boundary condition is smaller than that corresponding to the reflecting boundary condition, as the amount of product is decreased. The additional reflected waves induce oscillations in P_t and P_m.

Consider the time-evolution of the mixing fractions $\Xi = P_t/P_m$ and Θ. For the outflow boundary condition, Ξ and Θ are larger than for the reflecting boundary condition, as the reflected rarefaction wave increases the mixing layer width and, thus, decreases the overall mixing as measured by these fractions.

The time-evolution of the volume-averaged streamwise and spanwise velocities $\langle u \rangle_{xy}$ and $\langle v \rangle_{xy}$, and pressure $\langle p \rangle_{xy}$ are shown in the bottom row of Fig. 44. As expected, $\langle u \rangle_{xy}$ does not approach zero at late times in the case of the outflow boundary condition, but remains at a nearly constant value following reshock. In both cases, $\langle v \rangle_{xy} = 0$. The volume-averaged pressure $\langle p \rangle_{xy}$ also remains at a nearly constant value following reshock.

The results presented here reveal the effects of a rarefaction wave interacting with an evolving mixing layer. It is observed that a reflected rarefaction wave causes the mixing layer to grow, consistent with the additional vorticity and energy deposition caused by the wave. The mixing, as measured by the integrated fractions Θ and Ξ, is reduced by a reflected rarefaction wave. In fact, the reflected rarefaction wave increases the width of the mixing layer resulting in smaller values of the mixing fractions.

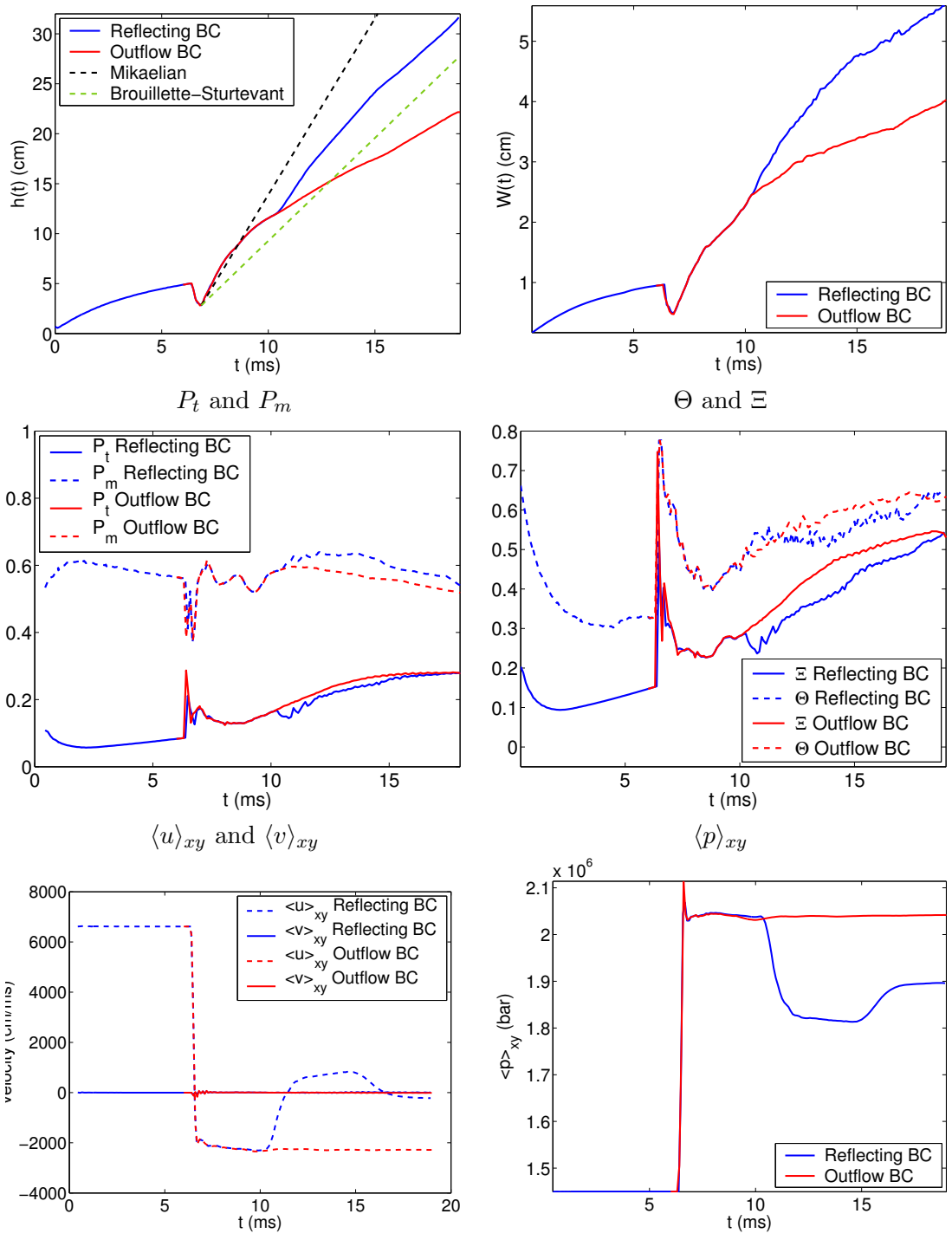

Figure 44: Time-evolution of the mixing layer widths $h(t)$ and $W(t)$, the production fractions P_t and P_m, mixing fractions θ and ξ, and volume-averaged velocities $\langle u \rangle_{xy}$, $\langle v \rangle_{xy}$ and pressure $\langle p \rangle_{xy}$ for reflecting and outflow boundary conditions.

4.6.2 The effects on statistics

A comparison of the evolution of statistics for reflecting and outflow boundary conditions is shown in Fig. 45. Consider the fluctuating kinetic energy per unit mass $E(t)$ and its components $E_{u''u''}(t)$ and $E_{v''v''}(t)$. In the case of the outflow boundary condition, the energy is not increased by the reflected waves, and therefore decays. The reflected rarefaction wave also increases the energy in the spanwise component, contributing to the statistical isotropization of the flow. This is not observed in the case of the outflow boundary condition, in which both components retain their separation.

Consider the evolution of the fluctuating enstrophy $E_{\omega''\omega''}(t)$. The enstrophy for the case of reflecting and outflow boundary conditions is very similar, indicating that the reflected waves do not increase the enstrophy significantly.

The behavior of the density variance $E_{\rho'\rho'}(t)$ is unusual. Note that $E_{\rho'\rho'}(t)$ corresponding to the outflow boundary condition is greater than $E_{\rho'\rho'}(t)$ corresponding to the reflecting boundary condition, indicating that the reflected rarefaction wave decreases the density fluctuations.

The behavior of the pressure variance $E_{p'p'}(t)$ indicates that the pressure fluctuations are nearly constant in the absence of reflected waves. By contrast, the fluctuations corresponding to the reflecting boundary condition undergo a sudden transient increase following the interaction with reflected waves, and approach the nearly constant value corresponding to the outflow boundary condition shortly thereafter.

The results above characterize the effects of the reflected rarefaction wave on the mixing layer. The reflected rarefaction wave, while not significantly increasing the energy content in the layer, plays an important role in achieving statistical isotropy by exciting fluctuations in the periodic direction. The results also indicate that the reflected rarefaction wave has a small impact on the enstrophy and the pressure variance evolution. By contrast, reshock causes a compression of the layer and a significant deposition of energy that allows the layer to grow very rapidly with the formation of complex structures. The reflected rarefaction wave instead "stretches" the mixing layer, causing it to grow, but provides little additional energy causing the overall mixing to decrease, as measured by the mixing fractions. The additional mixing provided by the reflected waves is responsible for the statistical isotropy observed earlier.

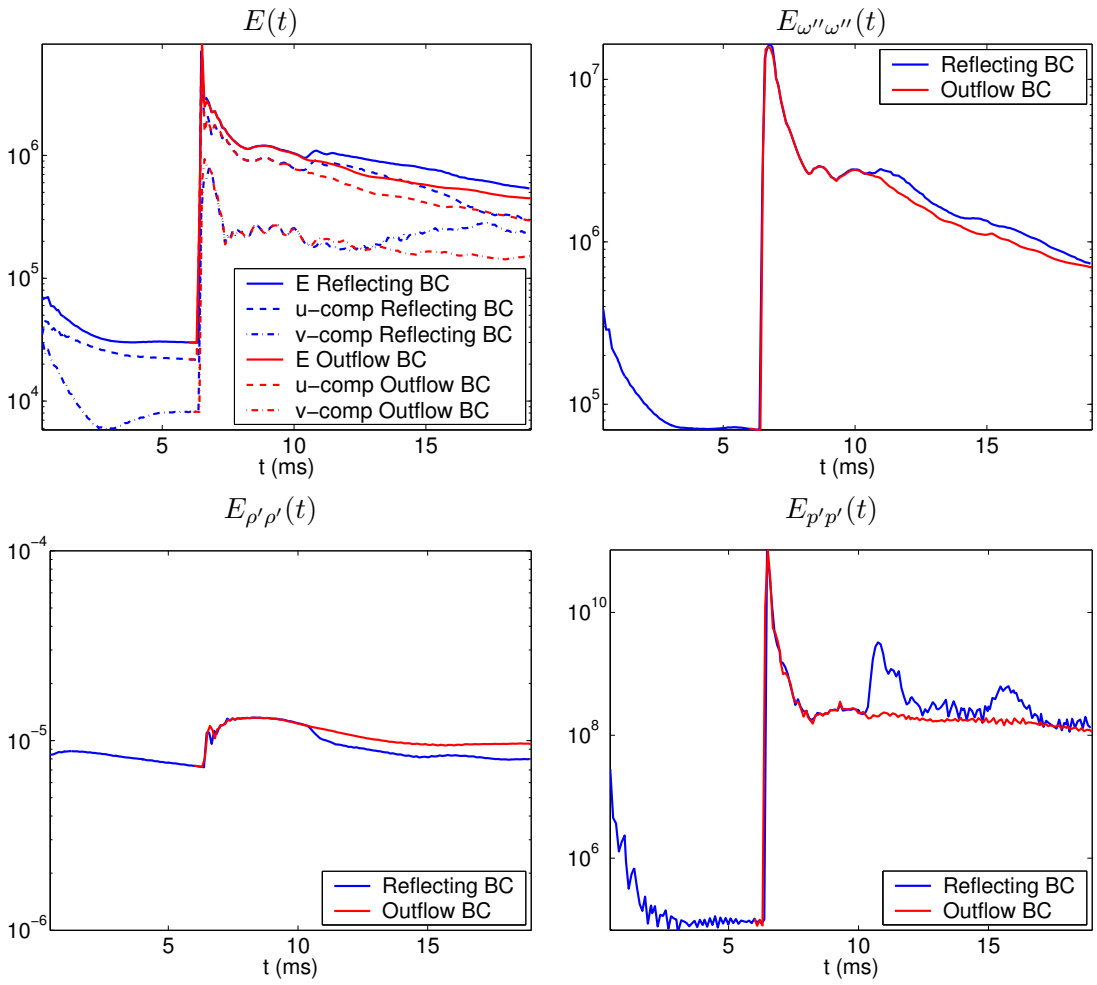

Figure 45: Time-evolution of the fluctuating kinetic energy $E(t)$ and its components, the fluctuating enstrophy $E_{\omega''\omega''}(t)$, density variance $E_{\rho'\rho'}(t)$, and pressure variance $E_{p'p'}(t)$ for outflow and reflecting boundary conditions.

5 The effects of spatial resolution and order of spatial reconstruction on mixing properties, circulation, spectra, and statistics

The effects of the spatial (grid) resolution and order of spatial reconstruction on the mixing quantities are self-consistently and quantitatively investigated in this section. Third-, fifth-, and ninth-order reconstructions are considered, together with grid resolutions of 128, 256, and 512 points per initial perturbation wavelength λ. The objective of this study is to determine the sensitivity of mixing quantities to the order of reconstruction (formal, or design, order of accuracy in sufficiently smooth flow regions) and to the spatial resolution. Most simulation studies involving the solution of the Euler equations have focused on the numerical 'convergence' of some small set of quantities (or a quantity) (*e.g.*, perturbation amplitude or mixing layer width in Rayleigh-Taylor [120, 44, 32] and Richtmyer-Meshkov instability [49, 48, 28]) over a limited range of time with respect to increasing spatial resolution. The comparison of quantities obtained using different orders of reconstruction and grid resolution in the present work is conducted in the spirit of the investigation of Shi, Zhang and Shu [114], who considered double Mach reflection and Rayleigh-Taylor instability in two dimensions using the fifth- and ninth-order WENO method. Their investigation emphasized the computational advantage of higher-order WENO schemes over lower-order WENO schemes for complex flows mainly using qualitative (visual) comparisons. The present investigation is both quantitative and qualitative, and examines to what extent different orders of WENO reconstruction and different spatial resolutions capture specific physical quantities characterizing Richtmyer-Meshkov instability-induced mixing. The investigation is applied to all of the quantities considered in the previous section, including mole fractions, mixing fractions, energy spectra, and statistics. To our knowledge, *this is the first systematic investigation of profiles, spectra, and statistics as a function of both spatial resolution and order of reconstruction* in the case of the Richtmyer-Meshkov instability. The `HOPE` code is ideal for such an investigation, as it is possible to perform numerical simulations identical in every other respect except the order of reconstruction: this allows a self-consistent study that is distinct from utilizing *different numerical methods* with different formal orders of spatial and temporal accuracy (see [30] where the results from a second-order centered essentially non-oscillatory (CENO) method, a second-order Godunov method, and a spectral/compact finite-difference method applied to the two-dimensional Richtmyer-Meshkov instability are compared).

The present study constitutes *the first systematic investigation of the effects of the order of flux reconstruction and grid resolution on the Richtmyer-Meshkov instability evolution.* The results were obtained for a two-dimensional Euler flow, so that the differences in the evolution depend solely on the numerical dissipation of the method and not on a physical dissipation or vortex stretching in three-dimensional simulations. In Part 4 of this report [70], three-dimensional simulations are performed using the fifth-, ninth-, and eleventh-order WENO method, and a systematic investigation of two- and three-dimensional effects is presented.

The following conventions are adopted in the presentation of the results in this section. Quantities obtained using third-, fifth-, and ninth-order WENO reconstruction are shown in green, red, and dark blue, respectively; different line styles are used to present results with varying grid resolution. The simulations obtained with an initial resolution of 512, 256, and 128 points per initial perturbation wavelength are denoted as *fine*, *medium*, and *coarse* grid, respectively, and are presented using a solid line, dashed line, and dash-dot line, respectively.

The results presented in § 4 were obtained using the medium resolution grid and fifth-order reconstruction: this choice was based on the fact that the fifth-order WENO method has been used by a large number of investigators, while the ninth-order WENO method is relatively new [14].

This section is organized as follows. First, details of the numerical simulations are presented in § 5.1. The results for the mixing layer width are presented in § 5.2, followed by the results for the time-evolution of local mixing quantities and mixing fractions in § 5.4 and § 5.5, respectively. The results for spectra and statistics are presented in § 5.6 and § 5.7, respectively. Finally, the time-evolution of the density and vorticity fields is shown at intervals of 1 ms in § 5.8 to provide qualitative comparisons.

5.1 Grid resolutions and orders of reconstruction

Numerical simulations were performed using uniform grid resolutions with $\Delta x = \Delta y$. The grids were chosen so that points of the medium grid corresponded with every other point of the fine grid. Similarly, the coarse grid was chosen so that its points would correspond to every other point of the medium grid and with every four points of the fine grid.

To define the grids, first chose the grid spacings

$$\begin{aligned} \Delta x &= \Delta y \\ &= \frac{\lambda}{N}, \end{aligned} \tag{265}$$

rounding to a rational number divisible by four, yielding $(\Delta x)_{fine} = 0.01158984375$ cm (slightly larger than the theoretical value $\Delta x = \lambda/512 = 0.01158854167$ cm). This choice corresponds to 768 points in the domain with $L_y = 8.9$ cm. Similarly, $(\Delta x)_{medium} = 0.0231796875$ cm with $N = 384$, and $(\Delta x)_{coarse} = 0.046359375$ cm with $N = 192$. To align the grids, the starting and ending points of the computational domain were adjusted to account for the distribution of points by the numerical method. In the y-direction, the first and second grid points are at locations $y_1 = -\Delta x/2$ and $y_2 = \Delta x/2$. For this reason, if the starting location is chosen to be at $y = 0$ for all grids, then the grids would not be aligned. Thus, choose $y = 0$ for the fine grid, corresponding to the first two grid points at $y_1 = -(\Delta x)_{fine}/2$ and $y_2 = (\Delta x)_{fine}/2$. For the medium grid, shift by $(\Delta x)_{fine}/2$ to the left so that the position of the first two points are at $y_1 = -3(\Delta x)_{fine}/2$ and $y_2 = (\Delta x)_{fine}/2$. For the coarse grid, shift by $3(\Delta x)_{fine}/2$, yielding $y_1 = -5(\Delta x)_{fine}/2$ and $y_2 = (\Delta x)_{fine}/2$. In all three cases, the points at y_2 coincide. A similar procedure is followed for the x-direction. The actual values for the number of grid points in the y-direction and for the length of the domain L_y used in the simulations were double the values described above, as the symmetry option in the `HOPE` code was activated (see [68]). The grid resolutions are summarized in Table 3.

5.2 The effects on the mixing layer width

Shown in Fig. 46 is a comparison of the dependence of the mixing layer width on the grid resolution and on the order of the WENO reconstruction up to $t = 18$ ms. Also shown in Fig. 46 is the ratio of the widths with respect to the width measured for the ninth-order simulation on the fine grid. Prior to reshock, the mixing layer width is weakly-dependent on the resolution and on the order of reconstruction, with all simulations giving very similar results. This is due to the fact that the flow is dominated by a single, large-scale evolving bubble (or spike),

	Fine grid	Medium grid	Coarse grid
N per λ	512	256	128
Δx (cm)	0.01159	0.02318	0.04636
N_y	1536	768	384
L_y (cm)	$[0, 17.8]$	$[-0.00579, 17.79621]$	$[-0.01739, 17.78462]$
N_x (initial)	801	401	201
L_x (cm) (initial)	$[0, 9.271875]$	$[-0.00579, 9.26608]$	$[-0.01739, 9.25449]$

Table 3: The initial grid resolutions used in the numerical simulations. The choice of starting and ending points ensures that all of the grids are aligned with one another.

the front of which is not significantly affected by dissipation. However, following reshock, the dependence on both order and resolution becomes significant. In particular, decreasing the order of the WENO reconstruction, as well as decreasing the grid resolution, results in smaller mixing layer widths. Note that the differences are further amplified by the arrival of the reflected rarefaction wave at $t \approx 10$ ms and further increase later. These differences can be understood as follows. Lower order of reconstruction and coarser grids correspond to higher numerical diffusion. Increased numerical diffusion damps the velocity fluctuations and in particular, the streamwise fluctuations associated with the growth of the mixing layer. Therefore, increased numerical diffusion is consistent with smaller mixing layer widths. In addition, the formation of small-scale structures is also inhibited, resulting in smaller baroclinic circulation deposition during a wave-interface interaction compared to a high-resolution, high-order simulation exhibiting small-scale structures. As a result, the mixing layer width is further decreased. This mechanism is clearly illustrated in § 5.8 where a comparison of the flow features before and after reshock is presented.

Consider the flow evolution following reshock, but prior to the arrival of the reflected rarefaction wave during the time interval $t \in [6.5, 10.5]$ ms. The mixing layer widths become closer as the grid resolution doubles and the order of reconstruction increases. At late times, the widths from the third-order simulations differ by ≈ 5 cm as the grid is refined. By contrast the widths obtained from the fifth- and ninth-order simulations differ by ≈ 1 cm as the grid is refined. The plot of the ratio of the widths show evidence of 'convergence' as the value approaches unity for the ninth-order simulations.

The flow at late times after $t = 15$ ms shows jumps and oscillations as the cutoff value used to determine the mixing layer width is approached. In fact, high-resolution, high-order simulations show significant fragmentation of the mixing layer, resulting in the creation of small structures that may or may not cross the cutoff value used to determine the layer width. These issues persist even as the cutoff value is decreased or increased. One approach to address this issue is to use the lengthscale W obtained from integrating the product of the volume fractions. However, it is not clear how W is related to the mixing layer width h, although they have similar qualitative behavior.

Consider a comparison of the mixing layer amplitude obtained using third-, fifth-, and ninth-order spatial reconstruction on the fine, medium, and coarse grids with the experimental data and with the predictions of the Zhang-Sohn Padé, Vandenboomgaerde Padé, Matsuoka et al. Padé, and Sadot models. Note that the model parameters are computed using the results from shock refraction theory and the parameters of the simulation, i.e., the parameters are the same as those used in § 3.3.7.

The normalized mixing layer amplitude for simulations performed on the coarse, medium, and fine grid (when third-order reconstruction is used) are compared in Fig. 47 to the experimental data and to the predictions of the nonlinear models. First note that the coarse grid simulation shows a large initial discrepancy and a growth that proceeds in steps. This behavior can be explained by considering that the coarse grid has separation $\Delta x = \Delta y = 0.046$ as reported in Table 3. This, in conjunction with the initial diffusive interface (which spreads the interface across additional grid points), contributes to the large initial discrepancy. The growth in steps can also be explained in terms of the large grid separation. The plots show that later into the nonlinear regime the mixing layer amplitude is very similar across all simulations. This is consistent with the observation made earlier regarding the weak dependence of the mixing layer width on the order of reconstruction and on the grid resolution for times prior to the arrival of the reflected rarefaction wave. In all cases, the results of the numerical simulations lie between the experimental data points and are very close to the predictions of the nonlinear Zhang-Sohn Padé model. The Vandenboomgaerde model is the next closest model, with the Sadot model overestimating the data. This observation is further confirmed by considering the ratios of the amplitudes, which show that the predictions of the Zhang-Sohn models are within 2-3% of the mixing layer amplitude obtained from the numerical simulations.

Figure 48 shows the comparisons when fifth-order spatial reconstruction is used. The plot on the coarse grid also shows an initial discrepancy, but not as severe as observed for the third-order simulation on the coarse grid. Note that the growth also proceeds in steps. The comparison to experimental data in the nonlinear regime shows that the mixing layer amplitude lies between the experimental points for the medium and coarse grid simulation, and slightly below the experimental data for the fine grid simulation. The comparison to the predictions of the nonlinear Padé models shows that the Zhang-Sohn model is in best agreement with the data. The predictions from the Vandenboomgaerde model give the next best agreement, and the predictions of the Sadot model give the least agreement. The plots of the ratios support this conclusion.

Figure 49 shows the comparisons when ninth-order spatial reconstruction is used. The plot on the coarse grid no longer shows the discrepancy at early times, but still shows the step-like growth behavior. The data from the simulations now lies very close to the experimental points as in the case of the coarse grid simulation, or slightly below the experimental data as in the case of the medium and fine grid simulations. The Zhang-Sohn Padé model shows the best agreement with the data.

The results above show that the mixing layer width and amplitude exhibit little dependence on the order of reconstruction and on the grid resolution prior to reshock. However, following reshock but prior to the arrival of the reflected rarefaction wave, large differences are observed. As the order of reconstruction and grid resolution are increased, the differences between the mixing layer widths and amplitudes decrease, providing putative evidence of 'convergence'. Following the arrival of the reflected rarefaction wave, the differences increase further. Finally, at late times, high-order, high-resolution simulations display significant fragmentation of the complex structures, causing oscillations in the amplitude as the cutoff limit used in the determination of the amplitude is reached. The differences in the widths and amplitudes observed following reshock can be attributed to the effects of numerical dissipation, which prevents the formation of small-scale structures in low-resolution, low-order simulations. Small structures do not have a direct effect on the width or amplitude prior to reshock. However, the energy deposited into the layer by the reshock process is directly related to the presence of small-scale structures, which explains the differences in the widths and amplitudes, as less energy is de-

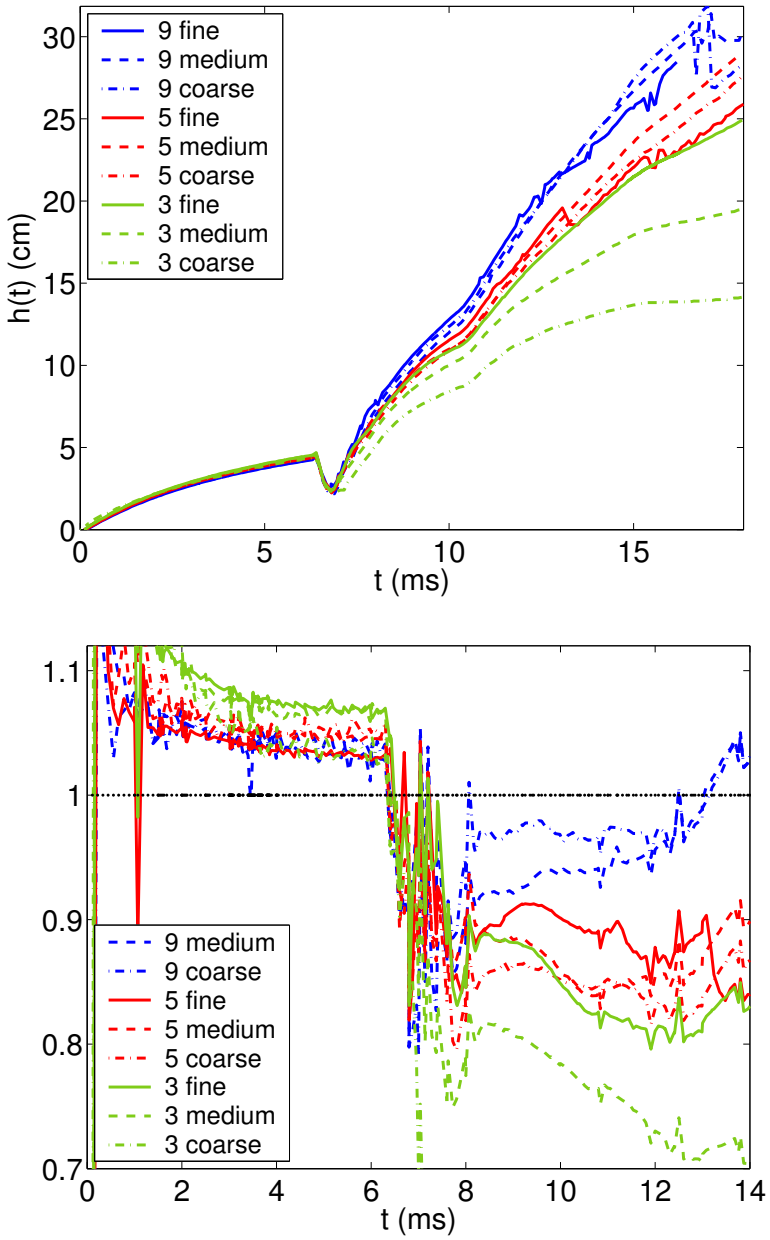

Figure 46: The effects of grid resolution and order of reconstruction on the mixing layer width (top). For times prior to reshock, a weak dependence on the resolution and order is observed. For times following reshock, a stronger dependence is observed, with lower-order reconstructions and coarser grids resulting in smaller post-reshock widths. This is due to the increased numerical dissipation associated with lower-order reconstruction and coarser grids. The ratios of the mixing layer width with respect to the ninth-order simulation on the fine grid are also shown (bottom). Following reshock, the ratios corresponding to the ninth-order simulations on the medium and coarse grids are bounded between ≈ 0.95–1.05 for $t > 10$ ms, providing evidence for 'convergence'. The mixing layer widths obtained from the fifth- and third-order simulations show no 'convergence', even at late times following reshock.

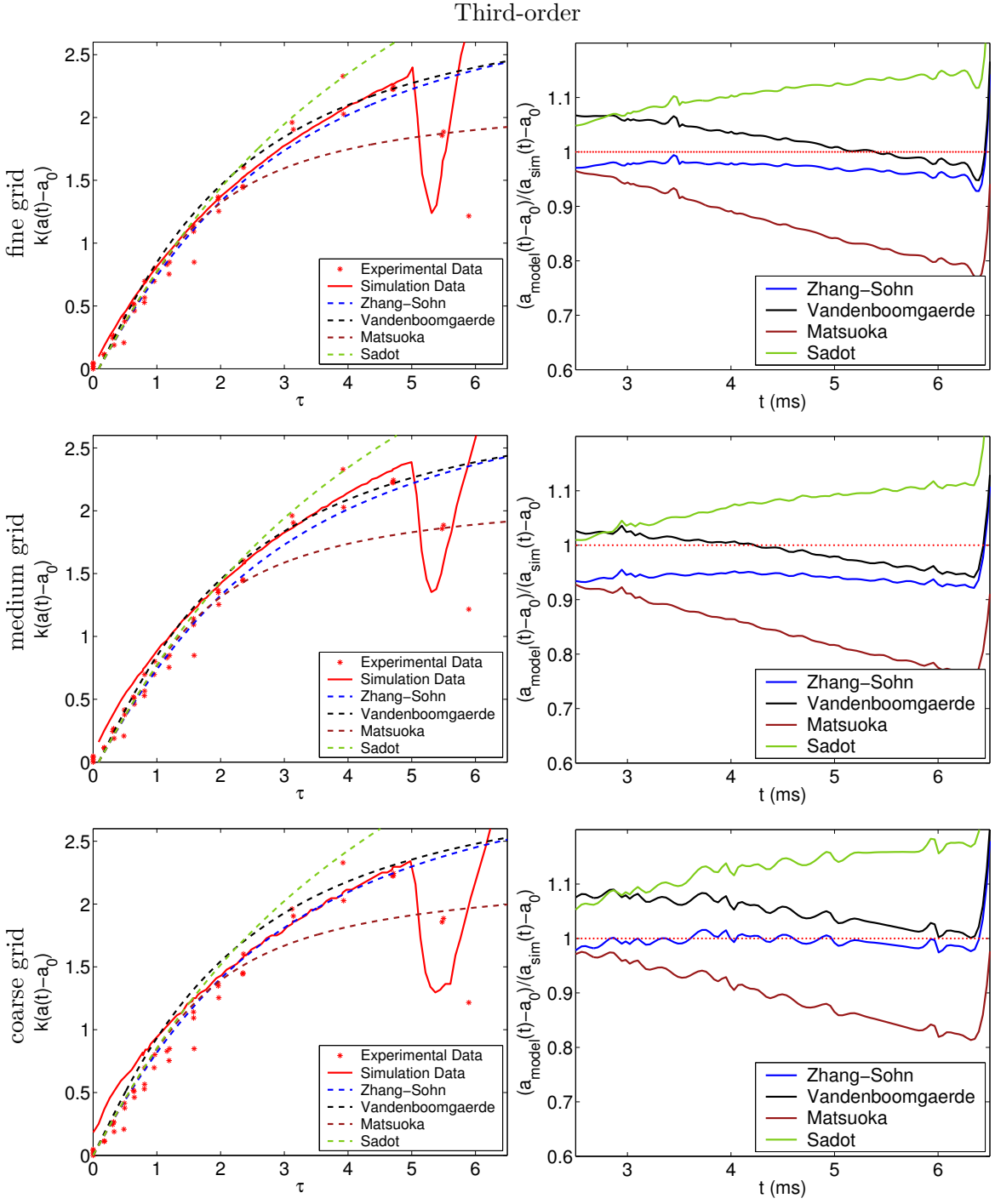

Figure 47: Comparison of the normalized mixing layer amplitude obtained using third-order spatial reconstruction on the fine, medium, and coarse grids to the experimental data and with the predictions of the Zhang-Sohn Padé, Vandenboomgaerde Padé, Matsuoka et al. Padé, and Sadot models (left column). The ratios of the model predictions to the numerical data are also shown (right column).

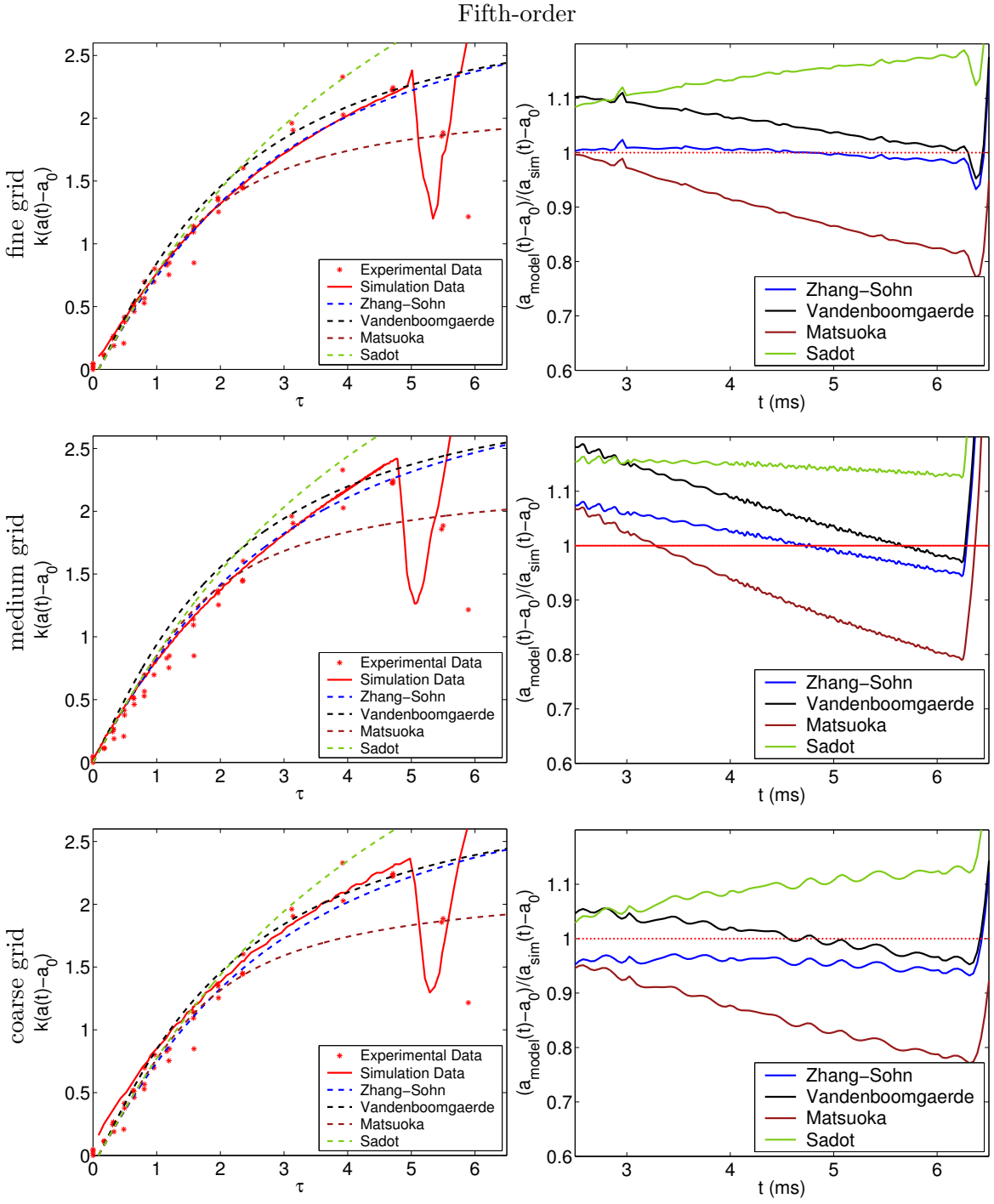

Figure 48: Comparison of the normalized mixing layer amplitude obtained using fifth-order spatial reconstruction on the fine, medium, and coarse grids with the experimental data and to the predictions of the Zhang-Sohn Padé, Vandenboomgaerde Padé, Matsuoka et al. Padé, and Sadot models (left column). The ratios of the model predictions to the numerical data are also shown (right column).

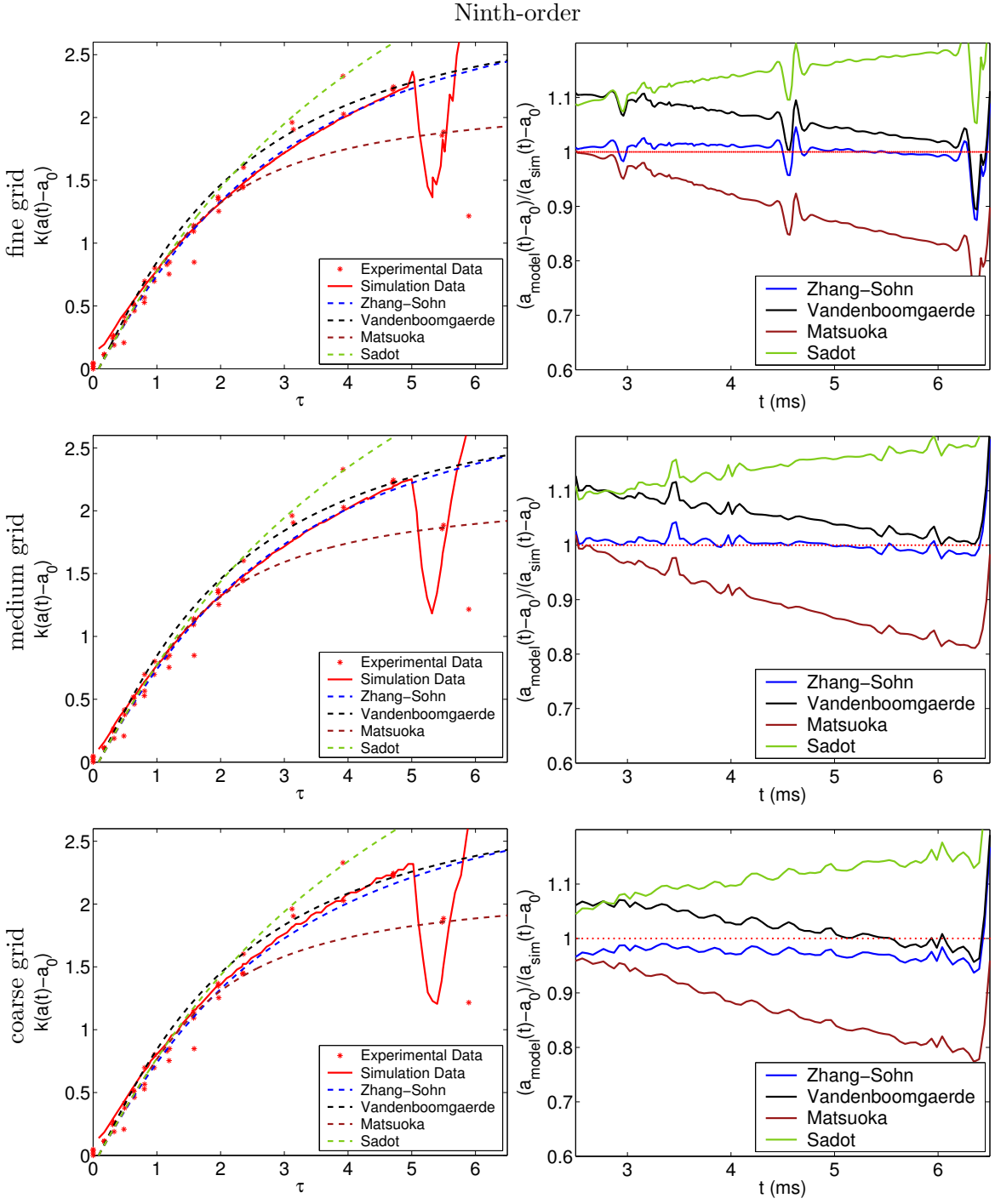

Figure 49: Comparison of the normalized mixing layer amplitude obtained using ninth-order spatial reconstruction on the fine, medium, and coarse grids with the experimental data and to the predictions of the Zhang-Sohn Padé, Vandenboomgaerde Padé, Matsuoka et al. Padé, and Sadot models (left column). The ratios of the model predictions to the numerical data are also shown (right column).

posited in low-order, low-resolution simulations. This analysis is revisited later in this report where the energy deposition at reshock is investigated.

5.3 The effects on the circulation

Presented in this section is an investigation of the effects of order of reconstruction and of grid resolution on the evolution of the circulation (corresponding to the deposition of vorticity on the interface). Figure 50 shows the effects on the negative Γ^- and positive Γ^+ circulation with closeups before and after reshock. Before reshock, the circulation obtained from all of the simulations is qualitatively similar. Note that the circulations of low-resolution, low-order simulations are smaller. This is consistent with the higher numerical dissipation of low-resolution, low-order simulations. Following reshock, the results are qualitatively similar until the arrival of the reflected rarefaction wave at $t = 10$ ms. After the arrival of the reflected rarefaction, the symmetry of the simulations breaks, resulting in significantly different values for the positive and negative circulation. No clear correlation between the computed values and the order of reconstruction or grid resolution is apparent. However, a clear correlation emerges if the total circulation $\Gamma = \Gamma^+ + \Gamma^-$ is considered, as shown in Fig. 51. The plot shows that the values of the total circulation for simulations with the same resolution but different orders of reconstruction are very similar. In particular, the circulations from simulations with the coarsest resolutions are closest to zero and also apparently grow linearly. The circulations from the simulations with the finest resolution are farthest from zero and also appear to grow linearly. Note that the total circulation does not appear to be affected by the reshock or the arrival of the reflected rarefaction wave.

The results above indicate that the circulation Γ is affected in the following way by the grid resolution and order of flux reconstruction. Prior to reshock, low-order, low-resolution simulations give smaller values (in magnitude) of the positive and negative circulation, consistent with an increased numerical dissipation in these simulations. However, following reshock, but prior to the arrival of the reflected rarefaction wave, no direct connection can be established between the magnitudes of the negative and positive circulations and the grid resolution and order of flux reconstruction. This indicates that additional mechanisms influence the magnitude of the circulation following reshock. Finally, following the arrival of the reflected rarefaction wave, symmetry breaks and the magnitudes of the positive and negative circulations become very different, as expected. However, if the positive and negative circulations are summed, the resulting total circulation shows a linear growth in time that is strongly dependent on the grid resolution of the simulation. The total circulation increases more rapidly for simulations with higher resolution, and the total circulation is independent of the order of flux reconstruction.

5.4 The effects on the mixing profiles

An analysis of the effects of grid refinement and order of reconstruction on quantities representative of local mixing are presented in this section. The comparisons are conducted at time $t = 6$ ms immediately before reshock, at $t = 7$ ms immediately after reshock, at $t = 12$ ms late after reshock, and at $t = 18$ ms at very late time following reshock as in § 4.5.

Figure 52 shows comparisons of the mole fraction profile $\langle X \rangle$ at the selected times. At $t = 6$ ms, there is generally good agreement for sufficiently high order and resolution. The results corresponding to third-order reconstruction at medium resolution are closer to the results corresponding to fifth-order reconstruction at coarse resolution. Similar behavior is observed for times immediately following reshock at $t = 7$ ms, with results in generally good agreement

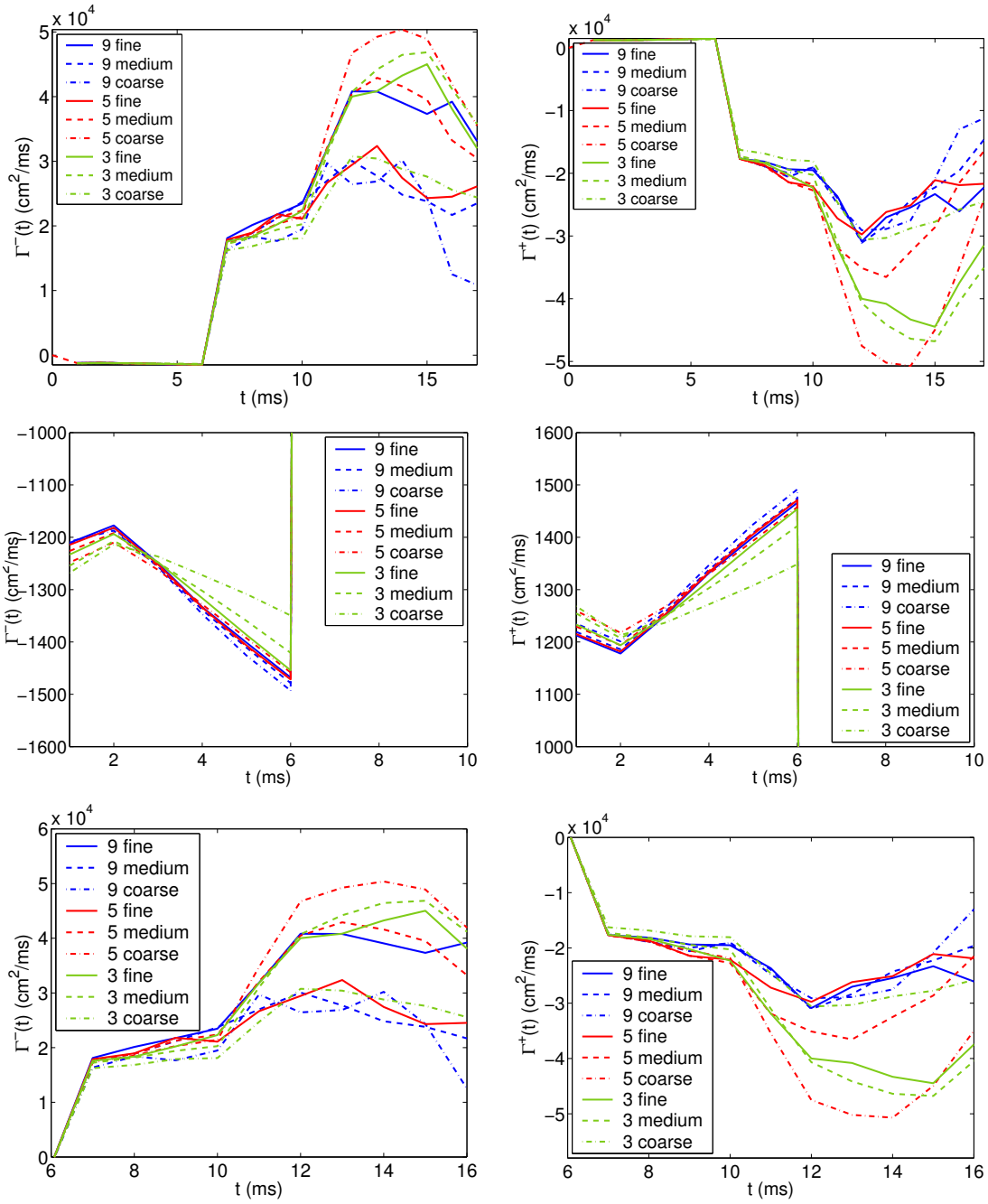

Figure 50: The effects of grid resolution on the negative circulation Γ^- (left column) and on the positive circulation Γ^+ (right column) with closeups before reshock (middle row) and after reshock (bottom row).

as the resolution and the order are increased. At $t = 12$ ms, the results begin to diverge, indicating that differences between the small-scale features are more pronounced, which are captured by the mole fraction. This behavior is also observed when considering the late-time behavior at $t = 18$ ms.

Figure 53 shows comparisons of the product mole fraction profile $\langle X_p \rangle$. This quantity is extremely sensitive to both the order and resolution for all times. Note that the spikes at the beginning and end (corresponding to the top of the bubble and bottom of the spike) are not captured equally between the methods, due to the different amounts of numerical dissipation that result in a larger or smaller well-mixed, diffusion layer. Consider time $t = 6$ ms before reshock and note that the larger values closer to the middle of the layer (corresponding to the roll-ups) appear different between the orders and resolutions, with no apparent agreement. This is due to the different structure of the roll-ups observed across the different orders and resolutions, as shown in § 5.8. As the order is increased and the grid points are doubled, additional spiral roll-ups appear, causing the product mole fraction to oscillate for high orders of reconstruction. At $t = 7$ ms, the product mole fraction obtained with increasing order of reconstruction and grid resolution exhibits differences across the entire mixing layer: these differences are further amplified for later times. Note that the results obtained using the third-order WENO method at coarse resolution are in very poor agreement with all of the other results. Again, this is due to the very large numerical dissipation present in low-order WENO reconstructions, and the different small-scale flow features that is further amplified following interactions with reflected waves.

Figure 54 shows the product mole fraction profile $X_p(\langle X \rangle)$. At $t = 6$ ms (before reshock), the profiles are in close agreement as the resolution and order of reconstruction are increased. This agreement persists at $t = 7$ ms immediately after reshock, but the agreement decreases at later times. The reason for this difference is that $X_p(\langle X \rangle)$ is most sensitive to the small-scale flow features. The differences in small-scale features are not captured by $X_p(\langle X \rangle)$ until long after reshock. Therefore, as the order is increased and the resolution is doubled, additional small-scale features with a different spatial distribution are observed at late times, causing $X_p(\langle X \rangle)$ to exhibit large variations.

Finally, Figs. 55 and 56 show the molecular mixing fractions θ and ξ, respectively. The molecular mixing fraction θ is very sensitive to the order and resolution at all times. Consider θ at $t = 6$ ms. No clear agreement is observed, with the smallest and largest values obtained from the ninth- and fifth-order simulations on the fine grid, respectively, indicating that θ is highly sensitive to the order and resolution. Note that ξ at $t = 6$ ms shows agreement as the order and resolution are increased, indicating that ξ is more robust than θ. Similar observations apply at $t = 7$ ms. At late times, the mixing fractions are very sensitive to the structure of the flow resulting from the differences in order and grid resolution. The high-amplitude oscillations in θ and ξ observed at late times indicate that the structures become more fragmented as the resolution and order are increased.

The above results indicate that the mixing parameters exhibit different levels of sensitivity to the grid resolution and to the order of reconstruction. Before reshock and immediately after reshock, flow structures agree to a large extent, with peaks of similar shape and structures at similar locations within the mixing layer. However, for intermediate and late times following reshock, the development of mixing is significantly affected by the order of reconstruction and grid resolution. Peaks now appear in different locations and have different shapes. In general, the high-order, high-resolution simulations exhibit the most structures, with more pronounced and localized peaks. By contrast, low-resolution, low-order simulations have fewer peaks that

are spread over a larger portion of the mixing layer. This observation can again be explained in terms of varying numerical diffusion. Simulations with low-order and low-resolution have larger numerical dissipation, which results in more complete mixing and therefore in peaks with higher amplitudes before reshock. Concomitantly, the large numerical diffusion suppresses the formation of small-scale structures. Reshock imparts more uniform energy on the interface, which combined with the stronger inverse cascade, leads to the formation of large-scale symmetric structures. These structures appear in the profiles as larger, uniform peaks. By contrast, high-resolution, high-order simulations have smaller numerical diffusion, resulting in smaller peaks prior to reshock. However, the small dissipation does not suppress the small-scale structures, which are then amplified by reshock, leading to the formation of additional small-scale complex structures. This fragmented structure is reflected in the profiles as a complex series of localized peaks. Note that due to the two-dimensional nature of the flow considered here, the effects of resolution and order of reconstruction can be directly related to the effects of numerical dissipation. In three-dimensional simulations, the additional mechanism of vortex stretching exists and must be considered. The results presented here clearly and quantitatively demonstrate that numerical dissipation effects are significant, as different characterizations of mixing are possible depending on the grid resolution and order of reconstruction.

5.5 The effects on the mixing fractions

The effects of grid refinement and order of reconstruction on the production and mixing fractions are presented in this section. The top row in Fig. 57 shows the time-evolution of the production fractions $P_t(t)$ and $P_m(t)$. The same observations noted for $\langle X_p \rangle$ and $X_p\left(\langle X \rangle\right)$ in Figs. 53 and 54 apply to $P_t(t)$ and $P_m(t)$. Specifically, the large differences observed for $\langle X_p \rangle$ at $t = 6$ ms, particularly in the regions outside the roll-ups where the difference is due to the width of the diffusion layer, result in increased values of P_t as the resolution and order of reconstruction are decreased. Diffusion is also central to understanding the large differences observed after reshock, and to the fact that the results using third-order reconstruction at low-resolutions are very different from the other results. The plot of P_m shows an interesting trend: before reshock, the values corresponding to third-order reconstruction at low resolution are the lowest, while after reshock the values corresponding to ninth-order reconstruction at high-resolution are the lowest. Smaller values of P_m indicate that the two fluids are less mixed, as less product is formed. Prior to reshock, the third-order results display roll-ups that are less tight when compared to the fifth- and ninth-order results, resulting in overall decreased product formation. Following reshock, the ninth-order results have the largest mixing layer width, resulting in less overall product formation. Note that the values of P_t and P_m for high-resolution, high-order simulations exhibit oscillations that are due to the change in the value of $h(t)$, as discussed above.

The bottom row of Fig. 57 shows the mixing fractions Ξ and Θ. As noted earlier, Ξ and Θ quantify (numerical diffusion-induced) mixing. Although both quantities provide similar physical insight into the mixedness of the fluids, the results obtained when comparing different orders of reconstruction and different grid resolutions exhibit differences. First consider Ξ. The ninth-order simulation at the highest resolution yields the lowest value of Ξ until shortly after reshock when it begins to increase. This is due to the rapid decrease in P_m observed above. The rapid increase corresponding to third-order reconstruction at coarse resolution is due to the increase in P_t observed above. The plot indicates that for simulations using the same order of reconstruction, Ξ decreases as the resolution increases. Now consider Θ, for which the lowest

value is given by the fifth-order reconstruction at high resolution for times before reshock and by third-order reconstruction at high resolution following reshock. Furthermore, note that no clear trend exists when the grid resolution is varied. For third-order reconstruction, Θ decreases as the grid resolution is increased, while for ninth-order reconstruction no such trend is observed. These results suggest that global mixing is most sensitive to changes in the grid resolution and in the order of reconstruction. Furthermore, the results indicate that it is difficult to predict a priori how a change in resolution or order of reconstruction affects these mixing quantities.

The results above indicate that integrated mixing fractions also depend significantly on the order of reconstruction and grid resolution. The differences in the results can be attributed to differences in the numerical dissipation. Low-order, low-resolution simulations have increased numerical dissipation, resulting in greater overall mixing as measured by the production mixing fractions P_t both before and after reshock. High-order, high-resolution simulations have smaller numerical dissipation, resulting in lower values of the mixing fraction P_t. The maximum production fraction P_m exhibits different behavior. Before reshock, the values of P_m are similar for all simulations, consistent with similar widths of the mixing layer and similar structures as the instability develops. Following reshock, the mixing layer width obtained from high-order, high-resolution simulations is larger and causes the value of P_m (as measured across the large mixing layer width) to decrease. High-order, high-resolution simulations having the largest mixing layer widths exhibit the smallest values of P_m. This change in behavior following reshock is reflected in the values of the mixing fraction Ξ. Prior to reshock, low-resolution, low-order simulations exhibit larger values of Ξ, consistent with increased overall mixing due to the larger numerical dissipation. However, following reshock, Ξ is not clearly correlated with the resolution and order of reconstruction. Similar mechanisms can also explain the values of the molecular mixing fraction Θ, which does not show an identifiable correlation with the order of reconstruction and resolution. In summary, the results show that the increased numerical dissipation observed in low-resolution, low-order simulations affects mixing as measured by the mixing fractions. In particular, the mixing fractions quantify mixing across the entire layer, and therefore the differences in width affect the mixing fractions in ways that cannot be predicted a priori easily. For this reason, mixing fractions must be considered in the context of other quantities such as the mixing layer width, and do not provide direct characterizations of the numerical mechanisms in the algorithm. This is in contrast to the mixing layer width, which correlates very strongly with the numerical dissipation.

5.6 The effects on the spectra

An analysis of the effects of grid refinement and of order of reconstruction on spectra is presented here. As the number of grid points increases, the range of scales resolved increases and, therefore, the tails of the spectra become longer. Also shown are plots of the ratio of each quantity to the value obtained from the ninth-order simulation on the fine grid (the ratio is shown only to the largest value of k obtained from the third-order, coarse grid simulation).

Figure 58 shows a comparison of the fluctuating kinetic energy spectrum $E(k,t)$. At all times considered, differences among all results are apparent across all orders of reconstruction and grid resolutions. This difference in energy becomes more apparent at late time ($t = 18$ ms) when all of the low-wavenumber modes in the spectrum have been damped out. The levels of energy observed in the fifth-order simulation at fine resolution are similar to the energy observed in the ninth-order simulation at medium resolution. This provides further

evidence that doubling the resolution gives qualitatively similar results as increasing the order of reconstruction. At intermediate and small scales, the spectra become steeper as the order increases. At late times, the ninth-order simulation on the finest grid has the lowest energy content in the largest scales and the most energy content in the intermediate scales. Figure 59 shows the ratio of the fluctuating kinetic energy spectrum from the simulations to the spectrum obtained from the ninth-order simulation on the fine grid. Large differences exist at $t = 6$ ms, with the ratios oscillating about unity. As time progresses, the oscillations damp out and it becomes clear that the energy content from the ninth-order simulation is the largest. At $t = 18$ ms and at large wavenumbers, the energy spectrum from the third-order simulation on the coarse grid is larger than the energy spectrum from the ninth-order simulations. This is due to aliasing, which causes the energy to accumulate at large wavenumbers as the Nyquist wavenumber (187) is approached [43, 23].

Figure 60 shows a comparison of the fluctuating enstrophy spectrum $E_{\omega''\omega''}(k,t)$, which is extremely sensitive to both the order and the resolution at all times. In particular, as the resolution and the order of reconstruction increase, the fluctuating enstrophy content of both the small and large scales increases. The fluctuating enstrophy spectrum from the ninth-order fine grid simulation differs from that corresponding to the third-order coarse grid simulation by an order of magnitude in the large scales and by several orders of magnitude in the intermediate and small scales. The plots in § 5.8 show that the vorticity corresponding to higher resolutions and higher orders increases in magnitude and is more localized, which is also reflected in the fluctuating enstrophy spectrum. At $t = 18$ ms, all of the oscillatory modes have been damped out and the spectrum begins decaying. The lower order and lower resolution spectra are much steeper than those at higher order and higher resolution. As the vorticity is constructed from the difference of two velocity gradients, its high-frequency components are more sensitive to numerical damping than are primitive fields such as the velocity. This sensitivity is amplified quadratically as the enstrophy is proportional to the square of the vorticity. Figure 61 shows the ratio of the fluctuating enstrophy spectrum from the simulations to the spectrum obtained from the ninth-order simulation on the fine grid. The ratio is always below unity for all times and for all simulations, indicating that the fluctuating enstrophy spectrum is very sensitive to the order of reconstruction and to the grid resolution. The relationship between the fluctuating enstrophy spectrum and the numerical dissipation present in the algorithm is a subject of future study.

Figure 62 shows the density variance spectrum $E_{\rho'\rho'}(k,t)$. The density variance spectra are very similar for small wavenumbers, but decrease steeply and rapidly as the wavenumber increases due to the numerical dissipation (which smooths out the fluctuations). As the order is increased or the grid resolution is increased, the numerical dissipation is decreased and the smoothing effects occur at progressively larger wavenumbers. Therefore, the density variance spectrum provides a useful measure of the effects of the numerical dissipation on the flow. The lower order and lower resolution spectra are steeper than those at higher order and higher resolution. Note that the density variance spectrum from the ninth-order simulation on the finest grid apparently exhibits an inertial subrange over slightly more than a decade in wavenumbers at $t = 12$ and 18 ms. Figure 63 shows the ratio of the density variance spectrum from the simulations to the spectrum obtained from the ninth-order simulation on the fine grid. At early times, large fluctuations exist near unity indicating a non-uniform modal distribution of the density variance. At later times, as the apparent inertial subrange develops, the ratio approaches unity, decreasing rapidly as the cutoff wavenumber is approached.

Finally, Fig. 64 shows the pressure variance spectrum $E_{p'p'}(k,t)$. As the resolution in-

creases, the pressure variance spectrum exhibits differences even in the low-wavenumber range, with higher resolutions and higher orders resulting in increased energy. This is due to the fact that the pressure is obtained from the energy equation with increased amounts of energy deposited on the interface as the resolution and order are increased. The steep decline in the spectrum is also due to the numerical dissipation, which smooths out large-wavenumber fluctuations. The lower order and lower resolution spectra are steeper than those at higher order and higher resolution. Note that the pressure variance spectrum from the ninth-order simulation on the finest grid apparently exhibits an inertial subrange over approximately a decade in wavenumbers at $t = 12$ and 18 ms. Figure 65 shows the ratio of the pressure variance spectrum from the simulations to the spectrum obtained from the ninth-order simulation on the fine grid. The figure at $t = 6$ ms indicates that increased energy is observed for the simulation on the medium grid at high wavenumbers. In particular, a closer examination of the corresponding plot in Fig. 64 shows that there is a sudden increase in pressure variance similar to that observed from aliasing. This result is unexpected, and it is not clear what mechanism is responsible for this. It is noteworthy that this phenomenon is observed in all of the simulations. In particular, the ninth-order simulation on the fine grid also exhibits an increase in the pressure variance in the large wavenumbers. However, the increase occurs at larger wavenumbers than for the ninth-order simulation on the medium grid.

As shown above, the effects of grid resolution and order of reconstruction on the spectra can be understood based on the presence of small-scale features and the intrinsic numerical dissipation of the method. The difference in magnitude observed in the kinetic energy spectrum across different resolutions and orders of reconstruction is a direct consequence of the presence of small-scale flow features. High-resolution, high-order simulations support small-scale features resulting in larger fluctuations. These fluctuations are further amplified during reshock and yield energy spectra that are similar in shape but much larger in magnitude. Consider instead the density variance spectrum: all curves overlap for a portion of the spectrum, but show a steep decline depending on the resolution and order of the method. This is a direct consequence of the numerical dissipation damping the fluctuations beyond a certain critical scale. Comparing simulations with different orders of flux reconstruction and different grid resolutions for the enstrophy shows both the effects of small-scale structures and the effects of numerical dissipation. Similarly, the pressure variance spectrum also shows a dependence on both mechanisms. As observed from the ratio of each spectrum from the simulations with different orders and resolutions to the spectrum obtained from the ninth-order simulation on the fine grid, there is no apparent 'convergence' of the spectra: this indicates that quantities sensitive to the small-scale structure of the flow do not generally exhibit 'convergence' while quantities determined primarily by the large-scale structures appear to be 'converged' at sufficiently high order of reconstruction and grid resolution, *i.e.*, the mixing layer amplitude or width (as shown in § 5.2).

5.7 The effects on the statistics

An investigation of the effects of grid refinement and order of reconstruction on the statistics (*i.e.*, wavenumber-integrated energy spectra) is presented here. Figure 66 shows the fluctuating kinetic energy and its components. As the order of reconstruction and resolution are increased, the overall energy increases before reshock. However, this is no longer the case following reshock. For example, consider $E_{u''u''}(t)$. The ninth-order result at coarse resolution has the lowest energy, which can be explained by recalling that the mixing layer width obtained

from the ninth-order simulation is larger than that obtained from the third-order simulation, resulting in less overall energy. Also note that $E_{v''v''}(t)$ is much more sensitive to the spatial resolution and to the order of reconstruction than $E_{u''u''}(t)$, both before and after reshock (particularly at late times). Following reshock, the lowest resolution simulations are no longer the simulations with the least energy content: this is again due to the reduced mixing layer width observed for coarser simulations, which yields increased levels of energy.

The differences become very significant as the grid resolution and order of spatial reconstruction are varied when the fluctuating enstrophy $E_{\omega''\omega''}(t)$, shown in Fig. 66, is considered. First, note that the fluctuating enstrophy increases as the order and spatial resolution increases. The fluctuating enstrophy also increases as the grid resolution is increased. Furthermore, note that the fluctuating enstrophies from simulations with increased grid resolution or higher order of reconstruction are very similar. It is interesting to note that the difference in enstrophies is apparent both before and after reshock, with the fluctuating enstrophy from the ninth-order fine grid simulation differing from that obtained from the third-order coarse grid simulation by an order of magnitude. This behavior can be explained by noting that the enstrophy measures the squared fluctuations of vorticity. Vorticity fluctuations are responsible for the dissipation of kinetic energy and the transfer of energy to smaller scales. Hence, a larger enstrophy from simulations with higher grid resolutions and order of reconstruction is an indication of the formation of additional small-scale structures. This is consistent with a reduced numerical dissipation in simulations with higher order of spatial reconstruction and higher grid resolution.

The density variance $E_{\rho'\rho'}(t)$ shown in Fig. 66 exhibits agreement once the order and grid resolution are sufficiently high. This result is consistent with the previous observation that the density variance spectrum does not significantly change as a function of grid resolution and order of reconstruction, with the exception of a steep decline at large wavenumbers. Contributions from the small scales (large wavenumbers) are not heavily weighted in the computations of statistics, which is consistent with the small changes. The density variance is rapidly damped in the third-order, coarse and medium grid simulations. The pressure variance $E_{p'p'}(t)$ shown in Fig. 66 exhibits little sensitivity to changes in the order of reconstruction and grid resolution.

The investigation presented here shows that statistics are affected differently by changes in order of reconstruction and grid resolution. The fluctuating enstrophy shows the most variation and indicates that the higher numerical dissipation associated with low-order, low-resolution simulations significantly decreases the fluctuating enstrophy. This result is also consistent with the large variations observed in the fluctuating enstrophy spectra where a cascade to larger wavenumbers was observed in high-order, high-resolution simulations. The cascade causes the statistics to have larger values, as an increased number of modes with similar energy is obtained. Increased values of the enstrophy are consistent with the formation of small-scale structures observed in simulations performed using higher grid resolution and higher order of spatial reconstruction. The fluctuating kinetic energy and pressure variance exhibit little variation, as the differences in spectra observed earlier are not reflected in the statistics. The periodic component of the fluctuating kinetic energy shows variations following reshock due to the presence of small-scale disordered flow structures in high-order, high-resolution simulations.

5.8 Temporal progression of the density and vorticity fields

Presented here is the time-evolution of the density and vorticity fields at intervals of 1 ms in the single-mode, two-dimensional Richtmyer-Meshkov instability with reshock obtained from WENO simulations with third-, fifth-, and ninth-order of reconstruction and grid resolutions of

128, 256, 512 points per initial perturbation wavelength. The following convention is adopted in the presentation of the results. The top, middle, and bottom rows show the results of the ninth-, fifth-, and third-order simulations, respectively. The left, middle, and right columns display results obtained with increasing spatial resolution. The purpose of this section is to qualitatively illustrate how the evolution of the instability changes as the numerical order of flux reconstruction and the grid resolution are varied. The figures also aid in interpreting the results in previous sections.

At early times, the interface is more diffused for the lower order and lower resolution simulations. As time evolves, a qualitative correspondence in both the density and vorticity occurs between the simulations on the diagonal, *i.e.*, results obtained using a $(2n-1)$-th order method with $n = 2, 3$ and N grid points per initial perturbation wavelength are similar to those obtained using a $(2n-1)$-th order method with $n = 3, 5$ and $N/2$ grid points per initial perturbation wavelength, respectively. The higher-order and finer grid results show sharper, smaller-scale features with well-defined roll-ups (more concentrated vortex cores), as well as thinner diffusion layers. The vortex cores are larger in the lower order and lower resolution simulations.

The amplitudes from the higher order and higher resolution simulations are slightly larger than those from the lower order and lower resolution simulations before reshock. After reshock, the difference in amplitude increases due to the mechanisms described in § 5. The third-order simulations remain highly diffuse for all grid resolutions, even at late times following reshock. As shown in the figures with $t \geq 7$ ms, the third-order simulations retain significant coherency and symmetry following reshock. The third-order results are characteristic of simulations with a high degree of numerical diffusion, as well as simulations that are under-resolved. By contrast, simulations performed using fifth- and ninth-order spatial reconstruction show breaking of symmetry. The breaking of symmetry, which has not been reported in other simulations with reshock using formally lower order methods (see [89, 28]), can be attributed to numerical instabilities that are not damped by the numerical dissipation in the method.

By $t = 6$ ms, the medium grid ninth-order simulation exhibits additional small-scale structure within the roll-ups. This additional structure was also reported by several investigators using the piecewise-parabolic method (PPM) [128, 101], and is apparently a manifestation of a physical process observed in experiments [51, 97, 29]. By contrast, the fine grid ninth-order simulation begins to show asymmetrical and fragmented structure within the roll-ups, as well as on the interface. Such structure was also observed in ninth- and eleventh-order numerical simulations at high resolutions conducted at Brown University; it is speculated that as the roll-ups form, the interface separating the two gases is stretched increasingly thinner and the differences in flow velocities across the interface, along with the numerical perturbations, cause the formation of an instability similar to the Kelvin-Helmholtz instability [33]. It is believed that this is a manifestation of a numerical instability due to the small numerical diffusion that is unable to provide sufficient regularization of the Euler equations as the grid Reynolds number [118, 100]

$$Re_{\Delta x} = \frac{c_s \, \Delta x}{\nu_{num}} \tag{266}$$

increases (where ν_{num} is some parameterization of the numerical viscosity of the method and c_s is the speed of sound). It would be of interest to perform a grid convergence study using explicit molecular dissipation and diffusion to determine whether this fragmentation persists. Following reshock, the ninth-order simulations exhibit the most small-scale, disordered structure with significant fragmentation of the density and of the vorticity, and are most reminiscent of the

experimental PLIF images in Collins and Jacobs. By contrast, the lower order and lower resolution simulations continue to exhibit relatively ordered structure, even following reshock.

The study presented here can also be used to confirm and substantiate the mixing analysis performed in the previous section, as well as the study of the effects of spatial resolution and order of reconstruction in this section. The mass transfer measured by the averaged mole fraction $\langle X \rangle$, the degree of mixedness as measured by the reaction mole fraction $\langle X_p \rangle$, and the presence of large unmixed regions measured by $X_p\left(\langle X \rangle\right)$ can be qualitatively confirmed by considering the density plots. Furthermore, the qualitative differences discussed as the resolution and order of reconstruction are changed can also be confirmed by comparing to the density plots presented below. The structure of the vorticity qualitatively confirms the formation of large- or small-scale structures and provides indirect support to the analysis of the time-evolution of the spectra. The difference in vorticity structures observed as the resolution and the order of reconstruction are changed is also consistent with two-dimensional turbulence phenomenology. As the resolution is increased and the order of reconstruction is increased, the inverse cascade also decreases, resulting in the formation of more fragmented and smaller-scale structures. By contrast, as the resolution is decreased the inverse cascade is stronger, leading to the formation of large vortical structures. Therefore, the consistency between the mixing analysis and the density plots, and between the spectral analysis and the vorticity plots indicates that the quantities considered in the present investigation provide a physically useful characterization of the mixing process.

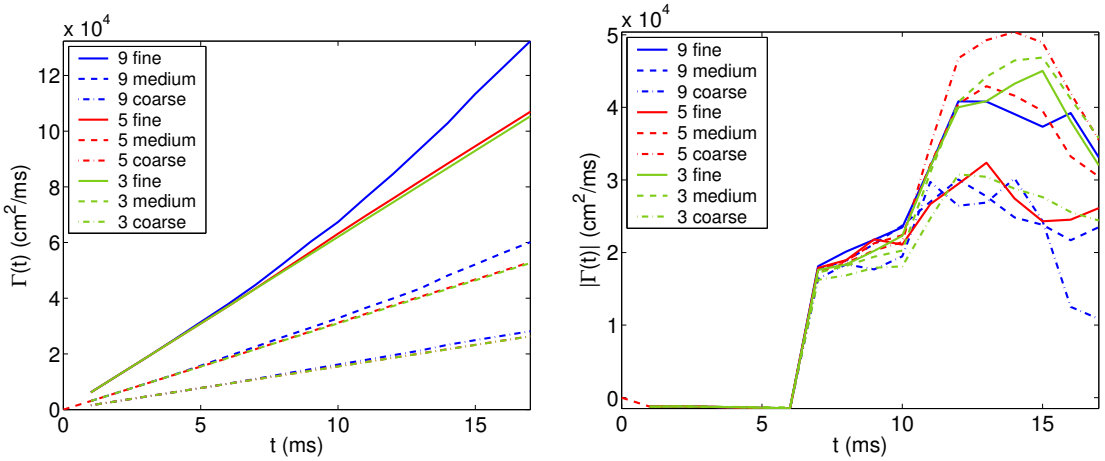

Figure 51: The total circulation $\Gamma = \Gamma^+ + \Gamma^-$ (left) and absolute value of the circulation $|\Gamma|$ (right), when the order of reconstruction and the grid resolution are varied.

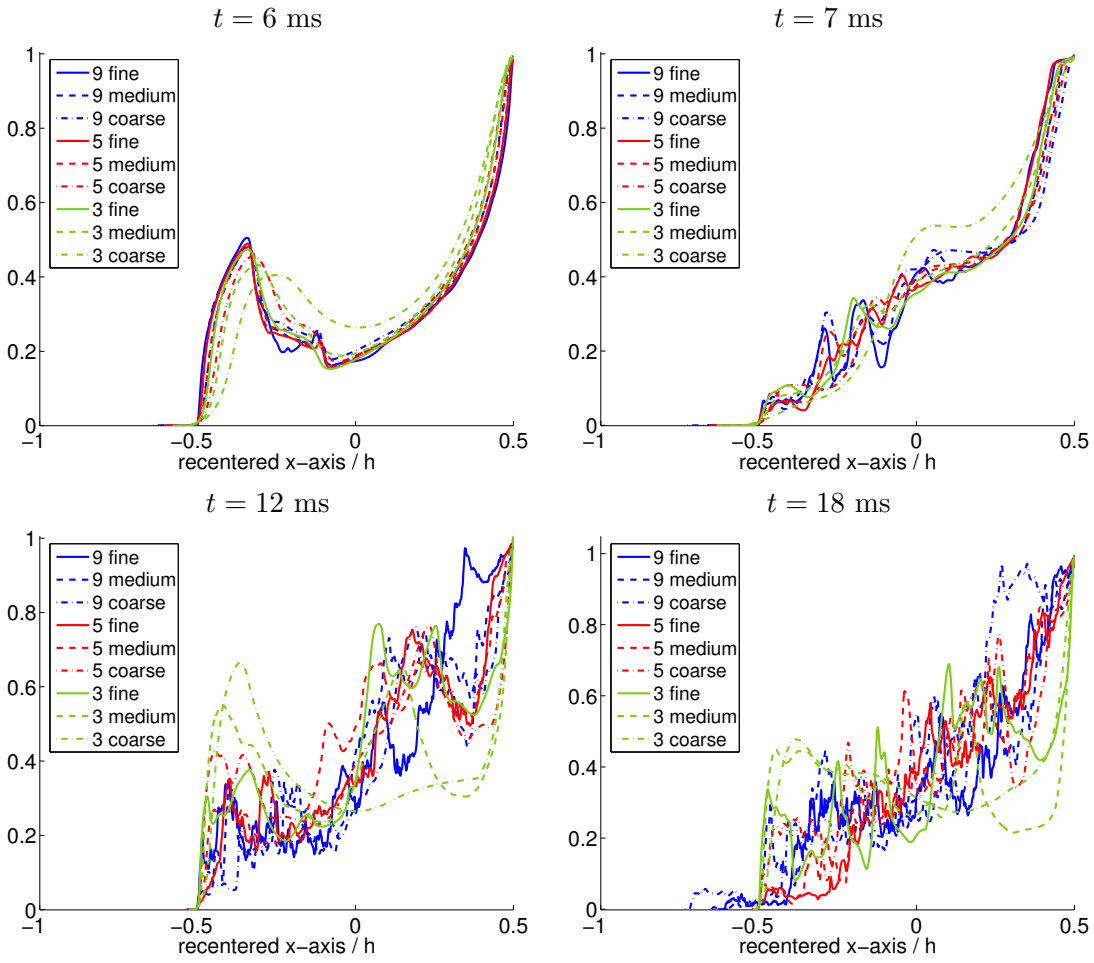

Figure 52: Comparison of the mole fraction profile $\langle X \rangle$ at $t = 6, 7, 12, 18$ ms when the order of reconstruction and the grid resolution are varied.

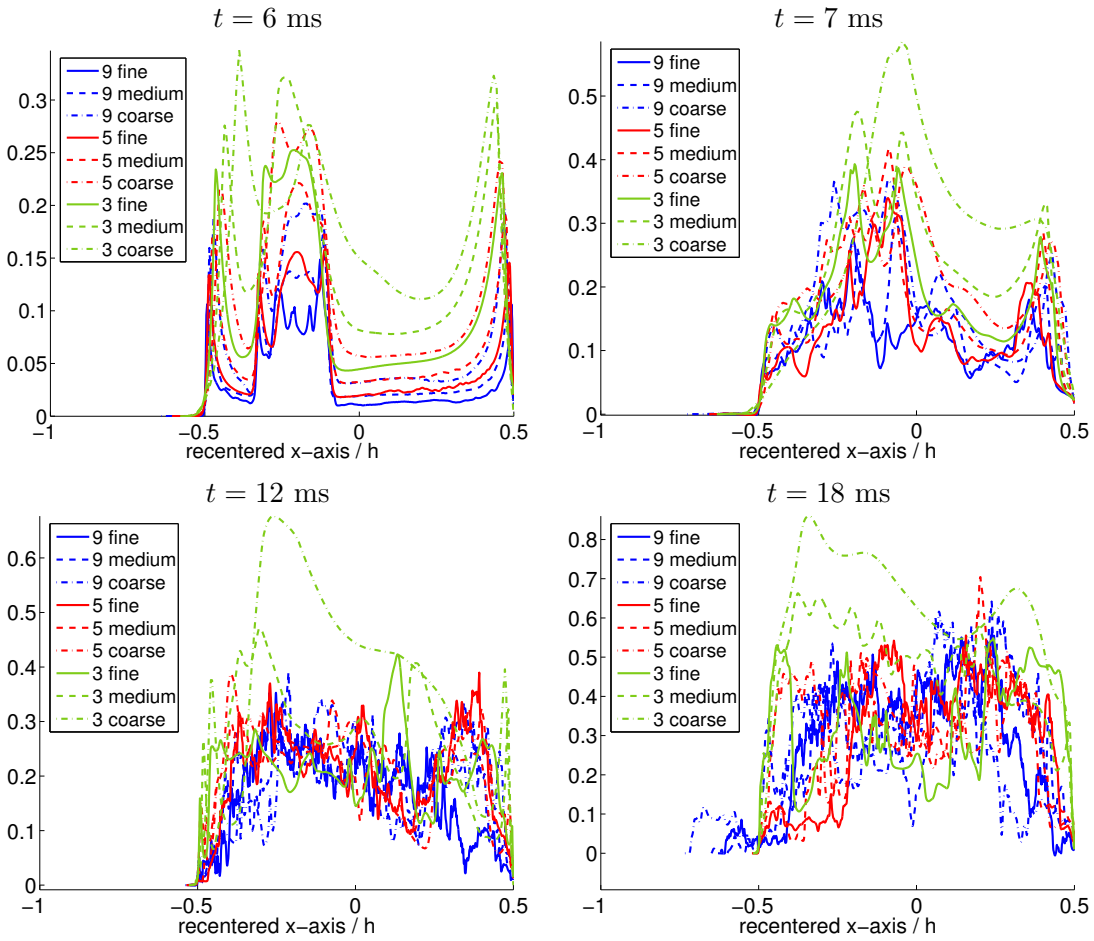

Figure 53: Comparison of the product mole fraction profile $\langle X_p \rangle$ at $t = 6, 7, 12, 18$ ms when the order of reconstruction and the grid resolution are varied.

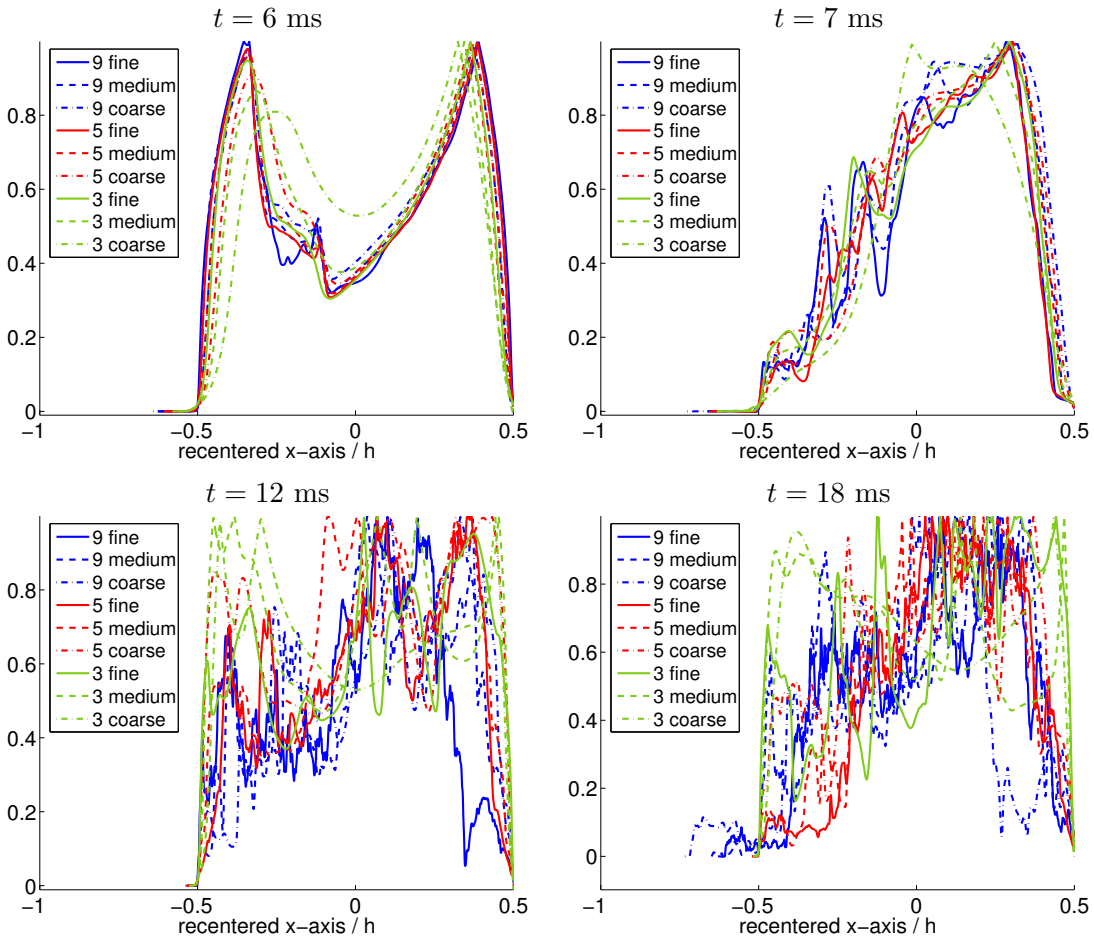

Figure 54: Comparison of the product mole fraction profile $X_p(\langle X \rangle)$ at $t = 6, 7, 12, 18$ ms when the order of reconstruction and the grid resolution are varied.

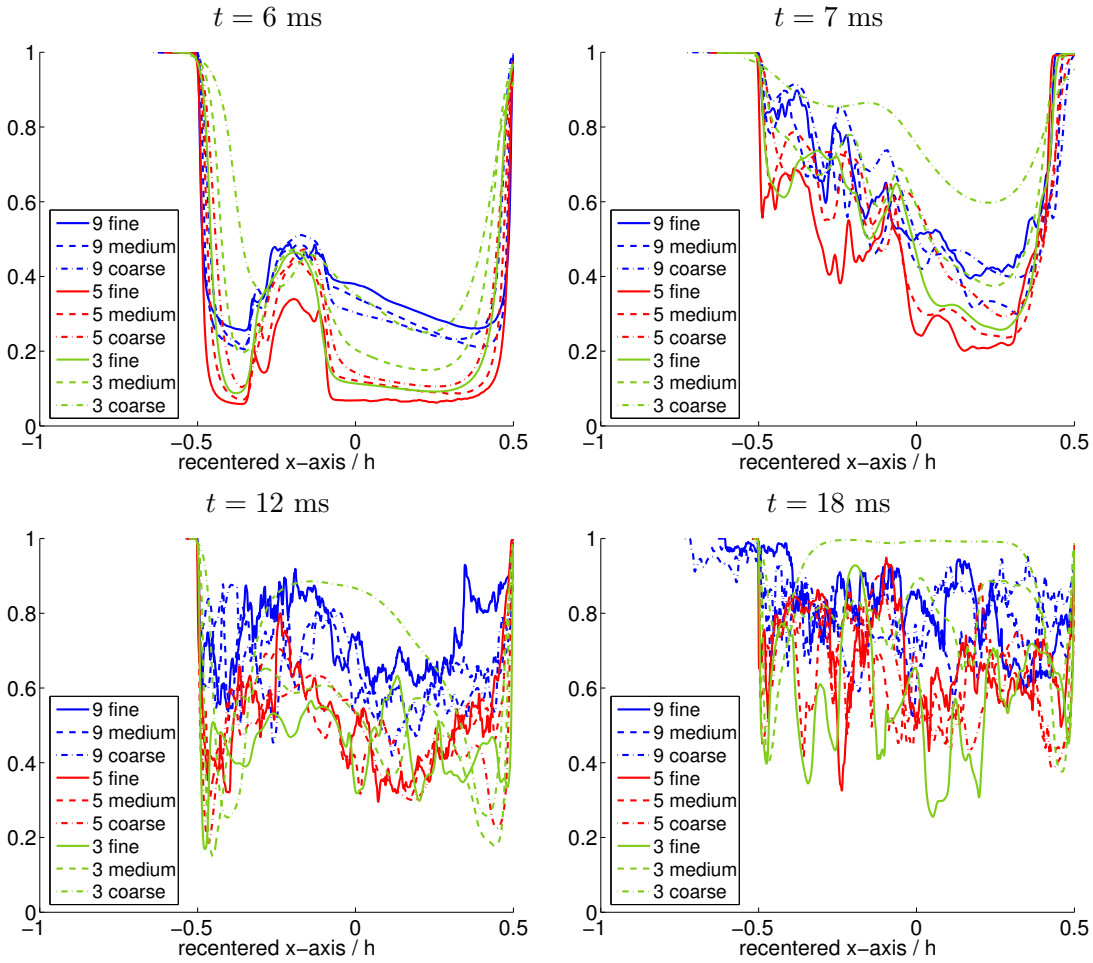

Figure 55: Comparison of the molecular mixing fraction θ at $t = 6, 7, 12, 18$ ms when the order of reconstruction and the grid resolution are varied.

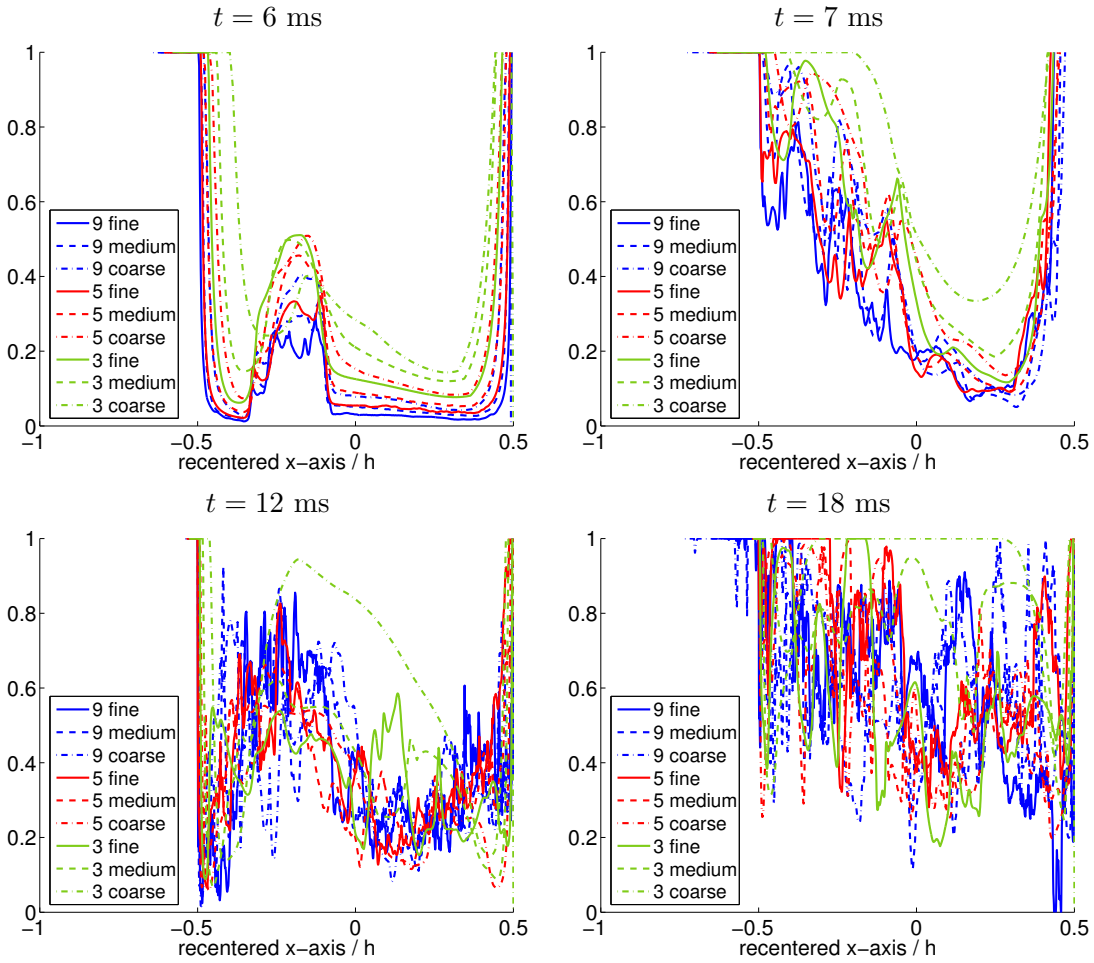

Figure 56: Comparison of the molecular mixing fraction ξ at $t = 6, 7, 12, 18$ ms when the order of reconstruction and the grid resolution are varied.

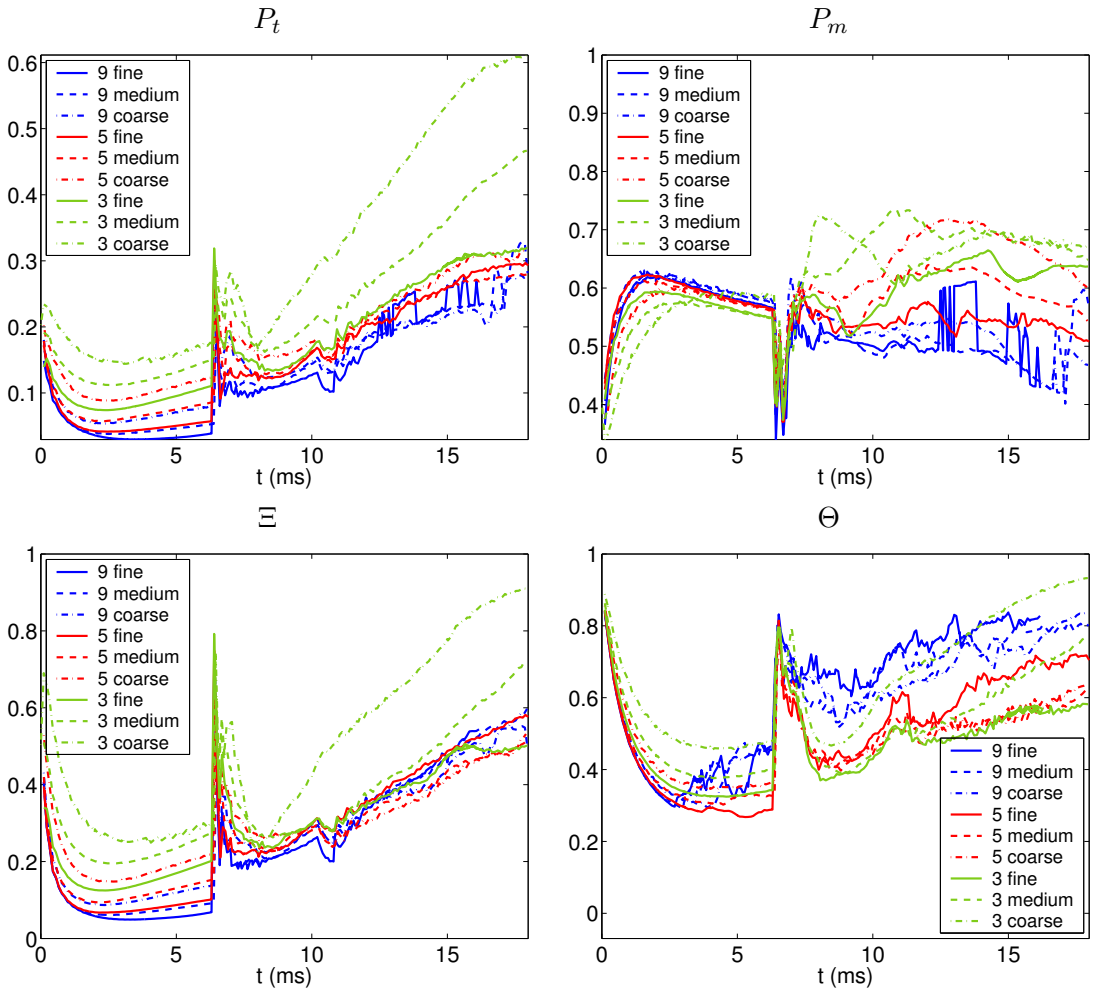

Figure 57: Comparison of the mixing fractions P_t, P_m, Ξ, and Θ when the order of reconstruction and the grid resolution are varied.

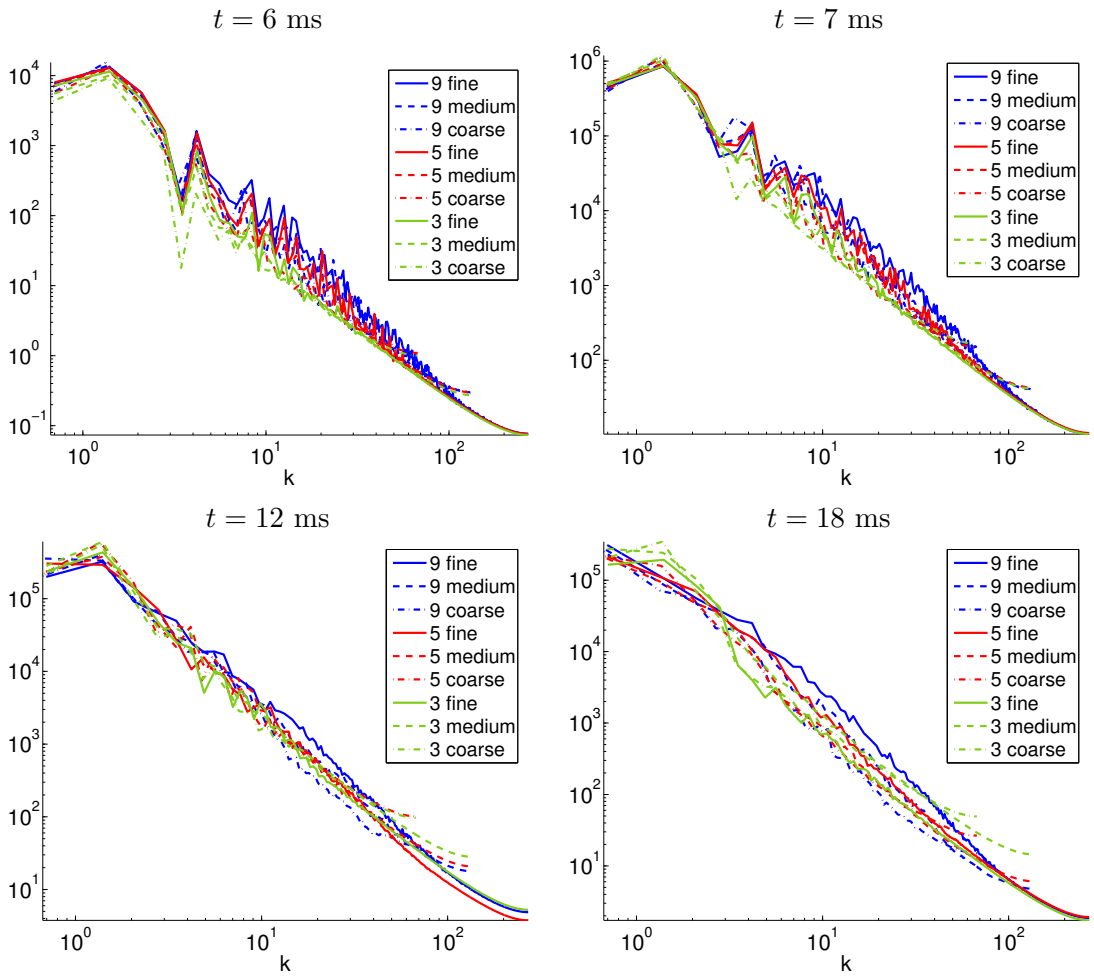

Figure 58: Comparison of the fluctuating kinetic energy spectrum $E(k,t)$ at $t = 6, 7, 12, 18$ ms when the order of reconstruction and the grid resolution are varied.

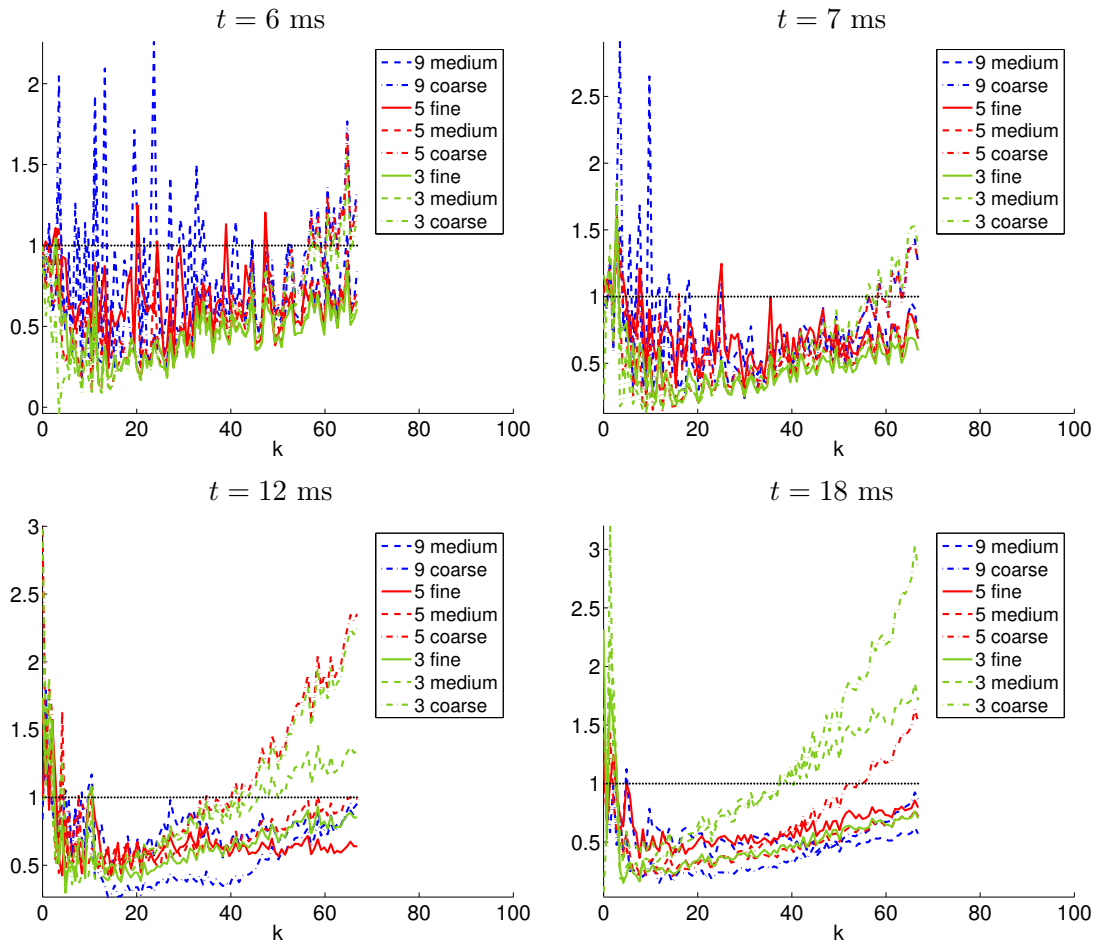

Figure 59: Ratio of the fluctuating kinetic energy spectrum from the simulations to the spectrum from the ninth-order simulation on the fine grid at $t = 6, 7, 12, 18$ ms when the order of reconstruction and the grid resolution are varied.

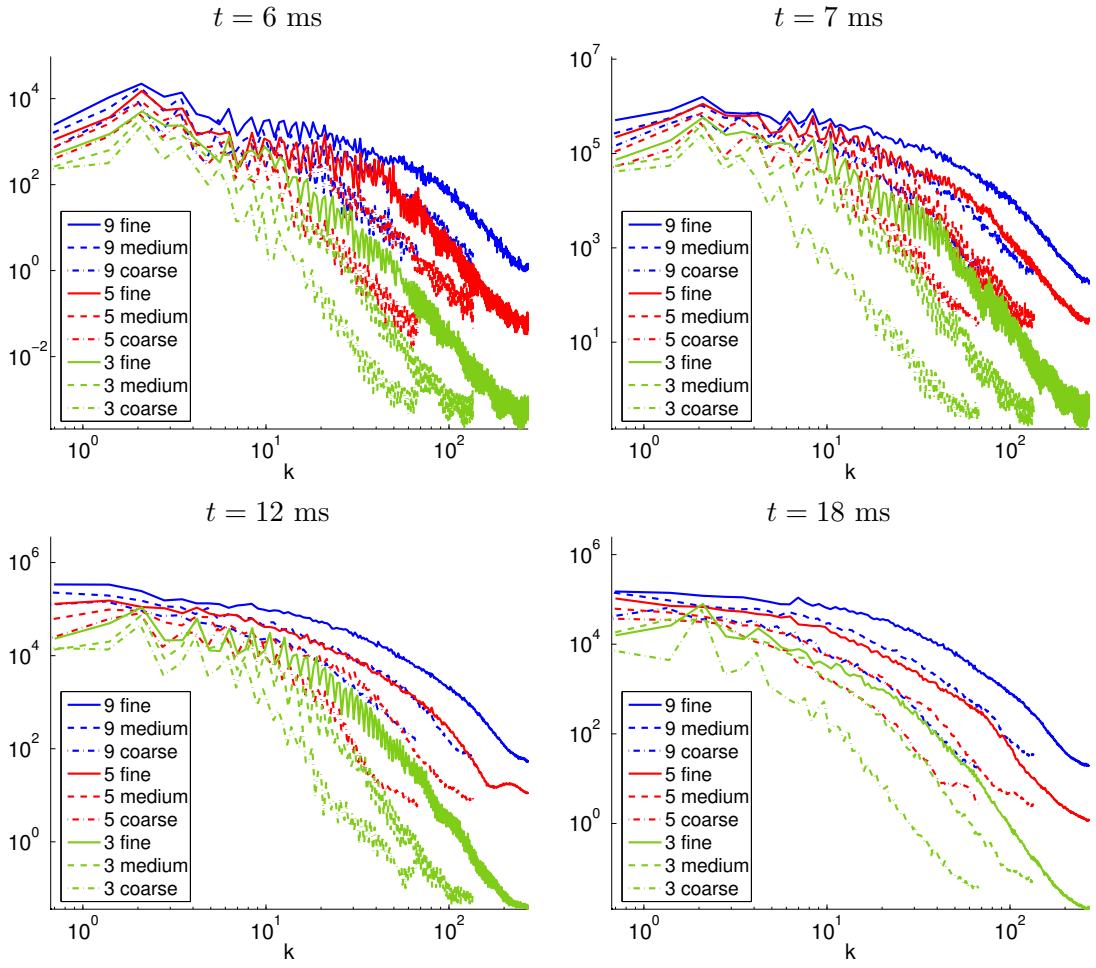

Figure 60: Comparison of the fluctuating enstrophy spectrum $E_{\omega''\omega''}(k,t)$ at $t = 6, 7, 12, 18$ ms when the order of reconstruction and the grid resolution are varied.

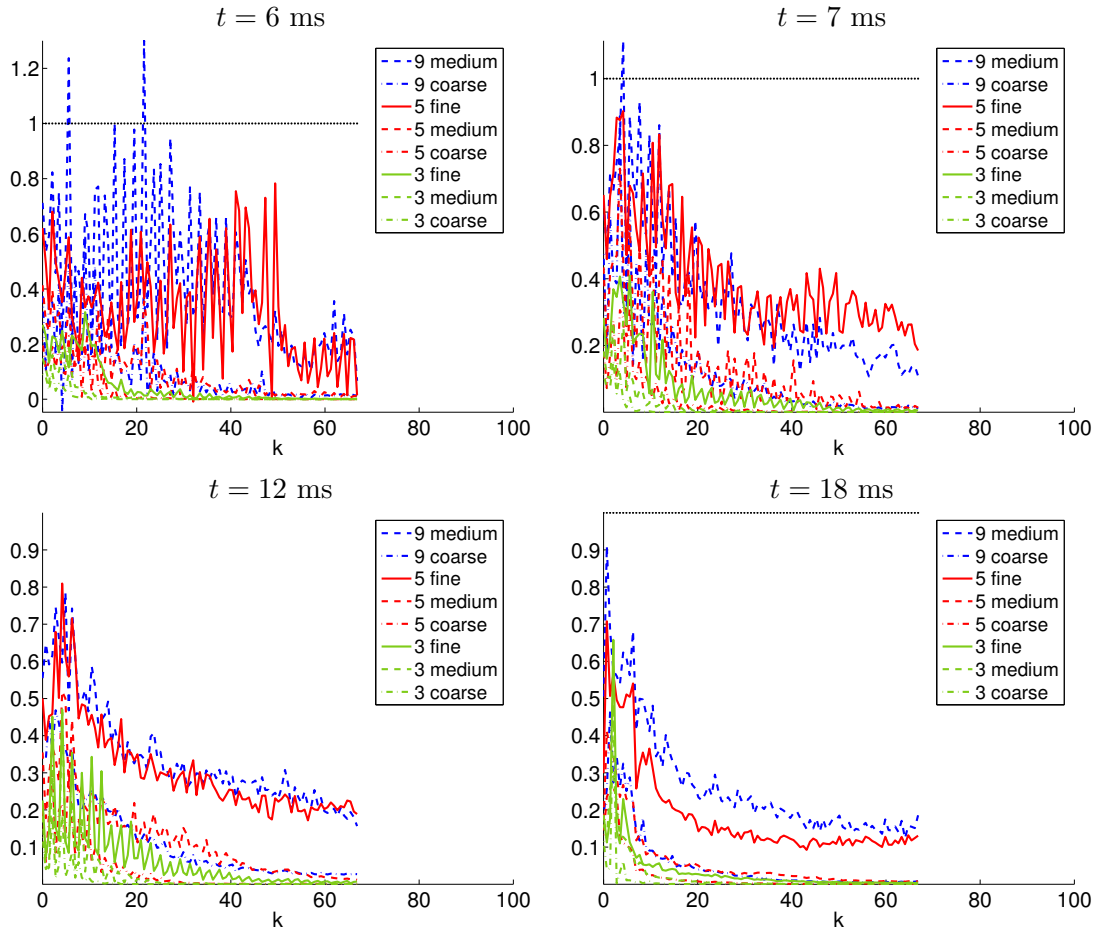

Figure 61: Ratio of the fluctuating enstrophy spectrum from the simulations to the spectrum from the ninth-order simulation on the fine grid at $t = 6, 7, 12, 18$ ms when the order of reconstruction and the grid resolution are varied.

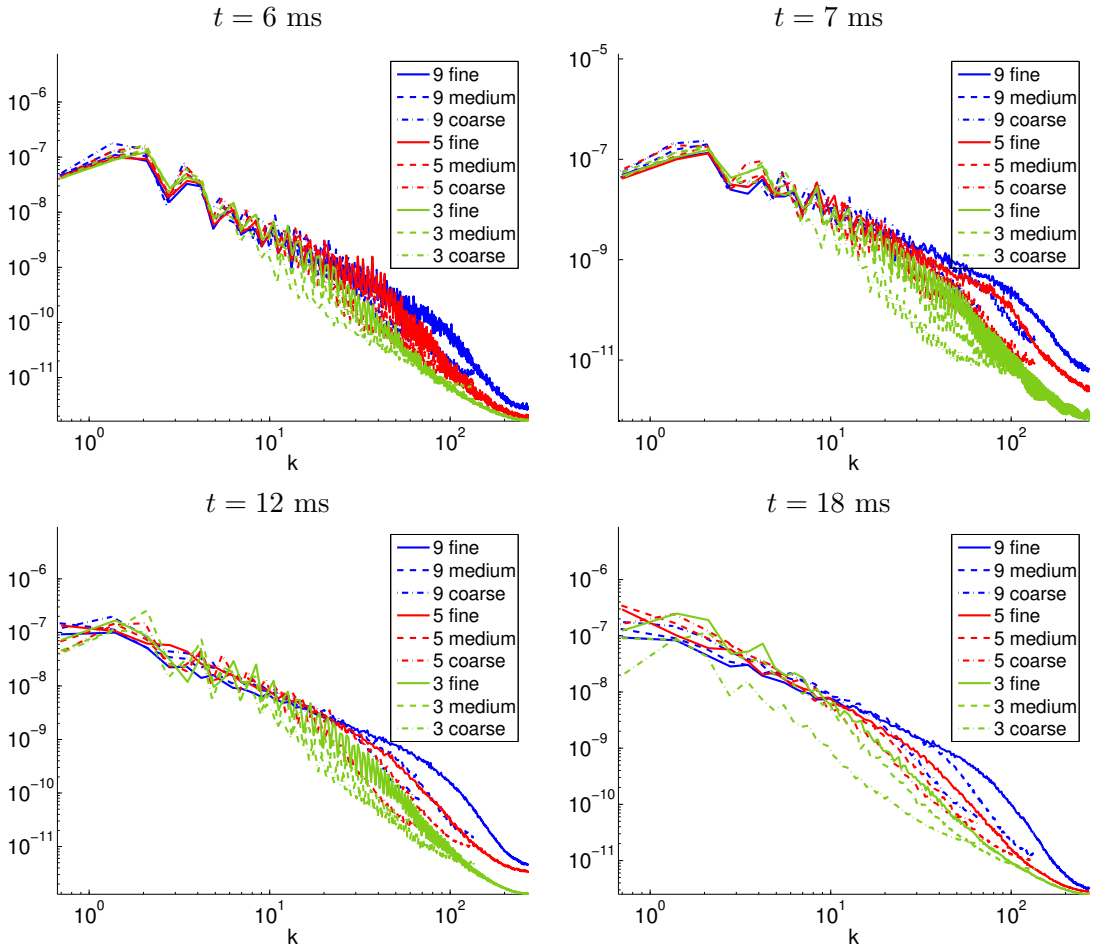

Figure 62: Comparison of the density variance spectrum $E_{\rho'\rho'}(k,t)$ at $t = 6, 7, 12, 18$ ms when the order of reconstruction and the grid resolution are varied.

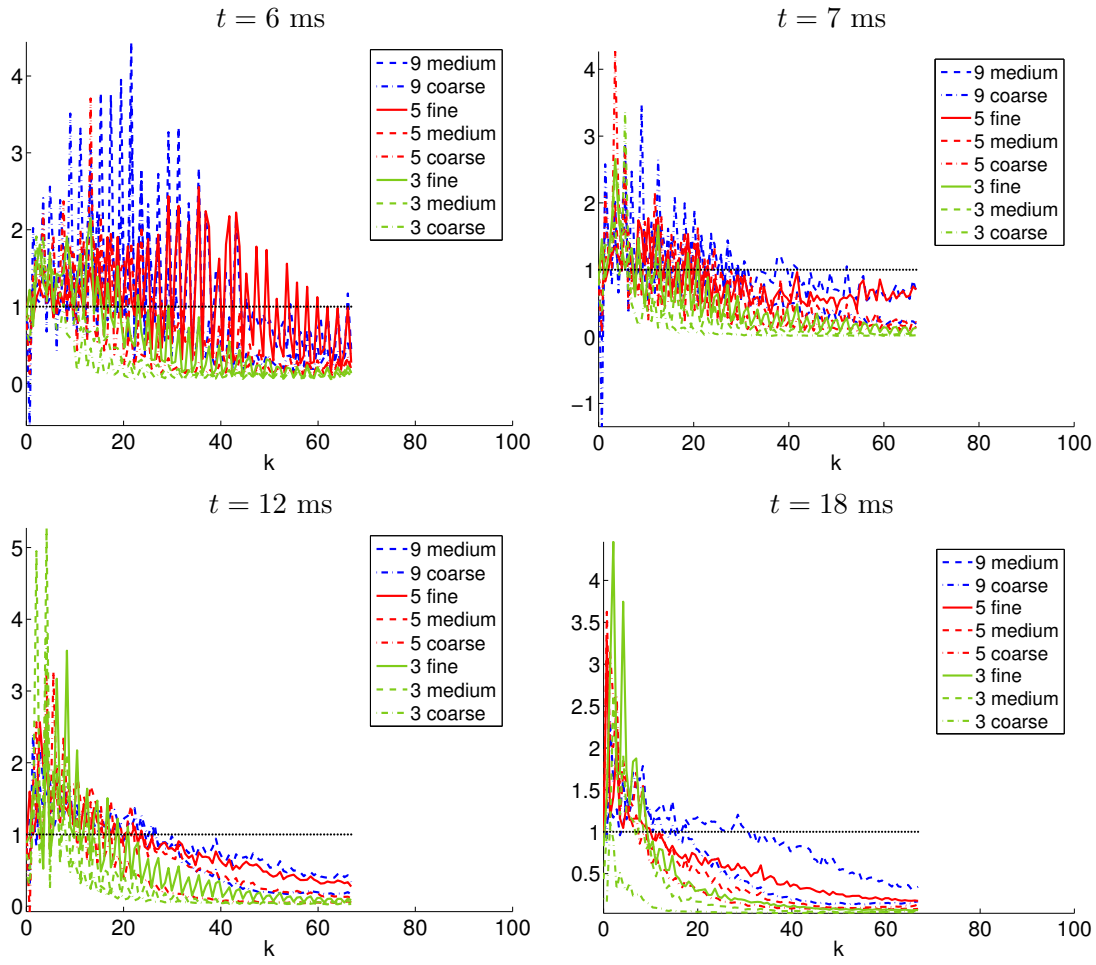

Figure 63: Ratio of the density variance spectrum from the simulations to the spectrum from the ninth-order simulation on the fine grid at $t = 6, 7, 12, 18$ ms when the order of reconstruction and the grid resolution are varied.

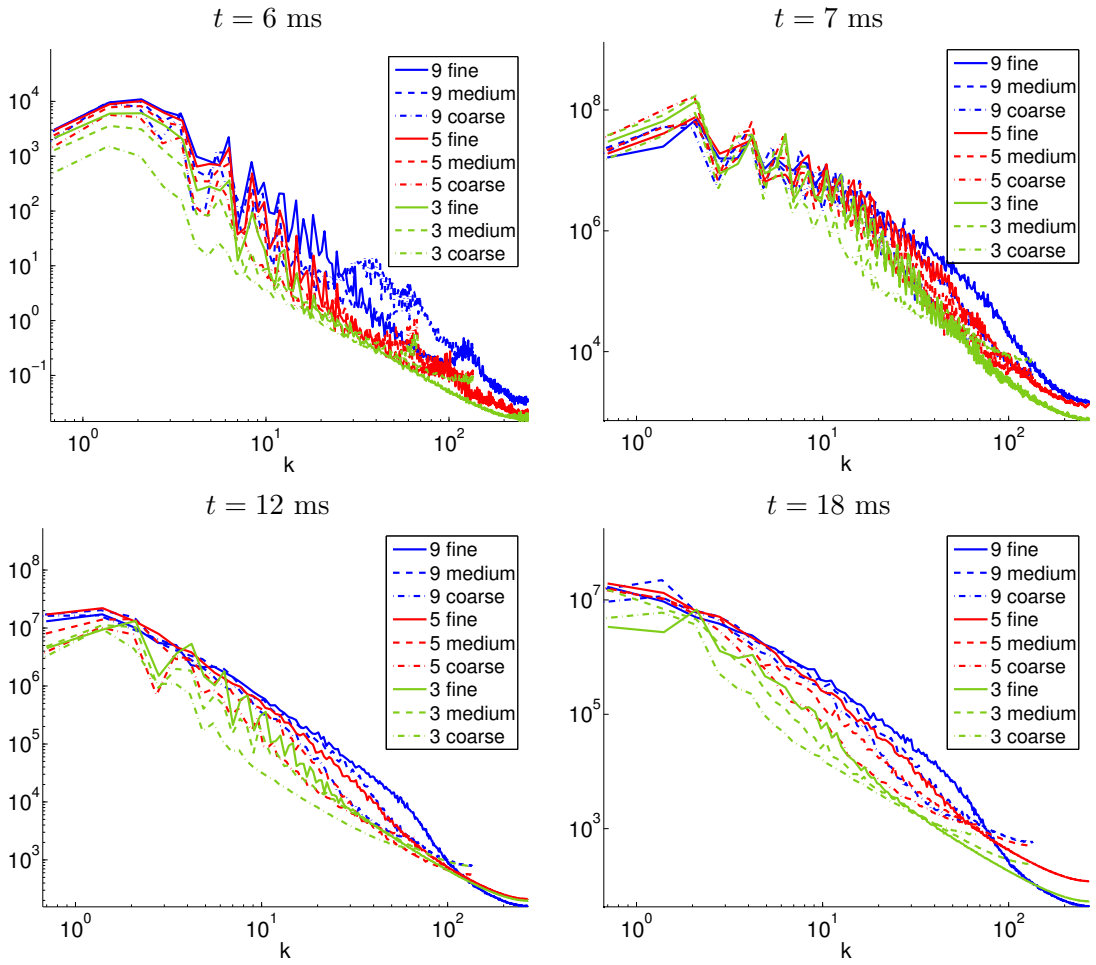

Figure 64: Comparison of the pressure variance spectrum $E_{p'p'}(k,t)$ at $t = 6, 7, 12, 18$ ms when the order of reconstruction and the grid resolution are varied.

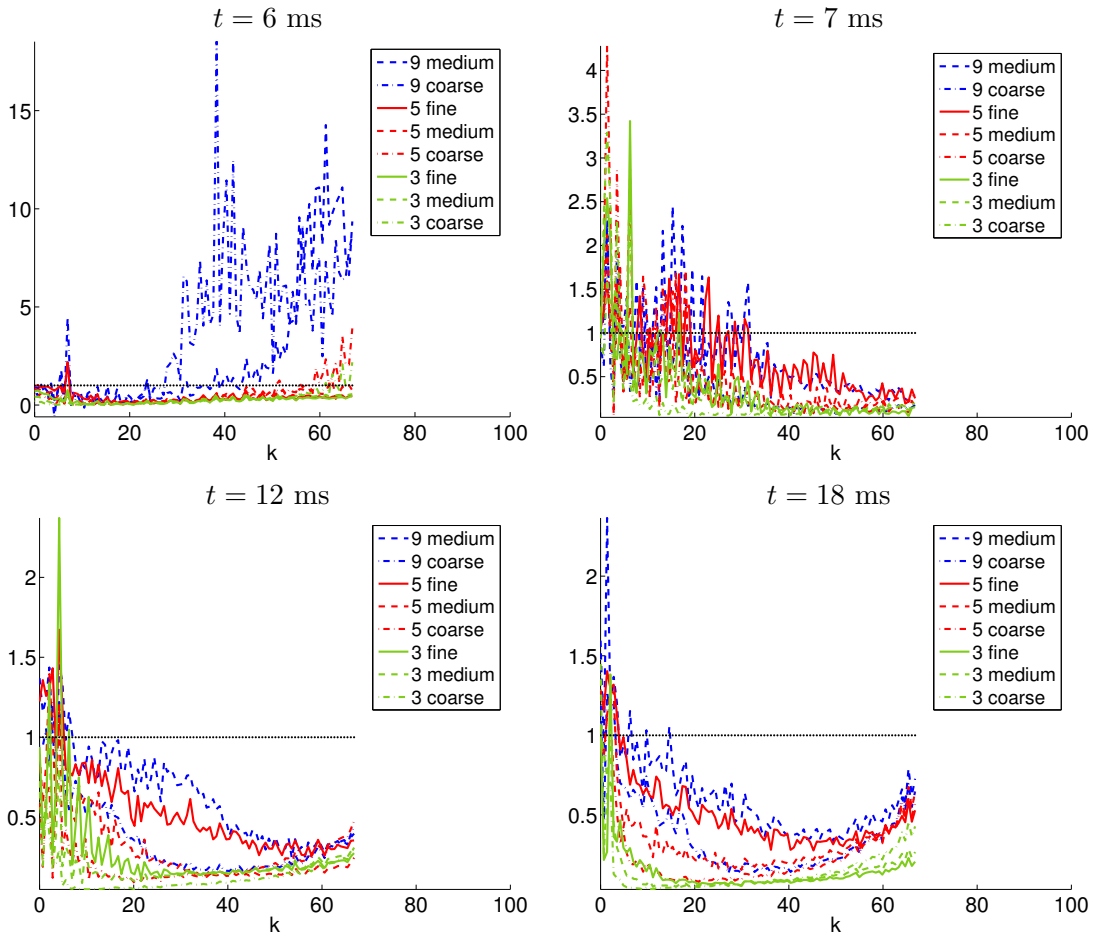

Figure 65: Ratio of the pressure variance spectrum from the simulations to the spectrum from the ninth-order simulation on the fine grid at $t = 6, 7, 12, 18$ ms when the order of reconstruction and the grid resolution are varied.

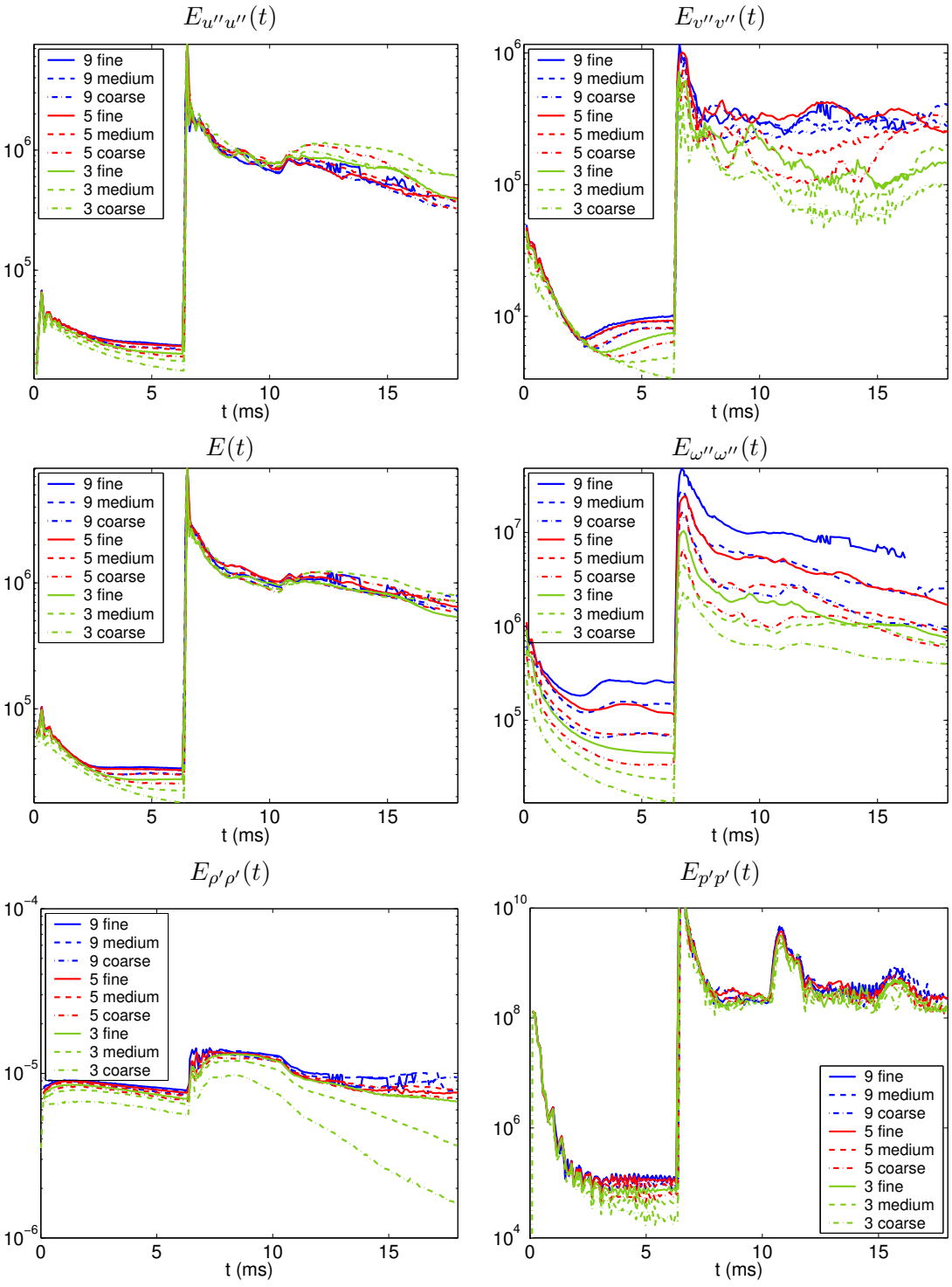

Figure 66: Comparison of $E_{u''u''}(t)$, $E_{v''v''}(t)$, $E(t)$, $E_{\omega''\omega''}(t)$, $E_{\rho'\rho'}(t)$, and $E_{p'p'}(t)$ when the order of reconstruction and the grid resolution are varied.

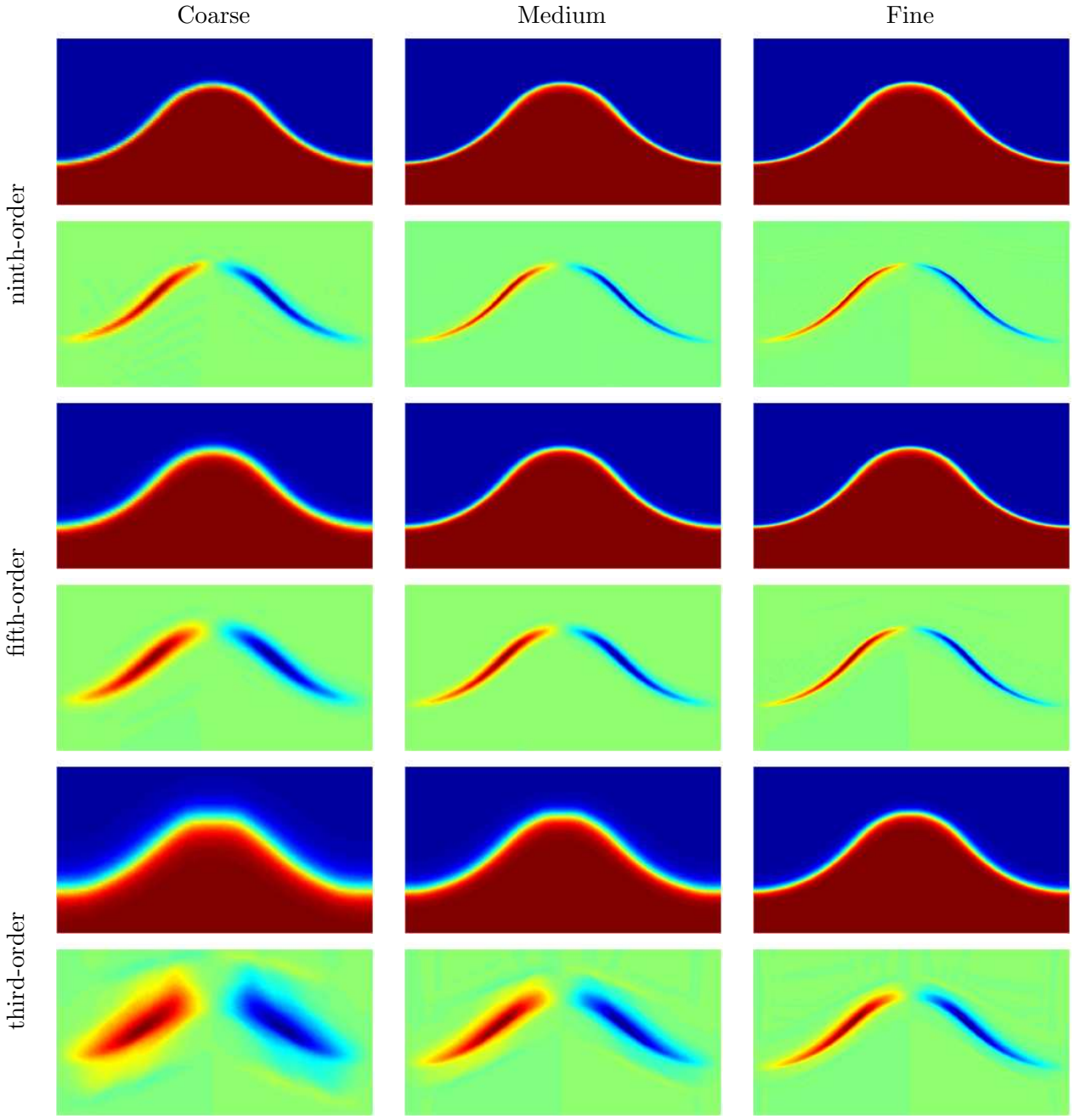

Figure 67: Density and vorticity at $t = 1$ ms.

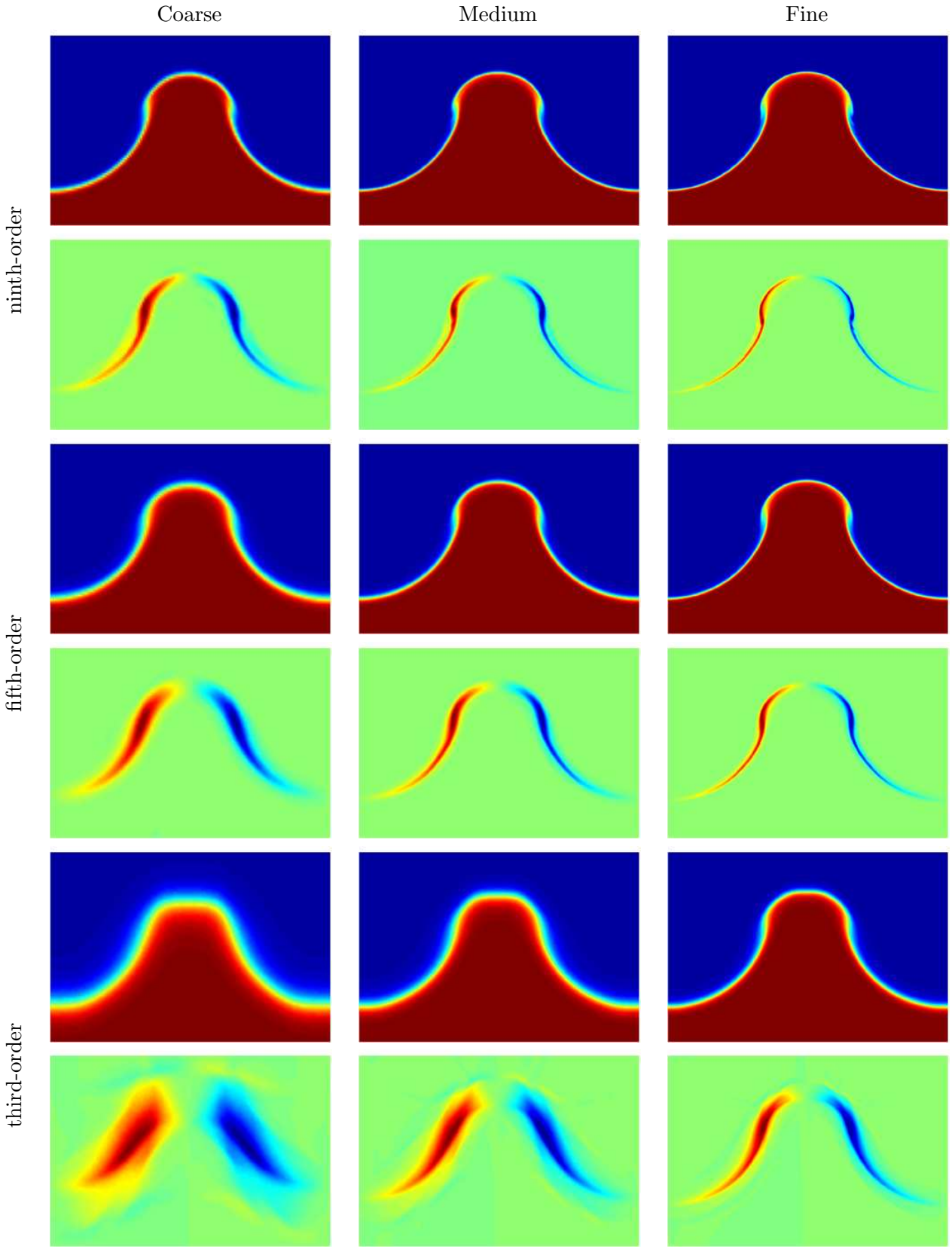

Figure 68: Density and vorticity at $t = 2$ ms.

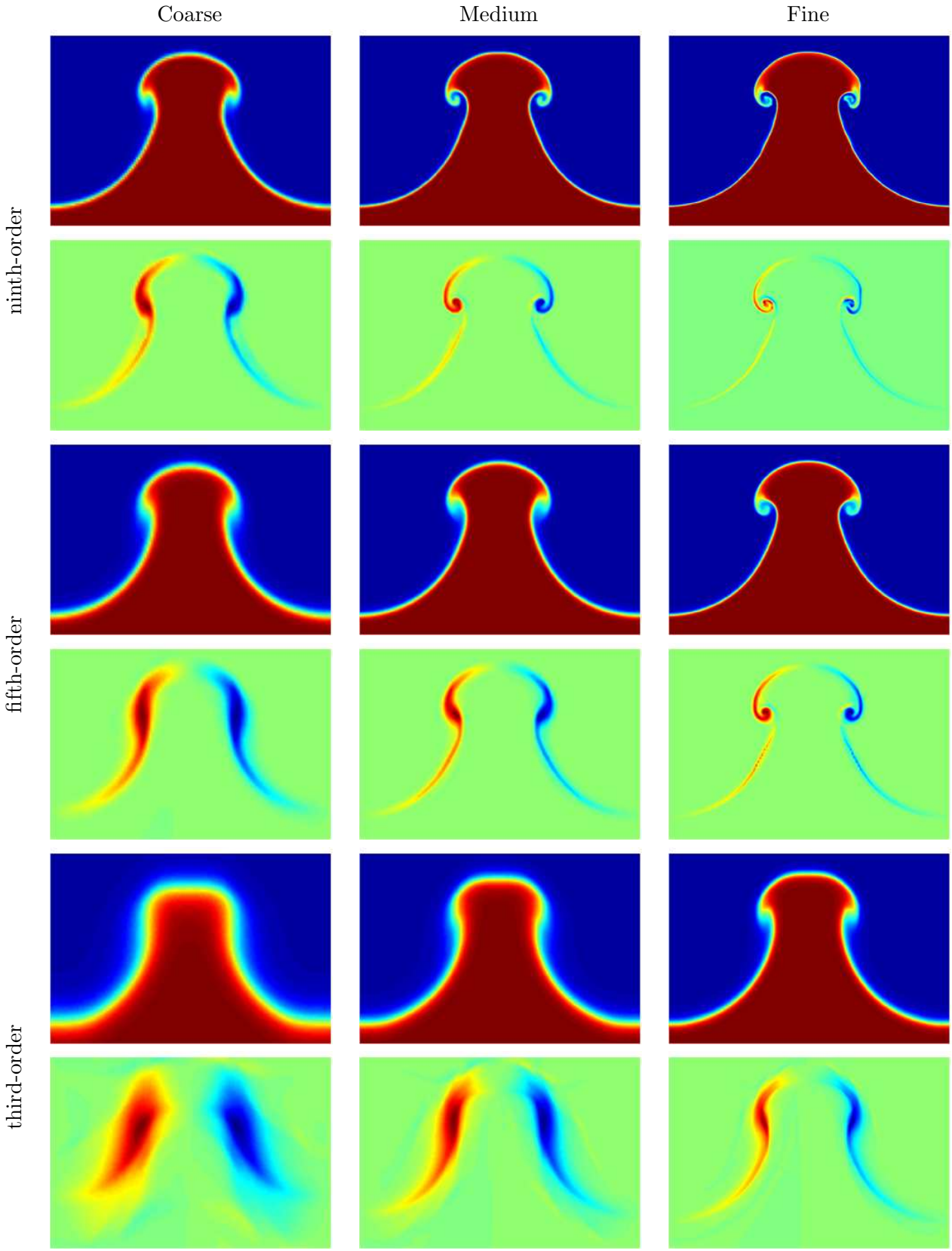

Figure 69: Density and vorticity at $t = 3$ ms.

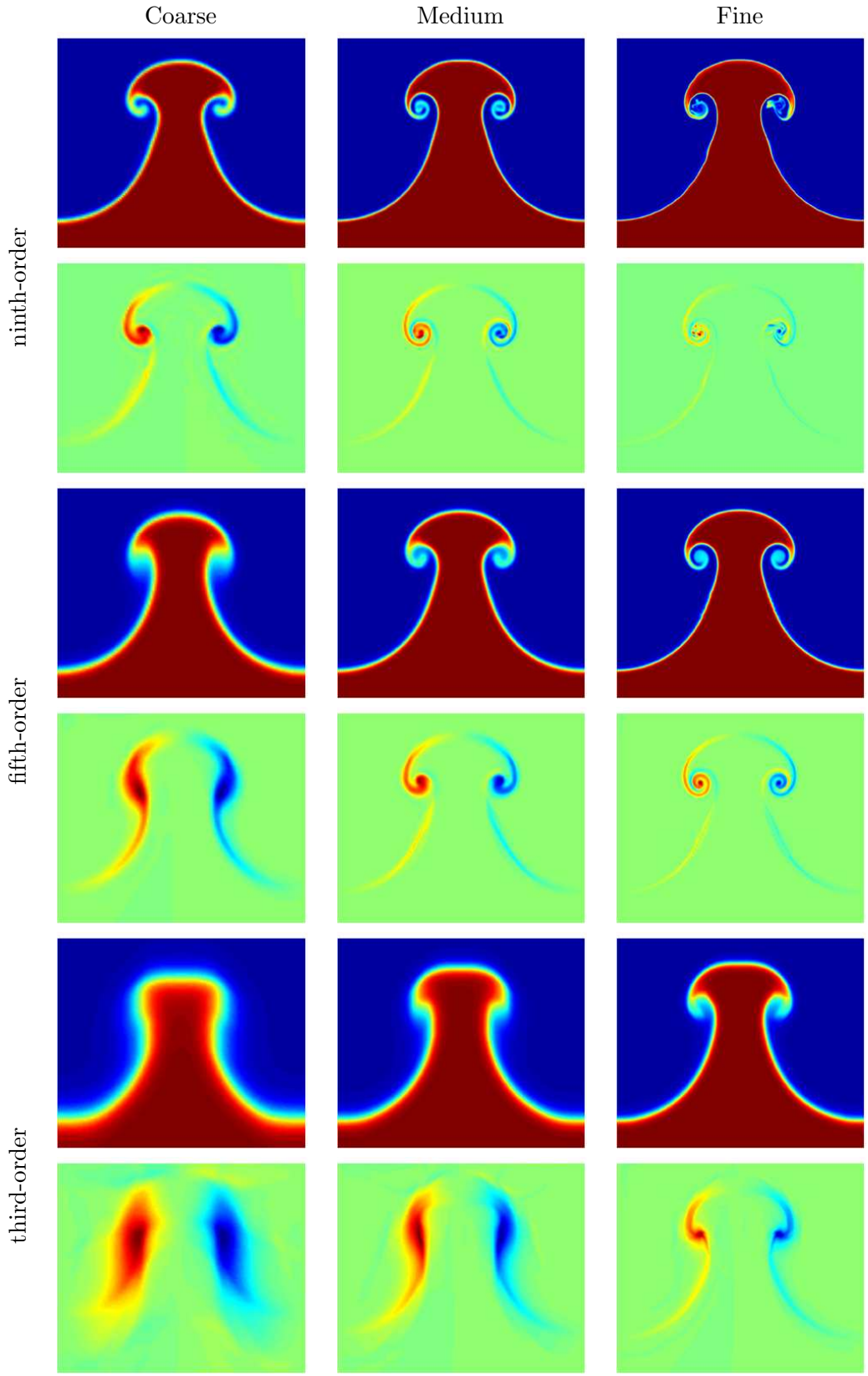

Figure 70: Density and vorticity at $t = 4$ ms.

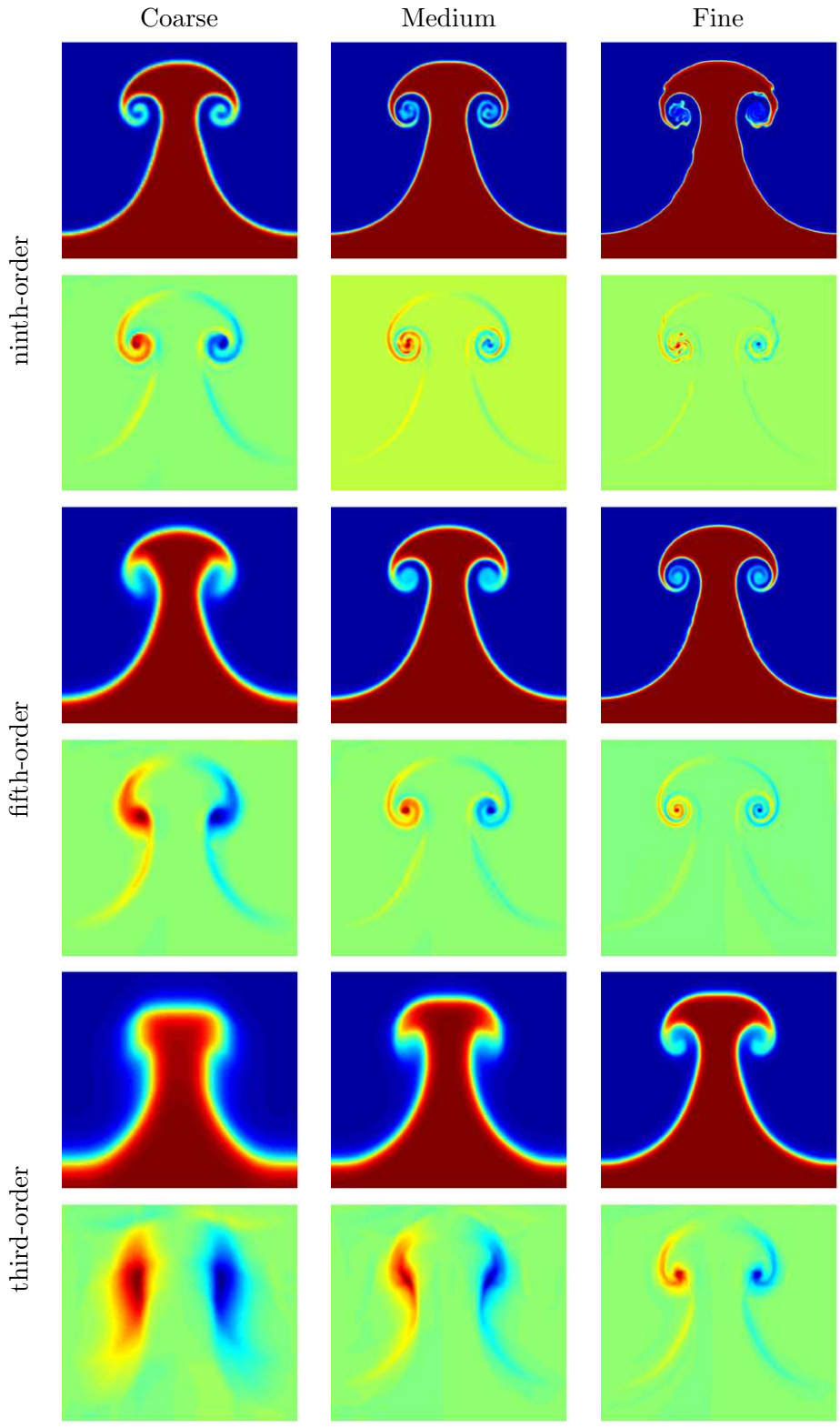

Figure 71: Density and vorticity at $t = 5$ ms.

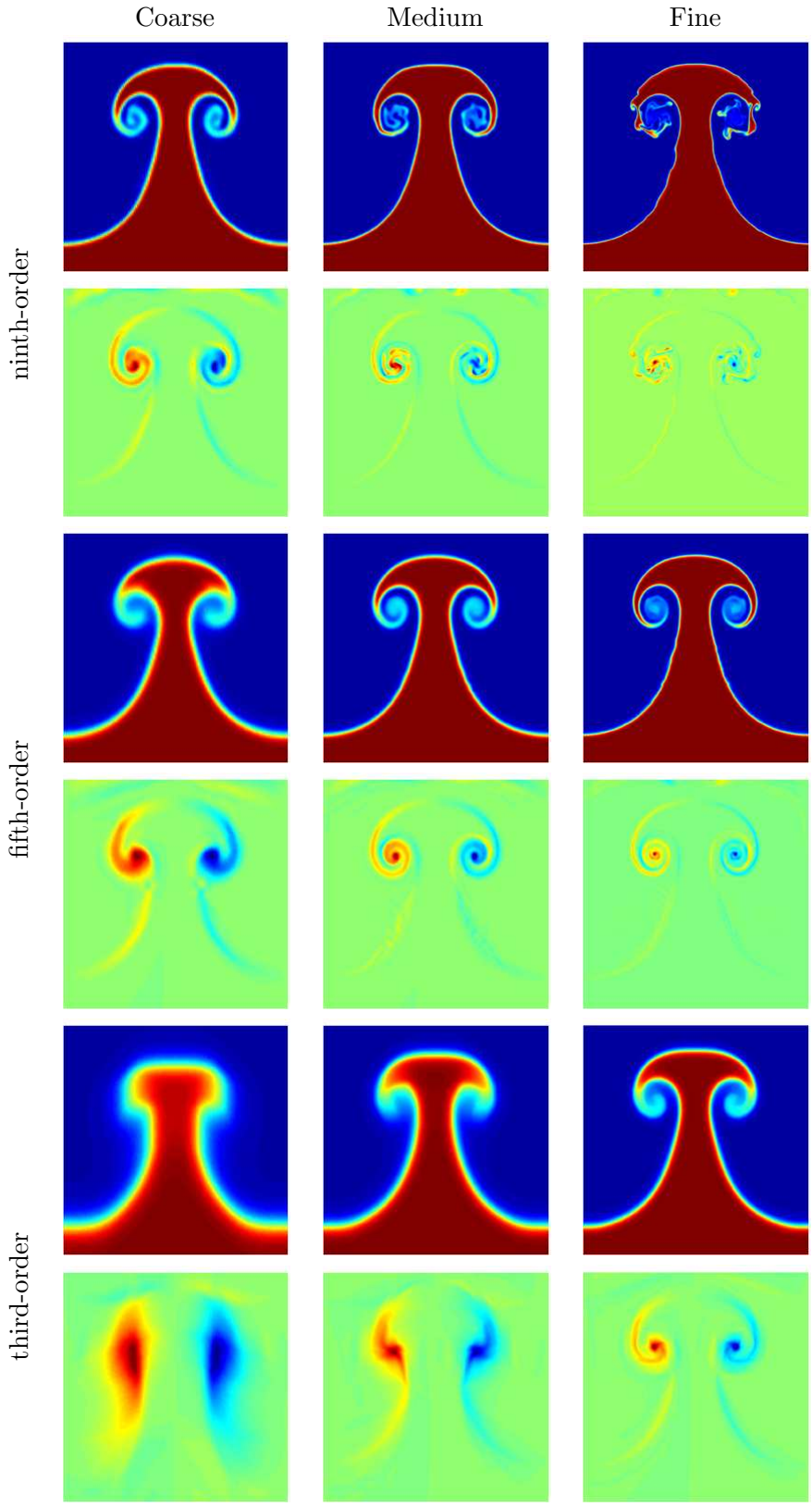

Figure 72: Density and vorticity at $t = 6$ ms.

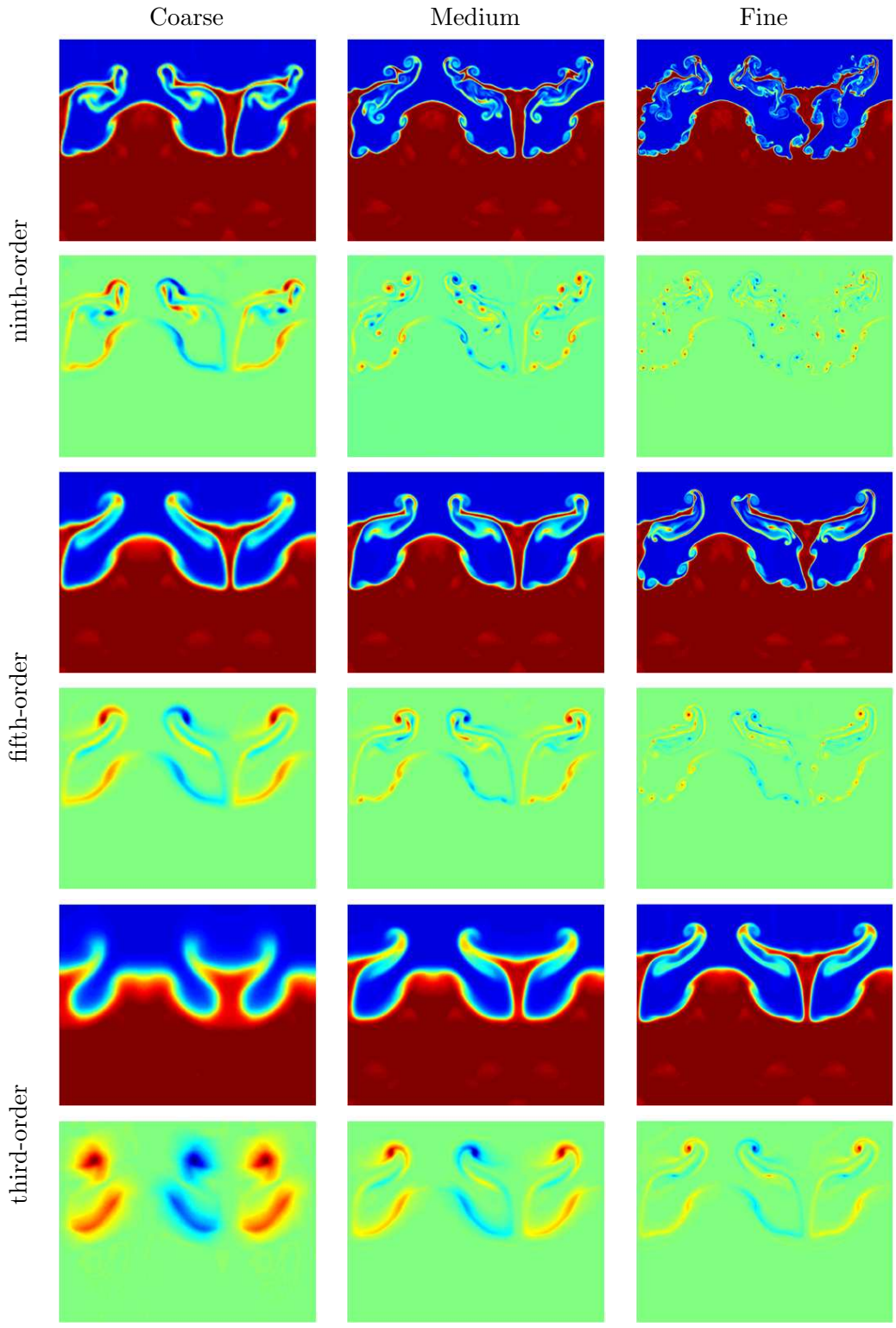

Figure 73: Density and vorticity at $t = 7$ ms.

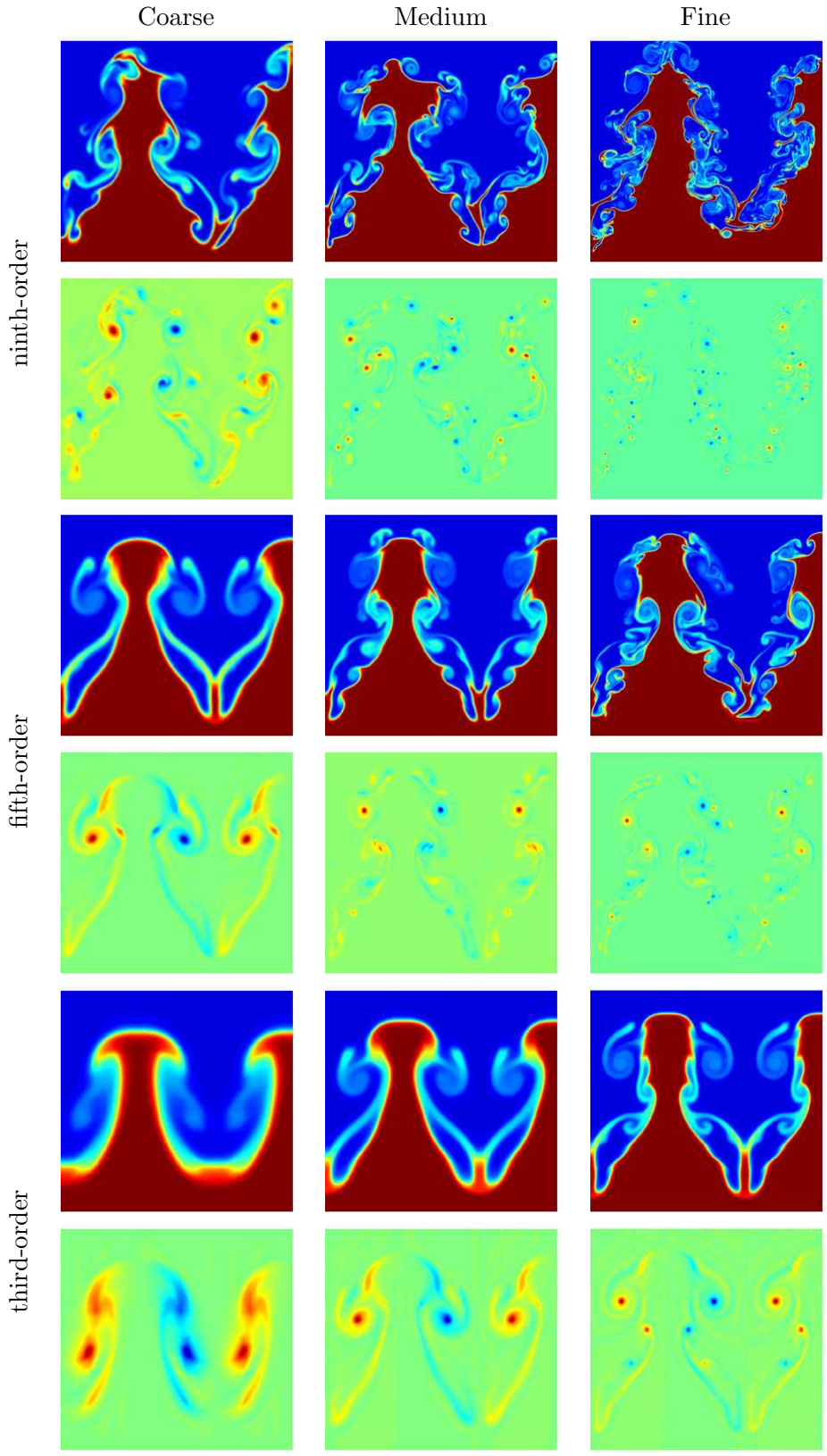

Figure 74: Density and vorticity at $t = 8$ ms.

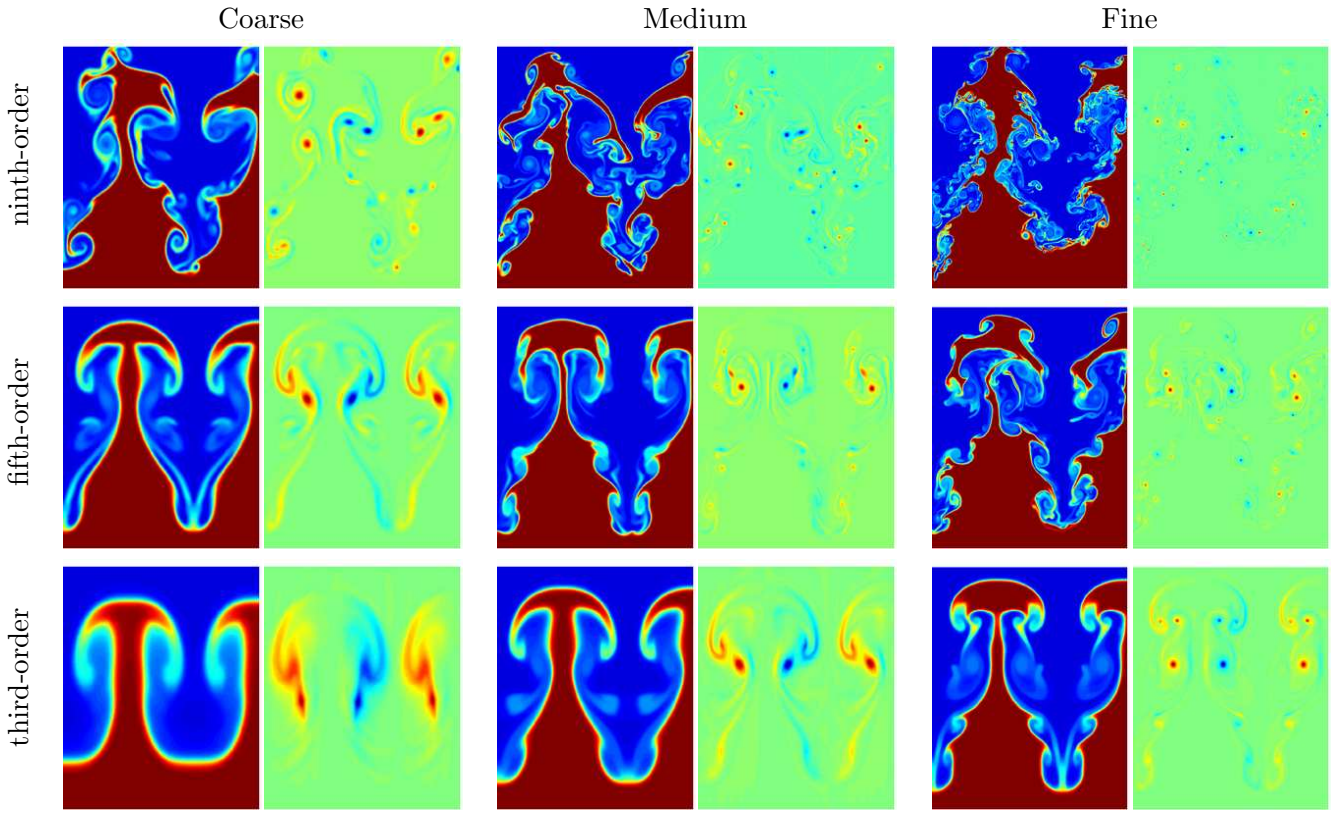

Figure 75: Density and vorticity at $t = 9$ ms.

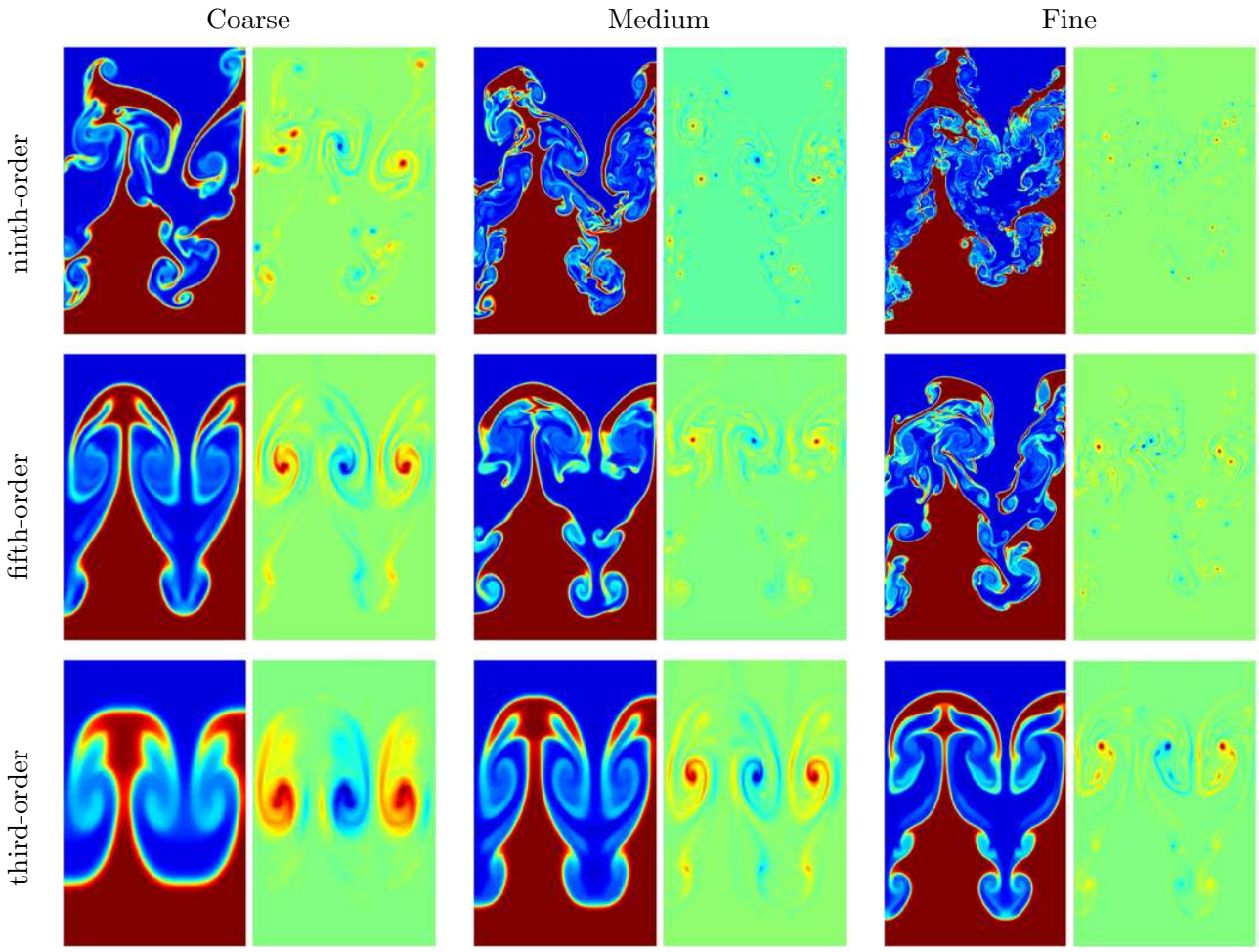

Figure 76: Density and vorticity at $t = 10$ ms.

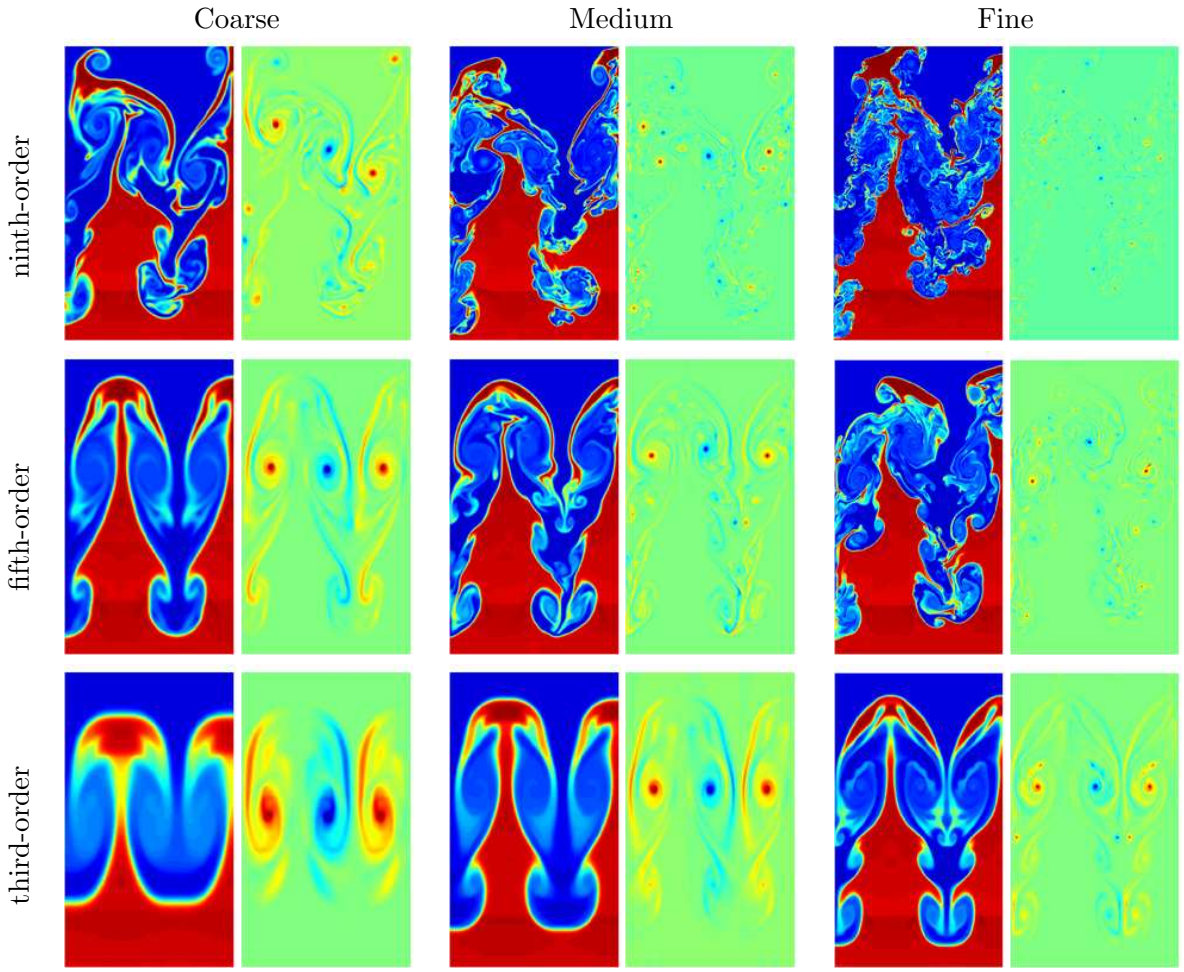

Figure 77: Density and vorticity at $t = 11$ ms.

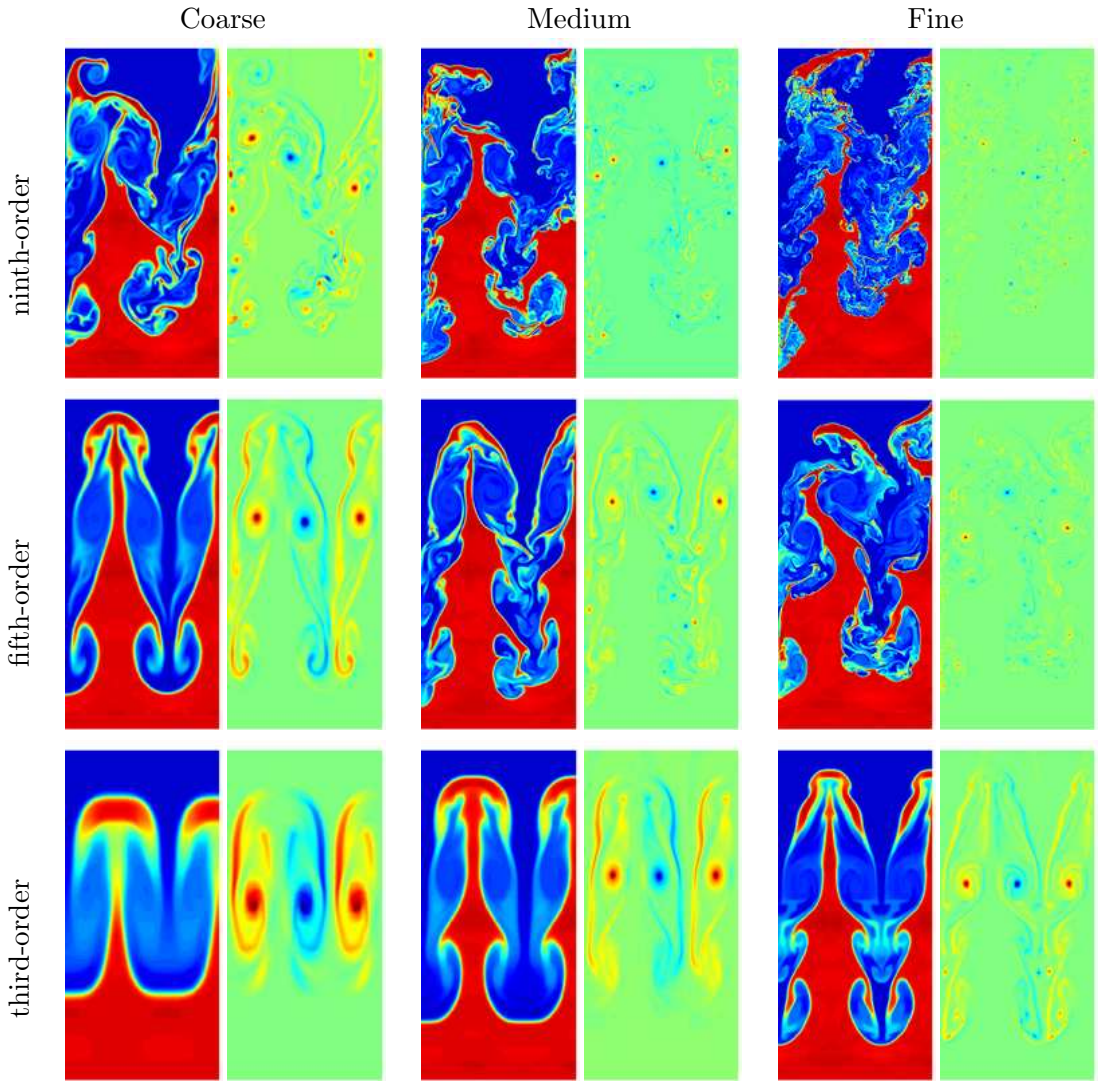

Figure 78: Density and vorticity at $t = 12$ ms.

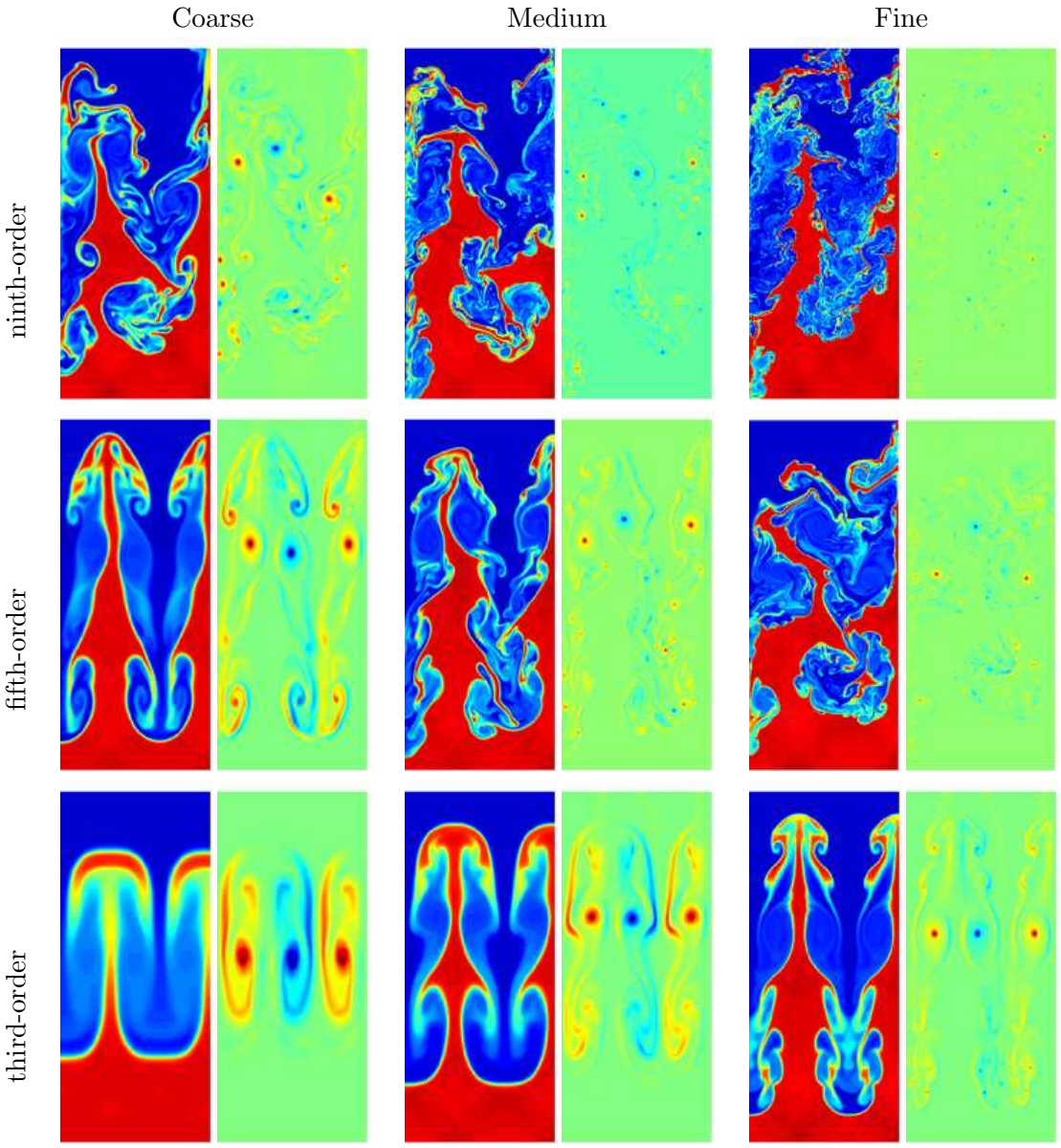

Figure 79: Density and vorticity at $t = 13$ ms.

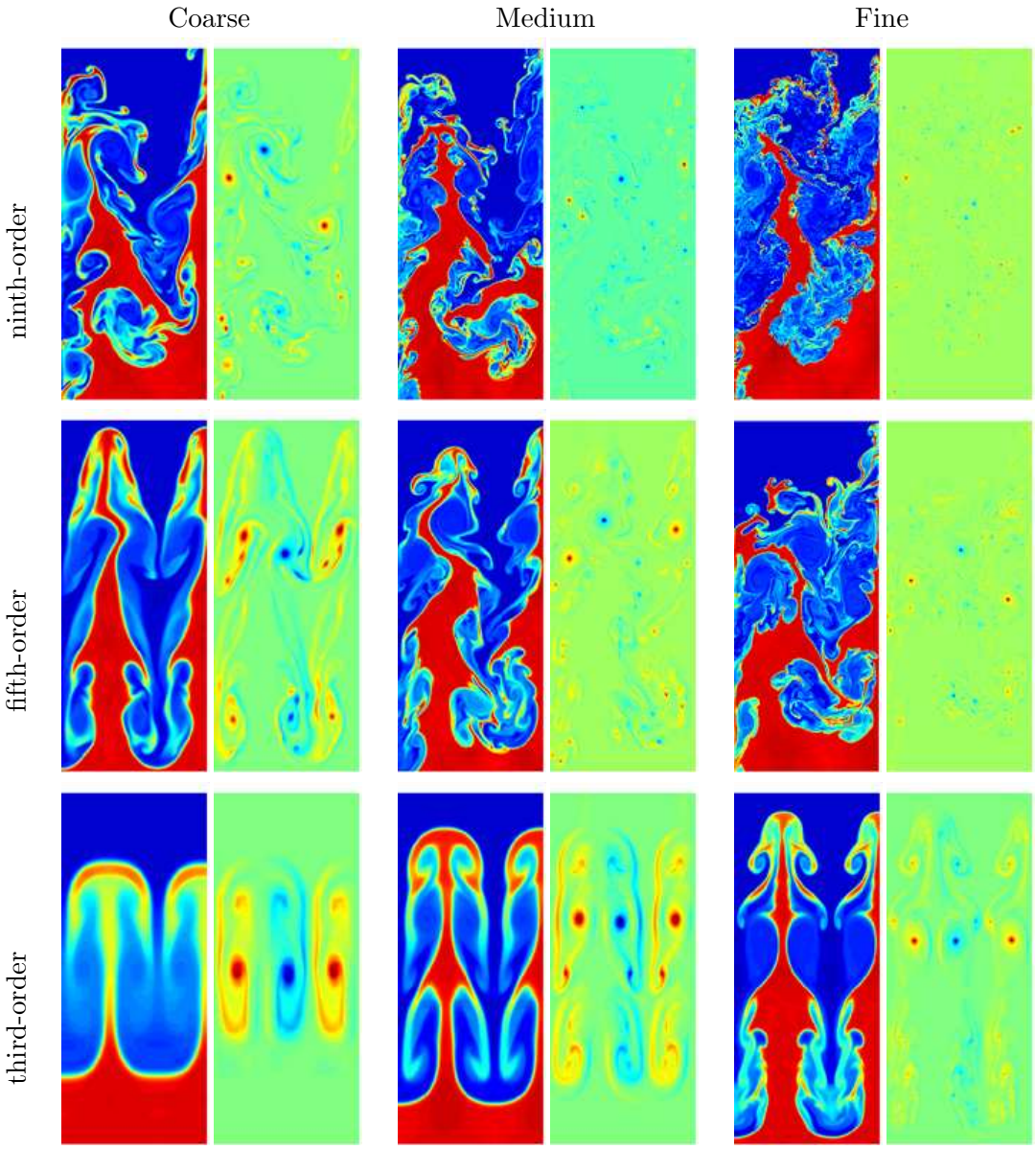

Figure 80: Density and vorticity at $t = 14$ ms.

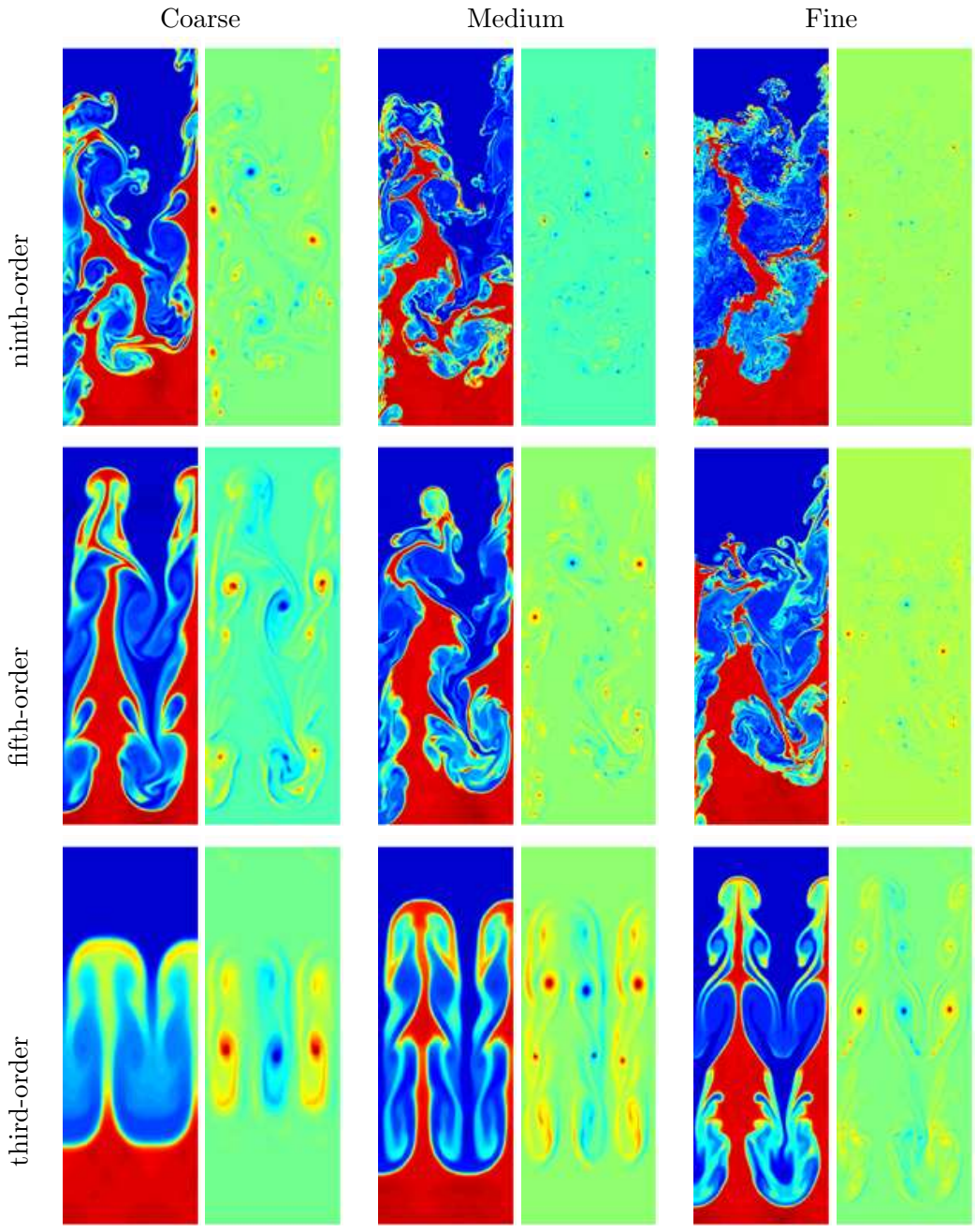

Figure 81: Density and vorticity at $t = 15$ ms.

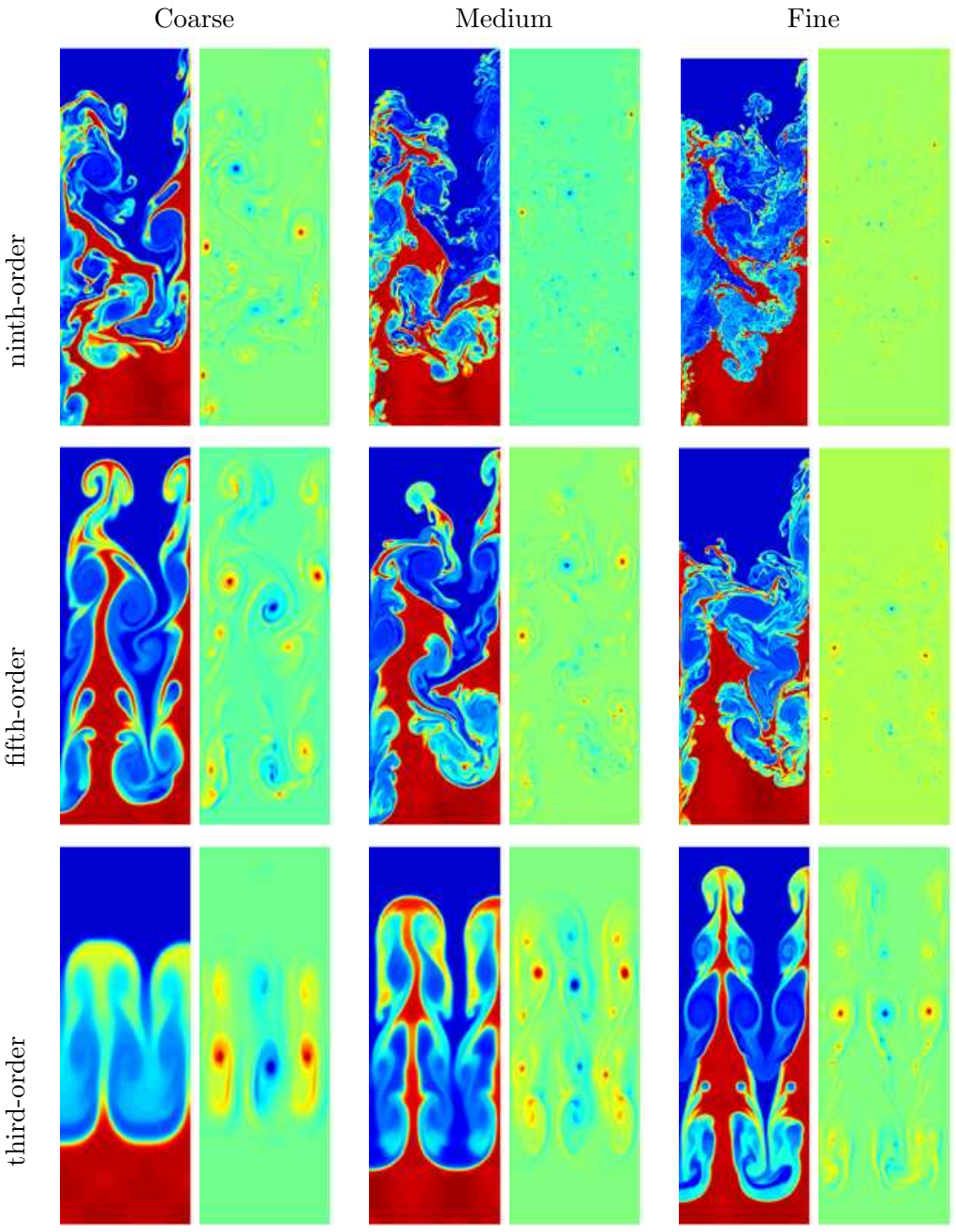

Figure 82: Density and vorticity at $t = 16$ ms.

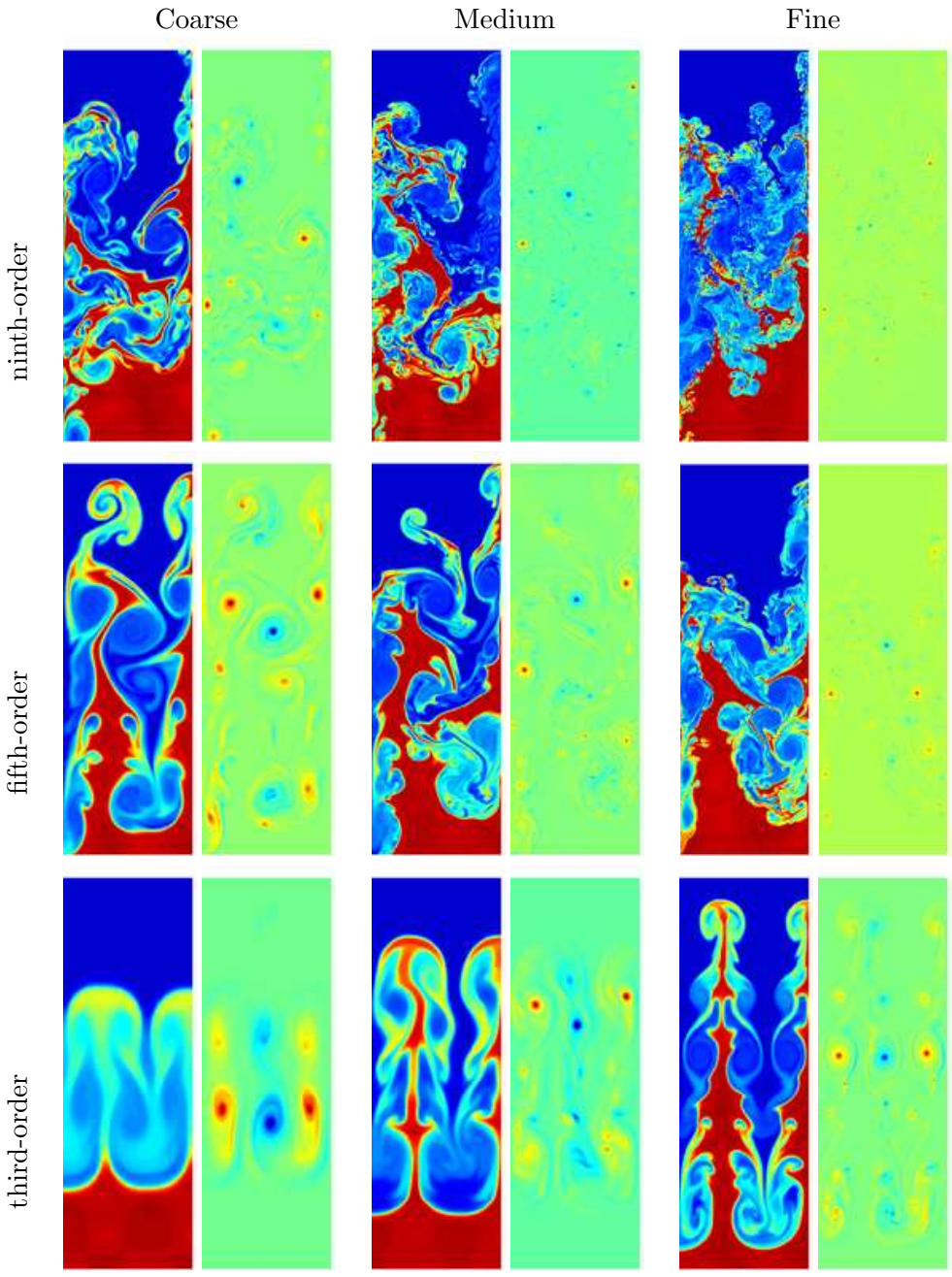

Figure 83: Density and vorticity at $t = 17$ ms.

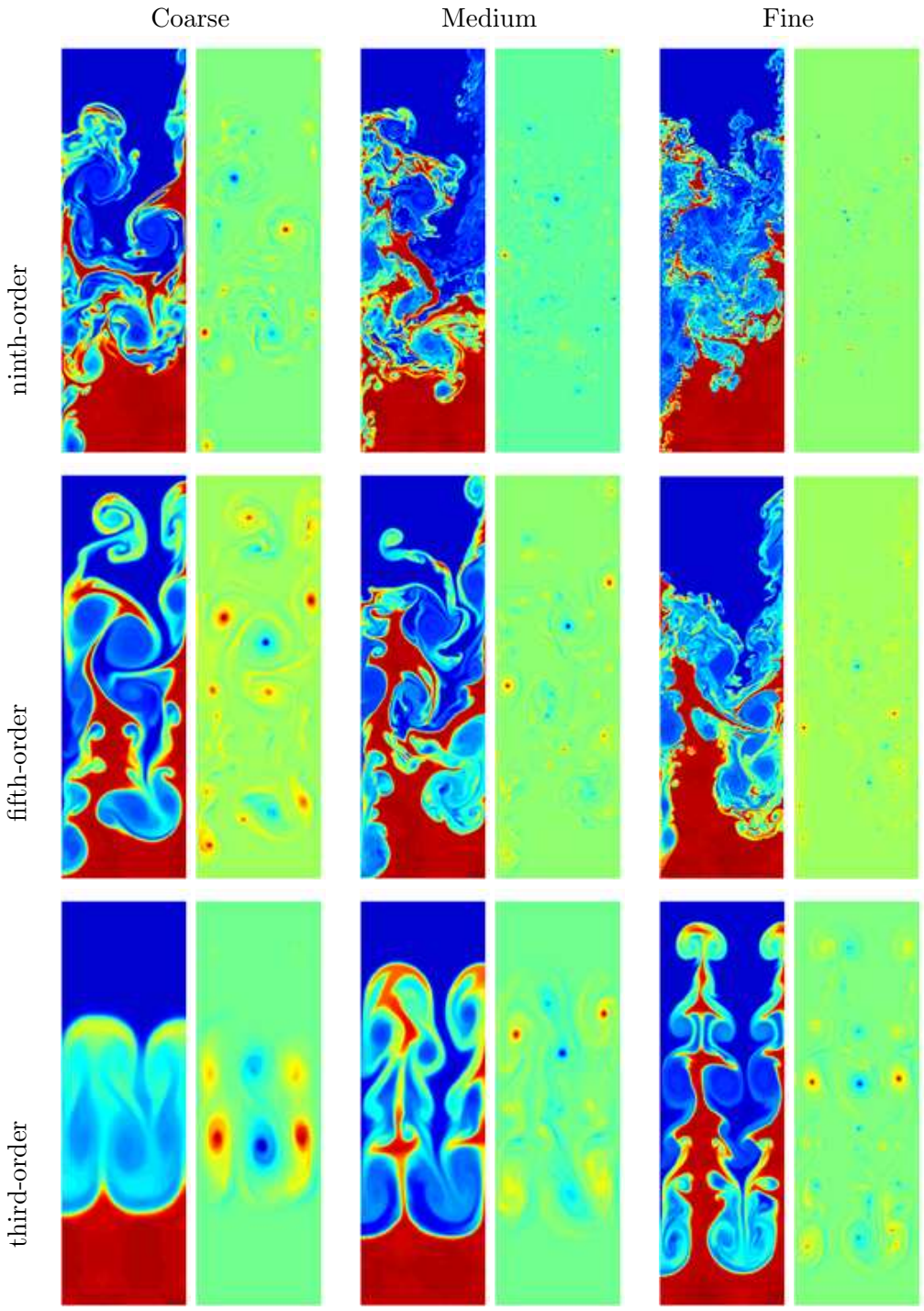

Figure 84: Density and vorticity at $t = 18$ ms.

Order	Coarse grid	Medium grid	Fine grid
9	0.4	2.3	20.7
5	0.2	1.0	9.5
3	0.17	0.8	7.1

Table 4: Ratio of CPU times for advancing the simulations by $\Delta t = 0.1$ ms compared with the time needed for the fifth-order simulation at medium resolution.

5.9 Computational scaling of the simulations

The simulations presented in this report were conducted on the Blue Pacific computer at the Lawrence Livermore National Laboratory. For each case, 32 nodes were used with a total of 128 processors. Each simulation was carried out to a time of at least $t = 18$ ms. The CPU times required to advance the simulation between $t = 12.5$ ms and $t = 12.6$ ms were compared to the time required for the fifth-order medium grid simulation. The late times are chosen because at earlier times the domain increases due to the adaptive domain feature of the `HOPE` code [68]. The ratio of the CPU times for the simulations and the time needed for the fifth-order medium grid case are presented in Table 4. Increasing the order of WENO reconstruction requires twice the computational time, whereas doubling the grid resolution requires five to eight times more computational time.

The analysis presented here suggests that similar results are observed when either the order of reconstruction was increased, keeping the grid resolution fixed, or the resolution was doubled, keeping the order of reconstruction fixed. The CPU times suggest that the use of high-order methods is less computationally expensive than increasing the grid resolution. Thus, the use of high-order methods can lead to a significant advantage in three-dimensional simulations of complex hydrodynamic flows.

6 Summary and conclusions

The high-resolution weighted essentially non-oscillatory (WENO) shock-capturing method implemented in the `HOPE` code was applied to investigate the classical two-dimensional, single-mode Richtmyer-Meshkov instability in planar geometry with reshock. The current simulations were conducted in the spirit of monotone-integrated large-eddy simulation (MILES), *i.e.*, molecular dissipation and diffusion terms in the governing equations were neglected. The initial conditions and computational domain approximate the Mach 1.21 air(acetone)/SF_6 shock tube experiment of Collins and Jacobs [29]. Only the test section of the shock tube was simulated, so that the reflected rarefaction wave present in the experiment was not explicitly captured in the simulations. A single value of the adiabatic exponent was used, as additional algorithm development is required for a robust two-fluid implementation in the `HOPE` code. Future simulations with explicit molecular dissipation and with subgrid-scale models are also planned to more accurately model the flow physics. Simulations with eleventh-order reconstruction, and with a hybrid WENO/central difference method are also envisaged. Three-dimensional simulations and analysis of the classical multi-mode Richtmyer-Meshkov instability with reshock are the subject of Part 4 of this report [70].

The simulations were performed in two spatial dimensions using the Euler equations for the following reasons:

1. the initial conditions based on the Collins-Jacobs shock tube experiment are effectively two-dimensional, so that a two-dimensional simulation is expected to capture the essential flow features prior to reshock;

2. it is possible to achieve much higher spatial resolution in two dimensions than in three dimensions, thereby affording highly-resolved simulations that are less affected by numerical diffusion;

3. two-dimensional simulations allow the study of the breakup of structures and the transfer of energy to small scales in the absence of the vortex stretching mechanism, and facilitate comparisons to previous two-dimensional simulations and to the predictions of linear and nonlinear amplitude growth models;

4. it is computationally challenging to perform three-dimensional simulations with explicit molecular dissipation and diffusion that capture all of the spatio-temporal scales present in a complex flow, particularly following reshock, while sharply capturing the shock.

The complex issues concerning the consequences of the reduction of the accuracy of numerical solutions of nonlinear problems to first-order upon shock passage [77, 34, 24, 25] are not addressed in the present work. In this sense, the spatial truncation error of a higher-order method can be parameterized in terms of the grid resolution Δx by

$$\varepsilon(r, \Delta x) = c\,\Delta x + c_r\,(\Delta x)^r \ , \tag{267}$$

where c and c_r are constants dependent upon the flow and on the specific numerical scheme, and r is the spatial order of accuracy of the scheme (*n.b.*, the error increases with increasing shock strength). The first term on the right side is the error due to the shock, and the second term on the right is the error in a smooth flow region. Note that only those regions in the computational domain where information propagates through a shock are susceptible to such

shock-capturing errors. While these issues are common to *all* shock-capturing methods (irrespective of their formal order of accuracy) when the initial shock passes through a perturbed interface to generate the Richtmyer-Meshkov instability and when the reshock of the evolving interface occurs, it is quite apparent from the present investigation that the properties of the relatively smooth and nearly-incompressible flow following reshock are strongly affected by the order of the method. This topic deserves further investigation, analysis, and discussion of its physical implications.

Numerical simulations were performed using third-, fifth-, and ninth-order spatial flux reconstruction and uniform spatial grid resolution with 128, 256, and 512 points per initial perturbation wavelength. To our knowledge, *the present work represents the first comprehensive application of the WENO method to the computational study of the classical Richtmyer-Meshkov instability with reshock*. It should be noted that a detailed numerical study of the single-mode, 'impulsive Richtmyer-Meshkov' instability experiment with reshock of Jacobs, Jones and Niederhaus [54, 97, 98] was performed by Kotelnikov and Zabusky [63] and Kotelnikov, Ray and Zabusky [62] using the vortex-in-cell method and the contour advection semi-Lagrangian method (*n.b.*, Kotelnikov, Ray and Zabusky [62] also simulated the Jacobs et al. [53] and Rightley et al. [107] Mach 1.2 experiment with reshock using a Godunov method, and compared the results with their incompressible results). Furthermore, to our knowledge, *the present work is the first systematic investigation of the effects of both order of reconstruction and grid resolution in a given high-resolution method, as applied to this instability*. The comparison of results obtained with different grid resolutions and reconstructions is similar in spirit to the work of Cook, Cabot and Greenough [30], in which a centered ENO scheme, a higher-order Godunov method, and a filtered spectral/compact difference method (applied to the Shu-Osher problem, Collins-Jacobs experiment prior to reshock, and Taylor-Green vortex) were compared. The comparison of results obtained with fifth- and ninth-order WENO reconstruction in the present study showed that similar structures can be obtained using the higher-order reconstruction with one-half of the grid resolution in each direction—a similar conclusion obtained previously for the Rayleigh-Taylor instability [114]. This result can be explained using (267) as follows. The error can be decreased by halving Δx or by doubling r. Let $\varepsilon(r, \Delta x)$ in Eq. (267) represent the error for a given Δx and r. Let $\Delta x' = \Delta x/2$ and $r' = 2r$ (corresponding to doubling the grid resolution and doubling the order). Doubling the grid resolution gives

$$\begin{aligned} \varepsilon(r, \Delta x') &= c\,\Delta x' + c_r \left(\Delta x'\right)^r \\ &= c\,\frac{\Delta x}{2} + c_r \left(\Delta x\right)^r \left(\frac{1}{2}\right)^r , \end{aligned} \tag{268}$$

while doubling the order of spatial reconstruction gives

$$\begin{aligned} \varepsilon(r', \Delta x) &= c\,\Delta x + c_{r'} \left(\Delta x\right)^{r'} \\ &= c\,\Delta x + c_{r'} \left(\Delta x\right)^r \left(\Delta x\right)^r . \end{aligned} \tag{269}$$

If $c_{r'} \sim c_r$ then, comparing the truncation errors in Eqs. (268) and (269) indicates that doubling the order of reconstruction yields an overall smaller truncation error in the smooth region of the flow as $\Delta x < 1/2$. As much of the instability evolution occurs in regions far away from the shock, this explains why doubling the order of reconstruction gives comparable results to doubling the grid resolution. Note that near the shock, doubling the grid resolution results in a smaller error than doubling the order of reconstruction. This reflects the trade-off

between the formal design order of a scheme and spatial resolution, which becomes even more computationally significant in three spatial dimensions. In the present study, it was found that doubling the grid resolution incurred an approximately nine-fold increase in computational cost; by contrast, increasing the order of spatial reconstruction incurred an approximately two-fold increase in cost.

While the numerical simulations presented here have several limitations (including the consideration of only the shock tube test section, and two-dimensional flow), the excellent agreement with experimental data prior to reshock provides encouragement for the continued use of the WENO method for the quantitative investigation of complex hydrodynamic flows induced by shocks. In particular, Part 3 [69] and Part 4 [70] of this report will consider the oblique single-mode Richtmyer-Meshkov instability in two dimensions and the multi-mode Richtmyer-Meshkov instability with reshock in three dimensions, respectively. Presented below is a summary of the principal findings in each of the three main subjects of investigation in the present report.

6.1 Mixing layer growth

A comprehensive analysis of the instability evolution was presented in the first part of the report in § 2 and 3, including: (1) a comparison of the density from a fifth- and ninth-order WENO simulation (using a uniform grid resolution of 256 points per initial perturbation wavelength) to experimental PLIF images; (2) a comparison of the mixing layer growth before and after reshock with the predictions of analytical, semi-analytical, and phenomenological amplitude (mixing layer) growth models, and; (3) an investigation of the circulation deposition. The simulations were performed up to time $t = 18$ ms–much later than reported in the Collins and Jacobs [29] experiment ($t = 11$ ms).

6.1.1 Comparison of density and experimental PLIF images

The comparison of density and experimental PLIF images shows that it is possible to achieve very good agreement between a two-dimensional, high-resolution, shock-capturing simulation with high-order flux reconstruction and density PLIF images from a Richtmyer-Meshkov experiment with a two-dimensional initial perturbation before reshock when three-dimensional effects are not very significant. The comparison of densities from the simulation with fifth- and ninth-order reconstruction demonstrates that higher-order reconstruction better captures secondary instabilities, the roll-ups appear tighter and sharper, and more fine-scale structures are present. Following reshock, the experiment and simulations show distinctively different flow structures. This is due to the absence of the initial rarefaction wave and the increased importance of three-dimensional effects (including vortex-stretching) that are not captured in the two-dimensional simulations. As a result, the density fields obtained from the simulation and the corrected density PLIF images from the experiment lag in time by ≈ 1 ms. Simulated density Schlieren images were also presented to illustrate the complex wave interactions occurring during the reshock process, *i.e.*, the reflected and transmitted waves, and the focusing effects that are very difficult to image experimentally. At late times, the densities from the simulations show the formation of large-scale structures consistent with the inverse cascade of kinetic energy from small scales to larger scales observed in other two-dimensional simulations. The comparison of fifth- and ninth-order simulations shows that finer asymmetric structures appear in the higher-order simulations, consistent with reduced numerical dissipation and a reduced inverse cascade.

6.1.2 Comparison to the predictions of linear and nonlinear models prior to reshock

The amplitude growth prior to reshock was compared to the experimental data and to the predictions of various classical and recent models for amplitude growth in the linear and weakly-nonlinear regimes. Excellent quantitative agreement was found between the amplitude obtained from the fifth-order simulation on the medium resolution (256 points per initial perturbation wavelength) grid and the experimental data points prior to reshock. As expected, the simulation data was also in excellent agreement with linear models at early times t satisfying $kv_0t \lesssim 1$, where v_0 is given in Eq. (12). At later times, the simulation data was shown to be in best agreement with the predictions of the Zhang-Sohn Padé amplitude growth model. Thus, this component of the present work provides further validation of the `HOPE` code and of the WENO method against experimental data corresponding to the Richtmyer-Meshkov instability.

6.1.3 Comparison to the predictions of models using parameters determined from experimental and numerical simulation data

The experimental parameters from the Collins and Jacobs experiments and the parameters from the present simulation were used to compute the terms in the nonlinear mixing layer growth models. It was shown that small variations in these parameters have a dramatic effect on the predictions of nonlinear amplitude growth models. In particular, it was shown that when experimental data is used, the prediction of the Sadot model is in best agreement with the experimental and simulation mixing layer width; by contrast when the simulation data is used, the prediction of the Zhang-Sohn model is in best agreement. Computation of the root-mean-square of the difference between the simulation results and the model predictions indicates that: when the model parameters are obtained from experimental data, the root-mean-square is minimized with the Sadot model; when the model parameters are obtained from the simulation data, the Zhang-Sohn model minimizes the root-mean-square error.

6.1.4 Comparison to the predictions of models accounting for reshock

Following reshock, it was shown that the instability evolution did not agree with the experimental PLIF images, as the rarefaction wave and three-dimensional effects were not accounted for in the numerical simulation. The absence of the reflected rarefaction wave allows a comparison of the mixing layer amplitude growth following reshock from the numerical simulation with the predictions of the Mikaelian [87] and Brouillette-Sturtevant [21] post-reshock growth models. The simulation data was shown to be consistent with the linear-in-time growth predicted by the Mikaelian model immediately following reshock. The Brouillette-Sturtevant model also predicts a linear growth, but with a smaller slope than the Mikaelian model. At later times following reshock, the simulation data lies between the predictions of the Mikaelian and Brouillette-Sturtevant models. As expected, the amplitudes turn over and grow at a slower rate at sufficiently large times following reshock. In general, it is clear that additional experimental data is needed to provide a more complete validation, especially following reshock of the evolving mixing layer.

6.1.5 Baroclinic deposition of circulation on the interface

To quantify the driving mechanism for the evolution of the Richtmyer-Meshkov instability, the circulation deposited on the interface by the shock was computed. Immediately following the first interaction with the shock, the circulation has a sinusoidal distribution on the interface. Integrating over an entire period yields zero total circulation, as expected. The positive and negative components of the circulation show an increase following the shock interaction, consistent with secondary baroclinic vorticity deposition. This secondary instability is responsible for the complex structures observed in the roll-ups of the Richtmyer-Meshkov instability and for additional vorticity deposition on the interface. Reshock causes the deposition of additional vorticity of opposite sign, which is further amplified by the secondary baroclinic vorticity deposition. Following the interaction with the reflected rarefaction wave, complex structures form and symmetry breaks, resulting in large discrepancies between the positive and negative vorticity: this results in a non-zero total circulation.

6.2 Local and global mixing analysis

The second part of the report in § 4 presented an extensive investigation of mixing before and after reshock including the time-evolution of the: (1) volume fraction and mixing fraction profiles; (2) mixing fractions and volume-averaged quantities; (3) fluctuating kinetic energy, fluctuating enstrophy, density variance, and pressure variance spectra, and; (4) statistics. In addition, the effects of reflected waves (outflow and reflecting boundary conditions) on these quantities were also investigated.

6.2.1 Volume fraction and mixing fraction profiles

The analysis included an examination of the profiles of mole fractions and other quantities characterizing the mixing over the extent of the layer as a function of time. Many of these quantities were adopted from previous analysis of Rayleigh-Taylor mixing, suitably modified for their application to shocked compressible flow. The profiles were recentered by the location of the midpoint of the interface and rescaled by the total mixing layer width in order to investigate the dynamics of mixing within the layer and the apparent collapse of the profiles at late times. The observed characteristics of the mixing averaged over the direction of shock propagation were qualitatively explained using the product mole fraction profiles, volume fraction profiles, and other related quantities.

The analysis indicates that the mole fraction profile $\langle X \rangle$ is appropriate to measure the evolving redistribution of mass within the mixing layer caused by the creation of bubble- and spike-like structures. In particular, prior to reshock the principal mechanisms affecting the mole fraction are the creation of a single, dominant bubble and spike; following reshock, the principal mechanism is the excitation of many smaller bubbles and spikes contributing to the highly-irregular, topologically-complex structure observed. These additional bubbles and spikes are responsible for elongating the mixing layer, resulting in a distribution of mass that is nearly uniformly increasing across the layer from the air(acetone) to the SF_6 side. The analysis also suggests that $\langle X_p \rangle$ and $X_p\left(\langle X \rangle\right)$ are necessary to understand how well the mass is mixed across the layer. Large peaks are observed at early times due to the diffusive initial conditions; as the spike and bubble evolve through the linear phase, the two peaks separate and as the roll-ups form, additional peaks are observed corresponding to well-mixed fluids within the roll-ups; following reshock, several smaller roll-ups form, contributing to a larger number of peaks,

indicating large regions with localized well-mixed air and SF_6; at late times the formation of large-scale structures contribute to the appearance of large, wide peaks with smaller peaks of well-mixed fluid. This late-time behavior is consistent with the inverse cascade of small-scale velocity fluctuations to larger scales observed in two-dimensional turbulent flows. Finally, the mixing fractions θ and ξ provide similar characterizations of the mixing process, showing large areas of localized mixing within the layer at late times.

6.2.2 Time-evolution of mixing fractions and volume-averaged quantities

This analysis included integrating $\langle X_p \rangle$ and $X_p(\langle X \rangle)$ over the mixing layer to obtain the production fractions P_t and P_m, respectively, and the mixing fraction Ξ. The molecular mixing fraction Θ was also considered, with a behavior qualitatively similar to that of of Ξ. The evolution of P_t and P_m prior to reshock is dominated by the formation of the bubble of unmixed fluid, which causes P_m to decrease and Ξ to increase. Following reshock the layer is compressed, causing a well-mixed region to form, as shown by the formation of a sharply-peaked value in the mixing fractions. This well-mixed region is characterized by the rapid production of small-scale structures by the reshock process, as shown earlier. Subsequently, the mixing layer undergoes a rapid growth as the inversion occurs, causing the overall mixing to decrease rapidly over a time interval of approximately two milliseconds.

6.2.3 Time-evolution of the fluctuating kinetic energy, fluctuating enstrophy, density variance, and pressure variance spectra

The investigation of the spectral evolution both prior to and following reshock provides a spectral quantification of the complex features observed in the density and Schlieren images. In particular, the investigation of spectra showed that a fairly broad range of scales already exists prior to reshock, despite the fact that the roll-up from a single-mode initial perturbation is considered. This indicates that the Richtmyer-Meshkov instability develops non-trivial spectral content from its inception. At reshock, the fluctuations in all fields (except for the density) are amplified nearly uniformly across all scales. From the results obtained here, reshock does not appear to broaden the range of scales, but primarily imparts energy into structures of all sizes. At late times, dissipation mechanisms smooth the spectra. When the shock is far away and the reflected waves become weaker, a very slow decay is observed in the spectra. Compared to the kinetic energy spectrum, the fluctuating enstrophy spectrum shows a more pronounced cascade toward small scales, as expected by two-dimensional turbulence phenomenology. Compared to the other spectra, the pressure spectrum shows the effects of reflected waves with increased values observed following reshock at $t = 7$ ms and during the arrival of the reflected rarefaction wave at $t = 11$ ms. Thus, quantities depending on pressure fluctuations cannot be neglected in turbulent transport and mixing models. By contrast, density fluctuations do not exhibit such strong sensitivity to reshock. The density spectrum shows that the density fluctuations remain small and are not affected strongly by reshock. The decomposition of the energy spectrum into the streamwise and spanwise components, indicates that the streamwise component is dominant, as expected, and that significant statistical anisotropy exists even at late times. To our knowledge, *this represents the first examination of the fluctuation enstrophy, density variance, and pressure variance spectra in a reshocked Richtmyer-Meshkov mixing layer.*

6.2.4 Time-evolution of statistics

The time-evolution of volume-integrated (or wavenumber-integrated) variances were investigated. The fluctuating kinetic energy exhibited a sharp peak corresponding to reshock, with a rapid increase followed by a rapid decrease, followed then by a decay. The decay becomes more established following the interaction with the reflected rarefaction wave at $t = 11$ ms. The streamwise and spanwise components indicate that statistical isotropy is achieved at late times. In fact, the total energy content of the spanwise component increases following the interaction with reflected waves and the large values of the streamwise component decrease due to dissipation. The fluctuating enstrophy also exhibited a sharp peak corresponding to reshock and then a rapid decay following the interaction with the reflected rarefaction wave. The density variance is very small in magnitude and remains nearly constant, although signatures of the reflected shock and the reflected rarefaction are evident. The pressure variance showed narrow sharp peaks corresponding to the reshock and the arrival of the reflected rarefaction wave, and further showed the arrival of the reflected compression wave at late times. In all three cases, the waves excite fluctuations that are apparent in the increased values of the statistics. The fluctuations are damped and the variances decrease in magnitude as time evolves.

6.2.5 The effects of reflected waves: outflow and reflecting boundary conditions

The effects of reflecting or outflow boundary conditions at the shock tube end wall (end of the computational domain) on the amplitude growth and other properties were investigated. It was shown that the mixing layer width computed using the reflecting boundary condition was significantly larger than that computed using the outflow boundary condition following the arrival of the reflected rarefaction wave at $t \approx 10$ ms: the widths differed by ≈ 9 cm at a time 8 ms following the arrival of the reflected rarefaction wave. As the outflow boundary condition case eliminates wave-interface interactions subsequent to reshock, the flow transitions to a decaying flow at sufficiently large times after reshock. A quasi-decaying flow develops at late times in the reflecting boundary condition case, as multiple (successively weaker) wave-interface interactions occur. To our knowledge, *this is the first numerical study that removed the effects of reflected waves on the evolution after reshock, and showed their important role on the dynamics of the flow following reshock.*

The results also characterize the effects of the reflected rarefaction wave on the mixing layer. The reflected rarefaction wave, while not significantly increasing the energy content in the layer, plays an important role in achieving statistical isotropy by exciting fluctuations in the periodic direction. The results also indicate that the reflected rarefaction wave has a small effect on the fluctuating enstrophy and the pressure variance evolution. By contrast, reshock causes a compression of the layer and a significant deposition of energy that allows the layer to grow very rapidly, concomitant with the formation of complex structures. The reflected rarefaction wave instead "stretches" the mixing layer, causing it to grow, but provides little additional energy causing the overall mixing to decrease, as measured by the mixing fractions. The additional mixing provided by the reflected waves is responsible for the statistical isotropy. This comparison further supports the important role that reflected waves have in the dynamics of the flow following reshock. These results also have important implications for modeling turbulent transport and mixing induced by the Richtmyer-Meshkov instability with reshock.

6.3 The effects of order of reconstruction and of grid resolution

The dependence of the following quantities on the WENO order of spatial reconstruction and grid resolution was investigated: (1) the mixing layer width; (2) the circulation; (3) the mixing profiles; (4) the mixing fractions; (5) spectra; (6) statistics, and; (7) the density and vorticity fields. Third-, fifth- and ninth-order reconstructions were considered together with grid resolutions of 128, 256, and 512 points per initial perturbation wavelength λ. To our knowledge, *this is the first systematic investigation of profiles, spectra, and statistics as a function of both spatial resolution and order of reconstruction in the case of the Richtmyer-Meshkov instability.* The variation of the order of reconstruction and grid resolution in the present study investigated only the spatial discretization error in the method. It would be of interest to investigate the error in the temporal discretization by comparing the present results obtained using the third-order TVD Runge-Kutta scheme to those obtained using a second- and fourth-order Runge-Kutta time-evolution scheme, to investigate the cumulative effects of spatial and temporal discretization errors.

6.3.1 The effects on the mixing layer width

The mixing layer width exhibits little dependence on the order of reconstruction and grid resolution prior to reshock. However, following reshock but prior to the arrival of the reflected rarefaction wave, large differences in the mixing layer width are observed. As the order of reconstruction and grid resolution are increased, the differences between mixing layer widths decrease, providing evidence of 'convergence'. Following the arrival of the reflected rarefaction wave, the differences increase further. Finally, at late times, high-order, high-resolution simulations display significant fragmentation of the complex structures, causing oscillations in the widths as the cutoff limit used in the determination of the width is approached. The differences in the widths observed following reshock can be attributed to the effects of numerical dissipation, which suppresses the formation of small-scale structures in low-resolution, low-order simulations. Small structures do not have a direct effect on the width prior to reshock. However, the energy deposited into the layer by the reshock process is directly related to the presence of small-scale structures, which explains the differences in widths as less energy is deposited in low-order, low-resolution simulations.

The expression (267) suggests that the error of a high-order method vanishes in the limit $\Delta x \downarrow 0$. However, in general, there are no theoretical proofs of the convergence of multi-dimensional numerical solutions obtained using nonlinear methods for general flows described by the non-dissipative, compressible fluid dynamics equations (*i.e.*, Euler equations) [66]. Hence, *there is no guarantee of pointwise convergence of the numerical solution*, *i.e.*, grid refinement and increasing the order of resolution is not necessarily expected to yield pointwise-converged quantities. However, 'convergence' can be observed in large-scale quantities, such as the mixing layer width. In fact, as the order of reconstruction and the grid is refined, the mixing layer width prior to reshock also appears to 'converge'. It is interesting to note that some 'convergence' is also observed for the width following reshock ($t \geq 6$ ms), but prior to the arrival of the reflected rarefaction wave at $t \approx 10$ ms. As the grid is refined and the order of reconstruction is increased, the discrepancies between the widths decrease and the width obtained from the ninth-order simulation on the medium grid is nearly the same as that obtained from the ninth-order simulation on the fine grid. This 'convergence' is no longer apparent after the arrival of the reflected rarefaction wave, as the difference between the widths increases with time. The late-time width shows significant variation as the order of reconstruction is

increased and the grid is refined, indicating that the interpretation and parameterization of apparent power-law growth at late times using general expressions of the form

$$h(t) = a + b\,(t + t_0)^{\theta}\ , \tag{270}$$

where a, b, and θ are parameters, and t_0 is a virtual time origin [50], must be performed with great caution.

An analysis of the spectra from the simulations with different orders of flux reconstruction and grid resolutions compared to the spectrum obtained from the ninth-order simulation on the fine grid showed that there is no apparent 'convergence' of these spectra. This, together with an analysis of mixing fractions and other quantities sensitive to molecular mixing, shows that quantities sensitive to the small-scale structure of the flow do not generally exhibit 'convergence', while quantities determined primarily by the large-scale structures appear to be 'converged' at sufficiently high order of reconstruction and resolution. Hence, large-scale (*e.g.*, amplitude) data is insufficient to validate numerical simulation results, as quantities sensitive to fluctuations can differ significantly, while the large-scale structures are insensitive. These issues, and additional quantities such as probability distributions, other statistics, and turbulent transport quantities, will be discussed in Part 4 of this report [70]. Difference norms and other quantitative measures of the difference between simulation data of different order and resolution is relegated to future work.

6.3.2 The effects on the circulation

The positive and negative circulations weakly depend on the grid resolution and order of reconstruction. Prior to reshock, it is observed that low-order, low-resolution simulations yield smaller values of the magnitude of the positive and negative circulation, consistent with an increased numerical dissipation in these simulations. However, following reshock but prior to the arrival of the reflected rarefaction wave, no direct relationship can be established between the magnitudes of the negative and positive circulations and the grid resolution and order of flux reconstruction. This indicates that additional mechanisms influence the magnitude of the circulation following reshock. Finally, following the arrival of the reflected rarefaction wave, symmetry breaks and, as expected, the magnitudes of the positive and negative circulations become very different. However, if the positive and negative circulations are summed, the resulting total circulation shows a linear growth in time that is strongly dependent on the grid resolution of the simulation. It is found that the total circulation increased more rapidly for simulations with a higher grid resolution, and the values of the total circulations were independent of the order of flux reconstruction.

6.3.3 The effects on the mixing profiles

The mixing profiles exhibit different levels of sensitivity to the grid resolution and to the order of reconstruction. Before reshock and immediately after reshock, structures agree to a large extent, with peaks of similar shape and structures at similar locations within the mixing layer. However, for intermediate and late times following reshock, the development of mixing is significantly affected by the order of reconstruction and the grid resolution. Peaks now appear in different locations and have different shapes. In general, the high-order, high-resolution simulations contain the most structures, with more pronounced and localized peaks. By contrast, low-resolution, low-order simulations have fewer peaks that are spread over a larger

portion of the mixing layer. This observation can be explained in terms of varying numerical diffusion. Simulations with low-order and low-resolution have larger numerical dissipation, which results in more complete mixing and, therefore, in peaks with larger amplitudes before reshock. Concomitantly, the large numerical diffusion suppresses the formation of small-scale structures. Reshock imparts more uniform energy on the interface, which combined with the stronger inverse cascade, leads to the formation of large-scale, symmetric structures. These structures appear in the profiles as larger, uniform peaks. By contrast, high-resolution, high-order simulations have smaller numerical diffusion, resulting in smaller peaks prior to reshock. However, the small dissipation does not suppress the small-scale structures. These small-scale structures are then amplified by reshock and lead to the formation of additional small-scale, complex structures. This fragmented structure is reflected in the profiles as a complex series of localized peaks. Note that due to the two-dimensional nature of the equations considered here, the effects of resolution and order of reconstruction can be directly related to the effects of numerical dissipation. In three-dimensional simulations, the additional mechanism of vortex stretching exists and must be considered. The results presented here clearly and quantitatively demonstrate that numerical dissipation effects are significant, as different characterizations of mixing are possible depending on the grid resolution and order of reconstruction.

6.3.4 The effects on the mixing fractions

The integrated mixing fractions also depend significantly on the order of reconstruction and on the grid resolution. Again, the difference in results can be attributed to differences in the numerical dissipation. Low-order, low-resolution simulations have increased numerical dissipation, resulting in greater overall mixing as measured by the production mixing fractions P_t, both before and after reshock. High-order, high-resolution simulations have smaller numerical dissipation, resulting in lower values of the mixing fraction P_t. The maximum production fraction P_m exhibits different behavior. Before reshock, the values of P_m from all of the simulations are similar, consistent with similar widths of the mixing layer and similar structures as the instability develops. Following reshock, the mixing layer width obtained from high-order, high-resolution simulations is larger and causes the value of P_m (as measured across the large mixing layer width) to decrease. High-order, high-resolution simulations having the largest mixing layer widths exhibit the smallest values of P_m. This change in behavior following reshock is reflected in the values of the mixing fraction Ξ. Prior to reshock, low-resolution, low-order simulations show larger values of Ξ, consistent with increased overall mixing due to the higher numerical dissipation. However, following reshock, Ξ is not clearly correlated with the resolution and the order of flux reconstruction. Similar mechanisms can also explain the values of the molecular mixing fraction Θ, which do not show an identifiable correlation with the order of reconstruction and grid resolution. In summary, the results show that the increased numerical dissipation in low-resolution, low-order simulations affects mixing as measured by the mixing fractions. In particular, the mixing fractions quantify mixing across the entire layer, and therefore the differences in width affect the mixing fractions in ways that cannot be predicted easily a priori. For this reason, mixing fractions must be considered in the context of other quantities such as the mixing layer width, and do not provide direct characterizations of the numerical mechanisms in the algorithm. This is in contrast to the mixing layer width, which correlates very strongly with the numerical dissipation of the method.

6.3.5 The effects on the spectra

The effects of grid resolution and order of reconstruction on spectra can be understood based on the presence of small-scale structures and the numerical dissipation of the method. The difference in magnitude observed in the kinetic energy spectrum across different resolutions and orders of reconstruction is a direct consequence of the presence of small-scale flow features. High-resolution, high-order simulations support small-scale features resulting in larger fluctuations. These fluctuations are further amplified during reshock and yield energy spectra that are similar in shape but much larger in magnitude. Consider instead the density variance spectrum: all curves overlap for a portion of the spectrum, but show a steep decline depending on the resolution and order of the method. This is a direct consequence of the numerical dissipation damping the fluctuations beyond a certain scale. Comparing simulations with different orders of flux reconstruction and different grid resolutions for the enstrophy shows both the effects of small-scale structures and the effects of numerical dissipation. Similarly, the pressure variance spectrum also shows a dependence on both mechanisms. As observed from the ratio of each spectrum from the simulations with different orders and resolutions to the spectrum obtained from the ninth-order simulation on the fine grid, there is no apparent 'convergence' of the spectra: this indicates that quantities sensitive to the small-scale structure of the flow do not generally exhibit 'convergence' while quantities determined primarily by the large-scale structures appear to be 'converged' at sufficiently high order of reconstruction and grid resolution, *i.e.*, the mixing layer amplitude or width (as shown in § 5.2).

6.3.6 The effects on the statistics

Statistics are affected differently by changes in order of reconstruction and grid resolution. The fluctuating enstrophy shows the most variation and indicates that the higher numerical dissipation associated with low-order, low-resolution simulations causes the fluctuating enstrophy to decrease significantly. This result is also consistent with the large variations for the fluctuating enstrophy spectra where a cascade to larger wavenumbers was observed in high-order, high-resolution simulations. The cascade causes the integrated statistics to have larger values, as an increased number of modes with similar energy is obtained. The fluctuating kinetic energy and pressure variance show little variation, as the differences in spectra observed earlier are not reflected in the integrated statistics. The periodic component of the fluctuating kinetic energy shows variations following reshock due to the presence of small-scale disordered features in high-order, high-resolution simulations.

6.4 Conclusions

Very little experimental data is available after reshock to aid in validating and constraining numerical simulation data. The present simulations provide pointwise data that can be used to compute profiles across the mixing layer, measures of mixing, spectra, and statistics. Thus, this work is representative of an effort to use a validated shock-capturing method to obtain detailed data not presently available from experiments. For example, there are currently no experimental measurements of molecular mixing or data concerning the internal structure of the mixing layer. Also, energy spectra have not been obtained from experimental data. Experimental data accurately measuring quantities depending on spatial derivatives or quantities sensitive to small-scale mixing (*e.g.*, mixing fractions) would be very helpful in discriminating between the different simulation results obtained across a range of orders and resolutions.

The quantities investigated in this report are not exhaustive. Additional quantities will be considered in Part 4 of this report [70], including probability distribution functions and turbulent transport quantities. Detailed data from such simulations can be used to investigate turbulent transport and mixing model initialization, and the properties and predictions of turbulent transport and mixing models following reshock and late in time.

Acknowledgments

The authors thank Dr. Wai-Sun Don from Brown university for assistance with all aspects of the `HOPE` code. The authors also thank Dr. Karnig O. Mikaelian for useful comments on the perturbation amplitude models for the Rayleigh-Taylor and Richtmyer-Meshkov instability, and Dr. Jeffrey W. Jacobs from the University of Arizona for clarifying aspects of the experiments considered in this report. Marco Latini also acknowledges support from the Air Force Office of Scientific Research through the National Defense Science and Engineering Graduate Fellowship. This work was performed under the auspices of the U.S. Department of Energy by the University of California, Lawrence Livermore National Laboratory under Contract No. W-7405-Eng-48.

References

[1] S. I. Abarzhi, *Regular and singular late-time asymptotes of potential motion of fluid with a free boundary*, Phys. Fluids **12** (2000), 3112–3120.

[2] ———, *A new type of the evolution of the bubble front in the Richtmyer-Meshkov instability*, Phys. Lett. A **294** (2002), 95–100.

[3] ———, *Nonlinear evolution of unstable fluid interface*, Phys. Rev. E **66** (2002), 036301–1–036301–8.

[4] S. I. Abarzhi, J. Glimm, and A.-D. Lin, *Dynamics of two-dimensional Rayleigh-Taylor bubbles for fluids with a finite density contrast*, Phys. Fluids **15** (2003), 2190–2197.

[5] S. I. Abarzhi, K. Nishihara, and J. Glimm, *Rayleigh-Taylor and Richtmyer-Meshkov instabilities for fluids with a finite density ratio*, Phys. Lett. A **294** (2002), 95–100.

[6] U. Alon, J. Hecht, D. Mukamel, and D. Shvarts, *Scale invariant mixing rates of hydrodynamically unstable interfaces*, Phys. Rev. Lett. **72** (1994), 2867–2870.

[7] U. Alon, J. Hecht, D. Ofer, and D. Shvarts, *Power laws and similarity of Rayleigh-Taylor and Richtmyer-Meshkov mixing fronts at all density ratios*, Phys. Rev. Lett. **74** (1995), 534–537.

[8] U. Alon, D. Shvarts, and D. Mukamel, *Scale-invariant regime in Rayleigh-Taylor bubble-front dynamics*, Phys. Rev. E **48** (1993), 1008–1014.

[9] M. J. Andrews and D. B. Spalding, *A simple experiment to investigate two-dimensional mixing by Rayleigh-Taylor instability*, Phys. Fluids A **2** (1990), 922–927.

[10] D. Arnett, *The role of mixing in astrophysics*, Astrophys. J. Suppl. **127** (2000), 213–217.

[11] W. D. Arnett, *Supernova theory and supernova 1987A*, Astrophys. J. **319** (1987), 136–142.

[12] W. D. Arnett, B. A. Fryxell, and E. Müller, *Instabilities and nonradial motion in SN-1987A*, Astrophys. J. **341** (1989), L63–L66.

[13] S. Atzeni and J. Meyer-ter Vehn, *The Physics of Inertial Confinement Fusion: Beam Plasma Interaction, Hydrodynamics, Hot Dense Matter*, International Series of Monographcs on Physics, vol. 125, Oxford University Press, New York, 2004.

[14] D. Balsara and C.-W Shu, *Monotonicity preserving weighted essentially non-oscillatory schemes with increasingly high order of accuracy*, J. Comput. Phys. **160** (2000), 405–452.

[15] G. I. Barenblatt, *Nonlinear Dynamics and Turbulence*, Pitman, Boston, 1983.

[16] C. M. Bender and S. A. Orszag, *Advanced Mathematical Methods for Scientists and Engineers*, Springer-Verlag, New York, 1999.

[17] J. P. Boris, F. F. Grinstein, E. S. Oran, and R. L. Kolbe, *New insights into large eddy simulation*, Fluid Dyn. Res. **10** (1992), 199–228.

[18] M. Brouillette, *The Richtmyer-Meshkov instability*, Ann. Rev. Fluid Mech. **34** (2002), 445–468.

[19] M. Brouillette and B. Sturtevant, *Growth induced by multiple shock waves normally incident on plane gaseous interfaces*, Physica D **37** (1989), 248–263.

[20] ———, *Experiments on the Richtmyer-Meshkov instability: Small-scale perturbations on a plane interface*, Phys. Fluids A **8** (1993), 916–930.

[21] ———, *Experiments on the Richtmyer-Meshkov instability: single-scale perturbations on a continuous interface*, J. Fluid Mech. **263** (1994), 271–292.

[22] R. L. Burden and J. D. Faires, *Numerical Analysis*, Brooks/Cole Publishing Company, Pacific Grove, CA, 1997.

[23] C. Canuto, M. Y. Hussaini, A. Quarteroni, and T. A. Zang, *Spectral Methods in Fluid Dynamics*, Springer-Verlag, New York, 1990.

[24] M. H. Carpenter and J. H. Casper, *Computational considerations for the simulation of discontinuous flows*, Barriers and Challenges in Computational Fluid Dynamics (V. Venkatakrishnan, M. D. Salas, and S. R. Chakravarthy, eds.), Kluwer Academic, Dordrecht, 1998, pp. 63–78.

[25] ———, *Accuracy of shock capturing in two spatial dimensions*, AIAA J. **37** (1999), 1072–1079.

[26] S. Chandrasekhar, *Hydrodynamic and Hydromagnetic Stability*, Dover Publications, New York, 1961.

[27] A. J. Chorin and J. E. Marsden, *A Mathematical Introduction to Fluid Mechanics*, third ed., Texts in Applied Mathematics, vol. 4, Springer-Verlag, New York, 1993.

[28] R. H. Cohen, W. P. Dannevik, A. M. Dimits, D. E. Eliason, A. A. Mirin, Y. Zhou, D. H. Porter, and P. R. Woodward, *Three-dimensional simulation of a Richtmyer-Meshkov instability with a two-scale initial perturbation*, Phys. Fluids **14** (2002), 3692–3709.

[29] B. D. Collins and J. W. Jacobs, *PLIF flow visualization and measurements of the Richtmyer-Meshkov instability of an air/SF_6 interface*, J. Fluid Mech. **464** (2002), 113–136.

[30] A. W. Cook, W. H. Cabot, and J. A. Greenough, *A High-Order Method for Shock-Induced Mixing*, Tech. Report UCRL-JC-144109, Lawrence Livermore National Laboratory, 2001.

[31] A. W. Cook and P. E. Dimotakis, *Transition stages of Rayleigh-Taylor instability between miscible fluids*, J. Fluid Mech. **443** (2001), 69–99, Corrigendum, J. Fluid Mech. **457** (2002), 410–411.

[32] G. Dimonte, D. L. Youngs, A. Dimits, S. Weber, M. Marinak, S. Wunsch, C. Garasi, A. Robinson, M. J. Andrews, P. Ramaprabhu, A. C. Calder, B. Fryxell, J. Biello, L. Dursi, P. MacNeice, K. Olson, P. Ricker, R. Rosner, F. Timmes, H. Tufo, Y.-N. Young, and M. Zingale, *A comparative study of the turbulent Rayleigh-Taylor instability using high-resolution three-dimensional numerical simulations: The Alpha-Group collaboration*, Phys. Fluids **16** (2004), 1668–1693.

[33] W.-S. Don, 2004, Private communication.

[34] R. Donat and S. Osher, *Propagation of error into regions of smoothness for non-linear approximations to hyperbolic equations*, Comp. Meth. Appl. Mech. and Eng. **80** (1990), 59–64.

[35] P. G. Drazin, *Kelvin-Helmholtz instability of finite amplitude*, J. Fluid Mech. **42** (1970), 321–335.

[36] P. G. Drazin and W. H. Reid, *Hydrodynamic Stability*, second ed., Cambridge Monographs on Mechanics and Applied Mathematics, Cambridge University Press, Cambridge, 2003.

[37] D. Drikakis, *Embedded turbulence model in numerical methods for hyperbolic conservation laws*, Int. J. Num. Meth. Fluids **39** (2002), 763–781.

[38] ———, *Advances in turbulent flow computations using high-resolution methods*, Prog. Aero. Sci. **39** (2003), 405–424.

[39] R. E. Duff, F. H. Harlow, and C. W. Hirt, *Effects of diffusion on interface instability between gases*, Phys. Fluids **5** (1962), 417–425.

[40] S. W. Falk and W. D. Arnett, *A theoretical model for type II supernovae*, Astrophys. J. **180** (1973), L65–L68.

[41] G. Fraley, *Rayleigh-Taylor stability for a normal shockwave-density discontinuity interaction*, Phys. Fluids **29** (1986), 376–386.

[42] V. N. Goncharov, *Analytical model of nonlinear, single-mode, classical Rayleigh-Taylor instability at arbitrary Atwood numbers*, Phys. Rev. Lett. **88** (2002), 134501–1–134501–4.

[43] D. Gottlieb and S. A. Orszag, *Numerical Analysis of Spectral Methods: Theory and Application*, SIAM, Philadelphia, 1977.

[44] X. He, S. Chen, and R. Zhang, *A lattice Boltzmann scheme for incompressible multiphase flow and its application in simulation of Rayleigh-Taylor instability*, J. Comput. Phys. **152** (1999), 642–663.

[45] J. Hecht, U. Alon, and D. Shvarts, *Potential flow models of Rayleigh-Taylor and Richtmyer-Meshkov bubble fronts*, Phys. Fluids **6** (1994), 4019–30.

[46] L. F. Henderson, *On the refraction of shock waves*, J. Fluid Mech. **198** (1989), 365–386.

[47] D. J. Hill and D. I. Pullin, 2004, Private communication.

[48] R. L. Holmes, G. Dimonte, B. Fryxell, M. L. Gittings, J. W. Grove, M. Schneider, D. H. Sharp, A. L. Velikovich, R. P. Weaver, and Q. Zhang, *Richtmyer-Meshkov instability growth: experiment, simulation and theory*, J. Fluid Mech. **389** (1999), 55–77.

[49] R. L. Holmes, J. W. Grove, and D. H. Sharp, *Numerical investigation of Richtmyer-Meshkov instability using front-tracking*, J. Fluid Mech. **301** (1995), 51–64.

[50] L. Houas and I. Chemouni, *Experimental investigation of Richtmyer-Meshkov instability in shock tube*, Phys. Fluids **8** (1996), 614–627.

[51] J. W. Jacobs, *The dynamics of shock accelerated light and heavy gas cylinders*, Phys. Fluids A **5** (1993), 2239–2247.

[52] ———, 2005, Private communication.

[53] J. W. Jacobs, D. G. Jenkins, D. L. Klein, and R. F. Benjamin, *Nonlinear growth of the shock-accelerated instability of a thin fluid layer*, J. Fluid Mech. **295** (1995), 23–42.

[54] J. W. Jacobs, M. A. Jones, and C. E. Niederhaus, *Experimental studies of Richtmyer-Meshkov instability*, Proceedings of the Fifth International Workshop on Compressible Turbulent Mixing (R. Young, J. Glimm, and B. Boston, eds.), World Scientific, New York, 1996, pp. 195–202.

[55] J. W. Jacobs and J. M. Sheeley, *Experimental study of incompressible Richtmyer-Meshkov instability*, Phys. Fluids **8** (1996), 405–415.

[56] M. A. Jones and J. W. Jacobs, *A membraneless experiment for the study of Richtmyer-Meshkov instability of a shock-accelerated gas interface*, Phys. Fluids **9** (1997), 3078–3085.

[57] J. Kane, R. P. Drake, and B. A. Remington, *An evaluation of the Richtmyer-Meshkov instability in supernova remnant formation*, Astrophys. J. **511** (1999), 335–340.

[58] H. Kellay and W. I Goldburg, *Two-dimensional turbulence: a review of some recent experiments*, Rep. Prog. Physics **65** (2002), 845–894.

[59] S. Kida and S. A. Orszag, *Enstrophy budget in decaying compressible turbulence*, J. Sci. Comput. **5** (1990), 1–34.

[60] ———, *Energy and spectral dynamics in decaying compressible turbulence*, J. Sci. Comput. **7** (1992), 1–34.

[61] M. M. Koochesfahani and P. E. Dimotakis, *Mixing and chemical reactions in a turbulent liquid mixing layer*, J. Fluid Mech. **170** (1986), 83–112.

[62] A. D. Kotelnikov, J. Ray, and N. J. Zabusky, *Vortex morphologies on reaccelerated interfaces: Visualization, quantification and modeling of one- and two-mode compressible and incompressible environments*, Phys. Fluids **12** (2000), 3245–3264.

[63] A. D. Kotelnikov and N. J. Zabusky, *Vortex dynamics of a twice-accelerated interface in an incompressible ideal fluid*, Astrophys. J. Suppl. **127** (2000), 389–394.

[64] R. H. Kraichnan and D. Montgomery, *Two-dimensional turbulence*, Rep. Progr. Phys. **43** (1980), 547–619.

[65] K. Kremeyer, S. Nazarenko, and A. C. Newell, *Shock bowing and vorticity dynamics during propagation into different transverse density profiles*, Physica D **163** (2002), 150–165.

[66] C. B. Laney, *Computational Gasdynamics*, Cambridge University Press, New York, 1998.

[67] M. Latini, *Investigation of the Richtmyer-Meshkov Instability in Complex Geometries using the Weighted Essentially Non-Oscillatory Method and Vortex Methods*, Ph.D. thesis, California Institute of Technology, 2006, In preparation.

[68] M. Latini and O. Schilling, *Weighted Essentially Non-Oscillatory Simulations and Modeling of Complex Hydrodynamic Flows. Part 1. Regular Shock Refraction*, Tech. Report UCRL-TR-205132, Lawrence Livermore National Laboratory, 2004.

[69] ———, *Weighted Essentially Non-Oscillatory Simulations and Modeling of Complex Hydrodynamic Flows. Part 3. The Shock-Oblique Interface Richtmyer-Meshkov Instability*, Tech. report, Lawrence Livermore National Laboratory, 2004.

[70] ———, *Weighted Essentially Non-Oscillatory Simulations and Modeling of Complex Hydrodynamic Flows. Part 4. Multi-Mode Richtmyer-Meshkov Instability with Reshock*, Tech. report, Lawrence Livermore National Laboratory, 2004.

[71] D. Layzer, *On the instability of superposed fluids in a gravitational field*, Astrophys. J. **122** (1955), 1–12.

[72] M. Lesieur, C. Staquet, P. Le Roy, and P. Comte, *The mixing layer and its coherence examined from the point of view of two-dimensional turbulence*, J. Fluid Mech. **192** (1988), 511–534.

[73] R. J. Leveque, *Finite Volume Methods for Hyperbolic Problems*, Cambridge Texts in Applied Mathematics, Cambridge University Press, New York, 2002.

[74] O. A. Likhachev and J. W. Jacobs, *A vortex model for the Richtmyer-Meshkov instability accounting for finite Atwood number*, Phys. Fluids **17** (2005), 031704–1–031704–3.

[75] J. D. Lindl, *Development of the indirect-drive approach to inertial confinement fusion and the target physics basis for ignition and gain*, Phys. Plasmas **2** (1995), 3933–4024.

[76] ———, *Inertial Confinement Fusion: The Quest for Ignition and Energy Gain Using Indirect Drive*, AIP Press, New York, 1998.

[77] A. Majda and S. Osher, *Propagation of error into regions of smoothness for accurate difference approximations to hyperbolic equations*, Comm. Pure Appl. Math. **30** (1977), 671–705.

[78] A. Marquina and P. Mulet, *A flux-split algorithm applied to conservative models for multicomponent compressible flows*, J. Comput. Phys **185** (2003), 120–138.

[79] C. Matsuoka, K. Nishihara, and Y. Fukuda, *Nonlinear evolution of an interface in the Richtmyer-Meshkov instability*, Phys. Rev. E **67** (2003), 036301–1–036301–14.

[80] D. I. Meiron, G. R. Baker, and S. A. Orszag, *Analytic structure of vortex sheet dynamics. Part 1. Kelvin-Helmholtz instability*, J. Fluid Mech. **114** (1982), 283–298.

[81] R. Menikoff and C. Zemach, *Rayleigh-Taylor instability and the use of conformal maps for ideal fluid flow*, J. Comput. Phys **51** (1983), 28–64.

[82] E. E. Meshkov, *Instability of the interface of two gases accelerated by a shock wave*, Sov. Fluid Dyn. **4** (1969), 101–108.

[83] K. A. Meyer and P. J. Blewett, *Numerical investigation of the stability of a shock accelerated interface between two fluids*, Phys. Fluids **15** (1972), 753–759.

[84] K. O. Mikaelian, *Normal-modes and symmetries of the Rayleigh-Taylor instability in stratified fluids*, Phys. Rev. Lett. **48** (1982), 1365–1368.

[85] ———, *Rayleigh-Taylor instabilities in stratified fluids*, Phys. Rev. A **26** (1982), 2140–2158.

[86] ———, *Approximate treatment of density gradients in Rayleigh-Taylor instabilities*, Phys. Rev. A **26** (1986), 1216–1222.

[87] ———, *Turbulent mixing generated by Rayleigh-Taylor and Richtmyer-Meshkov instabilities*, Physica D **36** (1989), 343–357.

[88] ———, *Density gradient stabilization of the Richtmyer-Meshkov instability*, Phys. Fluids A **3** (1991), 2638–2643.

[89] ———, *Growth rate of the Richtmyer-Meshkov instability at shocked interfaces*, Phys. Rev. Lett. **71** (1993), 2903–2906.

[90] ———, *Freeze-out and the effect of compressibility in the Richtmyer-Meshkov instability*, Phys. Fluids **1** (1994), 356–368.

[91] ———, *Numerical simulations of Richtmyer-Meshkov instabilities in finite-thickness fluid layers*, Phys. Fluids **8** (1996), 1269–1292.

[92] ———, *Analytic approach to nonlinear Rayleigh-Taylor and Richtmyer-Meshkov instabilities*, Phys. Rev. Lett. **80** (1998), 508–511.

[93] ———, *Explicit expressions for the single-mode Rayleigh-Taylor and Richtmyer-Meshkov instabilities at arbitrary Atwood numbers*, Phys. Rev. E **67** (2003), 026319–1–026319–7.

[94] C. Mügler and S. Gauthier, *Numerical simulations of single-mode Richtmyer-Meshkov experiments*, Phys. Rev. E **58** (1998), 4548–4555.

[95] ———, *Two-dimensional Navier-Stokes simulations of gaseous mixtures induced by Richtmyer-Meshkov instability*, Phys. Fluids **12** (2000), 1783–1798.

[96] S. Nakai and H. Takabe, *Principles of inertial confinement fusion–physics of implosion and the concept of inertial fusion energy*, Rep. Prog. Physics **59** (1996), 1071–1131.

[97] C. E. Niederhaus, *Experiments on the Richtmyer-Meshkov Instability of Incompressible Fluids*, Ph.D. thesis, University of Arizona, 2000.

[98] C. E. Niederhaus and J. W. Jacobs, *Experimental study of the Richtmyer-Meshkov instability of incompressible fluids*, J. Fluid Mech. **485** (2003), 243–277.

[99] Sadot O., L. Erez, U. Alon, D. Oron, and L. A. Levin, *Study of nonlinear evolution of single-mode and two bubble interaction under Richtmyer-Meshkov instability*, Phys. Rev. Lett. **80** (1998), 1654–1657.

[100] E. S. Oran and J. P. Boris, *Numerical Simulation of Reactive Flow*, second ed., Cambridge University Press, Cambridge, 2001.

[101] G. Peng, N. J. Zabusky, and S. Zhang, *Vortex-accelerated secondary baroclinic vorticity deposition and late-intermediate time dynamics of a two-dimensional Richtmyer-Meshkov interface*, Phys. Fluids **15** (2003), 3730–3744.

[102] S. B. Pope, *Turbulent Flows*, Cambridge University Press, Cambridge, UK, 2000.

[103] J. K. Prasad, A. Rasheed, S. Kumar, and B. Sturtevant, *The late-time development of the Richtmyer-Meshkov instability*, Phys. Fluids **12** (2000), 2108–2115.

[104] J. Ray, *Circulation Deposition and Interface Growth Rate in Richtmyer-Meshkov Environments: Scaling Laws and Reduced Models*, Master's thesis, Rutgers University, 1997.

[105] K. I. Read, *Experimental investigation of turbulent mixing by Rayleigh-Taylor instability*, Physica D **12** (1984), 45–58.

[106] R. D. Richtmyer, *Taylor instability in shock acceleration of compressible fluids*, Comm. Pure Appl. Math. **8** (1960), 297–319.

[107] P. M. Rightley, P. Vorobieff, and R. F. Benjamin, *Evolution of a shock-accelerated thin fluid layer*, Phys. Fluids **9** (1997), 1770–1782.

[108] A. Rikanati, U. Alon, and D. Shvarts, *Vortex model for the nonlinear evolution of the multimode Richtmyer-Meshkov instability at low Atwood numbers*, Phys. Rev. E **58** (1998), 7410–7418.

[109] J. R. Ristorcelli and T. T. Clark, *Rayleigh-Taylor turbulence: self-similar analysis and direct numerical simulations*, J. Fluid Mech. **507** (2004), 213–253.

[110] O. Sadot, L. Erez, G. Oron, G. Ben-Dor, U. Alon, L. A. Levin, and D. Shvarts, *Studies on the nonlinear evolution of the Richtmyer-Meshkov instability*, Astrophys. J. Suppl. **127** (2000), 469–473.

[111] P. G. Saffman and D. I. Meiron, *Kinetic energy generated by the incompressible Richtmyer-Meshkov instability in a continuously stratified fluid*, Phys. Fluids A **1** (1989), 1767–1771.

[112] R. Samtaney, J. Ray, and N. J. Zabusky, *Baroclinic circulation generation on shock accelerated slow/fast gas interfaces*, Phys. Fluids **10** (1998), 1217–1230.

[113] R. Samtaney and N. J. Zabusky, *Circulation deposition on shock-accelerated planar and curved density stratified interfaces: models and scaling laws*, J. Fluid Mech. **269** (1994), 45–78.

[114] J. Shi, Y.-T. Zhang, and C.-W. Shu, *Resolution of high order WENO schemes for complicated flow structures*, J. Comput. Phys **186** (2003), 690–696.

[115] S.-I. Sohn, *Simple potential-flow model of Rayleigh-Taylor and Richtmyer-Meshkov instabilities for all density ratios*, Phys. Rev. E **67** (2003), 026301–1–026301–5.

[116] J. Sommeria, *Two-dimensional turbulence*, New Trends in Turbulence (Les Houches Summer School on Theoretical Physics LXXIV, 2000) (M. Lesieur, A. Yaglom, and F. David, eds.), Springer-Verlag, 2001, pp. 385–447.

[117] P. Tabeling, *Two-dimensional turbulence: a physicist approach*, Phys. Rep. **362** (2002), 1–62.

[118] J. C. Tannehill, D. A. Anderson, and R. H. Pletcher, *Computational Fluid Mechanics and Heat Transfer*, second ed., Series in Computational and Physical Processes in Mechanics and Thermal Sciences, Taylor and Francis, New York, 1997.

[119] G. I. Taylor, *The instability of liquid surfaces when accelerated in a direction perpendicular to their planes*, Proc. R. Soc. Lond. A Mat. **201** (1950), 192–196.

[120] G. Tryggvason, *Numerical simulations of the Rayleigh-Taylor instability*, J. Comput. Phys. **75** (1988), 253–282.

[121] M. Vandenboomgaerde, S. Gauthier, and C. Mügler, *Nonlinear regime of a multimode Richtmyer-Meshkov instability: a simplified perturbation theory*, Phys. Fluids **14** (2002), 1111–1122.

[122] M. Vandenboomgaerde, C. Mügler, and S. Gauthier, *Impulsive model for the Richtmyer-Meshkov instability*, Phys. Rev. E **58** (1998), 1874–1882.

[123] M. Vetter and B. Sturtevant, *Experiments on the Richtmyer-Meshkov instability of an air/SF_6 interface*, Shock Waves **4** (1995), 247–252.

[124] D. L. Youngs, *Numerical simulation of turbulent mixing by Rayleigh-Taylor instability*, Physica D **12** (1984), 32–44.

[125] ———, *Three-dimensional numerical simulations of turbulent mixing by Rayleigh-Taylor instability*, Phys. Fluids A **3** (1991), 1312–1320.

[126] ———, *Numerical simulation of mixing by Rayleigh-Taylor and Richtmyer-Meshkov instabilities*, Laser Part. Beams **12** (1994), 725–750.

[127] N. J. Zabusky, *Vortex paradigm for accelerated inhomogeneous flows: Visiometrics for the Rayleigh-Taylor and Richtmyer-Meshkov environments*, Ann. Rev. Fluid Mech. **31** (1999), 495–536.

[128] N. J. Zabusky, A. D. Kotelnikov, Y. Gulak, and G. Peng, *Amplitude growth rate of a Richtmyer-Meshkov unstable two-dimensional interface to intermediate times*, J. Fluid Mech. **475** (2003), 147–162.

[129] Q. Zhang, *Analytical solution of Layzer-type approach to unstable interfacial fluid mixing*, Phys. Rev. Lett. **81** (1998), 3391–3394.

[130] Q. Zhang and S. Sohn, *Non-linear theory of unstable fluid mixing driven by shock wave*, Phys. Fluids **9** (1997), 1106–1124.

[131] S. Zhang, N. J. Zabusky, G. Peng, and S. Gupta, *Shock gaseous cylinder interactions: Dynamically validated initial conditions provide excellent agreement between experiments and numerical simulations to late–intermediate time*, Phys. Fluids **16** (2004), 1203–1216.